

SPATIAL AND TEMPORAL DYNAMICS OF PRIMARY PRODUCTION IN
ANTARCTIC SEA ICE

A DISSERTATION
SUBMITTED TO THE DEPARTMENT OF
ENVIRONMENTAL EARTH SYSTEM SCIENCE
AND THE COMMITTEE ON GRADUATE STUDIES
OF STANFORD UNIVERSITY
IN PARTIAL FULFILLMENT OF THE REQUIREMENTS
FOR THE DEGREE OF
DOCTOR OF PHILOSOPHY

Benjamin Lundquist Saenz

May 2011

© 2011 by Benjamin Lundquist Saenz. All Rights Reserved.
Re-distributed by Stanford University under license with the author.



This work is licensed under a Creative Commons Attribution-
Noncommercial 3.0 United States License.
<http://creativecommons.org/licenses/by-nc/3.0/us/>

This dissertation is online at: <http://purl.stanford.edu/pr685xp6352>

I certify that I have read this dissertation and that, in my opinion, it is fully adequate in scope and quality as a dissertation for the degree of Doctor of Philosophy.

Kevin Arrigo, Primary Adviser

I certify that I have read this dissertation and that, in my opinion, it is fully adequate in scope and quality as a dissertation for the degree of Doctor of Philosophy.

Margot Gerritsen

I certify that I have read this dissertation and that, in my opinion, it is fully adequate in scope and quality as a dissertation for the degree of Doctor of Philosophy.

Leif Thomas

Approved for the Stanford University Committee on Graduate Studies.

Patricia J. Gumpert, Vice Provost Graduate Education

This signature page was generated electronically upon submission of this dissertation in electronic format. An original signed hard copy of the signature page is on file in University Archives.

SPATIAL AND TEMPORAL DYNAMICS OF PRIMARY PRODUCTION IN ANTARCTIC SEA ICE

Benjamin Lundquist Saenz, Ph.D.
Stanford University, 2011

Reading Committee Member: Kevin R. Arrigo, Ph.D.

Sea ice is an important driver of climate patterns and polar marine ecosystem dynamics. In particular, primary production by microalgae in sea ice has been postulated as a sink for anthropogenic CO₂, and as a critical resource in the life cycle of Antarctic krill *Euphausia superba*, a keystone species. Study of the sea ice ecosystem is difficult at regional and global scales, however, because of the expense and logistical difficulties in accessing such a remote and hostile environment. Consequently, models remain valuable tools for investigations of the spatial and temporal dynamics of sea ice and associated ecology and biogeochemistry. Recent advances in model representations of sea ice have called into question the accuracy of previous studies, and allow the creation of new tools to perform mechanistic simulations of sea ice physics and biogeochemistry. To address spatial and temporal variability in Antarctic sea ice algal production, and to establish the bounds and sensitivities of the sea ice ecosystem, a new, coupled sea ice ecosystem model was developed. In the vertical dimension, the model resolves incorporated saline brine, macronutrients concentrations, spectral shortwave radiation, and the sea ice algae community at high resolution. A novel method for thermodynamics, desalination, and fluid transfer in slushy, high-brine fraction sea ice was developed to simulate regions of high algal productivity. The processes of desalination, fluid transfer, snow-ice creation, and superimposed ice formation allowed the evolution of realistic vertical profiles of sea ice salinity and algal growth. The model replicated time series observations of ice temperature, salinity, algal biomass, and estimated fluid flux from the Ice Station Weddell experiment. In the horizontal dimension, sub-grid scale

parameterizations of snow and ice thickness allow more realistic simulation of the ice thickness distribution, and consequently, sea ice algal habitat. The model is forced from above by atmospheric reanalysis climatologies, and from below by climatological ocean heat flux and deep-water ocean characteristics. Areal sea ice concentration and motion are specified according to SSM/I passive microwave satellite estimates of these parameters. Sensitivity testing of different snow and ice parameterizations showed that without a sub-grid scale ice thickness distribution, mean ice and snow thickness is lower and bottom sea ice algal production is elevated. Atmospheric forcing from different reanalysis data sets cause mean and regional shifts in sea ice production and associated ecology, even when sea ice extent and motion is controlled. Snow cover represents a first-order control over ice algal production by limiting the light available to bottom ice algal communities, and changes to the regional, rather than mean, snow thickness due to the use of different ice and snow representations are responsible for large differences in the magnitude and distribution of sea ice algal production. Improved convective nutrient exchange in high-brine fraction (slush) sea ice is responsible for up to 18% of total sea ice algal production. A continuous 10-year model run using climatological years 1996-2005 produced a time series of sea ice algal primary production that varied between 15.5 and 18.0 Tg C yr⁻¹. This study represents the first interannual estimate of Antarctic sea ice algal production that dynamically considers the light, temperature, salinity, and nutrient conditions that control algal growth. On average, 64% of algal production occurred in the bottom 0.2 m of the ice pack. Production was spatially heterogeneous, with little consistency between years when examined at regional scales; however, at basin or hemispheric scales, annual production was fairly consistent in magnitude. At a mean of 0.9 g C m⁻² yr⁻¹, the magnitude of carbon uptake by sea ice algae will not significantly affect the Southern Ocean carbon cycle. Light availability was the dominant control on sea ice algae growth over the majority of the year; however, severe nutrient limitation that occurred annually during late spring and summer proved to be the largest control over sea ice algal productivity.

ACKNOWLEDGMENTS

This thesis was developed under the guidance and wisdom of Dr. Kevin Arrigo, a terrifically balanced mentor, scientist, and regular guy. Gert van Dijken humbly provided invaluable technical and science support and critique, without which this project would still be under construction. Stanford lab members past and present delivered invaluable council, support, laughs, and extremely tedious, yet productive, lab meetings: Al Tagliabue, Rochelle Labiosa, Tasha Reddy, Sudeshna Pabi, Lindsey Kropuenske Artman, Matt Mills, Mine Berg, Anne-Carlijn Alderkamp, Molly Palmer, Zach Brown, and Kate Lowry. Professors Rob Dunbar and Adina Paytan were instrumental in piquing my scientific interest in ocean science. Margot Gerristen performed much needed counseling concerning math, modeling efficiency and discretization. Leif Thomas showed patience and brains when wading through differential equations with me. Oliver Finger generously served as defense committee chair. My reading committee members Kevin Arrigo, Leif Thomas, Margo Gerristen, and defense committee member Karen Casciotti provided helpful critique on manuscripts that significantly strengthened this work. Beyond Stanford, this thesis benefited immeasurably from conversation, advice, and data from Steve Ackley, Don Perovich, Chris Fritsen, Ken Golden, Sharon Stammerjohn, and Ted Maksym. Thank you to my parents, Mike and Kathi Saenz, and my sister Becca for both encouraging me, and showing me, that you should pursue what you want to do. Kirsten, Alita and Dakota – my family – thank you for supporting me, distracting me when I needed it, and finally allowing me to push through to the ‘end.’

The work was made possible through a NASA Earth System Science (ESS) Fellowship to Benjamin Saenz, and NASA OES grant NR-A04-OSE-02 to Kevin Arrigo. I received additional financial support from Stanford University School of Earth Sciences, including a Robert G. Kirby Fellowship, BP Fellowships, and an Edmund Wattis Littlefield Fellowship. Parts of this study benefited from computational resources at the Center for Computational Earth & Environmental Sciences (CEES) at the School of Earth Sciences.

For Kirsten, Alita-Pita, and D-Dragon

TABLE OF CONTENTS

Introduction	1
Chapter 1 - Refining simulation of sea ice ecosystems: a quasi-empirical method for slush layer desalination	
1. Introduction.....	9
2. Model Description.....	14
3. Ice Station Weddell Site B Simulation.....	36
4. Ice Station Weddell Site A Simulation.....	58
5. Desalination Exploration.....	67
6. Discussion.....	86
Chapter 2 - Effects of snow and ice representation in hemispheric, biophysical simulations of sea ice	
1. Introduction.....	97
2. Model Description.....	99
3. Simulations.....	118
4. Validation.....	120
5. Results.....	129
6. Discussion.....	155
Chapter 3 - Spatial and temporal Antarctic sea ice algal dynamics	
1. Introduction.....	167
2. Methods.....	170
3. Model Validation.....	175
4. Results.....	180
5. Discussion	205
List of References	213

LIST OF TABLES

Chapter 1 - Refining simulation of sea ice ecosystems: a quasi-empirical method for slush layer desalination

Table 1.	Notation.....	16
Table 2.	Model parameters and constants.....	16
Table 3.	Intrinsic optical properties (IOPs) of ice and snow classes used by the delta-Eddington spectral shortwave attenuation model.....	25
Table 4.	Thickness-dependent salinity values (psu) used to derive initial salinity profiles for model runs, with initial ice thickness h	40
Table 5.	Forcing data sources.....	40
Table 6.	ISW model runs and parameters.....	42
Table 7.	Integrated convective brine flux volumes for ISWB simulations using different values of the minimum inter-layer brine salinity difference.....	55
Table 8.	Desalination exploration model runs and parameters.....	70

Chapter 2 - Effects of snow and ice representation in hemispheric, biophysical simulations of sea ice

Table 1.	Ice thickness distribution (ITD) category bounds	107
Table 2.	Lognormal snow thickness distribution multipliers	108
Table 3.	Monthly ocean heat flux values.....	113
Table 4.	Selected model constants and parameters	117
Table 5.	Thickness-dependent salinity values (psu) used to derive initial multi-year salinity profiles for model runs, with initial ice thickness z	117
Table 6.	Model run descriptions.....	119
Table 7.	Summary of matching ASPeCT observations and modeled snow and ice thicknesses.....	125
Table 8.	Annual mean snow and ice thickness.....	133
Table 9.	Annual ice production.....	137
Table 10.	SSM/I sea ice area and total ice presence.....	140
Table 11.	Annual algal productivity.....	148

LIST OF TABLES (continued)

Chapter 3 - Spatial and temporal Antarctic sea ice algal dynamics

Table 1.	Total annual (July – June) sea ice algal production.....	181
Table 2.	Annual (July – June) bottom ice algal production.....	181
Table 3.	Annual (July – June) interior ice algal production.....	182
Table 4.	Annual mean daily (July – June) ice extent.....	182
Table 5.	Annual (July – June) mean areal algal productivity	186
Table 6.	Significant pairwise correlations between measures of algal production and sea ice characteristics in pooled analysis sectors.....	199
Table 7.	Algal production-weighted mean snow and ice characteristics.....	202

LIST OF ILLUSTRATIONS

Chapter 1 - Refining simulation of sea ice ecosystems: a quasi-empirical method for slush layer desalination

<p>Figure 1. Cut-away section of sea ice showing sea ice internal structure and brine features that influence desalination</p> <p>Figure 2. Model conceptual schematic showing the major components of the sea ice model in the order that they occur</p> <p>Figure 3. The relationship between heat flux and sea ice growth rate using an empirical stable salinity relationship and sea ice state equations.</p> <p>Figure 4. Operational diagram of the desalination scheme.....</p> <p>Figure 5. Measured surface air temperature and observed snow depths at Ice Station Weddell used as forcing data for model simulations</p> <p>Figure 6. Vertical diagram of the different ice types and used as initial conditions for ISWB and ISWA simulations.....</p> <p>Figure 7. A comparison of observed and modeled temperature contours within the ice pack over time at ISW Site B</p> <p>Figure 8. Evolution of modeled slush layer salinity over a range of critical brine fractions</p> <p>Figure 9. ISWB sea ice model depth profile evolution over time of A) NO_3 concentration, and B) algal biomass.....</p> <p>Figure 10. Total ISWB ice column Chl α concentration observed and modeled using a range of ϕ_{crit}.....</p> <p>Figure 11. Daily convective brine flux volume during ISWB simulations with varied ϕ_{crit}.....</p> <p>Figure 12. Depth of the ISWB freezing front over time for different values of ϕ_{crit} as demonstrated by the -2 °C isotherm.....</p> <p>Figure 13. Depth of the ISWB freezing front over time for different model grid spacing as demonstrated by the -2 °C isotherm.....</p> <p>Figure 14. Evolution of modeled slush layer salinity over a range of model grid spacing.....</p> <p>Figure 15. Daily convective brine flux volume during ISWB simulations with varied model grid spacing.....</p> <p>Figure 16. Total ISWB ice column Chl α concentration observed and modeled using different model grid spacing.....</p> <p>Figure 17. Observed and modeled freezing fronts at ISWA.....</p> <p>Figure 18. Evolution of ISWA modeled slush layer salinity for model run using different values of ϕ_{crit}.....</p> <p>Figure 19. Total ice column Chl α concentration observed and modeled using a range of ϕ_{crit} for ISW Site A.....</p> <p>Figure 20. Vertical diagram of ice types used as initial conditions in the salinity exploration simulations.....</p>	<p>12</p> <p>15</p> <p>31</p> <p>32</p> <p>37</p> <p>39</p> <p>44</p> <p>46</p> <p>47</p> <p>48</p> <p>50</p> <p>51</p> <p>54</p> <p>56</p> <p>57</p> <p>59</p> <p>61</p> <p>64</p> <p>66</p> <p>68</p>
--	---

LIST OF ILLUSTRATIONS (continued)

Figure 21.	Physical parameters from ‘new ice’ runs (DX1-DX4).....	71
Figure 22.	Biological parameters from ‘new ice’ runs (DX1-DX4).....	72
Figure 23.	Ice column algal concentration from ‘new ice’ model runs (DX1-DX4) through time, plotted against the evolving ice column profile	73
Figure 24.	Physical parameters from ‘moderate flooding’ runs (DX5-DX8)...	77
Figure 25.	Biological parameters from ‘moderate flooding’ runs (DX5-DX8).	78
Figure 26.	Ice column algal concentration from ‘moderate flooding’ model runs (DX5-DX8) through time, plotted against the evolving ice column profile	79
Figure 27.	Physical parameters from ‘deep flooding’ runs (DX9-DX12).....	83
Figure 28.	Biological parameters from ‘deep flooding’ runs (DX9-DX12)....	84
Figure 29.	Ice column algal concentration from ‘deep flooding’ model runs (DX9-DX12) through time, plotted against the evolving ice column profile	85

Chapter 2 - Effects of snow and ice representation in hemispheric, biophysical simulations of sea ice

Figure 1.	The sea ice model domain with black representing the land mask...	101
Figure 2.	Diagram of the vertical model grid structure representing snow and ice.....	102
Figure 3.	Diagrammatic illustration of the changes to the model ice snow thickness distribution (STD) during flooding	110
Figure 4.	ASPeCT sea ice and snow cover observations, plotted according to location	121
Figure 5.	Comparison of the (A) frequency distribution and (B) monthly mean of snow thicknesses from ASPeCT observations and matching model output	122
Figure 6.	Comparison of the (A) frequency distribution and (B) monthly mean of sea ice thicknesses from ASPeCT observations and matching model output.....	124
Figure 7.	Plots of mean ice core algal biomass from 17 Antarctic field expeditions, overlaid with a line showing mean monthly sea ice biomass in the STND run	127
Figure 8.	Monthly histograms of sea ice algal biomass from the STND run, where n is the number of daily grid cell observations	128
Figure 9.	Spatial distribution of (A) mean model precipitation rate (ECMWF), (B) Total annual snowfall (ECMWF), (C) the difference in total annual snowfall over sea ice between the NCEP/DOE II reanalysis climatology, and the ECMWF Interim climatology, and (D) annual ice presence.....	130

LIST OF ILLUSTRATIONS (continued)

Figure 10.	Spatial distribution of simulated (A) mean annual snow thickness, (B) mean annual sea ice thickness, (C) Mean annual snow/ice interface temperature, (D) total annual bottom sea ice algal production, and (E) total annual interior ice algal production.....	132
Figure 11.	Time series plots of mean daily snow thickness from the entire model domain (A) and from different analysis sectors (B-F).....	135
Figure 12.	Time series plots of mean daily sea ice thickness from the entire model domain (A) and from different analysis sectors (B-F).....	139
Figure 13.	Spatial distribution of annual snow ice and congelation ice production the STND run	141
Figure 14.	Time series plots of total daily (A) and monthly (B-G) snow ice production for select model runs.....	142
Figure 15.	Time series plots of total daily (A) and monthly (B-G) congelation ice production for select model runs	144
Figure 16.	Comparison of mean surface and snow/ice interface temperatures over (A) the model domain and (B-F) analysis sectors for the STND and NCEP model runs	147
Figure 17.	Daily interior (>0.2 m above ice bottom) ice algae production over (A) the entire model domain and (B-F) different analysis sectors for select model runs	150
Figure 18.	Daily bottom (up to 0.2 m from ice bottom) ice algae production over (A) the entire model domain and (B-F) different analysis sectors for select model runs	153

Chapter 3 - Spatial and temporal Antarctic sea ice algal dynamics

Figure 1.	The sea ice model domain with black representing the land mask, divided into 5 sectors used to perform regional spatial analysis of model results.....	173
Figure 2.	Comparison of the (A) frequency distribution and (B) monthly mean ice thicknesses from ASPeCT sea ice observations and matching model output	177
Figure 3.	Comparison of the (A) frequency distribution and (B) monthly mean snow thicknesses from ASPeCT sea ice observations and matching model output	178
Figure 4.	Plots of mean ice core algal biomass from 17 Antarctic field expeditions, overlaid with modeled mean daily sea ice biomass, average over the 10-year model run	179
Figure 5.	Maps of the spatial distribution of total annual sea ice algal production over 10 model years	184

LIST OF ILLUSTRATIONS (continued)

Figure 6.	Spatial distribution of simulated (A) mean annual snow thickness, (B) mean annual sea ice thickness, (C) Mean annual snow/ice interface temperature, (D) total annual bottom sea ice algal production, and (E) total annual interior ice algal production.....	185
Figure 7.	Spatial distribution of mean annual bottom (A) and interior (B) sea ice algal production over the 10 years of the model run	187
Figure 8.	Maps of mean annual modeled ice presence (A) snow thickness (B), and ice thickness (C) over the 10 modeled years	188
Figure 9.	Mean seasonal sea ice algal biomass over 10 years of model output	190
Figure 10.	Mean total daily sea ice algal areal productivity (A) and mean total daily productivity (B), over 10 modeled years	192
Figure 11.	Mean daily biomass-weighted algal growth limitation terms	194
Figure 12.	Modeled mean daily interior and bottom sea ice algal production, compared to potential daily production with nutrient limitation removed	196
Figure 13.	Annual total and sector sea ice algal production plotted against ice presence	198
Figure 14.	Daily means of model ice thickness, snow thickness, and snow/ice interface temperature, compared to bottom and interior productivity weighted means of the same measures	201
Figure 15.	Algal grid cell productivities (A-bottom community, B-interior community) and total algal production (C-bottom community, D- interior community) classified by the ice snow thicknesses in which they occurred.....	204

INTRODUCTION

Sea ice covers up to 7% of the Earth surface during any given year, making it one of our largest ecosystems [Dieckmann et al. 2003]. The majority of sea ice forms in polar regions where solar insolation drops to zero, or near zero, during winter, and cold atmospheric temperatures cause ice to freeze at the surface of the ocean. In the Arctic, winter sea ice extent can reach 15 million km², and in the Antarctic up to 20 million km². During summer, much of the sea ice melts, but significant sea ice coverage remains at particular locations through the year. The vast majority of Antarctic sea ice melts and refreezes annually, with ~4 million km² surviving the summer. In the Arctic, where the ocean is located more pole-ward, a larger percentage of the winter sea ice pack currently remains year-round (~6 million km²), although the amount of this permanent ice has been decreasing by ~3% per year over the last 30 years [Comiso et al. 2008].

Sea ice has a disproportionately large effect on regulation of the Earth's climate, considering its area. Furthermore, its effects span a range of timescales from immediate to thousands of years. At the annual timescale, the albedo of sea ice and associated snow cover serve as the primary regulator of the absorption of solar radiation. Changes in the timing of the annual sea ice retreat and the total areal extent of sea ice cause shifts in the timing and magnitude of solar absorption in polar regions, with attendant effects on regional and teleconnected weather, and on the total heat content of the polar oceans [Curry et al. 1995; Gille 2008; Stammerjohn et al. 2008;

Mayewski et al. 2009]. Observations of these effects constitute some of the most dramatic examples of climate warming, including the reduction in summertime Arctic sea ice extent [Comiso et al. 2008], and >5°C surface warming in the Antarctic Peninsula region since 1950 [Turner et al. 2005].

At the intermediate scale, sea ice may act as a moderator of inorganic carbon flux between the atmosphere and ocean. When present, sea ice acts as a cap, preventing significant exchange and ventilation of ocean CO₂ with the atmosphere [Takahashi et al. 1993]. The timing of sea ice retreat, and the related timing of summertime phytoplankton growth, cause differential exposure of waters that vary in CO₂ saturation with respect to the atmosphere, with the result that net annual atmospheric CO₂ flux from polar waters may vary considerably [Takahashi et al. 2002; Sweeney 2003; Arrigo and van Dijken 2007; Arrigo et al. 2008a]. Through interaction with the annual cycle of primary production and inorganic carbon, known as the biological carbon pump, sea ice cover has played a role in the ocean's absorption of ~20-35% of anthropogenic CO₂ [Sabine et al. 2004; Houghton 2007]. Additionally, Yager et al. [1995] proposed that the growth of algae within the sea ice itself could lead to additional modulation of CO₂ flux. If early springtime sea ice algae growth significantly lowers the dissolved inorganic carbon concentration in surface waters, the flux of CO₂ from the ocean to the atmosphere may be lowered, with implications for Southern Ocean carbon budgets and estimation of climate change scenarios.

Sea ice also impacts the rate of deep-water mixing and production, thereby affecting the world's largest reservoir of inorganic carbon, macronutrients, and heat at the millennial timescale of deep ocean circulation [Orsi et al. 1999]. When sea ice

forms, dense, salty brine drains downward from the growing crystal structure, creating an unstable water column. In areas of intense sea ice formation, this extra salt, when mixed into the cold surface waters, can cause the entire water column to convect to the sea floor. The resultant bottom water created by this process, and the tracers it contains, may not be ventilated again to the atmosphere for 400-1000 years [Orsi et al. 1999].

Sea ice also plays a pivotal role in polar ecosystems. The timing of sea ice formation has profound effects on development of marine algal blooms, which form the base of the food web in both the Arctic and Antarctic. Blocking of most solar radiation by sea ice restricts water column algal blooms to periods during and after springtime ice retreat. Through modulation of variable freshwater input to the ocean during melt, sea ice may affect the magnitude of algal blooms as well [Hunt et al. 2002; Worthen and Arrigo 2003; Jin et al. 2007]. Sea ice provides a floating platform for myriad organisms that include invertebrates, fish, marine birds, and mammals, which use sea ice as a home or resting area. Finally, the sea ice itself is colonized by sea ice algae, which supports a microbial ecosystem within the ice pack [Garrison et al. 1986; Garrison and Mathlot 1996]. This sea ice ecosystem has also been linked to water column biology. Antarctic krill, a keystone species in the Southern Ocean, are frequently observed grazing on sea ice algae, and are found at shallower depths when beneath sea ice than when in the open ocean. Because sea ice algae have an extended growing season compared to phytoplankton, sea ice algae may provide a critical carry-over food resource for larval krill that may otherwise starve during the long Antarctic winters [Daly 1990; Quetin and Ross 2003].

It is important to note that our understanding of the impacts of sea ice on local and regional climate, and especially its ecological impacts, often result from anecdotal observations, local-scale studies, and inference [Heywood and Whittaker 1984; Legendre et al. 1992; Keeling et al. 1996; Battle et al. 2000; Mayewski et al. 2009]. The spatial and temporal distribution of sea ice characteristics and the physical and biological interactions of sea ice with the rest of the polar environment, remain largely unknown due to the relative difficultly of observing sea ice. The ocean-viewing satellite systems that guide the bulk of large-scale open water oceanography cannot make observation in ice-covered waters. The logistical and financial costs of making ship-based observations in remote, ice-covered waters means that the polar oceans are under-sampled compared to temperature and tropical oceans.

Because of these observational constraints, models provide the most practical method for estimating the climactic and biogeochemical impacts of sea ice. Detailed small-scale studies have provided parameterizations of sea ice physical processes that can be incorporated into large-scale simulations, and such efforts have provided useful estimates of an array of biophysical phenomena. When coupled to global climate models, sea ice models have demonstrated a feedback between the sea ice albedo and surface warming in the Arctic, where ice loss, and the commensurate loss in albedo, encourages more warming and further ice loss [Curry et al. 1995]. The distribution of sea ice, and timing of and location of melt has been shown to structure the marine food web by encouraging different classes of phytoplankton to bloom in distinct locations in the Ross Sea [Worthen and Arrigo 2003; Arrigo et al. 2003]. By coupling a model of sea ice algae to a hemispheric model of Antarctic sea ice, Arrigo et al. [1997, 1998]

were able to provide a first mechanistic estimation of the magnitude and timing of sea ice algae production and its various impacts on Southern Ocean ecology and the global carbon cycle.

Most sea ice is <4 m thick [Rothrock et al. 1999; Worby et al. 2008a] and when viewed from the surface, almost invariably appears uniformly white with a thin covering of snow. When compared to the water beneath, the thinness and opaqueness can give the impression that the sea ice cover is an homogenous skin covering the ocean. Nevertheless, sea ice contains a large degree of structure in both the vertical and horizontal dimension, and presents an extremely variable habitat to the organisms that depend on it. Model studies of sea ice distribution are generally of coarse resolution, however, and often do not make efforts to incorporate observed variability in sea ice structure [Flato and Hibler 1995; Winton 2000; Zhang and Rothrock 2003; Lipscomb and Hunke 2004]. Recently, models of sea ice that are sophisticated enough to capture some of the horizontal structure in sea ice thickness have resulted in improved climate simulations [Bitz et al. 2001; Holland et al. 2006; Vancoppenolle et al. 2009], indicating that capturing the heterogeneity in sea ice is crucial to gauging its various environmental roles.

Consideration of heterogeneity in sea ice characteristics is especially important for study of sea ice algae, which are sensitive to the temperature, salinity, and light and nutrient availability within the sea ice [Arrigo and Sullivan 1992; Ackley and Sullivan 1994; Lizotte 2001; Arrigo 2003]. These physical and chemical parameters vary widely across the ice pack, creating an extremely diverse habitat. Correspondingly, sea ice algae are most often found growing preferentially in vertical locations within

sea ice, where the intersection of sea ice physical characteristics creates relative optimum growth environments. These ice algal habitats evolve according to a number of different physical processes, including flooding of seawater on the ice surface, desalination during new ice growth, and other dynamic events tied to the evolution of the sea ice interior [Ackley and Sullivan 1994; Arrigo 2003].

Previous efforts to estimate the timing and magnitude of sea ice algae growth and related processes have not taken full account of the ice physics understood to affect sea ice growth and evolution, both because our understanding of sea ice has progressed, the because model tools and computational ability did not yet exist. In fact, most previous estimates of Antarctic sea ice algal production have been calculated using simple extrapolation of a handful of sea ice algal standing stock observations to the entire Antarctic [Burkholder and Mandelli 1965; Heywood and Whittaker 1984; Legendre et al. 1992]. Although Arrigo et al. [1997, 1998] performed the first large-scale model calculations of sea ice algal production, their model incorporated simplifying assumptions concerning brine convection, nutrient flux, and thermodynamics that have significant impacts on the evolution of sea ice characteristics, especially in slushy, high-brine fraction sea ice. Grose and McMinn [2007] used satellite classification of ice thickness to determine monthly sea ice algal habitat, and estimate sea ice algal biomass for the east Antarctic pack ice zone by extrapolating biomass measurements to particular ice thickness classes in early season, and assuming growth based on light availability. This approach ignores the dynamic evolution of the sea ice and the small-scale processes, such as nutrient flux, which

have the potential to control production at short time scales [Robinson et al. 1998; McMinn et al. 1999; Vancoppenolle et al. 2010].

In order to improve upon previous estimates of the sea ice ecosystem, the physical evolution of the sea ice must be coupled to the physiological abilities of the algal community. The sea ice responds to regional and local scale forcing by both the atmosphere and the ocean, therefore to build a distribution of sea ice algal distribution, model sea ice must respond to these forcings appropriately with respect to light availability, nutrient and fluid fluxes, and temperature and salinity characteristics that affect algal growth.

Building on recent advances in the model representation of sea ice, the following three chapters describe the development of a new coupled-biogeochemical model of sea ice, and its use in characterizing the spatial and temporal distribution of Antarctic sea ice algal production. Chapter 1 focuses on model development, using parameterizations designed to capture the processes important in developing the vertical biogeochemical structure of sea ice. To more accurately simulate high-porosity sea ice where elevated sea ice algal production is often found [Ackley and Sullivan 1994; Arrigo et al. 1997; Fritsen et al. 2001; Kattner et al. 2004], we introduce a new method for desalination that accounts for the unique thermal and convective properties of these ice types. Chapter 2 introduces the three-dimensional aspects of the model, explores the model performance at the hemispheric scale. In Chapter 3, the model is used to generate a 10-year continuous time series of pan-Antarctic sea ice characteristics, and associated sea ice algal production.

This study represents the first time that a model that incorporates the processes of sea ice desalination, brine convection, and surface ice and snow transformations have been coupled to a dynamic model of sea ice biology. Results from the simulations presented here provide the first mechanistic evaluation of variability in sea ice algal growth in different locations across the ice pack. The interannual time series of sea ice algal growth generated by the model gives bounds on the dynamics of Antarctic sea ice biology. I discuss ability of sea ice algae to affect the Southern Ocean carbon cycle, and explore the relative importance of the different controls of algal growth in the face of a changing polar climate. The model design allows for flexibility in adding new features, and I hope it may be used to address further questions concerning the role of sea ice in the earth systems.

CHAPTER 1

Refining simulation of sea ice ecosystems: a quasi-empirical method for slush layer desalination

1. Introduction

Porous, slushy layers within sea ice are a significant feature across much of the Antarctic ice pack. Composed of a mixture of brine and ice crystals of varying sizes, slush layers contain a high proportion of fluid relative to typical sea ice, often 50% or greater. These layers can arise via flooding of snow at the snow/ice interface due to high snow loading or ridging and rafting of ice floes, or via melting of near-surface sea ice due to inverted summertime temperature gradients ('gap layers' [Ackley et al. 2008]).

Slush layers play a significant physical and ecological role in the Southern Ocean. The freezing of slush layers can result in the rejection of a significant amount of salt into the water column below [Lytle et al. 1996]. High concentrations of sea ice algae are typical of slush layers, which are often stained brown with algal pigments [Ackley and Sullivan 1994; Fritsen et al. 1994; Kattner et al. 2004]. Primary production by sea ice algae in flooded layers is thought to constitute a large fraction of the total carbon fixed in Antarctic pack ice [Arrigo et al. 1997; Arrigo et al. 1998]. Establishing where and when slush layers form, as well as their fate, would further our understanding of carbon cycling in the Antarctic and how it may change under altered environmental conditions.

In-situ study of sea ice is necessarily limited in space and time because of logistical difficulties associated with sampling in such a remote and hostile environment. Models of sea ice have therefore served as important tools for investigating sea ice dynamics and estimating algal production and carbon flux [Arrigo et al. 1997]. Current models are relatively mature in their ability to simulate growth and advection of sea ice at a macro (global) scale [Hunke and Dukowicz 1997; Holland et al. 2008], however, the processes of fluid transfer and phase change that define the evolution of sea ice salinity and associated brine fluxes are typically restricted to micro-scale investigations [Wettlaufer et al. 1997; Schulze and Worster 1999; Jackson and Cheadle 1998; Maksym and Jefferies 2001]. Simulations by Vancoppenolle et al. [2009] provide the first estimates of hemispheric sea ice salinity evolution, although their ability to simulate slush layer evolution is diminished by tracking a single bulk salinity tracer.

After a slush layer is formed via seawater flooding or melting of ice or snow, the brine in the slush layer can become relatively isolated. Further fluid exchange with the ocean is possible under particular circumstances however, and results in alteration of the brine biochemistry [Ackley and Sullivan 1994; Kattner 2004]. This exchange between the slush ice and the underlying seawater is facilitated by several different mechanisms, including wave and ice floe motion and surface depression due to ridging and rafting of ice floes or snow loading [Arrigo et al. 2010]. The most notable cause of fluid flux with respect to primary production occurs during freezing of the slush layer, when brine density gradients resulting in desalination can cause rapid overturning of brine [Fritsen et al. 1994]. With the potential to replace brine in the slush layer

multiple times during the course of freezing, slush layers possess the ability to replenish nutrients to growing sea ice algal communities.

Recent modeling efforts have made large strides in representing desalination and fluid flux of sea ice via gravity drainage. Current studies indicate that the sea ice desalination and associated fluid flux is a continuous process promoted and limited simultaneously by both the ice growth rate and the ice geometry, and ideally should be modeled as a single process [Notz and Worster 2009]. Research evaluating sea ice as a 'mushy' structure allows use of continuum equations that in theory permit mechanistically modeled desalination and associated fluid flow at any location in the ice regardless of state. Convective desalination occurs when a Rayleigh number of the sea ice system reaches a critical value, with fluid flux determined by Darcy's Law [Worster 1991, Wettlaufer et al. 1997]. Using an approximate 1-dimensional collapse of the mushy layer equations to a parameterized advection-diffusion equation, Vancoppenolle et al. [2009] obtain reasonable sea ice salinity profiles, thereby generating a mechanistically derived fluid flux.

Several factors contribute to a potentially large level of uncertainty in such simulations, especially when considering slushy ice. These equations depend on a workable permeability parameterization for sea ice, and such a parameterization remains elusive for high-brine volume sea ice due to the geometric complexity of the ice interior (Figure 1). Permeability-porosity relationships have been measured [Freitag 1999, Eicken et al. 2002, Freitag and Eicken 2003] and modeled [Golden et al. 2007] with some success at low brine fractions; however, the majority of brine is rejected at higher brine fractions, and these parameterizations do not capture the fluid

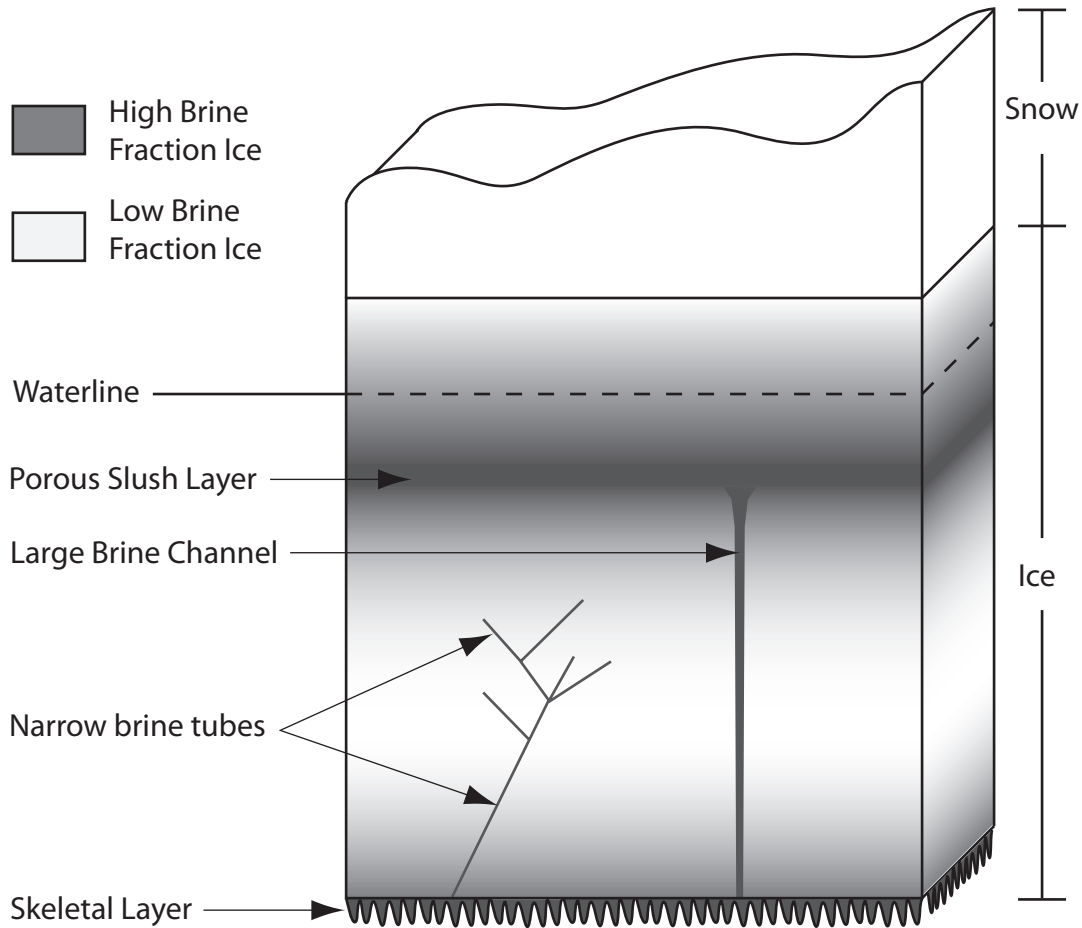


Figure 1. Cut-away section of sea ice showing sea ice internal structure and brine features that influence desalination. Here a porous slush layer (dark grey) below the waterline line is connected to the ocean below via a large brine channel, facilitating rapid desalination. Below the slush layer, the sea ice is less saline with a lower brine fraction (light grey), and contains connected narrow brine tubes. In the desalination model, the slush layer and skeletal layer desalinate rapidly according to a stable salinity scheme, while the remaining low brine fraction sea ice desalinated more slowly according to the equations of Cox and Weeks [1998].

dynamics of the warm, porous interior layers where algae thrive. Variations in measured permeability of up to an order of magnitude at a particular brine fraction point out the extreme heterogeneity of the sea ice environment. Furthermore, at high brine fractions, Darcy's Law may not be an appropriate predictor of fluid velocity, calling into question the calculations of fluid flux across a relatively thick slush layer using mushy layer equations that do not incorporate a faster type of fluid transfer. When combined, the above factors produce an uncertainty in the calculation of brine flux that currently is difficult to estimate due to the paucity of brine flux measurements. Finally, these problems are compounded when large-scale models must integrate naturally heterogeneous sea ice properties across grid sizes spanning hundreds of square kilometers. Given then the low resolution of global scale simulations, a simpler empirical calculation may suffice to estimate slush layer desalination and associated brine fluxes.

Here we present a coupled biological-physical model of sea ice appropriate for macro-scale estimation of slush layer dynamics. The model is developed from time series observations of sea ice and relies on previously published methods for simulation of cold, low-salinity sea ice [Eicken et al. 1992; Bitz and Lipscomb 1999; Kottmeier et al. 2003] and algal growth and physiology [Arrigo and Sullivan 1994]. To simulate slush layer physics, we introduce a quasi-empirical parameterization of convective desalination and brine exchange that is based upon established sea ice dynamics and the estimation of a 'stable salinity' after rapid desalination during initial sea ice formation [Nakawo and Sinha 1981; Cox and Weeks 1988; Petrich et al. 2006].

Without actual measurements of brine flux, researchers must calibrate models to proxies for the actual desalination process, such as the evolution of temperature and bulk salinity profiles and the changes in dissolved tracer concentrations within the brine. Our model is developed and tested using constraints of sea ice salinity, temperature, fluid flux, and sea ice algal growth from time series observations of these properties measured *in situ* in 1992 at Ice Station Weddell (ISW) Site B [Fritsen et al. 1994; Ackley et al. 1996; Lytle and Ackley 1996]. This study site contained a thick slush layer that froze during the course of observations. We further assess the robustness of the model by simulating ISW Site A, which contained a similar slush layer but with different, and more heterogeneous, ice and snow conditions. Finally, to examine model performance under a variety of initial and forcing conditions, we generate a series of model runs and examine the desalination process and salinity profiles. We discuss physicality of our desalination and convective heating parameterizations, limitations and applicability of the model, and possibilities for further refinement.

2. Model Description

Here we describe the logical components and computational flow of the sea ice ecosystem model, with justification of important parameterizations. The operations executed at each model time step are shown in Figure 2. Mathematical symbol notation and numerical constants can be found in Tables 1 and 2, respectively.

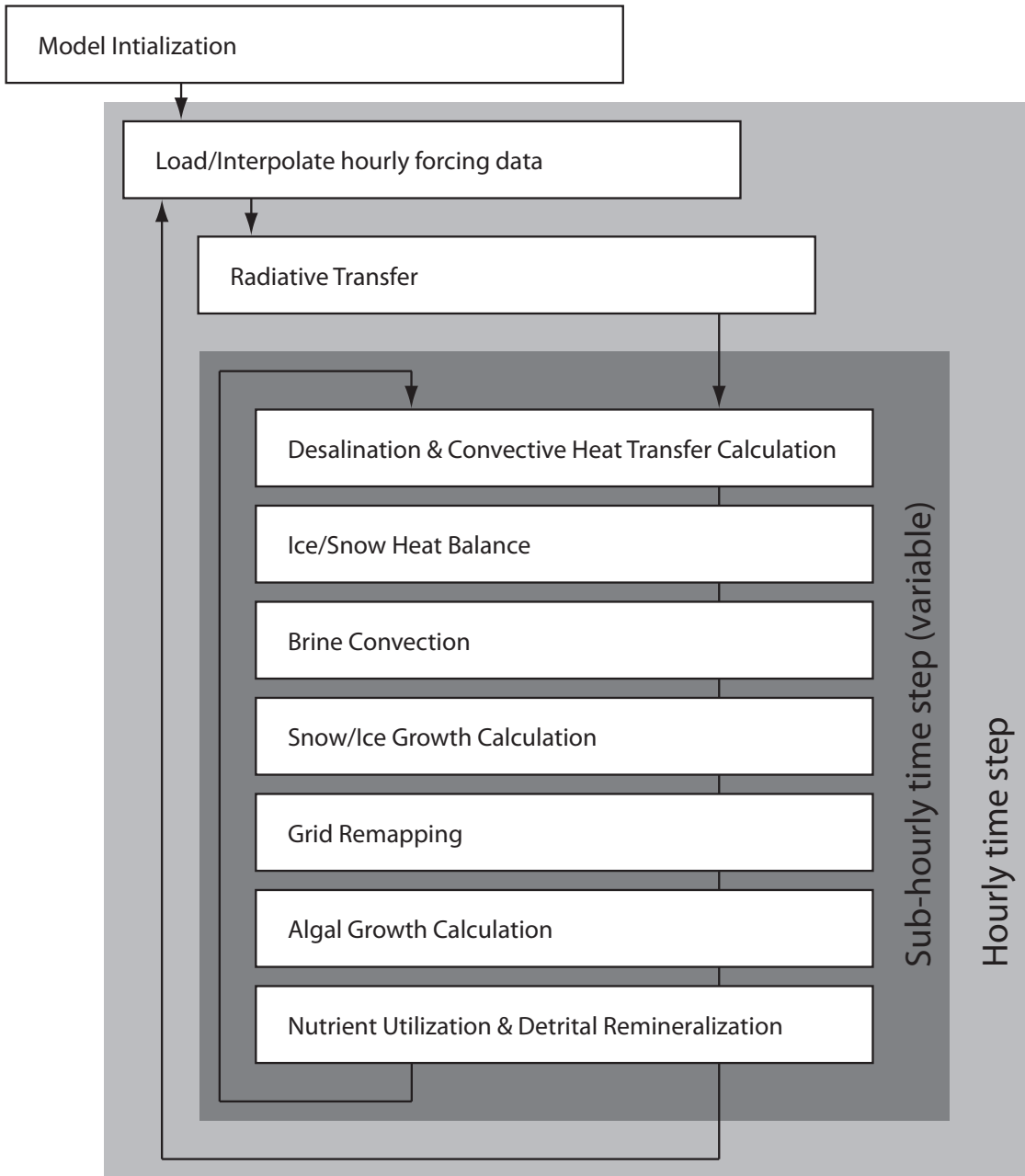


Figure 2. Model conceptual schematic showing the major components of the sea ice model in the order that they occur. Forcing data interpolation and radiative transfer are calculated using a 1-hour time step. The remaining physical, biological, and gridding processes use a smaller time step that is determined at run time to reduce numerical errors. Desalination and associated convective heat flux is calculated first, so it can be included in the following heat transfer calculation.

Table 1. Notation

T	Ice or snow Temperature [$^{\circ}\text{C}$, Kelvin]
S	Salinity of ice or brine [psu]
ϕ	Brine or ice fraction [fraction]
C	Solute concentration [mg m^{-3}]
V	Fluid volume [$\text{m}^3 \text{m}^{-2}$]
F	Energy Flux [W m^{-2}]
c	Specific Heat Capacity of ice or snow [$\text{J g}^{-1} \text{K}^{-1}$]
k	Thermal conductivity of ice or snow [$\text{W m}^{-1} \text{K}^{-1}$]
z	Vertical axis distance [m]
h	Ice or snow thickness [m]
ρ	Density bulk ice, pure ice, brine, or snow [g m^{-3}]
r	Stoichiometric ratio [mol mol^{-1} , g g^{-1}]
q	Volumetric heat [J m^{-3}]
R	Rate constant [s^{-1} , day^{-1}]

Table 2. Model Parameters and Constants

Parameter	Description	Value	Units
G_0	Maximum algal growth rate at 0°C	0.81	day^{-1}
R_g	Algal temperature-dependant growth rate constant	0.631	$^{\circ}\text{C}^{-1}$
R_m	POC remineralization rate	0.03	day^{-1}
f_e	Remineralization efficiency	1	fraction
$E'_{k_{max}}$	Maximum spectral photoadaptation parameter	18	$\mu\text{Ein m}^{-2} \text{s}^{-1}$
A	Spectral photoadapatation equation constant	1.4	dimensionless
B	Spectral photoadapatation equation constant	0.12	dimensionless
$r_{C:Chla}$	Algal/Detritus C:Chla ratio	35	g/g
$r_{C:N}$	Algal/Detritus C:N ratio	7	mol/mol
$r_{C:P}$	Algal/Detritus C:P ratio	106	mol/mol
$r_{C:Si}$	Algal/Detritus C:Si ratio	4	mol/mol
K_{NO3}	Half-saturation algal rate constant for NO_3 uptake	1	μM
K_{NH4}	Half-saturation algal rate constant for NH_4 uptake	1	μM
K_{PO4}	Half-saturation algal rate constant for PO_4 uptake	0.1	μM
K_{SiOH4}	Half-saturation algal rate constant for SiOH_4 uptake	60	μM
$C_{sw \ NO3}$	Seawater NO_3 concentration	30	μM
$C_{sw \ NH4}$	Seawater NH_4 concentration	0	μM
$C_{sw \ PO4}$	Seawater PO_4 concentration	2	μM
$C_{sw \ SiOH4}$	Seawater SiOH_4 concentration	80	μM
$C_{sw \ POC}$	Seawater detritus concentration	0	$\mu\text{g L}^{-1}$
μ	Liquidis slope of water	0.054	dimensionless
c_{i0}	Specific heat of pure ice	2.011	$\text{J g}^{-1} \text{K}^{-1}$
c_w	Specific heat of seawater at 0°C	3.96	$\text{J g}^{-1} \text{K}^{-1}$
L	Latent heat of fusion of water	334	J g^{-1}
κ_{NIR}	Spectrally-weighted near-IR absorption coeffiecient	7.18	m^{-1}

2.1. Model Grid

Ice and snow are represented by a variable number of discrete horizontal layers of equal thickness. The physical ice state and macronutrient, microalgae, and detritus concentrations are tracked in each layer. After initialization of a new snow or ice pack, the ice is divided into layers of equal size. During incremental adjustments of ice or snow thickness, the ice pack is divided again into an equal number of layers and tracers are remapped conservatively onto the new vertical grid. During these simulations, the standard layer thickness is ~ 1 cm, except where noted.

The model grid also incorporates a discrete skeletal layer at the ice/water interface that is fixed at the seawater temperature and has a 50% brine fraction. The maximum skeletal layer thickness is 2 cm after Arrigo and Sullivan [1994] and Fritsen et al. [1998]. The skeletal layer is represented by two grid layers that vary in thickness from 0.1-1 cm. During sea ice growth, the skeletal layers grow before the internal ice layer, up to the maximum specified thickness. After the skeletal layer has reached maximum thickness, further ice growth results in the transfer of ice and tracers from the skeletal layers to the bottom interior ice layer as congelation ice. New ice and water column tracer values are then incorporated into the skeletal layer in equal proportion to those removed to maintain skeletal layer thickness. During conditions of ice melt, the skeletal layer melts before the congelation ice.

2.2. Thermodynamics

The surface heat flux (W m^{-2}) at the boundary between the atmosphere and the sea ice or overlying snow cover (F_0) accounts for the fluxes of incoming longwave

radiation (F_L), outgoing longwave radiation (F_l), turbulent latent heat (F_e) and turbulent sensible heat (F_s), and conductive heat (F_c):

$$F_0 = F_L + F_l + F_e + F_s + F_c \quad (1)$$

Calculation of F_L , F_l , F_e , and F_s from measurements of atmospheric temperature, wind speed, and humidity, and surface temperature follows Kottmeier et al. [2003]. F_c takes the form of an ice thermal conductivity (k) times the temperature gradient between the ice surface and uppermost ice layer ($\partial T / \partial z$). Where measured values for atmospheric variables were not available, we applied linearly-interpolated 6-hourly surface atmospheric data from the European Centre for Medium-Range Weather Forecasts (ECMWF) Interim reanalysis. The maximum snow or ice surface temperature is set to 0°C.

Heat transfer within the snow and sea ice is accomplished using a form of the heat equation that is modified to account for internal heating by absorption of shortwave radiation (F_i – described in section 2.4:

$$\rho c \frac{\partial T}{\partial t} = \frac{\partial}{\partial z} k \frac{\partial T}{\partial z} + \frac{\partial}{\partial z} F_i \quad (2)$$

where ρ is the snow or ice layer density (g m^{-3}), c is the snow or ice specific heat capacity ($\text{J g}^{-1} \text{ K}^{-1}$), T is the temperature ($^{\circ}\text{C}$) and z is the vertical inter-layer distance (m). We use an equation for the thermal conductivity (k) of sea ice layers ($\text{W m}^{-1} \text{ K}^{-1}$)

following the measurements of Pringle et al. [2007]:

$$k = \frac{\rho}{\rho_i} \left(2.11 - 0.11T + 0.09 \frac{S}{T} - \frac{\rho - \rho_i}{1000} \right) \quad (3)$$

where ρ_i is the density of pure ice (918 kg m^{-3}) and S is the bulk sea ice salinity (psu), or the salinity of the resulting water should the ice be completely melted. For snow layers, we chose to fix the thermal conductivity (k) at $0.33 \text{ W m}^{-1} \text{ K}^{-1}$. Although the thermal conductivity of snow is variable at different snow densities and grain sizes, owing to the complexity of snow metamorphosis we choose to leave this parameter constant. This value was derived experimentally by Sturm et al. [2002], and similar snow conductivities have been used to effectively approximate sea ice growth in other models [Ebert and Curry 1993, Wu et al. 1999]. The volume-based heat capacity (c) is calculated as either c_i for sea ice layers or c_s for snow layers. For brine-containing sea ice, c_i ($\text{J g}^{-1} \text{ K}^{-1}$) is calculated as

$$c_i = 2.0113 + \frac{\mu S L_w}{T_0 T_1} \quad (4)$$

after Bitz and Lipscomb [1999], where T_0 and T_1 are the old and new temperatures of the layer across a model time step, L_w is the latent heat of fusion of pure water (334 J g^{-1}), and $\mu = 0.054$ (dimensionless) is the slope of the liquidus (freezing temperature) relationship. Above the liquidus temperature ($T_m = -\mu S$), the heat capacity of the resultant liquid brine (c_b) is assumed to equal the heat capacity of seawater at 0°C , or

$3.96 \text{ J g}^{-1} \text{ K}^{-1}$. The heat capacity ($\text{J g}^{-1} \text{ K}^{-1}$) of the snow (c_s) is assumed to be identical to that of pure ice [Fukusawo 1990]:

$$c_s = 0.185 + 0.00689T \quad (5)$$

where T is in units of Kelvins.

Heat flux across the bottom sea ice-water boundary is assumed to be purely conductive. The sum of an ocean heat flux $F_w (\text{W m}^{-2})$ from below and the conductive heat flux $F_c (\text{W m}^{-2})$ from above is balanced by the accretion and melting of ice at the boundary, such that

$$F_w + F_c = -q_b \frac{dh}{dt} \quad (6)$$

where $dh/dt (\text{m s}^{-1})$ is the change in ice thickness and $q_b (\text{J m}^{-3})$ is the salinity-dependent heat of fusion (J m^{-3}) of sea ice determined by integration of the ice specific heat capacity c_i and multiplying by the layer density $\rho (\text{g m}^{-3})$:

$$q_b = 2.0113\rho \left[(T_m - T) + L_w (1 - T_m/T) \right] \quad (7)$$

[Bitz and Lipscomb 1999].

The heat equation solutions for each layer are computed using an implicit space-centered 1st-order staggered-grid discretization [Tannehill et al. 1997]. When

combined with the top and bottom boundary fluxes, the ice and snow layer heat flux equations form a system of linear equations that, because of the dependence of c_i and c_s on T , is solved iteratively using Newton-Raphson stepping.

2.3. Sea Ice State

By assuming that the two-phase system of ice and brine is in thermal equilibrium, we may derive pertinent sea ice parameters from two state variables of bulk ice salinity S (psu), and temperature T ($^{\circ}$ C) [Cox and Weeks 1983]. Brine salinity S_b (psu), which refers to the salinity of small brine inclusions within sea ice, is purely dependent on temperature and is described by the following:

$$\begin{aligned} S_b &= T / \mu & 0 \geq T > -3.058 \\ S_b &= -0.0200T^3 - 1.0015T^2 - 22.7T - 3.992 & -3.058 \geq T > -22.9 \\ S_b &= -0.001025T^3 - 0.0609T^2 - 1.891T + 206.24 & -22.9 \geq T > -44.0 \\ S_b &= -0.03669T^3 - 5.501T^2 - 277.86T - 4442.1 & -44.0 \geq T > -54.0. \end{aligned} \quad (8)$$

For the ease of solving equations near the typical melting point of sea ice, we assume a linear liquidus slope from $0 \geq T > -3.058$ (Eq. 8 line 1). At $T = -3.058$, the linear liquidus slope meets the polynomial liquidus slope described by Assur [1958], and we use Eq. 8 lines 2-4 for calculating brine salinity for $T \geq -3.058$. Brine density ρ_b (g m^{-3}) is assumed to depend solely on brine salinity , and is calculated as

$$\rho_b = \rho_w + c_s S_b, \quad (9)$$

where the density of water $\rho_w = 1 \times 10^6 \text{ g m}^{-3}$ and coefficient $c_s = 800 \text{ g m}^{-3} \text{ psu}^{-1}$ [Cox and Weeks 1975]. Ice density $\rho_i (\text{g m}^{-3})$ [Weeks 1962] can then be derived:

$$\rho_i = \frac{\rho_0 \rho_b S_b}{\rho_b S_b - S(\rho_b - \rho_0)}. \quad (10)$$

The density of pure ice ρ_b is $9.18 \times 10^5 \text{ (g m}^{-3}\text{)}$. After Weeks [1962] the volumetric brine fraction of the sea ice ϕ_b (dimensionless) is:

$$\phi_b = \frac{\rho_i S}{\rho_b S_b}. \quad (11)$$

For heat accounting due to grid remapping and ice accretion or melting, we calculate an ice reference enthalpy q_i relative to 0°C (J m^{-3}). q_i is found similarly to q_b , with the addition of an extra term to account for the fully liquid phase

$$q_i = -2.0113 \rho_i \left[(T_m - T) + L_w (1 - T_m/T) \right] - \rho_{T_m} T_m c_w \quad (12)$$

where $\rho_{T_m} (\text{g m}^{-3})$ is the density of brine at the melting temperature T_m . Reference enthalpy (q_s) for snow (J m^{-3}) is found similarly:

$$q_s = \rho_s (-0.185T - 0.003445T^2) \quad (13)$$

After a change in enthalpy of an ice or snow layer under steady state conditions due a change in the vertical grid size, new layer state temperatures are derived by solving Eqs. 12 or 13 for T , thereby conserving total heat.

2.4. Solar Irradiance

Because scattering, rather than absorption, dominates attenuation of solar irradiance in snow and sea ice, exponential decay as represented by Beer's Law does not accurately simulate radiative transfer in the sea ice environment, especially when optically thin layers are present [Barber et al. 1991, Jin et al. 1994]. The large amount of scattering in snow and drained sea ice causes higher downwelling attenuation in the surface layers than is predicted by simple exponential decay. During preliminary modeling efforts, we found that simple attenuation of spectral irradiance using Beer's Law overestimated bottom irradiance at snow depths of less than 10 cm, and while this radiative transfer scheme had little to no effect on ice physics, it allowed excessive rates of sea ice algal growth. Since snow cover is thin over a large fraction of both the Arctic and Antarctic ice packs during spring when algae are growing, we incorporated a radiative transfer model that more accurately simulates thin-layer optical scattering.

We chose a two-stream spectral radiative transfer model based on the delta-Eddington approximation for the scattering phase function that accounts for multiple scattering effects on direct and diffuse radiation [Brieglib and Light 2007]. Levels of scattering in sea ice and snow show large variation with density, brine volume, ice grain size, and temperature [Warren 1982, Light et al. 2003]. The complexity of a continuous model of scattering, such as derived in Light et al. [2004], is too

computationally intensive to be incorporated into our model. Therefore, we have narrowed our scattering parameterizations to five different classes of snow and sea ice that demonstrate very different optical properties: 1) cold snow, 2) warm snow, 3) warm sea ice, 4) cold mirabilite-containing sea ice, and 5) eutectic sea ice. For each class, the inherent optical properties (IOPs) of the snow or sea ice were found by using published absorption and scattering phase function values, followed by hand tuning of scattering coefficients until modeled spectral albedos and asymptotic extinction coefficients matched observed values from Warren and Wiscombe [1980] and Grenfell and Maykut [1977]. Resulting IOPs for each class of snow and ice fall within bounds for these parameters reported by Brieglib and Light [2007], Light et al. [2008], and Ehn et al. [2008], and are listed in Table 3.

The delta-Eddington model calculates the spectral (upwelling and downwelling) irradiance and heat absorption in the photosynthetically available radiation (PAR) band, using 31 wavelength bins between 400 and 700 nm. Surface non-PAR shortwave solar radiation (350-400 nm and 700-4000 nm) is estimated as a constant fraction of total PAR, and attenuated as a single band using a spectrally-weighted absorption coefficient. For the purposes of shortwave heating, we take the mean of heat absorption across the snow distribution for each band, and then the total heat absorption from all bands is incorporated into the heat flux (Eq. 2) as F_i .

Direct and diffuse surface atmospheric irradiance that serve as input into the delta-Eddington model are calculated from the clear-sky radiative transfer model of Gregg and Carder [1990], and then corrected for clouds as in McClain et al. [1996].

Table 3. Intrinsic optical properties (IOPs) of ice and snow classes used by the delta-Eddington spectral shortwave attenuation model

	Scattering Coefficient σ (m ⁻¹)	Asymmetry Parameter g (dimensionless)	Absorption Coefficient κ (m ⁻¹)
New/Cold Snow	2500	0.89	$\phi_i \kappa_i(\lambda) + 0.3$
Warm/Old Snow	900	0.94	$\phi_i \kappa_i(\lambda) + 0.3$
Drained Surface Ice	900	0.94	$\phi_i \kappa_i(\lambda) + 0.3$
Sea Ice (> -2)	$15 + \gamma(C_{chl} + C_{POC})$	0.98	$\phi_i \kappa_i(\lambda) + \phi_b \kappa_w(\lambda) + \kappa_{chl}(\lambda) (C_{chl} + C_{POC})$
Sea Ice (-10 to -2 °C)	$15 + 9.6S(\text{abs}(T)-2) + \gamma(C_{chl} + C_{POC})$	0.98	$\phi_i \kappa_i(\lambda) + \phi_b \kappa_w(\lambda) + \kappa_{chl}(\lambda) (C_{chl} + C_{POC})$
Sea Ice (-22 to -10 °C)	$15 + 76.8S + \gamma(C_{chl} + C_{POC})$	0.98	$\phi_i \kappa_i(\lambda) + \phi_b \kappa_w(\lambda) + \kappa_{chl}(\lambda) (C_{chl} + C_{POC})$
Eutectic Sea Ice (< -22 °C)	$2400 + \gamma(C_{chl} + C_{POC})$	0.94	$\phi_i \kappa_i(\lambda) + \phi_b \kappa_w(\lambda) + \kappa_{chl}(\lambda) (C_{chl} + C_{POC})$

Sea Ice scattering coefficients incorporate algal scattering, represented by the combined algae and POC concentration in units of mg C m⁻³ times a scaling factor in units of m² mg⁻¹ (γ). Scaling factor $\gamma = 5.26 \times 10^{-3}$ for all model runs, and is calculated from the observation of scattering by large particles in seawater of 1×10^{-3} m²/mg dry mass [Babin et al. 2003] times a dry mass/carbon conversion ratio of 5.26 g/g C for diatoms [Sicko-Goad et al. 1984].

Atmospheric parameters from the NCEP/NCAR Reanalysis 2 along with TOMS ozone concentrations were used as input into the atmospheric radiative transfer model.

2.5 Biological Model

The biological component is described in detail in Arrigo and Sullivan [1994].

Dissolved nutrient species considered by the model include NO₃, NH₄, PO₄, and Si(OH)₄. To this model we add a detritus pool that receives grazed/dead microalgae and is allowed to convect with brine movement, while microalgae are able to maintain position within the ice sheet [Welch and Bergmann 1989]. Nutrients are recycled from the detrital pool to NH₄ and PO₄ according to:

$$C_N = f_e r_{N:C} C_{Det} e^{R_m t} \quad (14)$$

where C_N [M] is the nutrient concentration, C_{Det} [g C m⁻³] is the detrital concentration, f_e [dimensionless] is the fractional efficiency of remineralization, $r_{N:C}$ [dimensionless] is the nutrient:carbon ratio [mol N g C⁻¹] and R_m [day⁻¹] is the specific remineralization rate. Modeled algae have no preference for either nitrogen source, and utilize environmental NO₃ and NH₄ in proportion to their availability. The nutrient stoichiometry of microalgae is considered constant, and is reported in Table 2. Maximum microalgal growth rates are calculated according to Bissineger et al. [2008].

Sea ice algae have been observed to be motile within the ice [Welch and Bergman 1989], although the consequences of different rates of motility and the tradeoffs between thermo-, chemo- and photo-taxis in sea ice algae have not been explored. Here we follow Lavoie et al. [2005] in allowing sea ice algae to move toward the bottom of the ice sheet according to a linear relationship with the ice growth rate. At rates of ice growth below 1.5 cm day⁻¹, algae are allowed to move downward according to the relationship:

$$\Delta h_a = 1 - \frac{dh/dt}{1.5} \quad (15)$$

where Δh_a (cm day⁻¹) is the vertical distance of algal migration during a model time step, and dh/dt (cm day⁻¹) is the ice growth rate. In contrast to Lavoie et al. [2005], we

do not allow algae to migrate upwards in the ice pack during periods of bottom ice melt.

2.6. Desalination

Sea ice desalination has been previously divided by researchers into two classes, 1) interface or skeletal layer desalination near the freezing front of sea ice, and 2) interior desalination of the colder sea ice above the freezing front [Cox and Weeks 1988, Wettlaufer et al. 1997]. Interface desalination was considered to be responsible for rapidly rejecting the majority of salt, until a 'stable salinity' is reached where reduced permeability of the sea ice prevents further rapid desalination. The stable salinity was interpreted as a function of ice growth rate; more brine becomes trapped in the ice matrix at higher sea ice growth rates leading to higher stable salinities [Wakatsuchi and Ono 1983]. Interior desalination continues after interface desalination as long as the ice remains permeable; the rate of desalination depends on the resistance to fluid flow created by the geometry of connected brine pockets and tubes [Cox and Weeks 1975, Golden et al. 2007].

Our approach to desalination follows that of past researchers in dividing desalination into the same two classes. However, instead of restricting their use to the ice-water interface and interior portions of the ice pack, our model can apply either desalination method to a particular region of sea ice. A simple two-part test determines which desalination method to use. In any given ice layer, if the brine fraction is less than a threshold value (ϕ_{crit}), or the layer has reached a stable salinity, we consider the ice not slushy and apply the Cox and Weeks [1988] empirical gravity drainage

formula (hereafter CW88) for calculating the bulk salinity change in interior ice,

$$\frac{dS}{dt} = \Delta T(A + B\phi_b) \quad (16)$$

where ΔT is the temperature gradient between adjacent layers (K cm^{-1}), ϕ_b is the brine fraction of the ice layer, and numerical coefficients $A = 1.6810^{-5}$ ($\text{psu K}^{-1} \text{s}^{-1}$) and $B = -3.37 \times 10^{-7}$ ($\text{psu K}^{-1} \text{s}^{-1}$). Through the dependence on brine fraction (ϕ_b), this parameterization represents a permeability-mediated process since sea ice permeability increases with porosity.

If the brine fraction exceeds ϕ_{crit} in a particular layer, and the bulk salinity is higher than the calculated stable salinity, then we consider the ice slushy, and assume that the rate of desalination is instead controlled by the ice growth rate. In this case, we use the stable salinity relationship as summarized by Petrich et al. [2006] for ice interface growth to determine the bulk desalination rate. The stable bulk ice salinity (S_s) is calculated as

$$S_s = k_{eff} S_b, \quad (17)$$

where the stable salinity parameter k_{eff} [dimensionless] is determined experimentally as a powerlaw relationship of dh/dt (m s^{-1}) and a velocity coefficient 1.35×10^{-7} (m s^{-1}):

$$k_{eff} = 0.19 \left(\frac{dh}{dt} \frac{1}{1.35 \times 10^{-7}} \right)^{0.46}. \quad (18)$$

Assuming a constant brine salinity, the change in bulk salinity for a freezing region of sea ice by displacement of brine out of an ice layer of thickness z is:

$$\frac{dS}{dt} = (1 - k_{eff}) \frac{S_b}{z} \frac{dh}{dt}. \quad (19)$$

Using the stable salinity scheme calculation of dh/dt is not straightforward since the heat required to freeze sea ice of a particular salinity (q_f) depends on k_{eff} , which is in turn circularly dependent on dh/dt . Modelers have traditionally sidestepped this issue by assuming a fixed q_f at the bottom of the ice, and generally achieve accurate ice growth rates [Bitz and Lipscomb 1999]. As a workaround to estimate dh/dt for interior ice, we note that the stable salinity relationship can be exploited to estimate the latent heat of freezing q_f for an accreted volume of sea ice. Because the ‘stable salinity’ relationship predicts the salinity at a particular ice growth rate, we can predict the volume of ice frozen during a time step and derive a minimum heat flux. Assuming the layer conductive heat flux equals q_f (i.e. all extracted heat freezes ice rather than lowers temperature) we construct a relationship between the conductive heat flux F_c and dh/dt (Figure 3). We use two different least square regressions to approximate the relationship between dh/dt (cm s^{-1}) and F_c (W m^{-2}); one polynomial is more accurate at heat fluxes below 57.31 W m^{-2} , which is the case for desalination of most slush layers.

There are no data concerning k_{eff} below $2 \times 10^{-6} \text{ m s}^{-1}$, and growth rates above $2 \times 10^{-4} \text{ m s}^{-1}$ are rarely encountered; therefore, we cap predicted growth rates at these values.

$$\begin{aligned}
dh/dt &= 5 \times 10^{-6} & F_c &< 15.3 \\
dh/dt &= 1.45 \times 10^{-9} F_c^2 + 3.54 \times 10^{-7} F_c + 5.21 \times 10^{-8} & 15.3 \leq F_c < 57.3 \\
dh/dt &= 1.94 \times 10^{-13} F_c^4 - 6.00 \times 10^{-11} F_c^3 + 7.39 \times 10^{-9} F_c^2 + 1.76 \times 10^{-7} F_c & 57.3 \leq F_c < 210.0 \\
dh/dt &= 2 \times 10^{-4} & F_c \geq 210.0
\end{aligned} \tag{20}$$

Numerical coefficients from polynomial regression have units of $[\text{s m}^{2n} \text{ cm}^{-1} \text{ W}^{-n}]$, where n equals the exponent on F_c to which the coefficient is multiplied. F_c is calculated from the temperature gradient and thermal conductivity across an individual grid layer as $F_c = \Delta T k_i$, using the same space-centered staggered-grid method used in the heat conduction discretization. Positive F_c is in the upward direction. Henceforth, we refer to this slush layer desalination method as SLDL. A operational diagram of the desalination and fluid transport scheme is shown in Figure 4.

We note that the empirical parameterization for k_{eff} was derived from ice accreted to the bottom of an ice sheet, and may not be applicable at temperatures lower than standard seawater freezing temperatures. However, ice temperatures close to that of the underlying seawater are required to achieve large brine volumes. Therefore, Eqs. 17-20 are only invoked at brine temperatures close to that of seawater. As such, Eq. 20 provides a reasonable estimate of the accreted ice volume in the sea ice interior from which to estimate desalination.

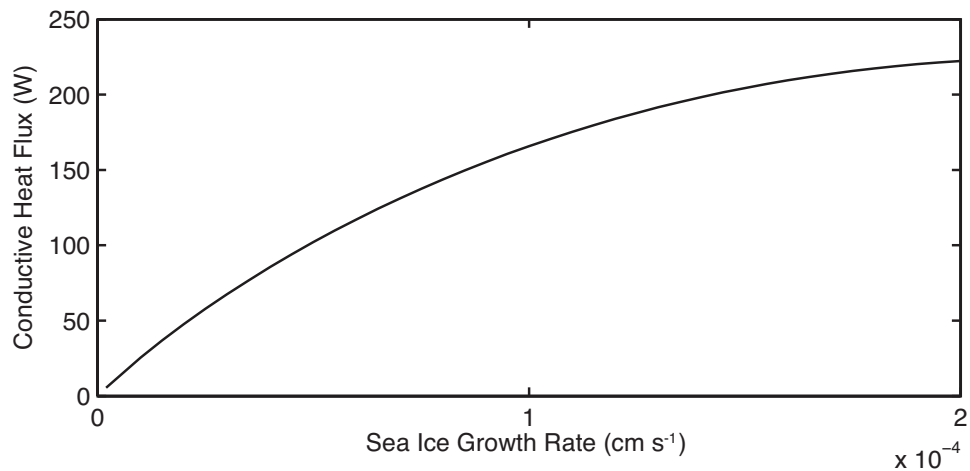


Figure 3. The relationship between heat flux and sea ice growth rate using an empirical stable salinity relationship [Petrich et al. 2006] and sea ice state equations [Cox and Weeks 1983] at a brine temperature of -1.8 °C. A least squares regression of the relationship allows prediction of the ice growth rate from the heat flux (positive upward) and is used in the model to calculate the desalination rate in high brine fraction sea ice.

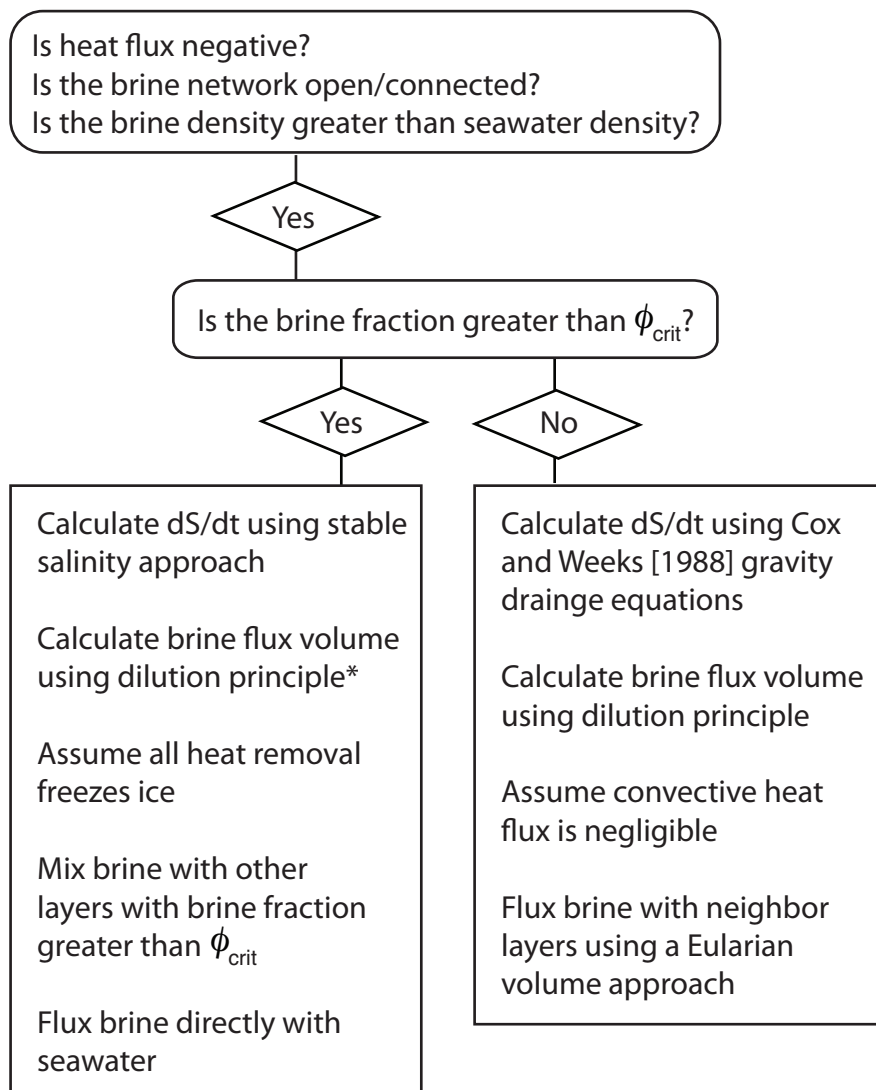


Figure 4. Operational diagram of the desalination scheme.

2.7 Convective Transport

Salinity – The total salt content of a particular layer of sea ice is only acted upon by the desalination routine. Therefore, after desalination is calculated independently for each layer, we simply remove an equivalent amount of salt from the bulk salinity. Other tracers, such as nutrients and detritus, are further modified by biology and we account for them differently using a fluid transport scheme described below. Algae are considered motile and do not move as a result of brine convection (see Biological Model below).

Heat - Typical models of sea ice heat conduction, including the model of Bitz and Lipscomb [1999] used here, do not account for changes in sea ice heat content due to desalination and associated changes in latent heat from changes in ice fraction. Without accounting for the heat flux associated with replacing brine with ice during desalination, such models can allow freezing to propagate too quickly through slushy layers. To simulate observed steep temperature gradients and slow freezing front propagation in ice desalinating via SLDM, we assume that latent heat flux accounts for all changes in the heat content of a desalinating layer with brine fraction above and ϕ_{crit} , and hold the temperature constant. The treatment of these slush layers is analogous to the treatment of the bottom of the ice column, where the interface temperature is fixed at the seawater temperature [Maykut and Untersteiner 1971, Bitz and Lipscomb 1999]. Effectively, a desalinating layer of the sea ice model with brine fraction above ϕ_{crit} becomes the thermal bottom of the ice sheet.

Nutrients and Tracers - The volume of fluid convected during desalination is calculated from the desalination rate using a simple dilution scheme involving the

layer below. Assuming the brine volume is constant in layer i over a time step, the change in salinity is equal to the product of the change in brine salinity with respect to the layer below, and the volume of convected brine.

$$\frac{dS^i}{dt} = \frac{dV_b^i}{dt} \frac{(S_b^{i+1} - S_b^i)}{z} \quad (21)$$

In layer i , the volume of brine is V_b^i (m), and the volume of brine convected through the layer is dV_b^i/dt ; $i+1$ denotes the layer below. Since the model time step is relatively small, and recognizing that the volume of new ice frozen is not necessarily linked to the amount of brine convected, we ignore the volume expansion associated with freezing new ice. Solving for dV_b^i/dt gives:

$$\frac{dV_b^i}{dt} = \frac{dS}{dt} \frac{z}{\Delta S_b}, \quad (22)$$

with ΔS_b equal to the difference in brine salinity between convecting layers. For the bottom layer of ice, and when layer brine fraction is greater than ϕ_{crit} , seawater salinity is used in place of S_b^{i+1} in the calculation of dV_b^i/dt . Due to the instability of Eq. 22 at very small brine differences between layers, we impose a minimum threshold on ΔS_b whose impact is explored through sensitivity analysis.

Fluid transport is also handled differently under the two desalination parameterizations. Below a brine fraction of ϕ_{crit} , brine is assumed to move and mix

between layers. Fluid flux volumes are calculated based on desalination derived from CW88. Because the dense brine is observed to exit from brine tubes, we assume that brine exiting a particular layer induces an equivalent exchange upon all the layers below, and consequently, the total convective volume in a layer is the sum of that induced by desalination in that layer as well as the layers above. The mass transport of solutes by brine is modeled using Fick's law [Arrigo et al. 1993], solved using a volume-based 1st-order accurate discretization.

Ice with brine fractions above ϕ_{crit} desalinates much more quickly using the SLDM, resulting in large brine volume fluxes. High levels of brine flux are associated with large-diameter brine tubes up to 2 cm across that occupy up to 15% of the horizontal ice cross-section [Fritsen et al. 1994]. Underneath a rapidly desalinating layer, such as flooded snow-ice, we assume that brine moves quickly through large brine tubes and bypasses the bulk of the brine matrix in underlying layers, arriving constitutionally intact to the site of desalination. Under the same assumption, dense brine exiting the desalination region quickly leaves the ice through brine tubes with little effect on the layers below. Accordingly, we use a simple volume replacement scheme to mix nutrients into this region of rapid desalination, where an amount of seawater equal to dV_b/dt replaces an equal amount of the layer brine, leading to the solute mass balance:

$$\frac{dC}{dt} = \frac{dV_b}{dt} \frac{1}{z} (C_{sw} - C) \quad (23)$$

where C is the brine solute concentration, C_{sw} is the seawater solute concentration. If multiple continuous layers exist with a brine fraction greater than ϕ_{crit} we assume that they share a fully-mixed brine.

3. Ice Station Weddell Site B Simulation

3.1. Observations

The Ice Station Weddell (ISW) experiment examined the physical and biological processes during fall at a drifting pack ice station in the Weddell Sea. At the ISW Site B study location (hereafter ISWB), a 22 cm layer of flooded slush, ~50% liquid by volume, froze under spring conditions near the surface of a 1.2 m thick snow-covered year-old ice pack. Freezing was initiated by rapidly dropping air temperature at the beginning of the study period (Figure 5). The freezing process, as measured by a thermistor string, lasted ~14 days, during which time the freezing front moved progressively through the slush layer. From an initial bulk salinity of 18 psu, the slush layer salinity was reduced to 6 psu by the end of the 15 days. The air temperature, ice temperature profile, ice and snow thickness, dissolved inorganic nitrogen (DIN) concentration, and ice algal pigment concentration was monitored to varying degrees over the course of 60 days [Fritsen et al. 1994, Lytle and Ackley 1996, Ackley et al. 1996].

We choose to tune the standard run of the model against the ISWB time series because of the continuity and consistency of observational data. The ISWB study area

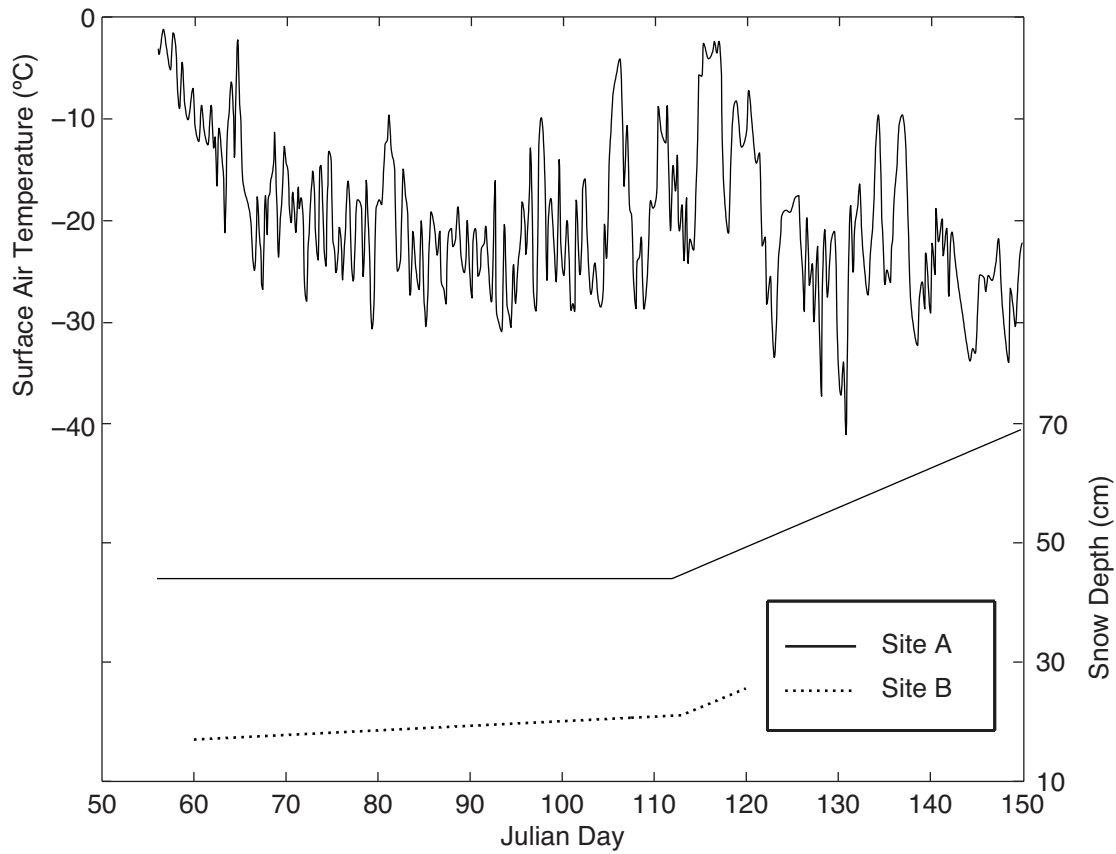


Figure 5. Measured surface air temperature and observed snow depths at Ice Station Weddell used as forcing data for model simulations. Surface air temperature was used at both Site A and Site B. Snow depths were calculated using accumulation rates estimated between Julian day 56 to 112, and 112 to 150 [Ackley et al. 1996].

is unique in capturing biological and physical time series measurements during almost an entire event of sea ice surface flooding until freeze-up.

3.2. Initial Conditions

Our simulation covers Julian days 60 – 120 during the ISWB period, and is initialized with a 22 cm slush layer beginning 8 cm below the ice surface. The salinity of the 8 cm layer of ice above the slush layer varies linearly between 6 psu at the surface and 18 psu at the slush layer, a gradient we assumed from the observation that freezing had begun before observations began on day 60. The slush layer itself is assigned the salinity of 18 psu [Lytle and Ackley 1996]. Below the slush layer was a granular ice layer 18 cm thick, to which we assigned a salinity of 8 psu. Congelation ice was below the granular layer, where we initialized salinities according to a standard C-shape salinity profile [ca. 4-5 psu, Table 4, Arrigo and Sullivan 1994] that correspond to measured salinities of first-year ice [Melnikov 1998]. An ice column diagram shows the vertical structure of the initial ISWB ice (Figure 6). The initial ice temperatures were matched to the thermistor data at the start of the simulation.

Snow depth was initialized at 17 cm on Julian day 60, with snowfall accumulation consistent with rates measured at ISWB. Rates of snow accumulation were 0.08 cm day⁻¹ between day 60 and 112 and 0.65 cm day⁻¹ during day 112-120 [Lytle and Ackley 1996; Figure 5]. The thermal conductivity of snow (k_s) was set at 0.4 W g⁻¹ K⁻¹ to achieve the observed rates of cooling, especially after slush layer desalination. This value of k_s is higher than is typically used when modeling sea ice, but is justified by

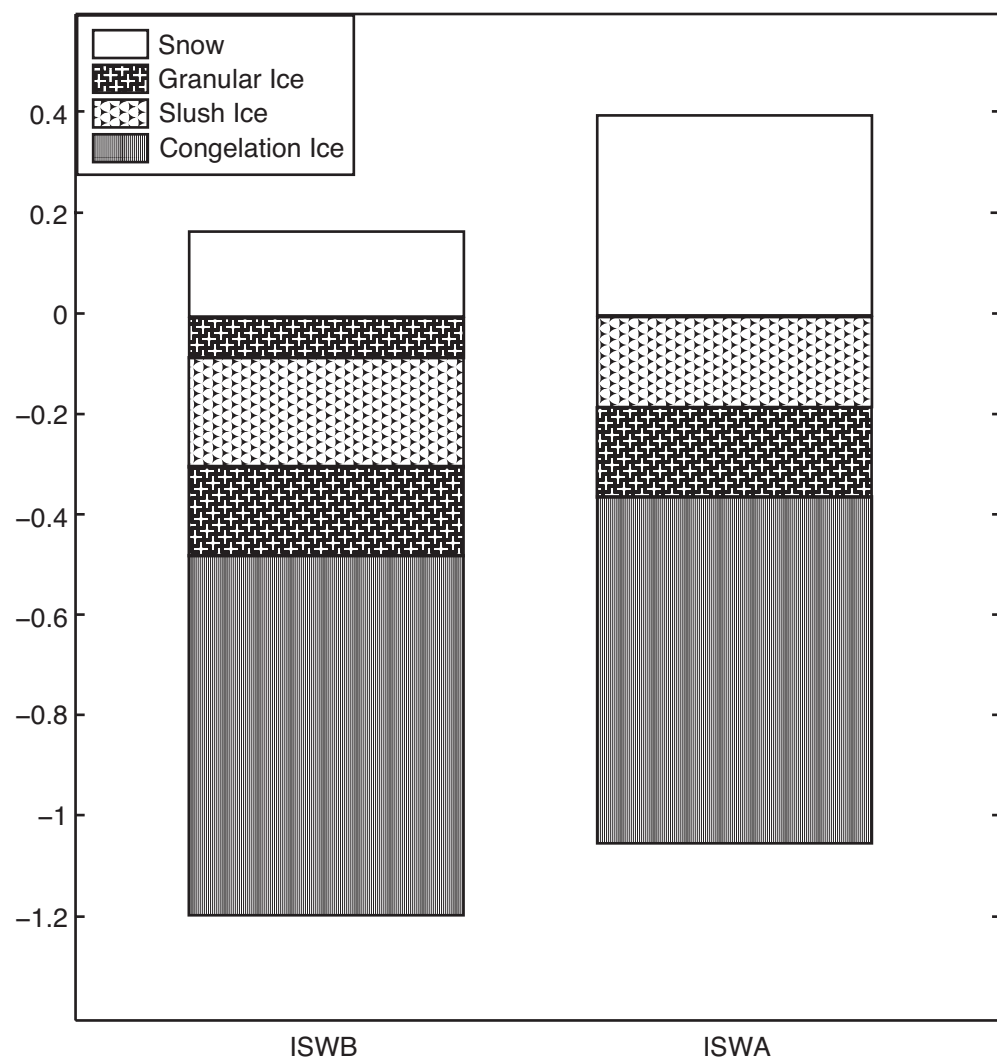


Figure 6. Vertical diagram of the different ice types and used as initial conditions for ISWB and ISWA simulations (scale in m).

Table 4. Thickness-dependent salinity values (psu) used to derive initial salinity profiles for model runs, with initial ice thickness h .

Ice Thickness	Bulk ice salinity
0	8
$h/9$	6.3
$2h/9$	5.6
$3h/9$	5.3
$4h/9$	5.2
$5h/9$	5.1
$6h/9$	4.9
$7h/9$	4.8
$8h/9$	4.8
h	6.2

Table 5. Forcing data sources

Simulation	Ice Station Weddell	Salinity Exploration
Air Temperature	Measured ^c	Specified
Wind Speed	ECMWF ^a	ECMWF ^a
Humidity	ECMWF ^a	ECMWF ^a
Surface Air Pressure	ECMWF ^a	ECMWF ^a
Cloud Cover	ECMWF ^a	ECMWF ^a
Ocean Heat Flux	Measured ^b	Measured ^b
Snow Depth	Measured ^b	Measured ^b
Initial Ice Salinity	Measured ^{b,c}	Measured ^{b,c}

^a ECMWF Interim Reanalysis

^b Lytle and Ackley 1996

^c Melnikov 1995

the multiple re-frozen, dense, icy layers observed in the ISW snow pack that conduct heat more quickly than loose snow [Lytle and Ackley 1996, Sturm et al. 2002]. Further physical forcing data are listed in Table 5.

Algal concentration was initialized to 200 mg C m^{-3} across the slush layer and underlying granular layer, and to 35 mg C m^{-3} elsewhere in the ice. The initial column integrated algal biomass was $2.88 \text{ mg Chl } a \text{ m}^{-2}$ which was concentrated in the high

brine fraction layers, consistent with observed values of 2.3-5.2 mg Chl *a* m⁻² [Fritsen et al. 1994]. Because water column nutrients were close to deep water values, we fixed the model water column nutrient concentrations at 30 μM NO₃, 2 μM PO₄, and 80 μM Si(OH)₄. Initial water and ice column NH₄ and POC concentrations are assumed to be zero. The nutrient concentrations in brine were initialized to 20% of seawater values, as observed by Fritsen et al. [1994].

3.3. Model Runs

We present results from 12 different ISWB model runs that encompass sensitivity to included parameterizations and an investigation of grid spacing. All ISW model runs are listed in Table 6, along with the varied parameters that define them.

Standard Run – (run W1) The new parameters introduced to the model by our desalination and fluid transfer scheme are the critical brine fraction (ϕ_{crit}) that determines which of the two desalination and fluid transfer methods will be used, and the minimum difference in brine salinity (ΔS_b) that is used to calculate the brine flux volume. During model development, we first tuned ϕ_{crit} until modeled slush layer salinity, temperature profiles, and algal biomass most closely matched observations. The parameter ΔS_b is relatively independent, and was tuned after ϕ_{crit} to match estimates of brine flux made by Fritsen et al. [1994] and Ackley et al. [1996]. Based on this model tuning and sensitivity analysis (presented below), values of 0.2 for ϕ_{crit} and 2 psu for ΔS_b result in the best overall fit to observed data.

Sensitivity to ϕ_{crit} – We examine model response to variation in ϕ_{crit} , including setting it higher (0.25; run W3) and lower (0.15; run W2) than the standard run value,

Table 6. ISW model runs and parameters

Run	Simulation	Latent Heat Flux ¹	ϕ_{crit} (fraction)	ΔS_b (psu)	Initial Slush Layer (cm)	Grid Size (cm)
W1*	ISWB	yes	0.2	2	22	1
W2	ISWB	yes	0.15	2	22	1
W3	ISWB	yes	0.25	2	22	1
W4	ISWB	no	--	2	22	1
W5	ISWB	no	0.2	2	22	1
W6	ISWB	yes	0.2	1	22	1
W7	ISWB	yes	0.2	1.5	22	1
W8	ISWB	yes	0.2	2.5	22	1
W9	ISWB	yes	0.2	3	22	1
W10	ISWB	yes	0.2	2	22	2
W11	ISWB	yes	0.2	2	22	5
W12	ISWB	yes	0.2	2	22	10
W13*	ISWA	yes	0.2	2	18	1
W14	ISWA	yes	0.15	2	18	1
W15	ISWA	yes	0.25	2	18	1
W16	ISWA	no	--	2	18	1

* Standard Run

¹ Latent heat flux derived from slush layer desalination method (SLDM)

turning off SLDM and replacing it with CW88 (run W4), and allowing desalination to process as in the standard run neglecting the associated latent heat flux (W5).

Sensitivity to ΔS_b – (runs W6-W9) This parameter directly controls the brine flux volume, which determines the amount of nutrients available to sea ice algae growing in a slush layer. These model runs encompass variations in ΔS_b between 1-3 psu.

Sensitivity to grid resolution – (runs W10-W12) To test the ability of our model to simulate slush layer dynamics at the lower resolution typical of global-scale models, we ran the model at additional layer spacings of 2, 5, and 10 cm in addition to the standard run at 1 cm. We note that many models actually use much larger effective grid sizes, representing sea ice with just 1-4 layers [Flato and Hibler 1995; Winton 2000; Zhang and Rothrock 2003; Lipscomb and Hunke 2004]. However, if surface flooding and other slush layer generating mechanisms are to be included in such

models, resolution of at least the slush layer itself will need to be increased. With larger grid sizes, the average brine fraction of a layer containing a slush layer would be too low, and consequently, would not trigger the appropriate rapid desalination and convection routines.

For each of the different vertical resolutions tested, care was taken so that the initial amounts of total salt, algae, heat, and nutrients were allocated as similarly as possible. For consistency, the time step was kept constant for these model runs.

3.4. Results

3.4.1 Standard Run

Temperature – The ISWB standard run (run W1) simulation matches measured temperature profiles with a maximum error of about $\pm 1^{\circ}\text{C}$ (Figure 7). The model tracks the observed -2°C isotherm accurately as the freezing front advances through the slush layer and captures the change in the downward rate of advance on Julian day 74. After this time the freezing front advances past the slush layer and cooling is more rapid.

The modeled uppermost ice cools faster than observations during the freezing of the slush layer. This can be attributed to SLDM and associated convective heat flux, which tends to desalinate the slushy regions progressively downward, one layer at a time. In reality, the entire slush region may be desalinating at once, allowing convective heat flux to warm the entire slush region and leading to slightly warmer observed temperatures near the ice surface when compared to model results.

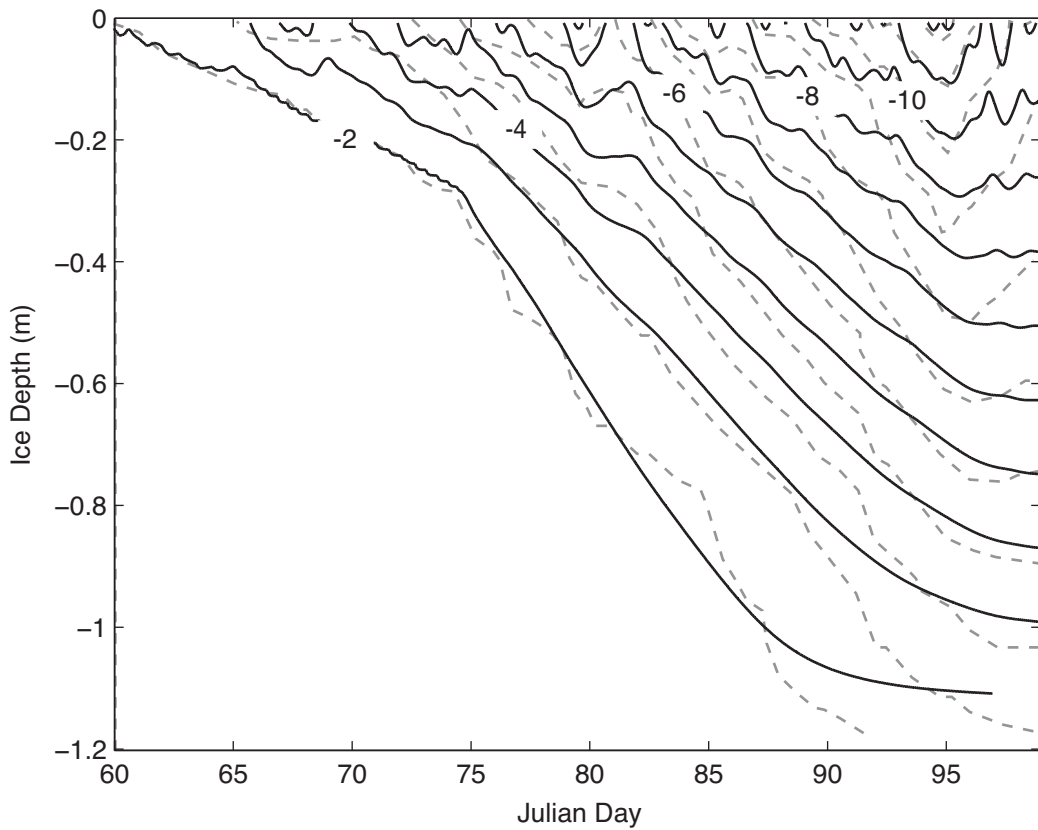


Figure 7. A comparison of observed and modeled temperature contours within the ice pack over time at ISW Site B ($^{\circ}\text{C}$). The model reproduces the initial freezing front as it passes through the slush layer between -0.07 – -0.29 m depth. Beyond day 74 the ice cools more rapidly from the top as brine convection becomes less significant. The model underestimates cooling later in the simulation by up to 1°C .

Following day 74, modeled and observed isotherms trend closer together at the ice surface.

Salinity – The slush layer desalinates rapidly according to the stable salinity desalination scheme during the first 14 days of simulation. Desalination slows as brine volumes drop below ϕ_{crit} after day 74, after which model desalination is governed by CW88. The mean salinity of the slush layer on day 74 is 6.6 psu, and is further reduced to 6.3 psu before desalination is cut off completely due to declining temperature and brine fraction (Figure 8). This final slush layer bulk salinity agrees well with the observed value of 6 psu.

Nutrients – Although the model includes a number of different nutrients, we restrict our discussion to nitrate since it is the first nutrient to become limiting to algae in our model. Nitrate values, initially at 20% of seawater concentration, increase rapidly in the brine once desalination of the slush layer begins and become equivalent to seawater values by Julian day 63, just three days after the simulation begins (Figure 9A). Algae, although increasing exponentially, are not able to reduce nutrient concentrations until after the slush layer freezes. Above the freezing front, desalination and fluid flux slow nutrient replenishment and resident algae quickly consume the remaining nitrate, leading to a downward progression of nitrate exhaustion in the slush layer.

Algal dynamics – The majority of algal biomass accumulates during the first three weeks of model time, matching observations (Figure 10). The maximum column-integrated biomass of 25 mg m^{-2} is within the range of $20 - 27 \text{ mg Chl } a \text{ m}^{-2}$ found in ice cores. After the freezing front passes, the convection-driven nutrient supply is cut

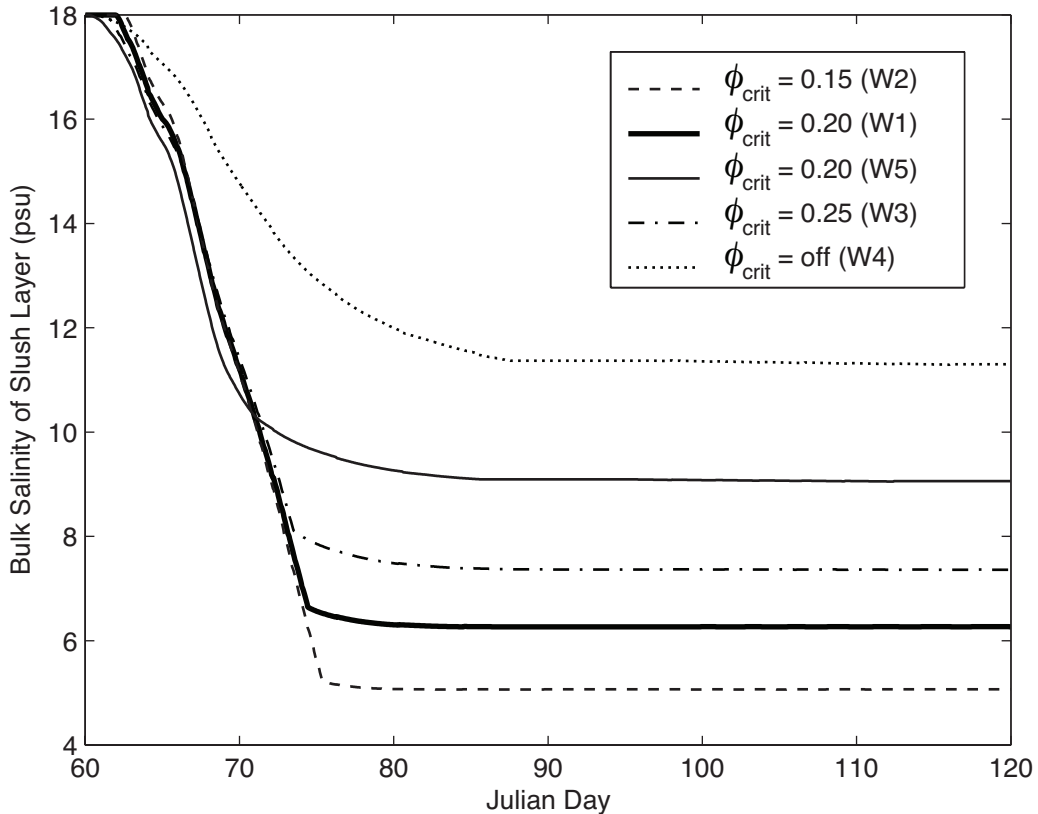


Figure 8. Evolution of modeled slush layer salinity over a range of critical brine fractions (ϕ_{crit}). Once freezing of the slush layer begins, rapid desalination causes the bulk salinity to decrease rapidly until completion of freezing on Julian day 74. In the case of $\phi_{crit} = 0.20$, the salinity decreases to close to 6 psu, in line with observations. In the case of only Cox/Weeks interior ice desalination ($\phi_{crit} = \text{off}$), the salinity decreases much more slowly, and never reaches below 13 psu. Included are results from a simulation where convective heat flux was omitted ($F_{cb} = 0$), to illustrate that feedback between the stable salinity scheme and the introduction of warm brine is critical to the magnitude and rate of desalination.

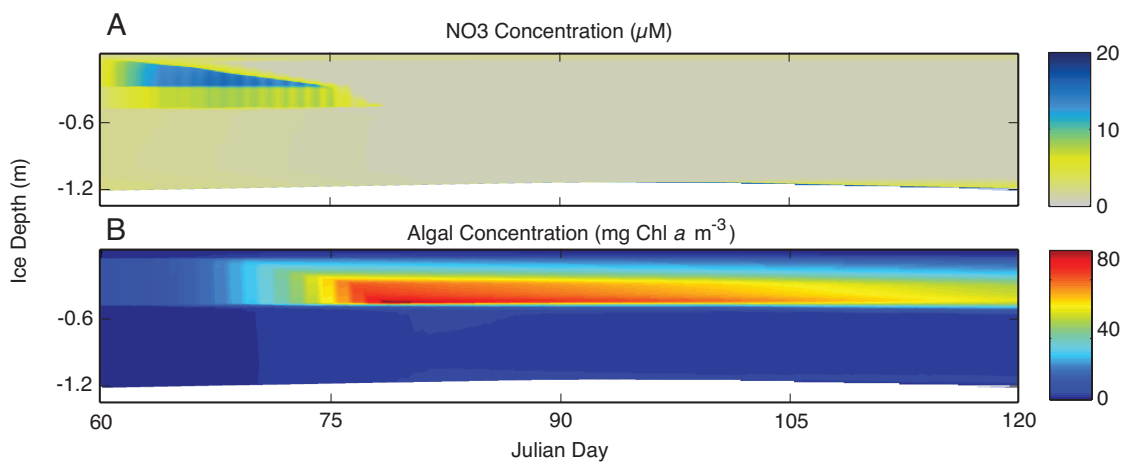


Figure 9. ISWB sea ice model depth profile evolution over time of A) NO_3 concentration, and B) algal biomass. Overlying snow is not shown. As the slush layer is cooled from above, it desalinates and freezes. The desalination induces rapid brine exchange during the freezing period and mixes in nutrients into the porous ice. The nutrient supply is largely cut off by day 75 after the slush layer freezes, and algae reach their peak biomass after exhausting the nutrients ~ 7 days later.

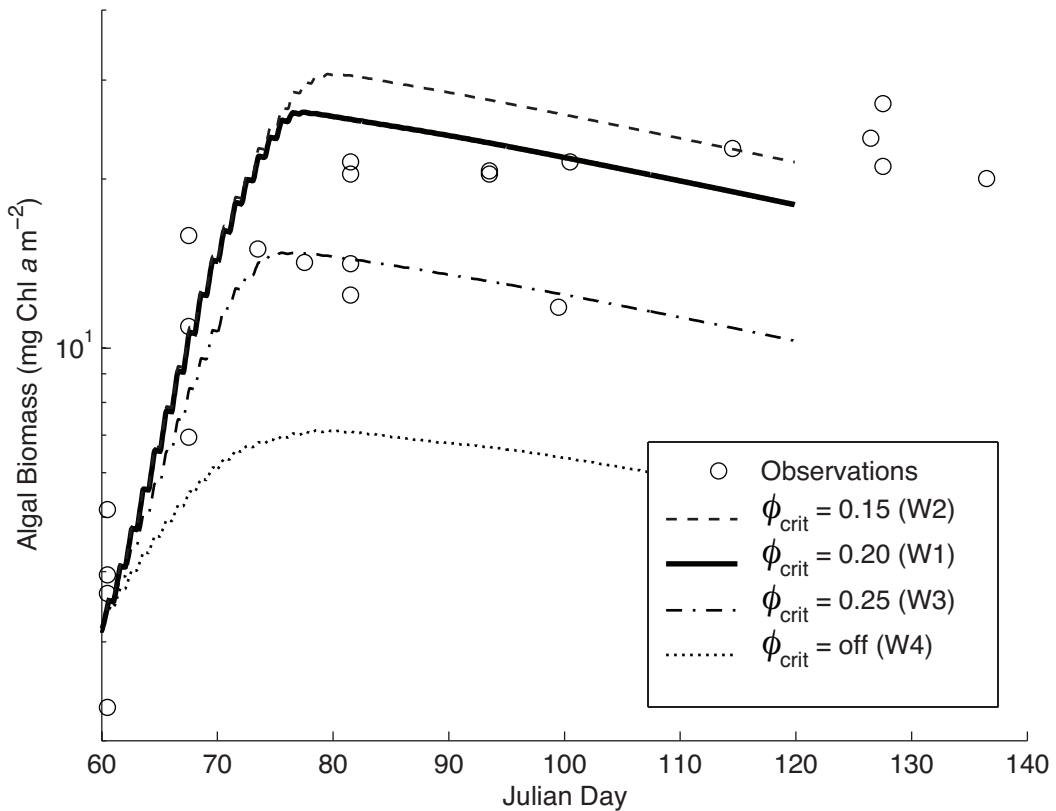


Figure 10. Total ISWB ice column Chl *a* concentration observed and modeled using a range of ϕ_{crit} . Simulations stopped at day 120. Without using the slush desalination scheme, algal growth is stunted by a lack of nutrients and algal biomass does not reach any of the observed values (run W4). Using $\phi_{crit} = 0.20$ best reproduces the observed Chl *a* concentration over time.

off, and algae quickly become nutrient limited. The maximum algal concentration of 84 g Chl a m $^{-3}$ is reached in the frazil ice below the slush layer (Figure 9B); continued flushing of the region by seawater nutrients in conjunction with a later freeze date allowed optimal growing conditions to persist below the slush layer longer than anywhere else in the ice. Cold temperatures and low nutrients restrict algal growth after Julian day 78.

Fluid flux – Total daily fluid transport shows a sharp decline after the slush-layer freeze-up on JD 74 (Figure 11). The total fluid replacement in the slush layer during the first 15 days of the simulation for the standard run was 1.14 m 3 m $^{-2}$ or 0.076 m 3 m $^{-2}$ day $^{-1}$, equating to a 10.4x turnover rate over course of the slush layer desalination. This fluid flux is in the middle of the range of volume fluxes of 0.8-1.8 m 3 m $^{-2}$ estimated to have convected during slush layer freezing at ISWB [Ackley et al. 1996].

3.4.2 Sensitivity to ϕ_{crit}

Model results from the simulation that neglected our slush layer desalination scheme (run W4) fail to replicate any of the temperature, bulk salinity, nutrient, or biomass observations. The freezing front passes rapidly through the slush layer by day 69, ~5 days earlier than observed (Figure 12). More importantly, the exclusive use of CW88 only reduces salinity to ~12 psu in the first 14 days (Figure 8), and because brine flux is small, nutrient levels do not increase enough to stimulate a large bloom. Maximum biomass accumulation is just 6.8 mg Chl a m $^{-2}$ (Figure 9).

When ϕ_{crit} is lowered from 0.2 to 0.15 (run W2), the slush layer cools more slowly and delays the transit of the -2°C isotherm through the slush layer (Figure 12). In

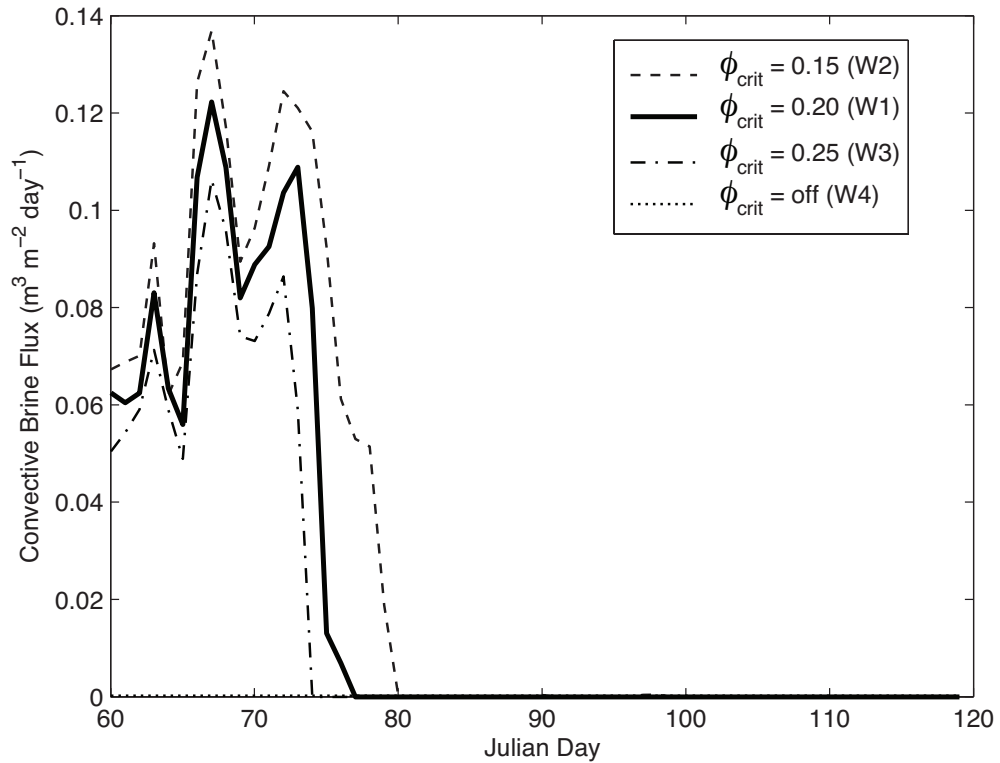


Figure 11. Daily convective brine flux volume during ISWB simulations with varied ϕ_{crit} . Fluxed volumes respond negatively when the slush desalination scheme is used over a smaller range of brine volumes (increases in ϕ_{crit}).

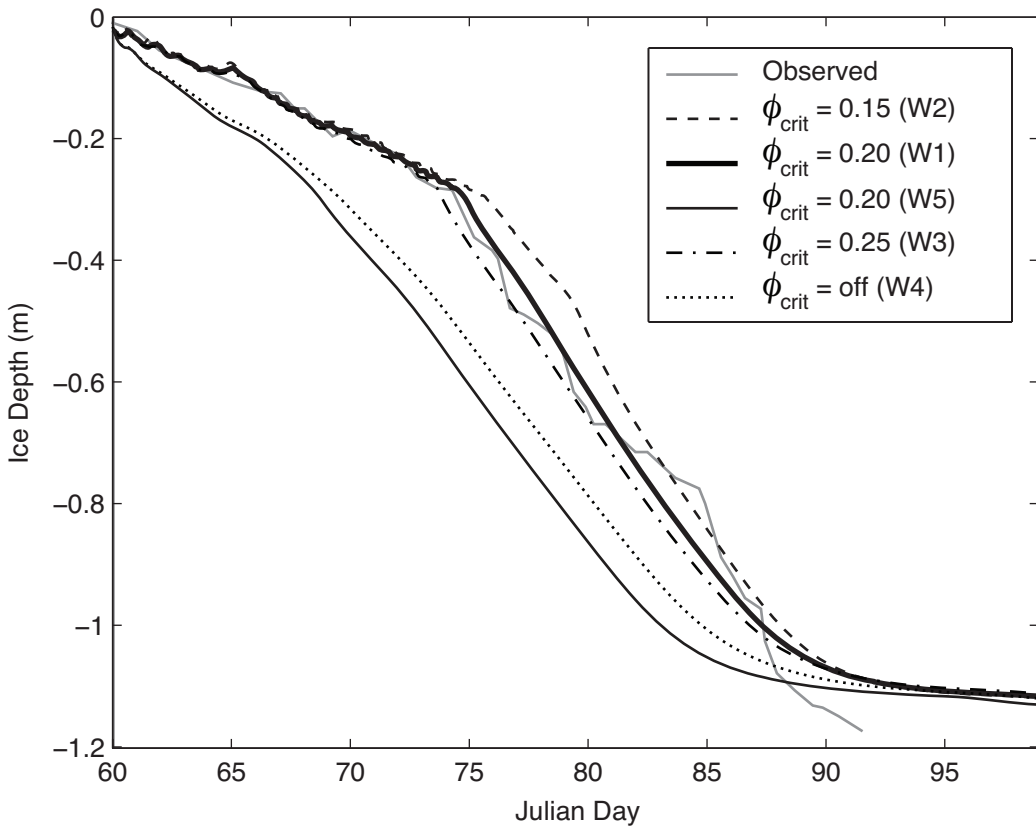


Figure 12. Depth of the ISWB freezing front over time for different values of ϕ_{crit} as demonstrated by the -2°C isotherm. With either no convective heat flux ($F_{cb} = 0$) or no rapid slush desalination ($\phi_{crit} = \text{off}$) the freezing front proceeds too quickly downward through the ice. The standard run ($\phi_{crit} = 0.20$) fits the observed data reasonably well; with $\phi_{crit} = 0.25$ appears to be a slightly better fit, however using $\phi_{crit} = 0.20$ results in salinities and algal growth that more closely matches observations.

addition, more salt is rejected from the slush layer so that it arrives at a final bulk salinity of 5 psu, lower than the observed value of 6 psu (Figure 8). Chl *a* concentrations follow a similar growth trajectory but the algae reach a higher than observed Chl *a* concentration of 30.3 mg Chl *a* m⁻², since nutrients are replenished via intense brine convection over a longer period of slush layer desalination (Figure 10). The brine flux volume maintains a pattern similar to the standard run, but is consistently higher, reflecting the additional desalination (Figure 10).

With ϕ_{crit} elevated from 0.20 to 0.25 (run W3), the slush layer desalination scheme is stopped at a higher brine fraction than in the standard run, and the freezing front descends more rapidly through the slush layer (Figure 12). Overall, the -2°C isotherm more closely tracks the observed data than in the standard run; however, the standard run exhibits salinities and algal growth that more closely match observations (Figures 8 and 10). The bulk salinity of the slush layer remains above 7.8 (Figure 8), higher than the observed value of 6 psu, and the brine flux volume is reduced, reflecting the reduced desalination (Figure 11). Chl *a* accumulation is reduced from the standard run due to colder temperatures from earlier freezing front advancement, and more importantly, due to shorter duration of significant brine convection, which reduces exposure to nutrients. The maximum integrated algal biomass of 14.2 mg Chl *a* m⁻² is below the majority of observations (Figure 10).

When $\phi_{crit} = 0.2$, as in the standard run, but the associated latent heat flux is switched off (W5), the freezing front proceeds too fast through the slush layer (Figure 12). Here, the slush layer freezes even faster than the case without SLDM (W4), since ice with a lower salt content has a smaller effective specific heat (q_b).

3.4.3 Sensitivity to ΔS_b

Because the brine flux volume is independent of the convective heat flux estimate, varying ΔS_b does not impact ice physics beyond that transport of brine and associated nutrients. The total brine flux volume increases with a decreasing ΔS_b (Table 7). Halving ΔS_b to 1 psu (run W6) effectively doubles the brine transport, and conversely, increasing ΔS_b (runs W8-W9) results in a lowering of brine transport. Convection is vigorous in all runs, however, and nutrient supply to the algae is not limiting in any of these test cases with respect to the standard run. Biomass accumulation is largely unaffected and therefore, these results are not shown.

3.4.3 Sensitivity to grid resolution

Overall, model results are remarkably consistent across vertical grid resolutions (Figure 13). [This suggests to me that you could use a slab layer model, i.e. one where the snow, slush, and ice layers are represented as separate, yet single layers. This would lower the computational cost of your model dramatically. While the physics is captured in slab layers, you could have the biological variables be gridded and modeled at a finer resolution. Perhaps comment on this in your conclusions.] At all resolutions, the transition from the slower freezing of slush layer to the faster freezing of the solid ice below at Julian day 74 is captured (Figure 13). At increased grid spacing, a step-like form is visible in the progression of slush layer freeze up. These steps are a result of the model resolution, and occur when the layer brine fraction crosses the ϕ_{crit} boundary and the desalination method is switched from SLDM to CW88. Despite the stepping, even when the slush layer includes just two layers, as in

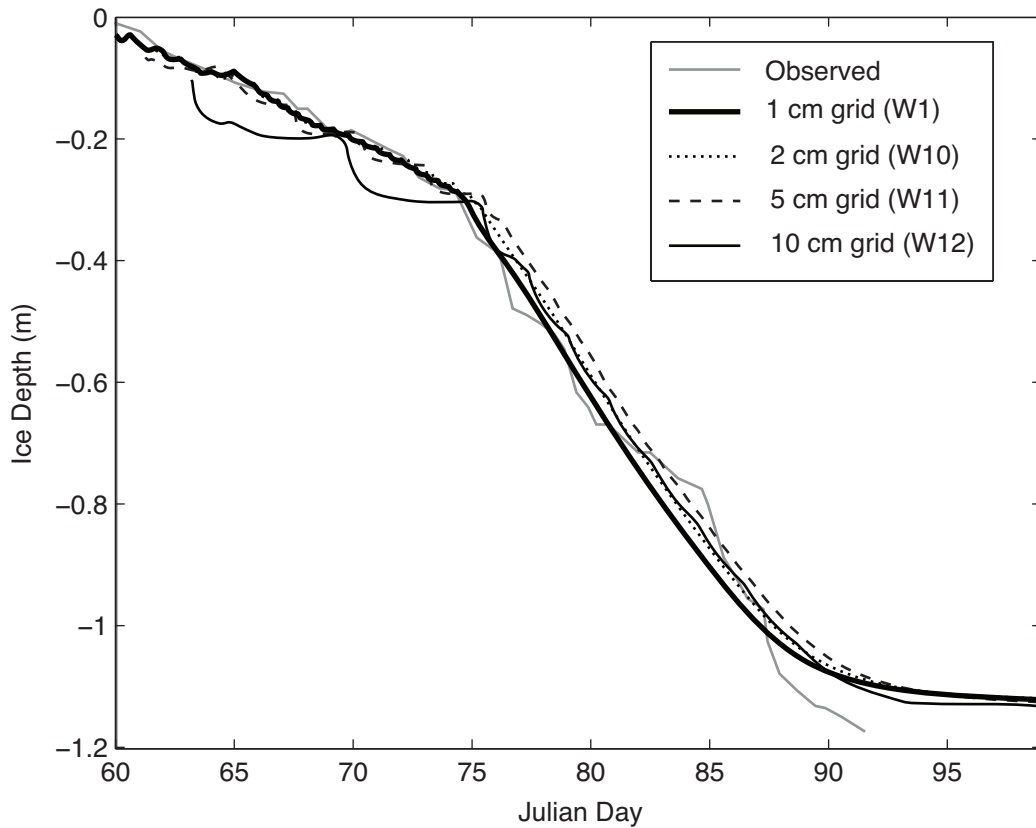


Figure 13. Depth of the ISWB freezing front over time for different model grid spacing as demonstrated by the -2°C isotherm. Grid size has little effect on the freezing front progression, although 'stepping' that occurs when the brine volume is reduced past ϕ_{crit} can be easily seen in the case of the 10 cm grid.

Table 7. Integrated convective brine flux volumes for ISWB simulations using different values of the minimum inter-layer brine salinity difference.

ΔS_b (psu)	Volume Fluxed (m ³)
1	2.37
1.5	1.58
2	1.18
2.5	0.95
3	0.79

the case of the 10 cm simulation, the average freezing rate is still modeled with reasonable accuracy.

From plots of slush layer salinity evolution, we see that most model runs arrive at a similar bulk salinity after desalination (Figure 14). The final slush layer salinity of 6.7 psu using a 10 cm grid spacing (run W12) is higher than the standard run with 1 cm grid spacing (6.3 psu; run W1). Because of the larger grid size, extra cooling appears to be required before desalination begins. Because the layer is slightly colder when the brine fraction reaches ϕ_{crit} , the brine salinity is higher leading to the bulk salinity of 6.7 psu.

Plots of daily brine flux volume show that the variability in brine flux increases with vertical resolution, and in the 10 cm case, ceases altogether for a day around Julian day 63 as the freezing front passes between model layers (Figure 15). Due to the similar bulk salt content and freezing rate, however, the total integrated brine flux is similar across the runs, varying between 1.14 and 1.31 m³ m⁻².

Regardless of vertical resolution, the modeled fluid flux is sufficient to supply algae with ample nutrients to fuel growth during slush layer desalination. Because of the continued flushing, algae are able to grow at their physiological maximum,

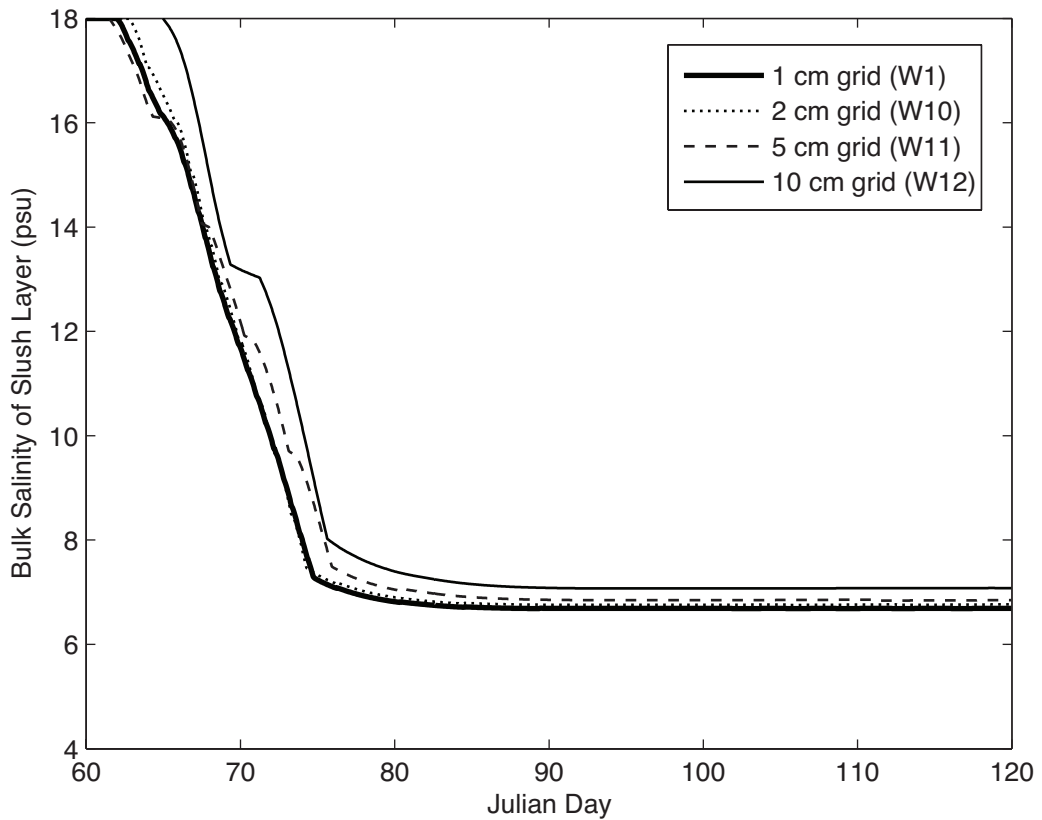


Figure 14. Evolution of modeled slush layer salinity over a range of model grid spacing. The modeled salinity is especially sensitive to grid spacing.

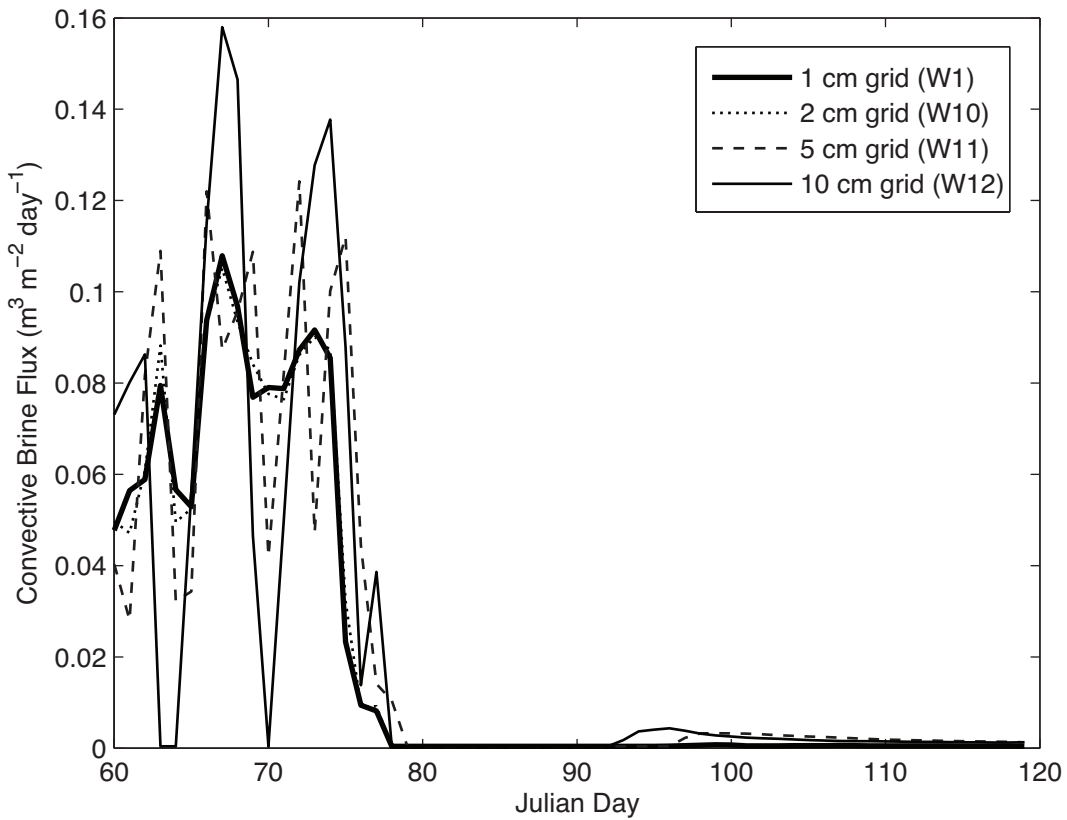


Figure 15. Daily convective brine flux volume during ISWB simulations with varied model grid spacing. The grid spacing causes the brine flux to be more highly variable on a daily basis, however the total volume fluxed during the simulation (i.e. integration of the above curves) only varies between 1.18 and 1.31 m³.

encountering nutrient limitation only after the slush layer has frozen. This leads to similar algal biomass accumulation between simulations with different grid sizes (Figure 16). Increasing vertical resolution does have a small positive influence of maximum biomass, with the 10 cm resolution reaching a maximum of 30.3 mg Chl *a* m⁻², compared to 25.2 mg Chl *a* m⁻² for the standard 1 cm run. Total Chl *a* initially accumulates at the same rate, but algae continue net growth later into the simulation with larger grid spacing. Because slush layers share a mixed brine, algae in the top of a thick grid layer have continued access to layer nutrients if the freezing front has not passed completely through the layer (i.e. SLM still active), which leads to elevated growth.

4. ISW Site A Simulation

4.1. Observations

Time series observations at Ice Station Weddell Site A (hereafter ISWA) include a detailed set of physical and biological ice monitoring data identical in scope to those at ISWB, but in a more varied ice floe where deformation produced a highly heterogeneous ice pack. Observations at ISWA begin on Julian day 56, 4 days earlier than at ISWB, when the ice pack was still isothermal due to very recent surface flooding and warm atmospheric temperatures. Because of the heterogeneous ice pack, different thicknesses of slush were observed depending on the sampling location, with 80% of locations below freeboard. [Fritsen et al. 1994, Lytle and Ackley 1996, Ackley et al. 1996].

Simulation of observed physical properties from a heterogeneous floe can be

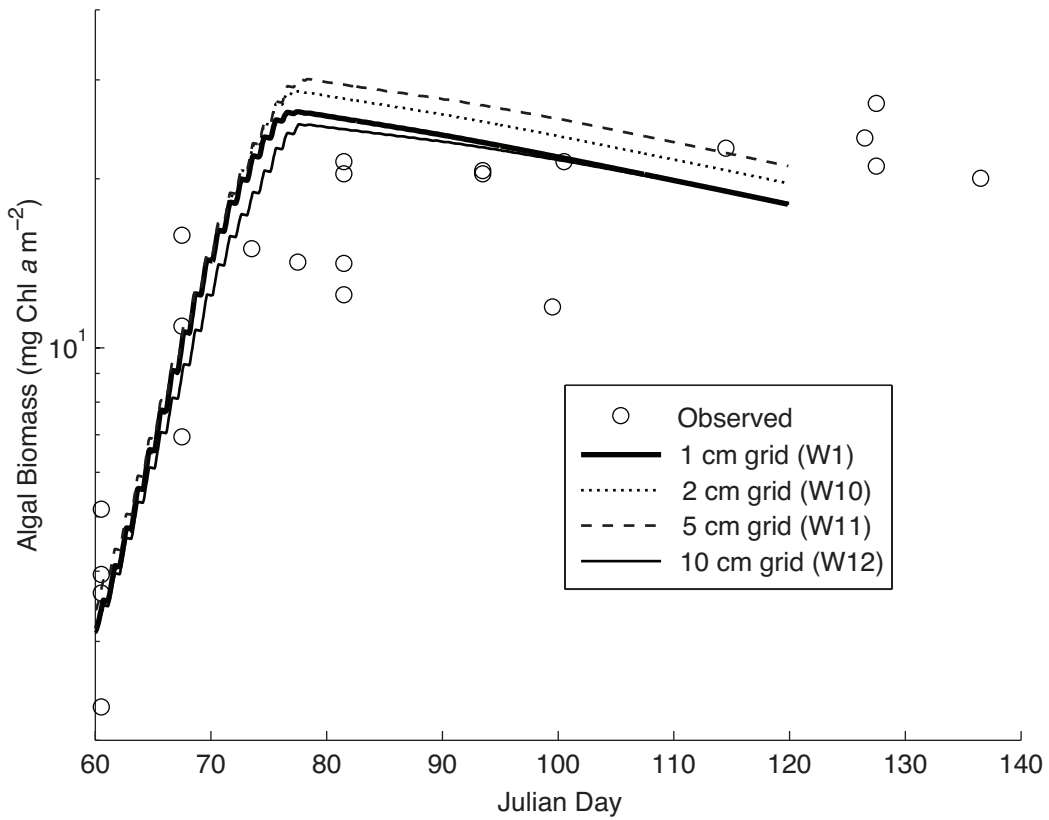


Figure 16. Total ISWB ice column Chl a concentration observed and modeled using different model grid spacing. Total Chl a initially accumulates at the same rate, but algae continue net growth later into the simulation with larger grid spacing. Algae in the top of a thick grid layer have continued access to layer nutrients if the freezing front has not passed completely through the layer, leading to elevated growth.

difficult using a one-dimensional model. Ice core biomass may vary by several orders of magnitude depending on whether gaps exist in ridged ice, or where large variations in snow depth drastically alter the light available to ice-bound algae. At ISWA, the installed thermistor string sampled a vertical profile of ice temperatures over time, but was likely influenced by nearby ice and snow of varying thicknesses that create horizontal temperature gradients [Sturm et al. 2002].

Nevertheless, observations at ISWA lend confidence that a one-dimensional model can capture the essential evolution of a heterogeneous ice pack. The use of multiple core samples captures some of the variability in observations of algal biomass. Furthermore, the initial ice (110 cm) and snow (40 cm) thicknesses at the site of the ISWA thermistor string are within one standard deviation of the mean floe ice and snow thicknesses (144 cm and 44 cm respectively [Lytle and Ackley 1996]), giving confidence that measured temperatures represent a median of the floe that can be modeled.

4.2. Initial Conditions

We assigned an initial slush layer thickness of 18 cm, equal to the mean slush layer thickness calculated for the ice floe [Lytle and Ackley 1996]. The depth of the slush layer at the thermistor string is unclear, although thought to be >6 cm [Ackley et al. 1996]. The temperature records show a delayed freezing front advancement across a depth greater than 6 cm, indicating that either there was lateral heat transfer from adjacent warm ice (perhaps due to further flooding, or differences in local snow depth) or the actual slush layer was much thicker than 18 cm (Figure 17). We assumed the

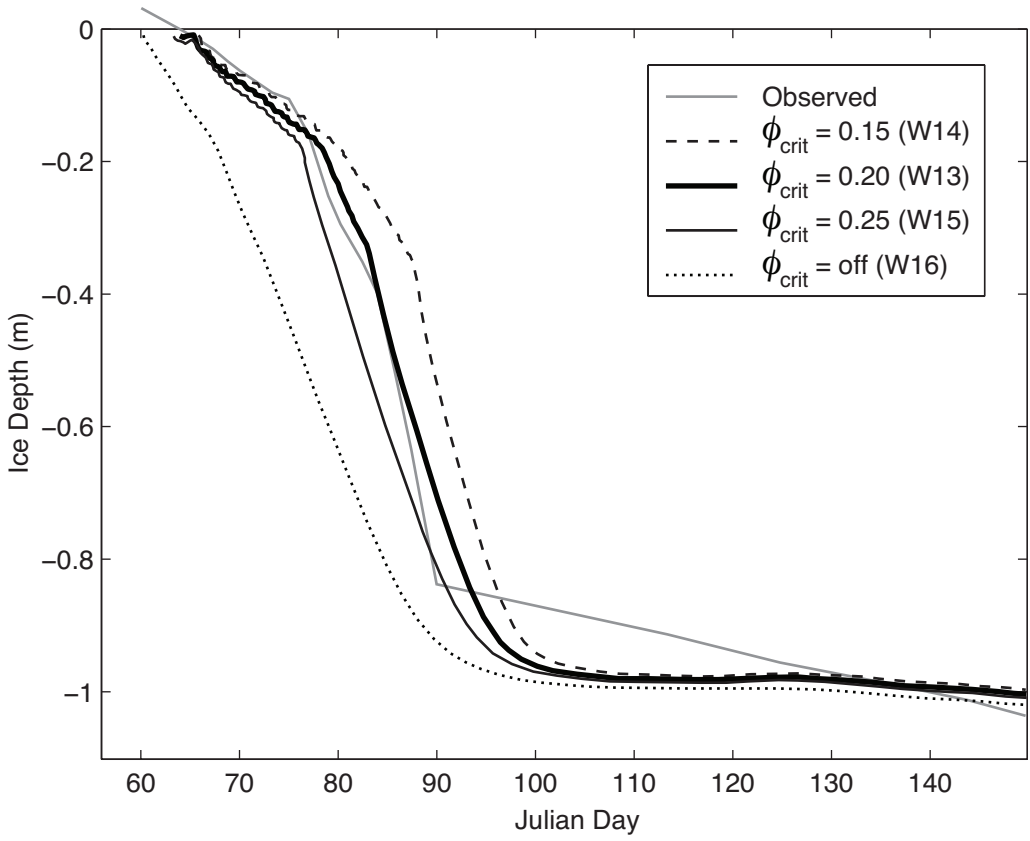


Figure 17. Observed and modeled freezing fronts at ISWA. The observed freezing front is the -1.8°C isotherm [Lytle et al. 1996], while the modeled fronts are -1.9°C isotherm. Because the reported seawater salinity is 34.1 psu, model desalination does not begin until the brine salinity reaches above 34.1 psu, which occurs at a temperature of -1.84°C . The isotherm at -1.9°C is a better metric of freezing for the model.

slush layer was on top of the more solid ice surface with a salinity of 16 psu [Ackley et al. 1996]. Without additional information concerning mean initial ice properties, we prescribed the initial salinity profile similarly to ISWB, with an 8 psu, 18 cm thick granular layer below the slush layer, and congelation ice below the granular layer with a standard C-shape salinity profile from Table 4 (see Figure 5 for ice column diagram). In accordance with observations, the ice temperature was initially isothermal at the seawater temperature, and a temperature gradient was assigned in the snow between seawater and the atmospheric temperature. Nutrients were initialized similarly to the ISWB simulations, and initial algal concentrations were assigned to match observations. The simulation period was from Julian day 56-150; air temperature and snow forcing are shown in Figure 6.

4.2. Model Runs

Standard Run – The ISWA standard run (W13) uses the same desalination parameters as the ISWB standard run.

Sensitivity to ϕ_{crit} – (W14-W16) The parameter ϕ_{crit} determines which slush layer desalination method will be used, a process that is influenced by the heat flux and sea ice geometry. Because the value of ϕ_{crit} that yields results most consistent with observations might change based on different ice conditions at ISWA and ISWB, we performed a sensitivity analysis of ϕ_{crit} similar to that for the ISWB simulation, using values above (0.25) and below (0.15) the standard run value of 0.2 derived for ISWB. We also performed one model run where the SLDM was turned off and replaced by CW88 (W16).

4.3. Results

4.3.1 Standard Run

Temperature - Using our chosen standard value for $\phi_{crit} = 0.20$ in the ISWA run (W13), the simulated depth of the freezing front tracks the observed freezing front reasonably well (Figure 17). The freezing front does not begin to enter the slush layer until after day 60 due to the insulating snow cover. The temperature observations show a transition from slow to fast cooling around day 75-76, approximately two days earlier than the model results. This transition marks the transit of the freezing front through the slush layer. The two extra days of slush layer freezing in the model is not unexpected since the thickness of the slush layer at the thermistor string may have been thinner than the ISWA floe average of 18 cm that was used in the model [Ackley et al. 1996]. Using a thinner slush layer in the simulation would likely result in a better match to observed temperatures, but we are interested in how well the model represents observations using mean floe values.

Salinity - The slush layer desalinated to 6.0 psu after freezing of the slush layer (Figure 18), matching observations the rate of desalination, and the final slush layer bulk salinity of 6 psu [Ackley et al. 1996].

Nutrients – Nutrients follow a similar pattern and profile to those at ISWB and are not shown. Nutrients in the slush layer brine increase rapidly and reach close to seawater values once the freezing and desalination of the slush layer begins. Nutrients are quickly exhausted by the large algal biomass once the slush layer freezes.

Algal dynamics - Algal time series measurements from ISWA show more scatter than at ISWB due to the more heterogeneous ice conditions. The standard ISWB run

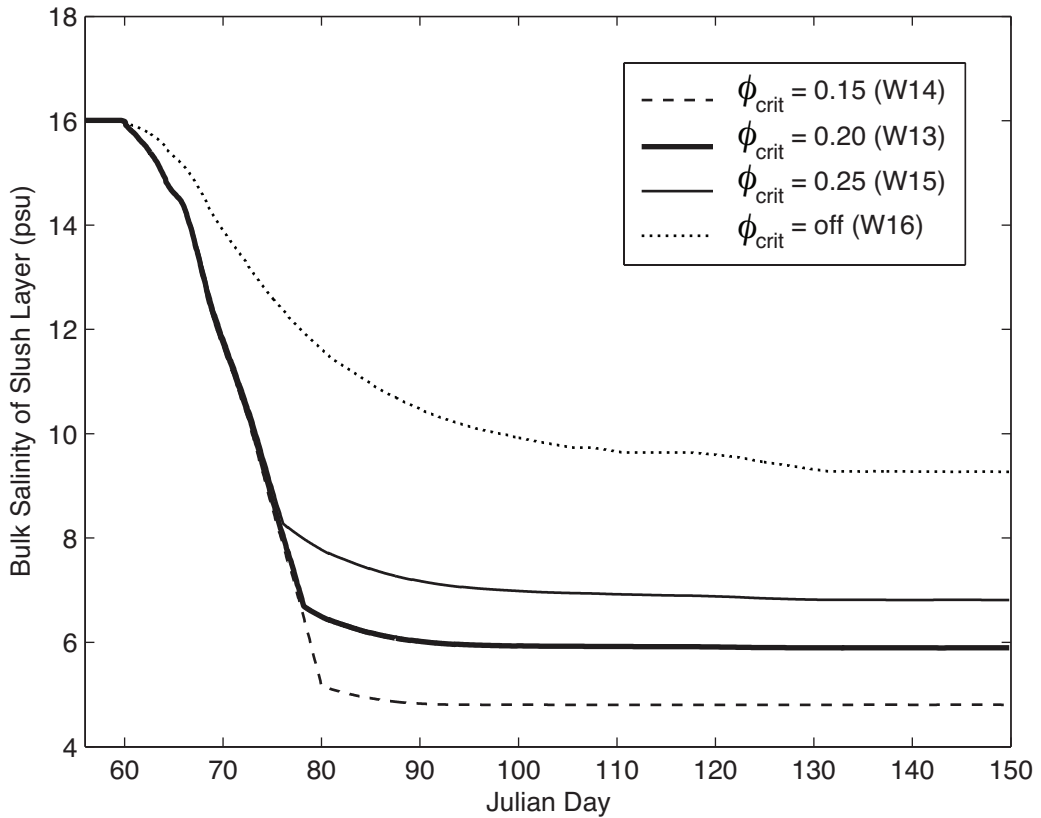


Figure 18. Evolution of ISWA modeled slush layer salinity for model run using different values of ϕ_{crit} . Similarly to ISWB results, using $\phi_{\text{crit}} = 0.20$ produced the most accurate desalination profile, with salinity reaching 6.2 psu, near the observed value of 6 psu.

($\phi_{crit} = 0.20$) algal biomass grows at a rate equal to observed increases in Chl *a*, and roughly tracks the middle of the range of observations (Figure 19). After reaching a peak biomass at day 85, the modeled algal biomass slowly declines for the remainder of the simulation. Similarly to ISWB simulations, algae exhaust available nutrients shortly after the slush layer freezes and rapid brine convection ceases. After day 120, there is a notable increase in algal biomass that is coincident with an extreme warm spell [Ackley et al. 1996]. While the model captures the ice temperature trends, modeled algae are still nutrient starved during the warm spell because of a lack of brine convection. The warm spell may have permitted additional surface flooding or wicking of brine into overlying snow, processes that were not captured by the model, and that would allow replenishment of nutrients in the ice interior.

4.3.2 Sensitivity to ϕ_{crit}

As in ISWB, using $\phi_{crit} = 0.20$ resulted in the most realistic simulation of observed data (run W13). Using $\phi_{crit} = 0.25$ (run W15) resulted in a slightly better match between modeled and observed freezing fronts, although modeled algal biomass was lower than the majority of observations. At $\phi_{crit} = 0.15$ (run W14), the slush layer took several days longer to freeze than in observations and desalinated too quickly and to too low a value (5.1 psu), and algal biomass was generally higher than the range of observations. Simulation with our slush desalination scheme disabled (run W16) resulted in unrealistically rapid cooling, overly high salinity, and depressed algal growth when compared to time series observations (Figures 17-19).

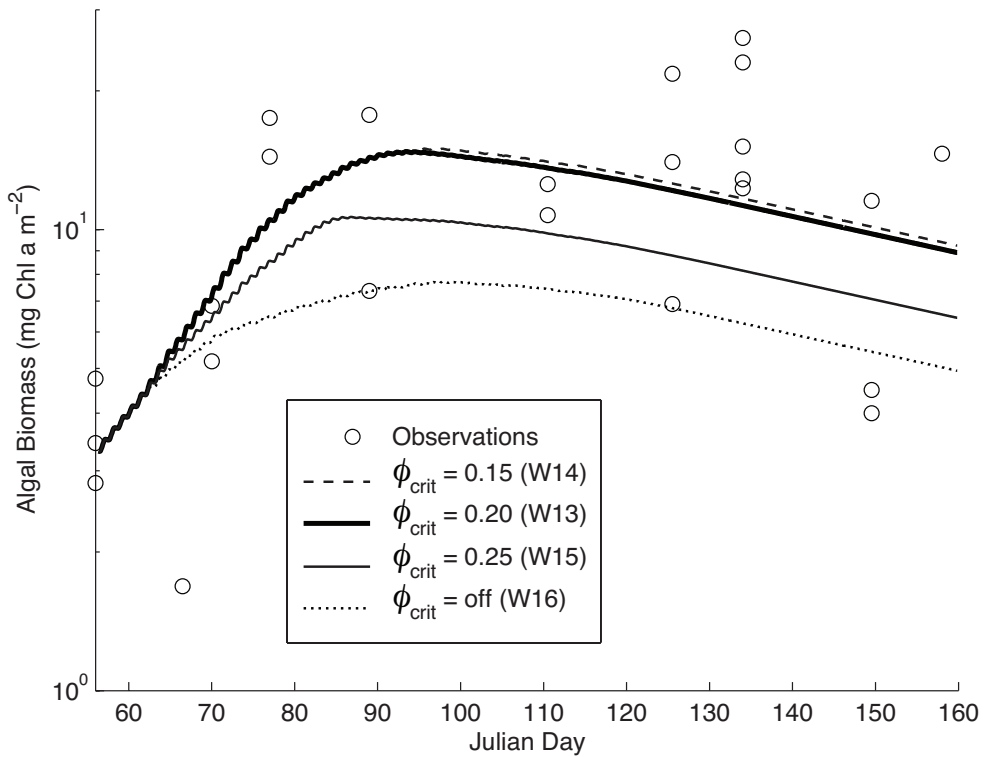


Figure 19. Total ice column Chl *a* concentration observed and modeled using a range of ϕ_{crit} for ISW Site A. At this site heterogeneous ice conditions produced variable Chl *a* observations. Without the slush layer desalination scheme ($\phi_{crit} = \text{off}$), algal growth to observed values is not achievable. As in the ISWB simulation, a ϕ_{crit} value of 0.20 results in a reasonable approximation of the magnitude of biomass accumulation.

5. Desalination Exploration

Sea ice bulk salinities can range from zero (fresh ice) to close to seawater salinity for slush ice and frazil ice. Snow ice that results from the freezing of flooded snow has salinities ranging from 3.3 to 22 psu [Maksym and Jeffries 2001]. To investigate the ability of our model to generate a range of bulk sea ice salinities from initial high-salinity slush, we set up a series of simulations that varied in initial slush layer thickness, total ice thickness, snow thickness, and ambient air temperature. Because our model operates under the principle that salt inclusion in the sea ice matrix is dependent upon the rate of freezing [Nakawo and Sinha 1981], we chose to vary these variables to generate a wide range of freezing conditions.

5.1 Initial Conditions

We modeled three different initial sea ice conditions. New ice simulations were initialized as 5 cm of 18 psu bulk salinity slush in an effort to simulate rapid, new ice growth from a small initial consolidated frazil or grease ice layer. Moderate flooding simulations were initialized as 10 cm of snow overlying a 10 cm slush layer, followed by 5 cm of granular ice and then 45 cm congelation ice at the bottom of the column. Under 10 cm of insulating snow, we examined the desalination of a larger, 10 cm, 18 psu slush layer. Deep flooding simulations started with the same snow and ice layer structure as moderate flooding simulations, but layers were thicker to simulate desalination after a large flooding event under heavy snow loading. These simulations were initialized as 30 cm of snow overlaying a 20 cm, 18 psu slush layer. Underlying the slush layer was 15 cm of 8 psu granular ice, followed by 65 cm of congelation ice,

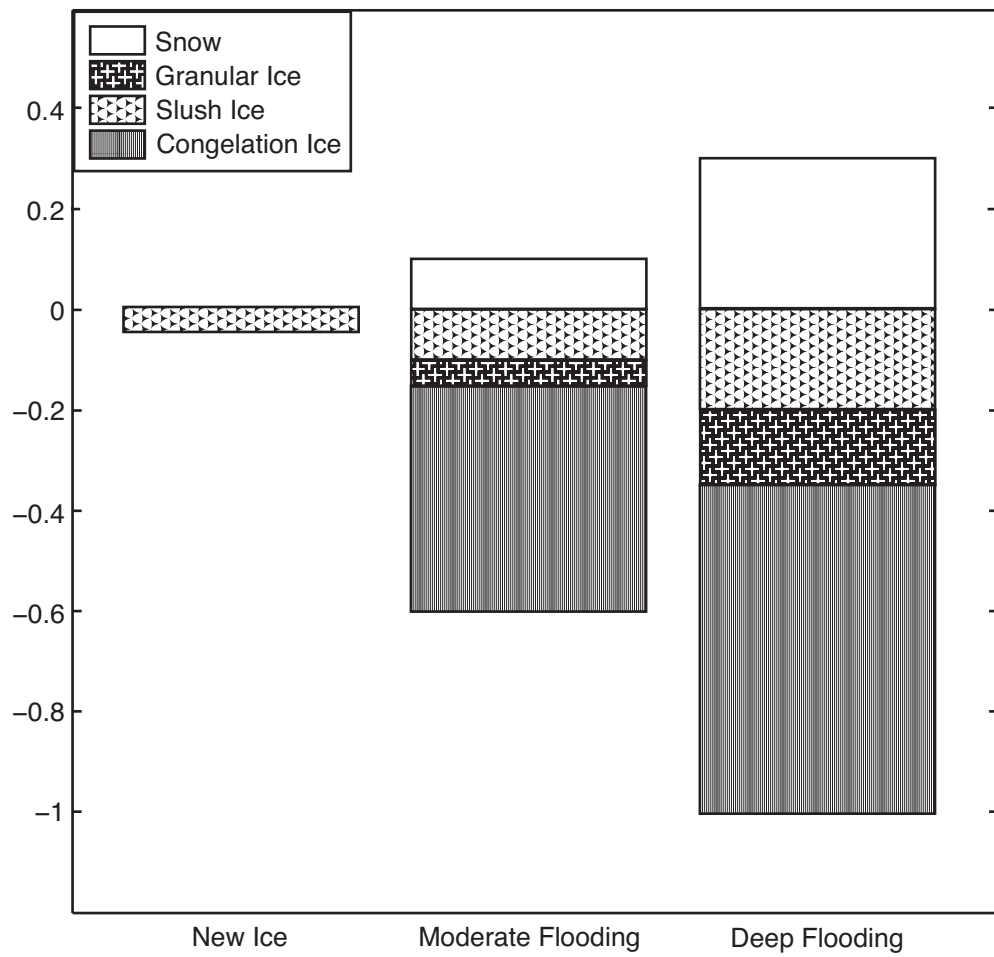


Figure 20. Vertical diagram of ice types used as initial conditions in the salinity exploration simulations (scale in m).

bringing the total initial ice thickness to 100 cm. Congelation ice salinities were initialized using the standard 1st year salinity profile (Table 4). Ice column diagrams of the three sets of initial conditions are shown in Figure 20.

5.2 Model Runs

All model runs shared atmospheric forcing, including incident shortwave radiation, with the ISWB runs, except air temperature, which we fixed at one of four values (-3, -6, -10, or -30°C). Using each of the four different atmospheric forcing temperatures across three different sets of initial conditions produced 12 total model runs, which are listed along with defining parameters in Table 8. All simulations were run for 50 days, from Julian day 60-110. The critical brine fraction ϕ_{crit} and ΔS_b were held constant at the values of 0.2 and 2 psu, respectively, for these simulations.

5.3 Results

5.3.1 New Ice

Ice Physics - Under a constant air temperature of -3°C (run DX1), desalination reduces the bulk salinity of the top 5 cm from 18 to 7.9 psu in the first 30 hours of simulation (Figure 21A, inset). After 30 hours, the brine fraction falls below ϕ_{crit} and desalination slows as the desalination method switches from SLDL to CWW88. Desalination in the top 5 cm continues for the rest of the simulation, albeit very slowly after Julian day 75, as the brine fraction approaches 0.05 (where the brine tube network is considered closed).

With air temperature fixed at -6°C (run DX2), the rate of desalination of the initial

Table 8. Desalination exploration model runs and parameters

Run	Air Temperature (°C)	Initial Slush Depth (cm)	Snow Depth (cm)	Initial Ice + Slush Depth (cm)
DX1	-3	5	0	5
DX2	-6	5	0	5
DX3	-10	5	0	5
DX4	-30	5	0	5
DX5	-3	10	10	60
DX6	-6	10	10	60
DX7	-10	10	10	60
DX8	-30	10	10	60
DX9	-3	20	30	100
DX10	-6	20	30	100
DX11	-10	20	30	100
DX12	-30	20	30	100

5 cm of slush is initially higher (Figure 21A, inset). Similar to the -3°C simulation, there is an inflection point near 7.9 psu where the brine fraction reaches ϕ_{crit} . As the desalination method switches from SLDM to CW88, convective heating ceases and the ice cools more rapidly than in the -3°C simulation. Cooler temperatures reduce the brine fraction, and we observe a slower desalination rate in the top 5 cm of ice in the -6°C simulation after the inflection point compared to the -3°C case. Cooling and desalination reduce the brine fraction to below 0.05 by Julian day 72, and the salinity remains constant at 6.2 psu until the end of the simulation.

In the -10 and -30°C runs (DX3-DX4), initial desalination rates in the top 5cm are higher than in the warmer runs, but desalination is then halted at 9 psu and 12 psu respectively. Low atmospheric temperatures cause high ice growth rates, leading to higher stable salinities. In these cases the slush layer desalinates to a stable salinity

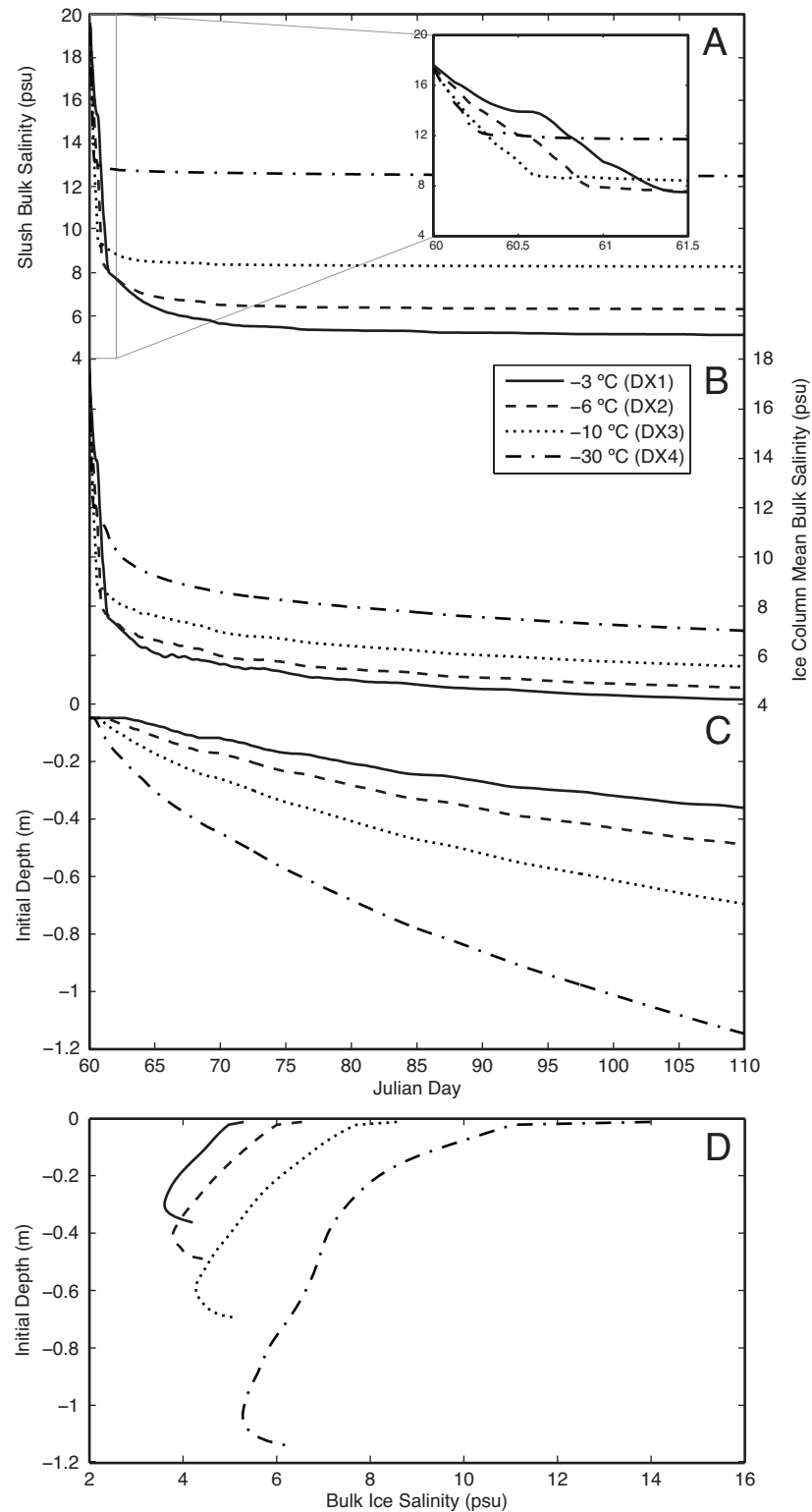


Figure 21. Physical parameters from ‘new ice’ runs (DX1-DX4). (A) Mean slush layer salinity (top 5 cm). (B) Mean ice column bulk salinity. (C) Ice column depth. (D) Final ice vertical salinity profile.

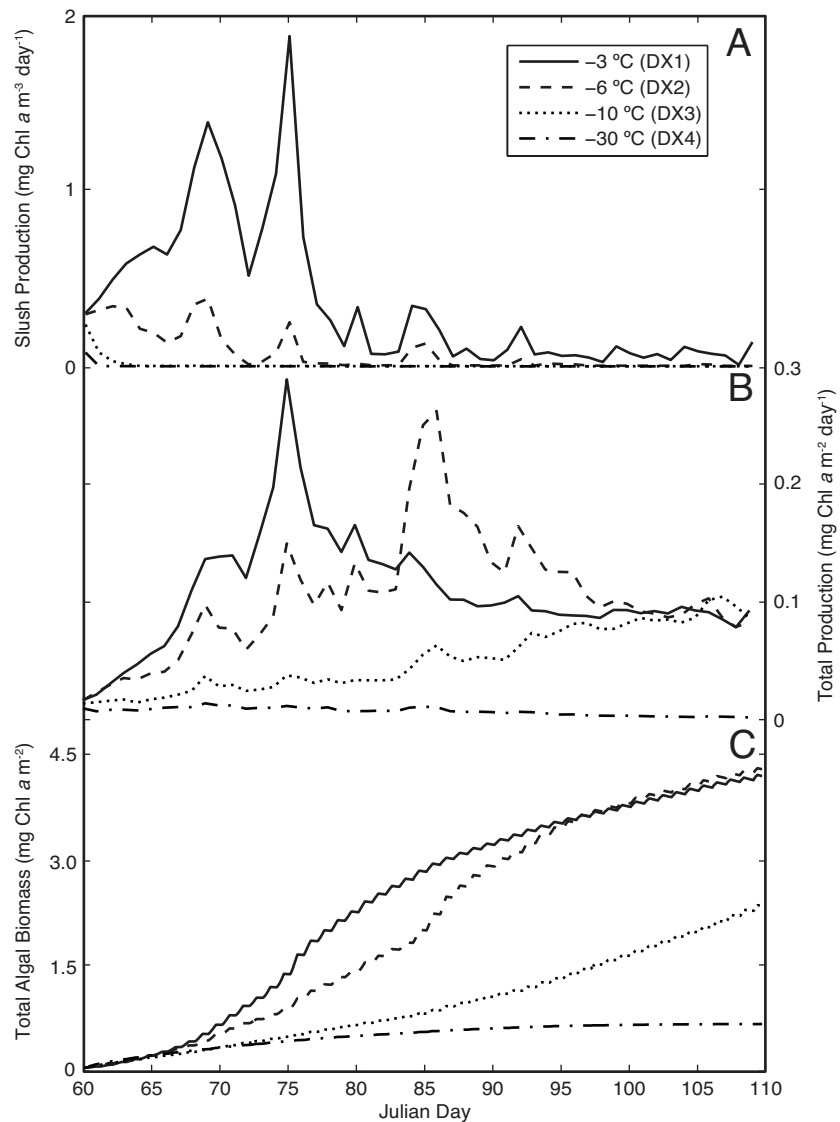


Figure 22. Biological parameters from ‘new ice’ runs (DX1-DX4). (A) Daily production in the slush layer (top 5 cm). (B) Total daily ice column production. (C) Total ice column algal biomass.

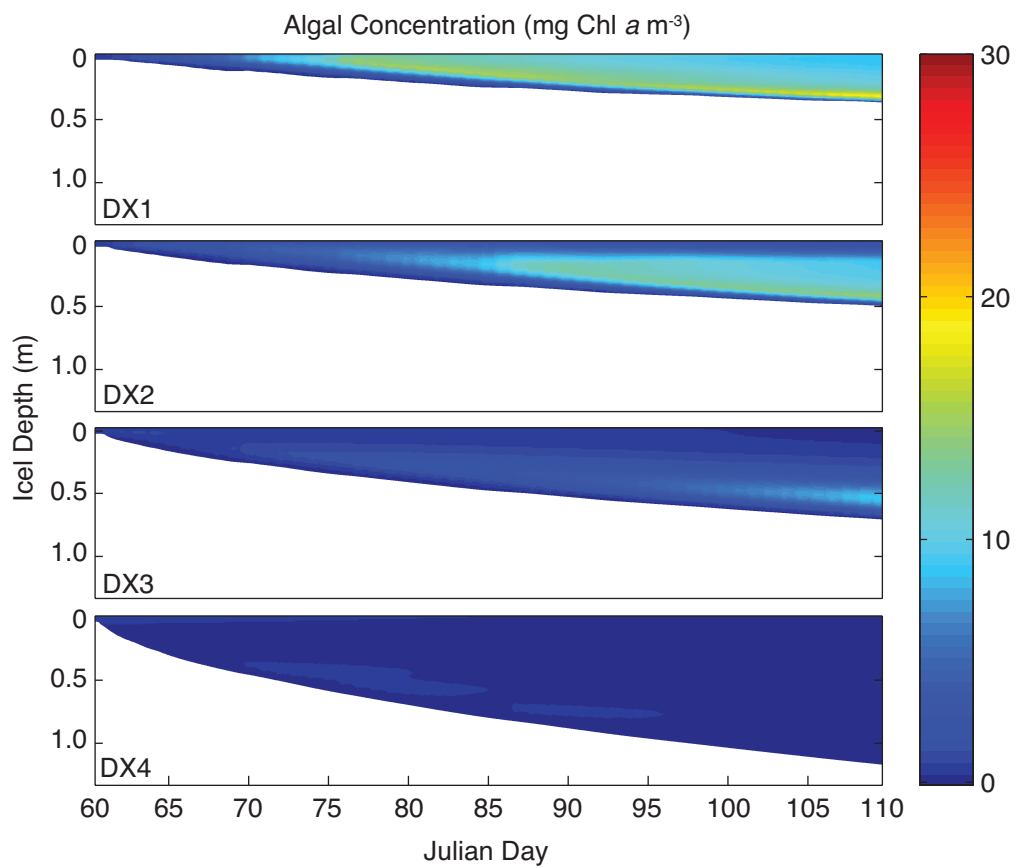


Figure 23. Ice column algal concentration from ‘new ice’ model runs (DX1-DX4) through time, plotted against the evolving ice column profile.

and triggers the switch to the slower desalination method (CW88) before the brine fraction reaches ϕ_{crit} .

Mean bulk salinities of the ice columns begin to deviate from the original slush layer salinities as the ice grows in thickness (Figure 21B,C). The warmest, thinnest ice (run DX1) maintains the lowest salinity and reaches 38 cm in thickness during the 50-day model run. In contrast, the coldest ice (run DX4) is the saltiest, and grows to 116 cm in thickness during the run. The mean bulk salinities and ice thicknesses of two runs using intermediate atmospheric temperatures (DX2-DX3) fall between the more extreme runs. All four new ice runs (DX1-DX4) show a C-shape salinity profile at the end of the 50-day run (Figure 21D).

Algal dynamics – All four new ice simulations show very little production in the initial slush layer, corresponding to the top 5 cm of the ice column. Production rates in this region of the ice peaked briefly in the warmest run (DX1) close to 2×10^{-3} mg Chl a m^{-3} day $^{-1}$, but generally remained below 5×10^{-4} mg Chl a m^{-3} day $^{-1}$ in all runs. Without insulating snow cover, the relatively rapid freezing of the slush layer (initial 5 cm of slush ice) in these four runs prevents algal growth due to cold temperatures and reduction of nutrient replenishment due to low porosity (Figure 22A).

Production in these runs is highest in the ice accreted below the initial 5 cm slush layer. Algae were concentrated near the near ice-water interface in the two warmer runs (DX1, DX2) where algae had access to nutrients due to convection at the growing ice edge (Figure 23). In the colder runs, (DX3, DX4) the ice grew too quickly for the algae to maintain an optimal position near the bottom of the ice; therefore, production was reduced by lower temperatures and nutrient concentrations in the interior ice

(Figure 22B,Figure 23). The warmer two runs (DX1, DX2) exhibited approximately equal total algal production, albeit with different timing. Production peaked earlier in the -3°C simulation (DX1) as warmer temperatures allowed algae to use nutrients incorporated during bottom accretion more quickly. Following these initial peaks, total production in the three warmest runs (DX1-DX3) all approximated a value close to 4×10^{-3} mg Chl a m $^{-2}$ day $^{-1}$ as the ice growth rates converged, and the growth became limited by the associated convective nutrient supply. In the -30°C run (DX4), fast ice growth rates and cold temperatures largely prevent significant production or biomass accumulation (Figure 22B,C).

5.3.2 Moderate Flooding

Ice Physics - Under 10 cm of insulating snow (Figure 24A), the slush layer in the moderate flooding simulations (DX5-DX8) desalinates much more slowly than in the new ice simulations (Figure 24A). The general pattern of desalination is the same, however, with slush layers in colder runs desalinating initially more rapidly, and with warmer runs having lower final slush layer salinities. Because of the damping effect of snow, the range of ice growth rates experienced by the moderate flooding runs is smaller than in the new ice simulations, and this is reflected in the final slush layer salinities which range between 7.2 and 5.9. In the two colder moderate flooding runs (runs DX7-DX8), SLDM is switched off when the slush layer bulk salinity reaches the stable salinity. In the warmer two runs (DX5, DX6), SLDM is switched off as the respective brine fractions reach ϕ_{crit} , causing the bulk salinities of both slush layers to converge toward a similar value.

Before the freezing of slush layers, the change in total bulk salinity of the ice column is driven primarily by the changes in the slush layer. After slush layer freezing, the total bulk salinity changes more slowly, with steady decreases in each run as the CW88 acts to slowly desalinate existing ice, and, in the cases of the colder runs, new lower salinity ice grows at the ice bottom (Figure 24B).

All moderate flooding runs show initial bottom melting; however, in all but the warmest run, the freezing fronts reach the bottom of the ice and new ice begins to grow. In the -30°C run (DX8) the net ice growth is 35 cm. The -10 °C run (DX7) manages a net growth of 8 cm, while the -6 °C and -3 °C have net ice losses of 4 and 8 cm, respectively (Figure 24C).

Final salinity profiles from the moderate flooding runs are similar in shape, showing bulges of relatively high salinity at the position of the initial slush layer. The two warmer runs (DX5, DX6) show very similar salinity profiles in the upper ice, which is reflective of reaching brine fractions equal to ϕ_{crit} during slush desalination. Lower down, the profiles deviate from one another as colder temperatures in the -6 °C run (DX6) cause greater desalination and new ice growth than in the -3 °C run (DX5). The salinity profiles of the colder runs (DX7, DX8) are higher on average, reflective of the elevated stable salinities characteristic of higher ice growth rates, both within the slush layer and in new ice growth at the ice bottom (Figure 24D).

Algal dynamics – Both slush layer and total production in -3°C, -6°C, and -10°C moderate flooding runs (DX5-DX7) follow the same growth trajectory for the first 5 days of simulation as algae quickly grow using the seawater-equivalent nutrients available in the ice at initialization. After day 65, production in the -10°C run drops

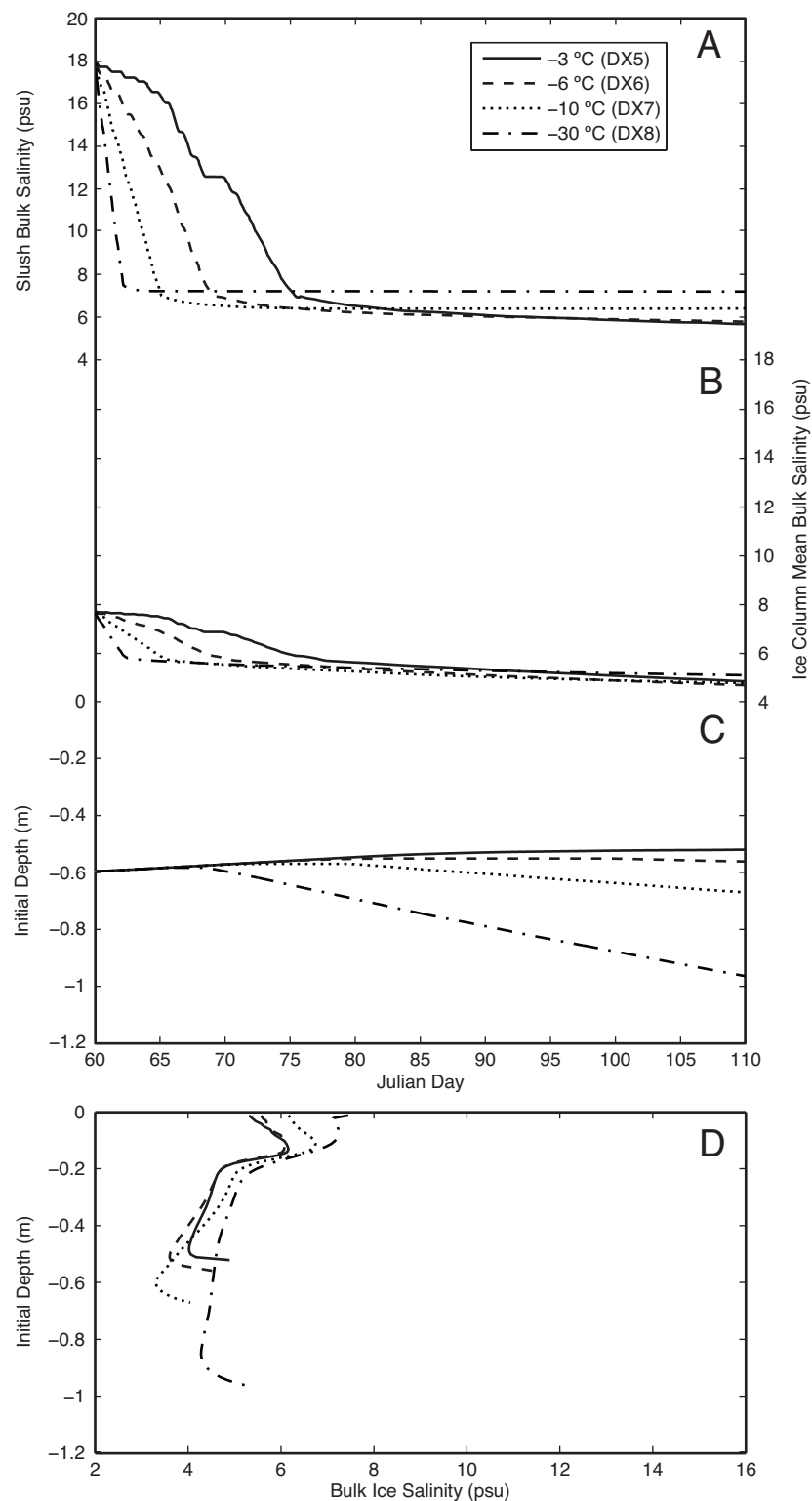


Figure 24. Physical parameters from ‘moderate flooding’ runs (DX5-DX8). (A) Mean slush layer salinity (top 10 cm). (B) Mean ice column bulk salinity. (C) Ice column depth. (D) Final ice vertical salinity profile.

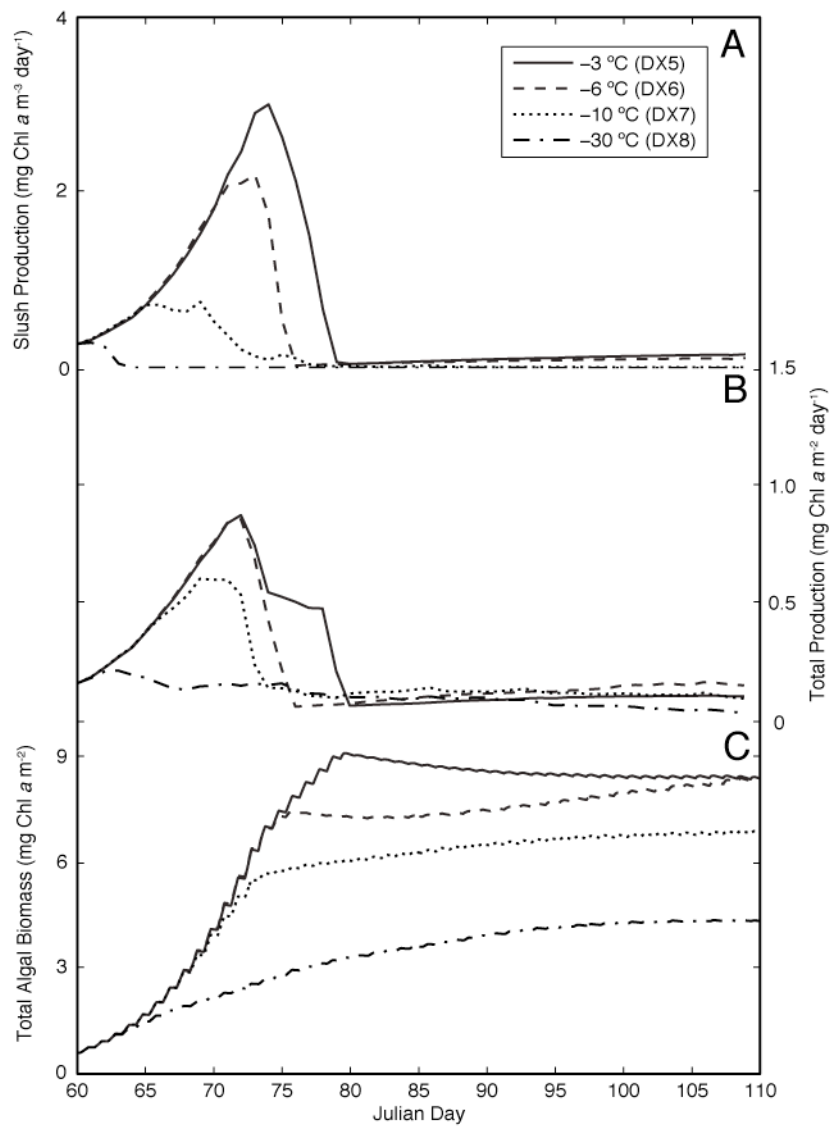


Figure 25. Biological parameters from ‘moderate flooding’ runs (DX5-DX8). (A) Daily production in the slush layer (top 10 cm). (B) Total daily ice column production. (C) Total ice column algal biomass.

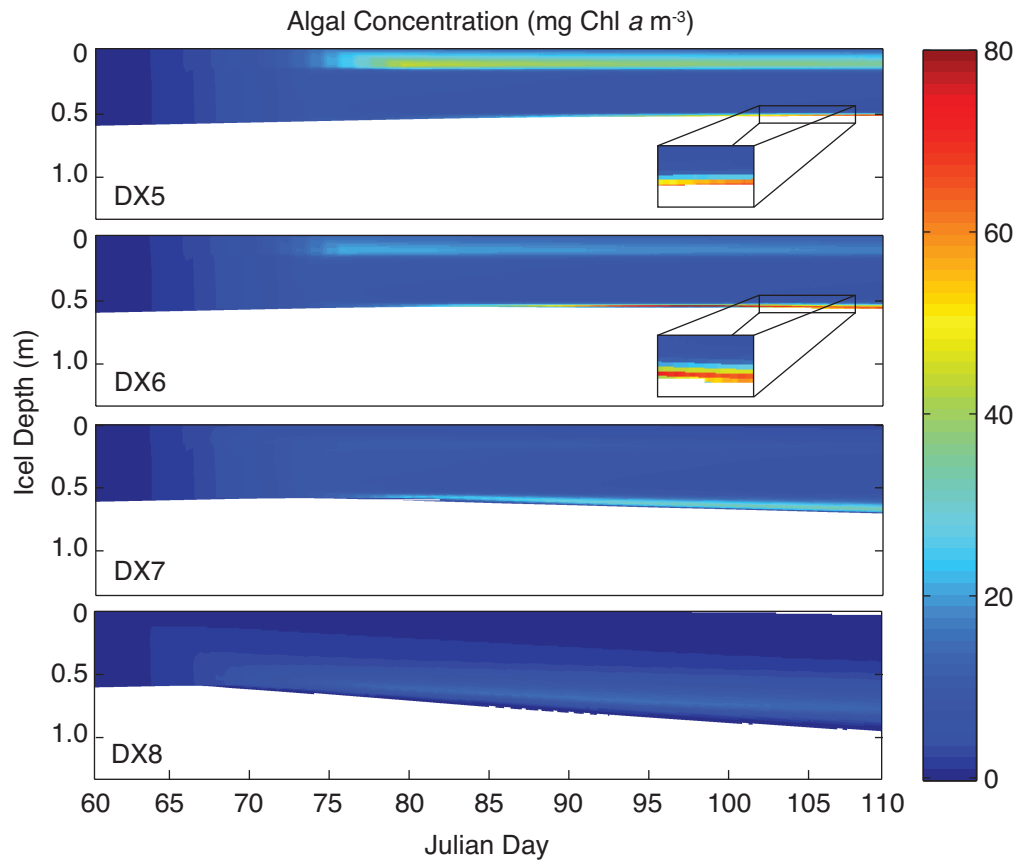


Figure 26. Ice column algal concentration from ‘moderate flooding’ model runs (DX5-DX8) through time, plotted against the evolving ice column profile. Inset panels show a 3x vertical magnification of the boxed profile, in order to highlight the thin layer of high algal biomass at the bottom of the ice.

below the two warmer runs as algal growth becomes temperature limited, and peaks at 0.6 mg Chl a m $^{-2}$ day $^{-1}$ (DX7). Production in the warmer runs both peak closer to 0.8 mg Chl a m $^{-2}$ day $^{-1}$. Production then declines in all three runs to a small baseline; however, the decline is delayed in the -3 °C run (DX4) relative to the other moderate flooding runs (Figure 25B). This delay is caused by production in the surface slush layer and the frazil ice below it that continues longer than in the colder moderate flooding runs (Figures 25A, 26). In the coldest run (DX8), internal production is restricted by cold temperatures and associated high brine salinity, and at the ice bottom by high ice growth rates (Figures 25, 26).

Algal concentrations are elevated in and near the slush layers, and also at the ice bottom once bottom ice growth begins (Figure 26; inset). The highest concentrations are found at the bottom of the two warmer runs (DX5, DX6) where algal biomass exceeds 80 mg Chl a m $^{-3}$. Algae near the slush layer do not have time to reach such high concentrations before freezing of the slush causes nutrient limitation. Because the vertical extent of the slush and bottom regions with elevated algal production are small compared to the total ice thickness, total production over the course of simulation is dominated by growth outside these regions (Figure 25A-B). It is also worth noting that despite overall lower production, algal biomass in the -6°C run (DX6) approaches that of the -3°C run (DX5) by the end of the simulation, and continues to increase throughout the colder runs despite extremely low levels of total production. This is caused by incorporation of water column algae into brine, which is fixed at a concentration of 1 mg Chl a m $^{-3}$, during bottom ice accretion. Once in the ice, this incorporated biomass may contribute to net production, as it does in warmer runs, or it

may begin to decline quickly after incorporation, as in the -30 °C run. Despite a net decline of ice-bound algae, incorporation from the water column causes a net increase in biomass in the colder runs (DX7-DX8; Figure 25C).

5.3.2 Deep Flooding

Ice Physics - The extra snow insulation and doubling of slush layer thickness with respect to the moderate flooding simulations (Table 8) cause very slow freezing of the slush layer in the deep flooding simulations (DX9-DX12). In the -3°C run, there is not enough heat extraction to fully desalinate and freeze the slush layer during the 50 day model run, and the final slush layer salinity is ~9 psu (Figure 27A). In the colder runs (DW10-DX12) cooling is adequate to desalinate the slush layer, and the slush layer salinities of these three runs converge near 6 psu (Figure 27A). The similarity of the desalinated slush layer salinities is due to the desalination method switching as the brine fraction in each slush layer reached ϕ_{crit} . The total ice salinities in these runs largely mirror the slush layer trends, since there is little new ice growth and small temperature gradients limit further desalination via CW88 (Figure 27B).

Freezing front advancement proceeds slowly in all deep flooding runs, and inhibits new ice growth at the ice sheet bottom in all cases except at the end of the -30°C run (DX12). New ice growth starting near Julian day 93 is able to replace ice melted earlier in the simulation resulting in a zero net change in ice thickness. In the warmer simulations (DX9-DX11), ice melts continuously throughout the model run, causing a net loss of ~12 cm in these runs (Figure 27C).

The remaining slush layer in the -3°C deep flooding simulation (DX9) is still clearly visible in the final salinity profile, exhibiting salinities of 16 psu. Interestingly, the initial slush layer region in the -6°C run (DX10) has a higher salinity than the cooler runs (DX11,DX12). Based on ice growth rates, we would expect that the -6°C run would arrive at a lower stable salinity. In this case however, the slush layer salinities appear higher because the slush layer is still desalinating (via CW88), while the slush layers in the cooler runs desalinated more quickly and reached a relatively stable salinity by the end of the runs (Figure 27D)

Algal dynamics – As in the moderate flooding runs, algal production in the deep flooding runs starts with similar positive trajectory, as all runs are initialized using the same starting parameters. Production begins to drop in the coldest run (DX12) by Julian day 68, with further departure in production from the warmer (DX9-11) runs apparent by Julian day 78 (Figure 28A-D). As in the new ice and moderate flooding simulations, the greatest algal production and biomass accumulation is achieved in the warmest (-3°C) run, with a maximum concentration of 161 mg Chl *a* m⁻³. At the end of this run, desalination in the slush layer was still refreshing nutrients in the ice interior, therefore peak biomass was not achieved during this simulation (DX9). In the -6°C run (DX10), the complete desalination of the slush layer causes nutrient limitation and curtailed most production by Julian day 102, and algal biomass reached a relative maximum of 26 mg Chl *a* m⁻². The two colder runs (DX11-12) experience slush layer nutrient limitation earlier, with proportionally lower peak algal biomasses.

Nutrients present upon initialization allow algal production throughout the ice pack until they are exhausted around Julian day 78. After day 78, production is

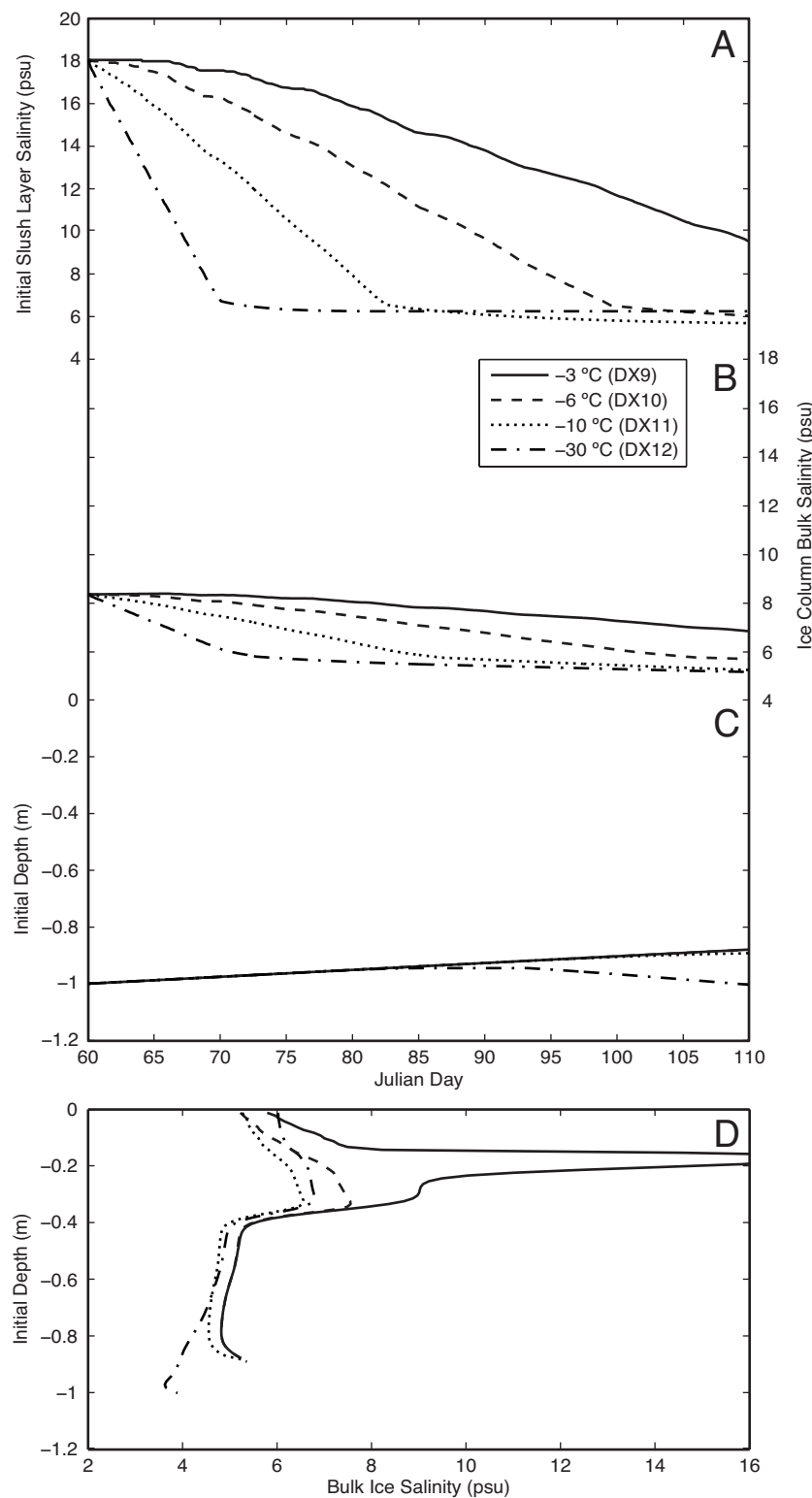


Figure 27. Physical parameters from ‘deep flooding’ runs (DX9-DX12). (A) Mean slush layer salinity (top 20 cm). (B) Mean ice column bulk salinity. (C) Ice column depth. (D) Final ice vertical salinity profile.

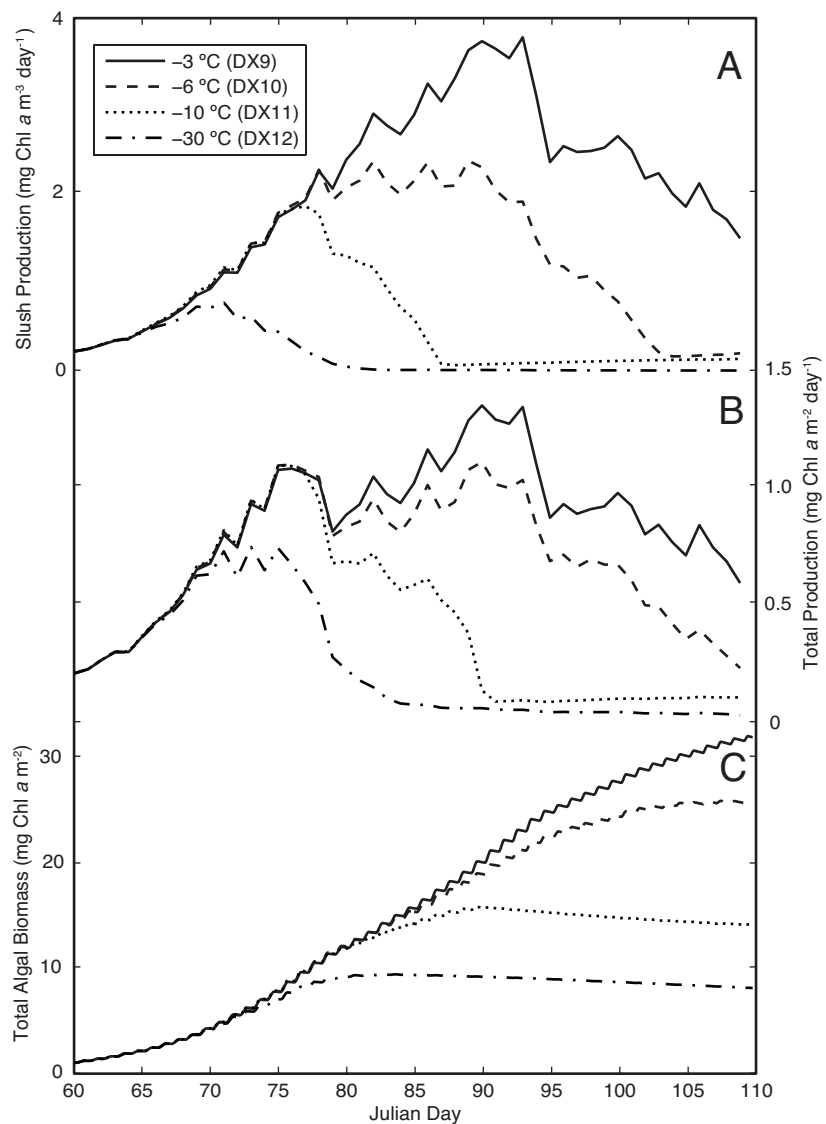


Figure 28. Biological parameters from ‘deep flooding’ runs (DX9-DX12). (A) Daily production in the slush layer (top 20 cm). (B) Total daily ice column production. (C) Total ice column algal biomass.

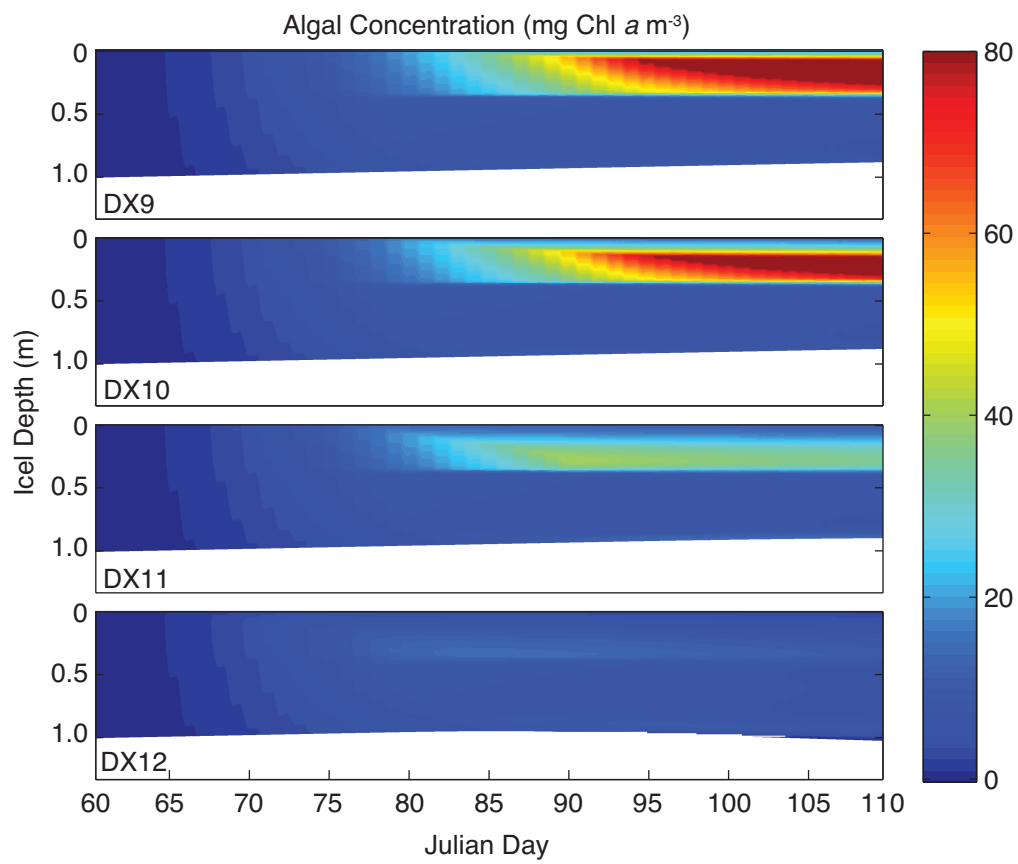


Figure 29. Ice column algal concentration from ‘deep flooding’ model runs (DX9-DX12) through time, plotted against the evolving ice column profile.

concentrated in and near the desalinating slush layer, analogous to the ISW standard runs (Figure 29). Production is low at the bottom of the ice column in the colder runs (DX11-12) due to local nutrient additions caused by slow, interior desalination (Figure 28 C-D). Biomass accumulation in the bottom layers is prevented, however, by light limitation of algal growth, as well as bottom ablation and associated loss of algae to the water column. In the -30°C run (DX12), biomass is added to the ice column during the second half of the simulation via accretion of water column algae. In contrast to the moderate flooding runs, total biomass decreases during this period because the rate of addition of water column algae is less than the loss of algae caused by death and grazing.

6. Discussion

6.1. Simulating ISW

Lytle and Ackley [1996] provide evidence that convective heat transfer due to brine exchange was a significant source of heat to the sea ice cover at ISW. With our new treatment of slush ice desalination, we are able to model observed ISW sea ice physics with enough precision to accurately simulate observed algal growth. If rapid desalination and associated convective brine flux is not explicitly modeled for interior high brine fraction ice layers, as is the case with most macro-scale sea ice models, our results show that freezing occurs too quickly, bulk salinities remain too high, and biomass accumulation is severely restricted compared to observations.

The ISW time series data have been previously used for sea ice model development, but these efforts are either simplified or do not include a fully coupled

desalination scheme. Fritsen et al. [1998] used the Ice Station Weddell time series data to specify slush layer conditions in a coupled model of sea ice similar to our study. In their model, the slush layer thermal properties were subject to a separate, non-heat-conservative thermodynamic term that required a porosity estimate, and the ice salinity was invariant at 8 psu. Although this treatment of the slush layer permitted simulation of algal production, the model is not readily portable because the slush layer physics are not predicted. Instead, they are specific to the test case. The same time series observations were also modeled by Andreas et al. [2005], where the slush layer was treated similarly to our simulations in that all heat extraction is in the form of freezing sea ice up to a cut-off brine fraction. However, ice salinity, desalination and brine flux were not explicitly modeled.

Our slush layer desalination and fluid transfer method (SLDM) constitutes a step forward from Fritsen et al. [1998] and Andreas et al. [2005], where the processes of desalination, brine exchange, and convective heat transfer are coupled to sea ice equations of state and conductive heat transfer, allowing most feedbacks between physical and biological processes to proceed as observed. The model is able to accurately track large changes in the physical properties of sea ice from highly porous slush to frozen, low brine fraction sea ice with enough accuracy to correctly simulate ice algal growth in the sea ice interior. We are pleased that despite the decidedly three-dimensional environment at ISWA, when mean snow and slush layer thicknesses are used, the model is able to simulate desalination and ice algal growth close to observed values.

6.2. Desalination Experiments

The desalination exploration model experiment was designed to examine the range of possible outcomes from different rates of freezing acting on various types of slushy ice that are frequently observed. While we have no time series observations with which to compare these results, we observe that the model is able to produce a diverse set of salinity profiles from slush ice that follow typically observed sea ice features including high salinity near the ice surface in new ice and snow ice, and the C-shape profile common to first year ice.

It is interesting that under different freezing rates, the trajectories of the declining slush layer salinities cross. At low freezing rates, the initial salinity remains high because desalination happens slowly, but given enough time, the slush layer will desalinate to a lower stable salinity than under a high freezing rate. This phenomenon serves as a reminder that ice history cannot be interpreted from single point measurements of the sea ice salinity, or any other measurement of sea ice state. The sea ice may have arrived at its salinity via many different paths, even if starting from similar initial conditions.

Under conditions of slow freezing common to interior slush layers, results from the desalination exploration experiment show that the switch from the SLDM to CW88 at ϕ_{crit} causes the convergence of salinities to values near 6 psu. As described in the methods, use of ϕ_{crit} is necessary to achieve the ISW bulk salinities measured after freezing of the observed slush layer. Otherwise, the stable salinity of the slowly-freezing slush layer defines the switch, resulting in modeled salinities that are too low. The general use of ϕ_{crit} calculated from ISWB data using our model is justified based

on recent study of sea ice permeability. Golden et al. [1998], and Golden (manuscript in preparation, 2010) perform theoretical investigations of the permeability of granular ice, and indicate that it may be less permeable than congelation ice at a given porosity. Because slush layers result in granular ice after freezing [Sturm and Massom 2009], we propose that slushy sea ice might desalinate to a higher stable salinity than the more permeable congelation ice. This would support the use of a parameter like ϕ_{crit} to restrict or slow slush layer desalination, since our method is derived from congelation ice stable salinity measurements [Nakawo and Sinha 1981].

The combination of sea ice permeability and brine density gradients ultimately determine the rate of desalination [Feltham et al. 2006]. Measured Arctic sea ice permeabilities span > 2.5 orders of magnitude over brine fractions between 0.05 and 0.25, with smaller brine fractions corresponding to smaller permeabilities [Golden et al. 2007]. The rate of change in permeability for brine fractions above 0.2 appears to slow and flatten out, however, indicating that our parameter $\phi_{crit} = 0.2$ may correspond to an inflection in the permeability curve, and may be more generally applicable to situations besides those tested here.

Below $\phi = \sim 0.2$, Golden et al. [2007] show that the permeability decreases as a continuous function, whereas in our model, the desalination method switches abruptly once an ice layer reaches ϕ_{crit} . Therefore, our model has the potential to accumulate errors in parameters related to the desalination scheme if the sea ice environment lingers at, or repeatedly transits, the ϕ_{crit} boundary. A more continuous transition between the two methods of desalination would help to mitigate such an error.

However, further refinement of the desalination method is not warranted without more detailed time series observations to test against.

6.3. Evidence for rapid desalination of slush layer

The Ice Station Weddell time series data begin after a large flooding event, followed by a 35 day period of cooling. This intense cooling period allowed for continuous desalination of a relatively thick slush layer, causing the ice pack to develop a series of large, two cm diameter brine tubes that undoubtedly facilitated brine drainage [Fritsen et al. 1994]. Neither the specific conditions under which large brine tubes form, nor their rate or formation, has been observed or determined experimentally. Therefore, it is possible that ice states different from those found at ISW might discourage such large brine tube formation. In this case, the fluid resistance of ice either within or underlying a slush layer could be significantly different from that at ISW, which might affect the value of ϕ_{crit} used in our model. The presence of superimposed fresh ice layer in the snow or ice pack might also affect the freeze dynamics of a slush layer by providing a low porosity barrier to convection.

Evidence suggests however, that if the seawater can find a path to flood the sea ice surface, then it can also find a way to exit again as more saline brine is formed. Hudier et al. [1995] describe observations of sea ice following a storm where the surface flooded and the resulting slush layer cooled over the course of several hours. After an initial rapid cooling to -2.32°C, the temperature of the slush layer warmed over the course of five hours to -1.7°C, despite air temperatures of -5 to -10 °C, indicative of convective heat transfer from the ocean to the slush layer. As such, fluid pathways

adequate for rapid convective exchange with underlying seawater must have been established in the first few hours after flooding. The observed salinities of frozen slush layers, or snow ice, support our estimate of initially vigorous slush layer desalination as well. Measured bulk ice salinities of snow ice average 6.5 psu in the Arctic [Toyota et al. 2007] and 9.3 psu in the Antarctic [Maksym and Jeffries 2001]. If slush layer desalination normally takes place more slowly than observed at Ice Station Weddell, one might expect to see average bulk salinities closer to that of the initial slush layers (~17-24 psu [Hudier et al. 1995; Lytle and Ackley 1996; Fritsen et al. 2001]).

6.4. Simulation of sea ice algal growth

The different freezing scenarios simulated here show that fate of slush ice, and its suitability as algal habitat, depends upon the ice state following slush formation. In particular, algal biomass accumulation is very sensitive to the freezing rate. At one end of the spectrum if the temperature is static or isothermal, density-driven convection will be largely prevented and, assuming the light, salinity, and temperature are permitting, algae will quickly become nutrient limited. Observational evidence supports nutrient limitation of algae in both Arctic and Antarctic sea ice [Maestrini et al. 1986; Gosselin et al. 1990; Lizotte and Sullivan 1992]. At the other end of the spectrum, when ice is growing quickly, our model results indicate that cold temperatures, high brine salinity, and the associated shutdown of brine convection curtails algal production. The optimum growth scenario was one of slow ice growth, where convective overturning of brine provided a continuous nutrient supply and warm ice temperatures allowed relatively fast algal growth rates.

Although the model was validated with data from ISW, which was dominated by a slush layer, there are other productive regions in sea ice. Bottom algal communities in particular can contain extremely high levels of biomass, and are productive early in the springtime while the ice surface remains cold and impermeable [Ackley and Sullivan 1994; Lizotte 2001; Arrigo 2003]. Bottom algal communities bloomed in our simulations under much the same conditions as those in the slush layer - during periods of slow ice growth. Ice melt inhibited production by these algae as biomass was lost to the water column. Rapid ice growth also reduced production in the bottom ice, as algae could not maintain their position near the ice-water interface, and were subjected to cold interior ice conditions.

Our simulations show significant increases in total ice column algal biomass through incorporation of water column algae during bottom freezing. The water column algal concentration used here ($1 \text{ mg Chl } a \text{ m}^{-3}$) is higher than observed values under thick, winter sea ice, but is lower than observations during the algal growth season [Fristen et al. 2008]. Concentration of water column material within sea ice during ice formation is commonly observed [Garrison et al. 1983; Ackley and Sullivan 1994; Fristen et al. 2008], but the processes responsible are not well quantified and were not included in the model. Higher levels of algal incorporation would increase both the biomass and the potential for production near the bottom of the ice. It is not clear, however, how this phenomenon might affect algal production since, as we have shown, the physical ice state strongly controls sea ice algal production.

The focus on ice algal production is traditionally placed on surface and bottom communities where high algal concentrations are frequently observed, although the ice

interior often contains significant algal communities as well [Garrison and Buck 1989; Arrigo 2010]. These interior communities, while typically less dense than at the surface or bottom, have the potential to contribute a large percentage of total production due to the relatively large volume of ice that they occupy.

During the salinity exploration simulations, a large percentage of production came from algal growth that was not concentrated in a particular layer. This bloom was a result of nutrient replete concentrations and warm temperatures present at the start of every simulation. An analogous situation exists during early springtime when nutrient concentrations adequate for an interior ice column bloom are present in first-year pack ice. These nutrients may either be frozen into the ice during the darkness of winter or result from remineralization of ice bound organic material [Arrigo et al. 2004].

A full discussion of the relative importance of different algal communities is beyond the scope of the results presented here, however the ability of our model to simulate these different communities using a physics-based approach will allow further examination of this issue.

In general, our simulations of ISW sea ice algal production and associated tracers matched closely with observations, with the exception of nitrate+nitrite measurements following slush layer freeze up. The general pattern for algal growth in both ISW simulations was exponential growth from the start of the simulation until shortly after the freezing front passed through the slush layer. In our simulations, passing of the freezing front through the slush layer caused the accumulated biomass to quickly exhaust available nitrate, and Chl *a* ceased to increase after Julian day 78 and 80 at ISWB and ISWA, respectively. This pattern of exponential growth followed by

relatively stable biomass for the remainder of the simulations agrees well with observations of Chl α from ISW ice cores. Limitation by nitrate seems unlikely at ISW, however, since nitrate+nitrite concentrations remained relatively high in measured ice cores [Fritsen et al. 1994; Ackley et al. 1996]. In the model, as in the observations, other factors that can limit algal growth (irradiance, temperature, and salinity) were still conducive for growth for some time after passage of the freezing front. Therefore, it is not clear what caused the cessation of biomass accumulation at ISW in the presence of high N concentrations. We theorize that another nutrient, such as silicic acid, may have been limiting growth at ISW. Silicic acid does not become limiting before nitrate in our model runs because the seawater is assumed to contain excess silicic acid compared to nitrate, based on the biochemical nutrient requirements of diatoms, the dominant sea ice alga.

6.5. Application to large-scale simulations

In a fully mechanistic model, the desalination rate of a slush layer would be determined by the balance of convective heating from the seawater below and atmospheric cooling from above, in combination with consideration of the fluid pathway. Such models are being developed. For example, Petrich et al. [2006] employ a hybrid fluid transport model that can simulate brine movement related to gravity drainage in highly porous sea ice using predicted permeabilities. Unfortunately, the two-dimensional nature of such simulations do not lend themselves to macro-scale investigations. However, patterns of slush layer dynamics and brine flux magnitudes

derived from such mechanistic modeling could be adapted and parameterized into models intended to be macro-scale, as we have done here.

Since interior slush layer desalination has not been examined in any mechanistic way that we are aware of, we have made use of adapted available quasi-empirical estimates of sea ice desalination to develop our model. Notz and Worster [2009] correctly point out that desalination in sea ice is a continuous process across a region of porous sea ice. Indeed salt does not segregate immediately to a stable salinity as is implied in our calculations of dS/dt . For the purposes of macro-scale simulation, however, the concept of a stable salinity is useful as an aggregator of micro-scale physics over space and time. When applied to a large-scale sea ice simulation, the desalination-related processes presented here have the ability to improve estimates of heat and salt fluxes in coupled climate models. The slush layers simulated by our model incorporate the processes required to simulate the magnitude and duration of the algal blooms common to such environments, which are thought to be responsible for the majority of carbon fixation in Antarctic sea ice [Garrison and Buck 1991; Legendre et al. 1992]. Our future work will involve applying the slush layer dynamics presented here to a hemispheric sea ice model, with the goal of examining pan-Antarctic sea ice algal production over time.

CHAPTER 2

Effects of snow and ice representation in hemispheric, biophysical simulations of sea ice

1. Introduction

Modeling remains the primary tool by which we can explore the dynamics of sea ice ecology across space and time. Unlike the open ocean, where ocean color-viewing satellites can provide detailed, global estimates of algal biomass and primary production, there are no methods for remotely observing sea ice biology. Furthermore, only a handful of time series observations of sea ice biology exist due to the logistical difficulties of sampling sea ice [Cota et al. 1987; Grossi et al. 1987; Fritsen et al. 1994]. These observations, while providing invaluable insight that guides our modeling efforts, are derived from single locations in a habitat that seasonally covers 1/12 of the surface of the earth.

To adequately describe the magnitude and spatial extent sea ice algal production, including its contribution to sea ice ecology and global carbon budget, details about sea ice state and physics need to be represented in global-scale models. Rates of primary production by ice algae, which form the base of sea ice food web, depend on the temperature, salinity, solar radiation, nutrient concentrations, and physiology of the standing algae crop found within the ice [Ackley and Sullivan 1994; Lizotte 1991]. Temperature and salinity of sea ice are used to calculate a maximum algal growth, which declines with increasing salinity and decreasing temperature [Arrigo and Sullivan 1992]. The spectral magnitude of solar radiation available for photosynthesis is required, along with knowledge of the photoadaptation of resident algae, to properly determine net growth [Palmisano et al. 1987, Cota et al. 1987; Arrigo et al. 1994, 1995]. Low availability of macronutrients can be limiting to sea ice algae [Maestrini

et al. 1986; Cota et al. 1987; Gosselin et al. 1990; Arrigo et al. 1993; Robinson et al. 1998, McMinn et al. 1999].

Determination of these facets of the sea ice state in turn requires careful consideration of atmospheric and ocean physics that impact the sea ice, as well as appropriate representation of dynamic transformations within the ice and associated snow cover. The ice freezing and/or melting rate is controlled by interaction with the typically cold atmosphere above and the relatively warm ocean [Weeks and Ackley 1986; Weeks 1998; Eicken 2003]. Mechanical thickening of sea ice occurs through ridging and rafting of ice floes into and onto one another [Haas 2003]. Snow cover can greatly influence sea ice thickness due to its optical and thermal properties, and can cause flooding of the ice surface when it becomes heavy enough to depress the ice below the ocean surface [Weeks and Ackley 1986; Massom et al. 2001]. The snow itself is subject to metamorphosis in terms of thickness and grain size, which significantly affect its optical and thermal properties [Sturm and Benson 1997; Massom et al. 2001; Sturm et al. 2002]. Finally, nutrient concentrations in the sea ice can be modified via fluid exchange with the ocean via several different mechanisms, including gravity-induced convection during ice freezing [Reeburgh 1984; Arrigo et al. 1993; Fritsen et al. 1994; Ackley et al. 1996], shear forces between the ice bottom and underlying seawater [Cota et al. 1987; Gosselin et al. 1990], and wave-induced pumping [Ackley and Sullivan 1994].

The couplings inherent to this two-phase-physical-biological system produce complex interactions and feedbacks that are sensitive changes in sea ice state. One example of such complexity is the effect of variable snow thickness on ice algae production. Observations show that there is often an optimum, shallow snow thickness over sea ice that allows maximum algal growth. With thinner snow cover, enhanced shortwave radiation causes algae to slough off from the ice with bottom ice

melt, whereas under deep snow there is not enough light for net algal growth [Grossi et al. 1987; Welch and Bergmann 1989; Mundy et al. 2005].

Given our understanding of the sea ice ecosystem, we are interested in knowing what level of model complexity is necessary to gain further insight into the extent and timing of sea algal production and related ecosystem dynamics. Recent advances in parameterization of sea ice and snow physics have improved prediction of sea ice areal extent and thickness distributions [Bitz et al. 2001; Holland et al. 2006; Chapter 1]; by selectively applying them, we can identify the changes that different model methods elicit in the simulated sea ice state, and biology that it hosts.

Herein, we describe and compare model results produced from application of different ice and snow parameterizations in a 16-month long hemispheric simulation of Antarctic sea ice and associated ice algal production. We build model complexity by considering single and multiple thickness categories and by incorporating a novel method to simulate a snow thickness distribution. We further gauge the importance of convective nutrient supply, different atmospheric forcing suites, and the creation of voids during ice ridging and rafting, by selectivity enabling and disabling these processes in the model. We compare model output and discuss differences in sea ice and snow cover and the effects these parameterizations have on modeled sea ice ecology.

2. Model Description

2.1. Model Domain and Gridding

The model domain consists of a subset of the southern hemisphere EASE grid [Brodzik and Knowles 2002]. The grid pixel size is 25 km square (625 km^2), spans 332 pixels along the 0/180° longitude (vertical) axis, and 316 pixels along the 90/270° longitude (horizontal) axis, and is centered on the South Pole. For analysis of regional

trends, we divide the model domain into five areas defined by longitude in accordance with previous studies (Figure 1). Sea ice, snow cover, and associated physics and tracers are represented in the vertical dimension by the sea ice ecosystem model of Saenz and Arrigo [Chapter 1] using a maximum of 42 horizontal ice layers and up to 26 snow layers.

Global-scale sea ice models typically use a small number of layers to represent sea ice and snow cover [Flato and Hibler 1995; Winton 1999; Zhang and Rothrock 2003; Lipscomb and Hunke 2004], despite the fact that ice physics and associated biology within sea ice vary at the centimeter scale [Ackley and Sullivan 1994]. Algae are often found growing in relatively narrow bands within the sea ice, and under conditions of high biomass, can shade algae growing below and thereby limit total ice algal production [Smith et al. 1988]. Snow and ice temperature can change rapidly in surface layers, and model results indicate that using ice layers that are too thick can impact ice model performance [Pogson et al. 2011]. For these reasons, we set the minimum thickness of any snow and ice layer to 0.02 m, with ice and snow layers added as required up to the maximum number. To accommodate ice growth beyond the maximum number of layers, interior layers thicken in a manner that preserves resolution at the interfaces. Thickness is added to the interior-most layers first, and layers thicken in a manner such that adjacent layers differ in thickness by <33% to reduce model numerical errors. Layers at interfaces (atmosphere-ice/snow interface, snow-ice interface, and ice-ocean interface) are fixed at 0.02 m. The resulting grid is accordion-like in vertical snow and ice structure, with higher vertical resolution at the boundaries where physical changes occur the fastest and where algae are most likely to grow (Figure 2). All tracers, including heat, are regridded conservatively when a change in the thickness of the ice or snow takes place.

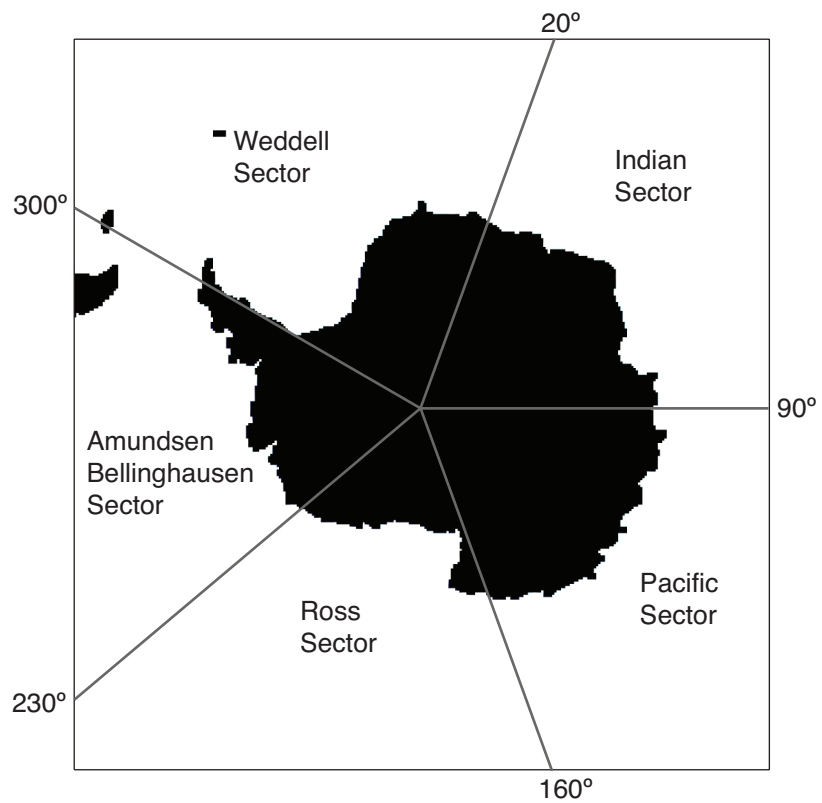


Figure 1. The sea ice model domain with black representing the land mask. The map is projected in the southern hemisphere 25km^2 EASE grid, centered on the south pole with 332 vertical and 316 horizontal pixels.

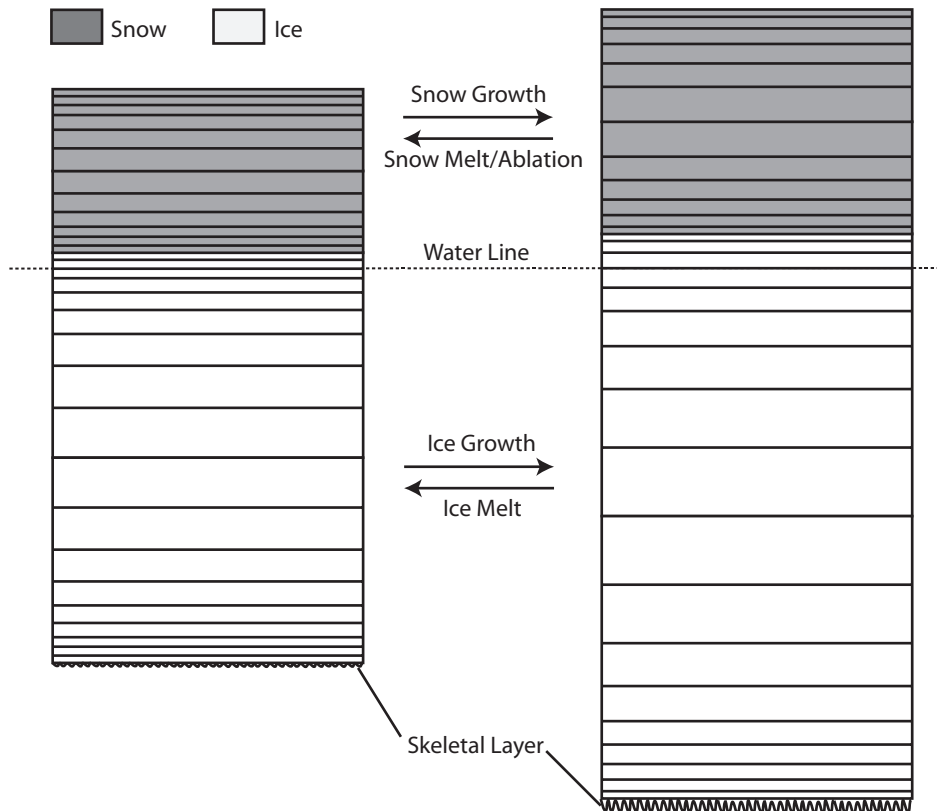


Figure 2. Diagram of the vertical model grid structure representing snow and ice. Under snow or ice pack growth or melting, the model grid shrinks and grows by adding disproportionately more thickness to the middle-most layers of ice and snow. In this way vertical resolution is preserved at the boundaries where change occurs the fastest, and where algae are most likely to grow.

2.2. Sea Ice Thermodynamics and Hydrodynamics

We used the one-dimensional, heat- and mass-conserving sea ice model of Saenz and Arrigo [Chapter 1] to represent the vertical ice and pack physics. The salient features and sources for this model are described briefly below.

Heat transfer in ice and snow is based upon the heat conduction model of Bitz and Lipscomb [1999], which accounts for changes in the effective heat capacity of sea ice associated with the freezing and melting of brine pockets. The thermal conductivity (k) of the sea ice varies with temperature and salinity [Pringle et al. 2007]. Energy flux at the boundaries (ice pack surface and bottom) is derived from the constant method of the CICE sea ice model [Hunke and Dukowicz 1997; Hunke and Lipscomb 2001].

We take special care to model shortwave radiative transfer in the snow and ice because sea ice algal physiology is sensitive to the spectrum of solar radiation [Morel 1978; Arrigo et al. 1991]. Shortwave radiative transfer is accomplished via a 2-stream model that uses a delta-Eddington scattering approximation [Brieglib and Light 2007]. Solar radiation is represented using 32 different wavelength bands, with 31 covering 400-700 nm photosynthetically available radiation (PAR) band (in 10 nm increments) and one additional band representing the solar energy outside the PAR band (300-400 nm, 700-2000 nm). Spectrally-dependent inherent optical properties (IOPs) of the snow and ice determine shortwave scattering and absorption. IOPs are calculated for each model layer of snow or sea ice as a function of the temperature, salinity, density, and algal content of the ice. Details of the IOP calculations are found in Saenz and Arrigo [Chapter 1].

The hydrodynamics of brine and seawater within the sea ice matrix is governed by gravity desalination. Desalination of warm, porous ice (porosity ≥ 0.2) is derived from a ‘stable salinity’ relationship [Nakawo and Sinha 1981; Petrich et al. 2006], which

was adapted to be a dynamic process [Chapter 1]. Desalination of colder, low porosity ice (porosity < 0.2) is governed by the gravity drainage equations of Cox and Weeks [1988]. Estimates of fluid flux are derived from the desalination rate, a calculation that is based upon estimates of fluid flux at the Ice Station Weddell experiment [Fritsen et al. 1994; Ackley et al. 1996]. Passive tracers in the brine and seawater, including nutrients (NO_3 , NH_4 , PO_4 , Si(OH)_4) and detritus are transported and mixed during fluid flow using a simple volume transport scheme.

2.3. Snow Dynamics

Snowfall over sea ice is determined primarily by climatological precipitation (see atmospheric and oceanic coupling). New fallen snow is assigned a density of 330 kg m^{-3} , a value typical of polar snow [Masson et al. 2001]. With the exception of superimposed ice formation, we neglect snow densification and more complex snowpack processes, considering them beyond the scope of the model. The thermal conductivity of snow is fixed at $0.33 \text{ W m}^{-1} \text{ K}^{-1}$ [Sturm et al. 2002]. Transmission of solar radiation in snow ice accomplished via the same methods as in sea ice, using snow-specific IOPs, as described in Chapter 1. Snow is considered pure, containing no salt, algae, detritus, or nutrients.

Besides precipitation, snow thickness may change via sublimation, melting, brine drainage, and ice surface flooding (where snow is converted to slushy sea ice). Sublimation results in loss of the snow mass from the topmost snow layer. Melting causes a redistribution of snow mass, where the liquid water resulting from surface snow melt is assumed to re-freeze at the snow-ice interface and create a layer of superimposed ice. Following Nicolause et al. [2003], the maximum density of superimposed ice is set to 850 kg m^{-3} . Once all snow has melted, the superimposed ice begins to melt, with the fate of the resulting melt water determined by ice porosity. If

ice porosity is above the percolation threshold of 0.05 [Golden et al. 2006], then melt water percolates downward through the ice pack and replaces the more salty brine. If the ice porosity is too low to permit percolation, melt water is assumed to move horizontally and drain through ice cracks into the ocean. Brine drains through ice layers above freeboard if the brine volume fraction reaches ≥ 0.2 . The brine from drained layers either percolates downward or flows horizontally according to same rules as melt water; the drained ice is then converted to snow. The model does not consider melt ponding at the ice surface, which is rare in the Antarctic [Andreas and Ackley 1982].

To determine snow flooding, we use Archimedes principle to calculate the freeboard of the ice pack. If the freeboard is greater than 0.02 m above the snow ice interface, and the ice pack porosity is above the percolation threshold, then snow below the freeboard is immediately flooded to the freeboard level with seawater. The enthalpy, salinity, nutrients, and detrital content of the seawater are mixed conservatively with the enthalpy and ice mass of the snow to create high brine-fraction snow ice. During the flooding process, we assume that snow compaction takes place such that the flooding snow is at least 50% ice by volume [Jeffries et al. 2001].

2.4. Ice thickness distribution

Because sea ice thickness can vary widely within an area equivalent to the horizontal dimension of a model grid cell, we chose to implement a method for accounting for this sub-grid scale variability in the model. Including the sea ice thickness distribution can markedly improve model performance compared to models that use only a single ice thickness category in each model grid cell [Bitz et al. 2001; Holland et al. 2006]. Here we implemented a sub-grid scale ice thickness distribution (ITD) patterned after Bitz et al. [2001], where each vertical ice category in a grid cell

is modeled separately. Ice thickness categories are defined by thickness boundaries (Table 1), and sea ice is allowed to grow and shrink between those bounds. If sea ice grows (or shrinks) beyond the thickness bounds of its designated category, then the ice, snow and tracers from that category are merged into the next highest (or lowest) category within the grid cell whose thickness bounds are inclusive of that particular sea ice. In addition to freezing and melting, the ice thickness distribution in a particular category may be modified by advection into and out of adjacent pixels, or by ridging during ice convergence (see section 2.7 Sea Ice Motion and Ridging).

Model runs presented here that use the ITD employ five ice thickness categories. A minimum of five categories was required to realize accuracy gains over model runs without using an ITD in the CICE global sea ice model [Bitz et al. 2001]. Observed ice thickness distributions are skewed toward thinner values, therefore, the category bounds are arranged to give higher resolution at the smaller thicknesses (Table 1).

2.5. Snow Thickness Distribution

Representation of a sub-grid scale snow thickness distribution (STD) may also improve model performance. Horizontal snow thickness variability over sea ice is generated by wind redistribution of and drifting of snow, and varies at typical length scales of 4-20 m [Sturm et al. 2002]. On average, snow thickness appears to be lognormally distributed [Arrigo et al. 1998], a fact that we exploit in our STD method. Small changes in snow thickness have a large effect on the light available for algal growth, leading Arrigo et al. [1998] to include a type of sub-grid scale STD in large-scale simulations of pack ice algal production. Thick snow is also responsible for flooding the ice surface, creating favorable habitat for sea ice algal growth. Observed surface flooding is just as patchy as the snow that causes it, leading to large

Table 1. Ice thickness distribution (ITD) category bounds

<i>Category Boundary</i>	<i>Boundary Depth (m)</i>
1 lower	0.20
1-2	0.99
2-3	1.83
3-4	2.83
4-5	4.19
5 upper	10.00

heterogeneity in horizontal ice properties and algal biomass at the meter scale [Weeks and Ackley 1986; Eicken et al. 1991; Tucker et al. 1992; McMinn and Hegseth. 2003].

We employ a sub-grid scale STD method for the purpose of estimating surface flooding by snow loading. The execution of this STD is very different from the ITD. Each grid cell, or each ice thickness category within a grid cell when using the ITD, contains a single snow depth that participates in thermodynamic, dynamic, and radiative transfer processes. Calculation of the freeboard level of ice is accomplished by assuming the snow thickness represents the mean of a lognormal distribution. We generate a distribution of snow thicknesses by multiplying the assumed mean snow thickness by nine different multipliers, where each multiplier represents 1/9 of the grid cell area (or ice category area). All nine multipliers together approximate a lognormal distribution with a mean of 1 and a standard deviation of 0.25 (Table 2).

The snow thickness distribution may be modified by either wind redistribution or surface flooding. Variability in the snow depth distribution is accomplished by the activation and deactivation of particular lognormal multipliers. The variable L ranges from 1 to 9 and specifies the number of active snow thickness bins in a grid cell (or ice thickness category), and thereby, the snow thickness distribution. For example, if $L=7$, then the STD contains 7 active bins whose snow thicknesses are calculated using values 1-7 from Table 2 (fractional categories are not considered). Under this

Table 2. Lognormal snow thickness distribution multipliers

<i>Number</i>	<i>Multiplier</i>
1	0.102
2	0.272
3	0.427
4	0.532
5	0.721
6	0.952
7	1.310
8	1.740
9	3.310

scenario, each bin represents 1/7 of the grid cell area (or ice category area, if using the ITD).

The different snow thicknesses generated by each lognormal multiplier are used to calculate the ice pack freeboard using Archimedes principle. Because sea ice surface flooding represents a very large physical change in heat content, salinity, and vertical ice structure, special consideration is given to flooded ice. To allow the flooded snow ice to undergo proper evolution, the areal portion of the ice that experienced flooding is assigned its own ice category along with the snow mass that caused the flooding. In this way, the STD splits the grid cell (or ice thickness category) into two different categories, a flooded and a non-flooded category. Flooded snow, ice and associated biology is modeled separately until the brine fraction of the upper half of the ice in the category has dropped below 0.2, at which point the ice is no longer considered flooded and the ice is merged back into the non-flooded category.

At the time of flooding, the change in the thickness distribution of the non-flooded snow is accomplished be decreasing L by the number of bins that flooded, and by changing the mean snow thickness to conserve mass. Due to the episodic nature of flooding and associated redistribution of snow depth, L never drops below 5, since the distribution is recalculated after each flooding event, and flooding only occurs at the

deep end of the snow distribution. A diagrammatic illustration of the process of surface flooding, the shifting of ice between categories, and deactivation of the snow thickness multipliers is presented in Figure 3.

In new ice, L is set to 5, which effectively simulates a flat distribution for the purpose of calculating surface flooding. The lognormal distribution is generated over time via a snow drifting routine derived from measurements of blowing snow. Wind-driven high-latitude snow transport begins in earnest at wind speeds $\geq 8 \text{ m s}^{-1}$. Observations indicate that snow transport reaches a maximum value, near 15 m s^{-1} under freezing conditions, above which further increases in wind speed do not transport more snow [Li and Pomeroy 1997]. We use these bounds to create a linear function of snow transport that grows the tails of the lognormal snow distribution with the use of a time-dependent constant.

The equation

$$L = L + L_{wind} \quad (1)$$

describes the change in STD, where L_{wind} represents growth of the tail of the lognormal snow distribution by activation of the larger snow thickness bins. L_{wind} is derived from wind speed as

$$L_{wind} = \begin{cases} 0, & v_{10} < v_{min} \\ (v_{10} - v_{min}) / ((v_{max} - v_{min})t_L), & v_{min} \leq v_{10} \leq v_{max} \\ 1/t_L, & v_{10} > v_{max} \end{cases} \quad (2)$$

where v_{10} is the wind speed (m s^{-1}) 10 m above the ice or snow surface, $v_{min} = 8 \text{ m s}^{-1}$, $v_{max} = 15 \text{ m s}^{-1}$, and t_L (hr) is a time constant of redistribution, such that the full lognormal snow distribution may be built over the course of t_L hours. In the simulations presented here, we set $t_L = 24$ hours, a value that was tuned by considering snow transport rates, typical Antarctic snow thicknesses, and the amount of resultant model surface flooding.

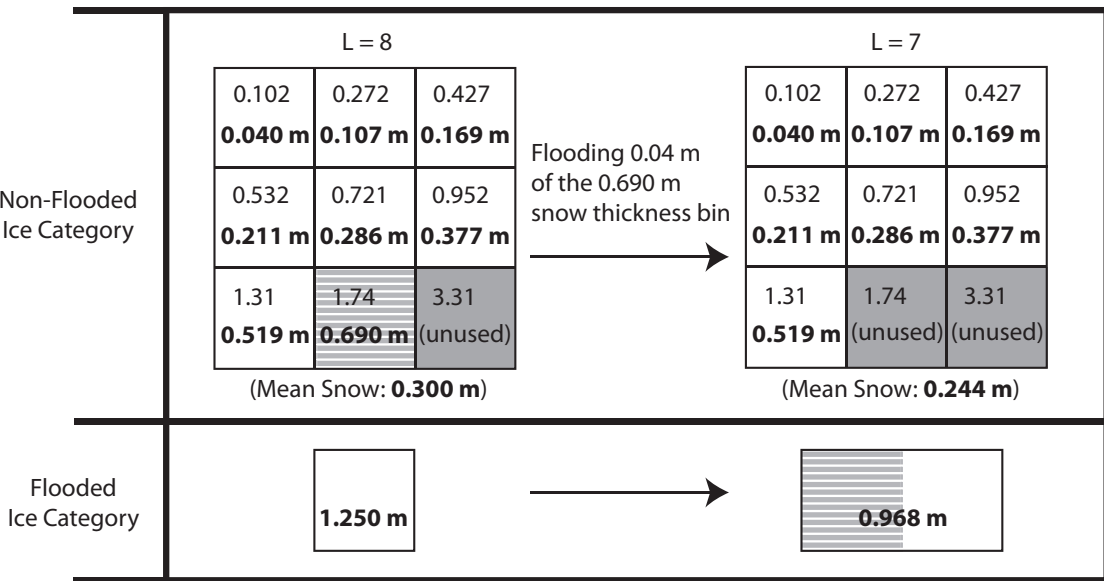


Figure 3. Diagrammatic illustration of the changes to the model ice snow thickness distribution (STD) during flooding. Snow thicknesses are shown in bold. The STD consists of two independent vertical ice categories. In the non-flooded ice category, a snow thickness distribution is generated by multiplying a mean category snow thickness by up to nine lognormally-distributed multipliers. The actual thickness distribution is defined by a number L , which specifies the number of active (white/no shading) multipliers. Larger multipliers are disabled (solid shading) if L is less than 9. If a particular snow thickness from the distribution is heavy enough to flood the ice surface (striped shading), the flooded snow and ice is removed from the non-flooded category and placed in the flooded category. L is reduced reflecting the change in the snow thickness distribution by the removal of ice and snow from the non-flooded category, and mean snow depths are adjusted in both ice categories to preserve snow mass.

Snow that has experienced a melt cycle is much less likely to undergo wind redistribution, as high temperatures cause rapid growth and sintering of snow grains, which greatly increase the mechanical strength of the snowpack [Li and Pomeroy 1997; Eicken et al. 1994; Sturm et al. 1998]. In the model, wind redistribution is only possible if there is >0.02 m of cold snow that has not experienced melting on top of the snowpack. A snow layer is considered to have undergone melt if it has reached a temperature $> -1^{\circ}\text{C}$. The melt status of each snowpack layer is stored as a tracer, and advects with other snowpack tracers, which include heat content and density.

The STD method is a first-order approximation of a snow thickness distribution for the purposes of generating snow ice. As a compromise between computation efficiency and model complexity, our snow thickness parameterization represents the simplest method we were able to conceive of for modeling the patchy, episodic, yet biologically important process of snow ice formation.

2.6. Atmospheric and Oceanic Coupling

The sea ice model is coupled to output from the European Center for Medium-Range Weather Forecasts Interim Reanalysis climatology (hereafter ECMWF) in all but one of the model runs. This reanalysis dataset was shown to permit accurate simulation of sublimation and turbulent latent cooling of snow covering Antarctic sea ice [Nicolaus et al. 2006]. ECMWF precipitation also matches well with snow accumulation rates on the Antarctic margins [Turner et al. 1999]. For comparison purposes, however, we also run the model coupled to the NCEP DOE II reanalysis climatology produced by the National Center for Environmental Predictions [Kanamitsu et al. 2002].

Values for 2 m surface air temperature, humidity, pressure, as well as 10 m wind speed and precipitation rate are linearly interpolated from a base periodicity (3-12

hours depending on the variable and climatology) into hourly measurements. To fit the higher resolution of the sea ice model grid, the climatological variables are regridded using a nearest-neighbor method; spatial interpolation is not performed.

The ice bottom is coupled to a static under-ice mixed layer of 2.5 m. Diffusion of deep-water nutrients and tracer concentrations throughout this mixed layer are calculated using standard Eulerian eddy diffusion with assumed eddy diffusion coefficient of $1 \times 10^{-3} \text{ m s}^{-1}$. This process effectively limits the speed at which nutrients may be delivered from the water column to the ice. Deep-water nutrient and tracer concentrations are static, and are listed in Table 1.

The ocean heat flux to the ice bottom is prescribed using monthly climatological values of ocean heat flux derived from seasonal heat flux calculations for Prydz Bay [Lei et al. 2010] (Table 3), and are linearly interpolated daily. By using a climatology, we will miss regional fluctuations in ocean heat flux that have been observed due to upwelling of warm water masses [McPhee et al. 1999]. However, we note that the vast majority of change in the surface temperature of the Southern Ocean comes from shortwave heating of ice-free water [Oshima and Nihashi 2005]. Typically ocean heat fluxes from the consolidated ice pack are low [Lytle and Ackley 1996; Lei et al. 2010]; therefore, changes in the character of the sea ice are likely to be mostly atmosphere-driven.

2.7. Areal Ice Concentration

The model uses SSM/I derived sea ice concentrations gridded on the EASE southern hemisphere projection, available from the National Snow/Ice Data Center (NSIDC) [Nolin et al. 1998]. In combination with sea ice motion (section 2.8), the changing ice concentration defines ice convergence (ridging), divergence, and new areal ice growth.

Table 3. Monthly Ocean Heat Flux Values

<i>Month</i>	<i>Ocean Heat Flux (W m⁻²)</i>
Jan	20
Feb	20
Mar	16
Apr	12
May	9
Jun	6
July	4
Aug	4
Sep	2
Oct	2
Nov	5
Dec	14

The model is active for 25 km² EASE grid cells that contain an SSM/I-derived ice fraction of 0.2 or greater. The accuracy of the SSM/I sea ice concentration product declines for ice fractions below 0.15, with new ice being harder to detect [Comiso 1986; Comiso and Sullivan 1986]. Therefore, we assume that newly frozen ice of 0.2 m thickness covers any grid cell that first exceeds the 0.2 ice fraction threshold. This new ice is initialized to be isothermal at seawater temperature with a brine fraction/porosity of 0.5. Brine is assumed to have properties equivalent to the underlying seawater. Cells that drop below an ice fraction of 0.2 are assumed to have either melted or advected out of the model domain.

2.8. Sea Ice Motion and Ridging

Sea ice transport is supplied by the NSIDC EASE-grid daily sea ice motion vectors dataset [Heil et al. 2006]. This dataset describes the direction and magnitude of sea ice movement with daily periodicity as estimated from a combination of satellite observations, including SSM/I passive microwave and Advanced Very High Resolution Radiometer (AVHRR) measurements. Advection ice volumes are

calculated through displacement of the square pixel onto neighboring pixels. Although this displacement method has the potential to overestimate divergence [Lipscomb and Hunke 2004], since we assimilate ice concentration into the model, this error should be minimized. During advection, ice and snow volumes and associated tracers merge within each thickness category so that mass is conserved.

Convergence and divergence are derived from the sea ice concentration and ice motion datasets. Over time (t), the ice area moving into (a_{in}) and out of (a_{out}) a pixel is estimated from pixel displacement of ice area at time t . The divergence (a_{div}) is then the difference between the current area (a_t) plus inputs and output, and the area at time $t+1$ (a_{t+1}):

$$a_{div} = a_{t+1} - (a_t + a_{in} - a_{out}) \quad (3)$$

If the ice is converging ($a_{div} < 0$), then the ice area is reduced via a ridging scheme after advection. If the divergence indicates that more ice present at time $t+1$ than was input during advection ($a_{div} > 0$), we assume new ice has grown in the grid cell (assuming atmospheric conditions permit).

The methods used to calculate SSM/I-derived sea ice products introduce considerable error for thin ice (<0.15 m) and high (>90%) ice concentrations [Comiso 1986; Comiso and Sullivan 1986]. Under these conditions, unrealistic levels of ice convergence and new ice growth are possible in areas of high or rapidly changing ice concentrations, respectively. Errors in ice thickness can accumulate quickly, especially along coastlines with heavy ice cover where errors in ice concentration and ice motion can produce massive convergence.

To compensate for these errors in the passive microwave sea ice products, we implemented several restrictions on ice convergence and new ice growth. Since sea ice strength grows with ice thickness, ridging and rafting becomes more difficult and less

probable in thick ice [Hibler 1979]. Most of the sea ice in the Antarctic is <2 m thick [Worby et al. 2008], so we restrict convergence of ice greater than 2 m in thickness, and prevent convergence in ice above 3 m in thickness. Similar restrictions have been used to improve the thickness distribution in mechanistic models of sea ice motion [Hibler 1980; Holland 2006]. Specifically, the allowed amount of convergence (a_{conv}) is derived from a_{div} as:

$$a_{conv} = \begin{cases} a_{div}, & 0 < z_i < 2 \\ a_{div}(3 - z_i)/2, & 2 \leq z_i < 3 \\ 0, & z_i \geq 3 \end{cases} \quad (4)$$

where z_i is the mean ice thickness (m) over the grid cell. In cases of convergence with $z_i > 2.0$ m, the extra ice area remains in the grid cell and the ice concentration is allowed to deviate from the SSM/I-specific value. If the grid cell ice concentration is above 90%, then the extra ice area is simply dropped from the model domain in a non-conservative manner. The total ice area dropped in this manner amounts to a tiny fraction (5×10^{-10} %) of yearly ice production, or a mean of 5 m^2 per grid cell per year. We also ignore ice growth if a_{div} indicates new ice growth under non-freezing conditions, again allowing the ice concentration to deviate from SSM/I derived values.

In model runs that do not use the ITD, ridging sea ice simply increases the sea ice thickness. This is performed in the model by increasing the thickness of all model layers using a thickness multiplier so that the total desired thickness is achieved. Then these inflated ice layers are regridded to fit the increased grid shape.

Ridging across multiple ice categories using the ITD follows the category participation and redistribution algorithms presented in Lipscomb et al. [2007], with the ridging participation parameter $\alpha^* = 0.05$. This method assumes redistribution of ridging ice into a thickness distribution with a minimum new thickness of twice the

ridging ice height, with an exponentially decreasing percentage of ridged ice ridging into thicker ice categories. Snow does not participate in ridging.

2.9. Biology

The sea ice ecosystem model of Arrigo and Sullivan [1994], with minor refinements presented in Chapter 1, is used to simulate algal growth in the fully coupled model. Briefly, this model considers algal growth to be controlled by the availability of light, macronutrients, salinity, and temperature. Algae maintain their position within the sea ice, rather than being transported with fluid flux, and have a limited ability to migrate downward when located at near the bottom of the ice sheet. Algae, along with other tracers, are entrained into the ice during freezing of seawater at seawater concentrations. Seawater is assumed to have fixed, deep-water nutrient concentrations and an algal concentration of $1 \text{ mg Chl } a \text{ m}^{-3}$, and algae have a fixed nutrient stoichiometry (Table 4). The minimum allowed algal concentration in the ice is $0.1 \text{ mg Chl } a \text{ m}^{-3}$. Algae are subject to a constant loss rate of $1\% \text{ day}^{-1}$, and are removed from the model domain when any layer they are growing in melts.

2.10. Initial Conditions

To define initial ice thicknesses at the start of a model run (1 March), we apply the equation of Arrigo et al. [1998] which relates the ice thickness to observed SSM/I ice concentration:

$$z_i = \begin{cases} z_{\min} + c_i(1.28 - z_{\min}) / 0.8, & 0.2 < c_i < 0.8 \\ 1.28, & c_i \geq 0.8 \end{cases} \quad (5)$$

where z_i is the ice thickness (m) and c_i is the SSM/I sea ice concentration (fraction). At this time of year, we assume that ice surviving over the summer has been subject to snow melt percolation, and we assign a standard multi-year ice salinity profile

Table 4. Selected Model Constants and Parameters

<i>Parameter</i>	<i>Description</i>	<i>Value</i>	<i>Units</i>
$r_{C:Chla}$	Algal/Detrital C:Chla ratio	35	g/g
$r_{C:N}$	Algal/ Detrital C:N ratio	7	mol/mol
$r_{C:P}$	Algal/ Detrital C:P ratio	106	mol/mol
$r_{C:Si}$	Algal/ Detrital C:Si ratio	4	mol/mol
K_{NO_3}	Half-saturation algal rate constant for NO_3 uptake	1	μM
K_{NH_4}	Half-saturation algal rate constant for NH_4 uptake	1	μM
K_{PO_4}	Half-saturation algal rate constant for PO_4 uptake	0.1	μM
K_{SiOH_4}	Half-saturation algal rate constant for $SiOH_4$ uptake	60	μM
$C_{sw\ NO_3}$	Seawater algal concentration	1	$\mu G\ L^{-1}$
$C_{sw\ NO_3}$	Seawater NO_3 concentration	30	μM
$C_{sw\ NH_4}$	Seawater NH_4 concentration	0	μM
$C_{sw\ PO_4}$	Seawater PO_4 concentration	2	μM
$C_{sw\ SiOH_4}$	Seawater $SiOH_4$ concentration	80	μM
$C_{sw\ POC}$	Seawater Detrital concentration	0	μM

Table 5. Thickness-dependent salinity values (psu) used to derive initial multi-year salinity profiles for model runs, with initial ice thickness z . Layer salinities are interpolated linearly between the table values.

<i>Ice Thickness</i>	<i>Bulk ice salinity</i>
0	0.1
$z/9$	0.2
$2z/9$	0.2
$3z/9$	0.6
$4z/9$	1.9
$5z/9$	3.1
$6z/9$	3.4
$7z/9$	3.6
$8z/9$	3.9
z	6.2

described in Table 5. Initial snow thicknesses are derived from EASE gridded SSM/I brightness temperatures [Armstrong et al. 1994] using the algorithm and methods of Markus and Cavalieri [1998]. Valid snow thicknesses calculated in this manner are averaged over the seven days preceding March 1 to arrive at the initial snow thickness values for each grid cell. Initial snow and ice temperatures are calculated following Arrigo et al [1993]. Initial nutrient, detrital, and algal concentrations in the ice are set to seawater values in proportion to the initial brine fraction of each layer. If either the ITD or the STD is employed, flat distributions are assumed at model start.

2.11. Computation

Atmospheric forcing data and satellite sea ice data are linearly interpolated to produce hourly values and remain constant across the hour. The delta-Eddington shortwave radiation transfer is calculated once per hour due to its large computational expense, and the resulting irradiance is assumed constant over the hour.

With a 0.02 m minimum layer thickness, model physics and biology operate at a maximum model time step of 0.2 hr. Adaptive time stepping may decrease the time step if the ice temperature changes too quickly or fluids flux too rapidly.

All components of the model were written in the FORTRAN 95 programming language, except the delta-Eddington radiation transfer model, which was written in C to run on commodity graphics (GPU) hardware to increase efficiency. The model is capable of running on a multi-core desktop personal computer, and requires 16 Gb of memory when configured to use five ice thickness categories and the STD scheme.

3. Simulations

We present seven model runs that vary in their physical representation of ice and snow to determine how different model parameterizations impact the simulation of sea

Table 6. Model Run Descriptions

<i>Model Run</i>	<i>Ice Thickness Categories</i>	<i>Snow Thickness Distribution</i>	<i>Atmospheric Climatology</i>	<i>Model Features</i>
STND (standard)	5	yes	ECMWF Interim	MWP, SIF, SC
1N	1	no	ECMWF Interim	MWP, SIF, SC
1Y	1	yes	ECMWF Interim	MWP, SIF, SC
5N	5	no	ECMWF Interim	MWP, SIF, SC
NCEP	5	yes	NCEP DOE II	MWP, SIF, SC
NSC (no slush convection)	5	yes	ECMWF Interim	MWP, SIF
SS (simple snow)	5	yes	ECMWF Interim	SC

MWP = melt water percolation; SIF = superimposed ice formation; SC = slush convection

ice ecology (Table 6). The standard model run ‘STND’ contains the highest resolution (five ice categories ITD plus within-category SDT) and employs all model features. The ‘1N’ run contains only one ice category, and the snow is level across the grid cell. The ‘1Y’ model run is similar to ‘1N’ except the STD method is used on the single ice category. The ‘5N’ run explores the use of an ITD with five ice categories and a flat snow distribution in each category. ‘NCEP’ is similar to the ‘STND’ run, except the NCEP/DOE II reanalysis climatology was used in place of the ECMWF Interim climatology to test the effect that differences in atmospheric forcing have on model results. The simple snow ‘SS’ model run turns off snow features including superimposed ice formation, melt water and brine percolation, and surface layer drainage while retaining the process of snow ice formation. Finally, we performed a run ‘NSC’ (no slush convection) where nutrients were prevented from exchanging with underlying seawater in interior high-brine fraction sea ice layers [Chapter 1], following the formation of those layers.

Model runs begin on 1 Mar 1997. This date was selected to be near the minimum annual sea ice extent such that errors due to assumptions about initial ice characteristics are minimized. The model run progresses through June 30 1998, and

we perform analyses of model output over the period 1 July 1997 to 30 June 1998 that captures the annual ice algal growth cycle.

4. Validation

4.1. Ice and Snow Thickness

For model validation of snow and ice thickness, we compare modeled snow thickness distributions with observations from the Antarctic Sea Ice Processes & Climate (ASPeCT) database [Worby et al. 2008]. The observations from ASPeCT come from discrete field campaigns to the Antarctic that are necessarily limited in space and time (Figure 4), introducing bias into summary statistics generated from the dataset. To reduce bias, we match each individual ASPeCT snow thickness observation with model output for the same location and time of year. Interannual differences in timing of sea ice advance, retreat, and overall extent result in a fraction of ASPeCT observations being collocated with open water in the model. Therefore, we include only those ASPeCT observations that are collocated with SSM/I sea ice, which reduces the total dataset to 8227 observations (56% of total observations). ASPeCT observations span the time period of 1981-2005 while model runs encompass only a single year; nevertheless, the similarity in patterns of ice growth and movement make comparisons meaningful.

The STND model run matches the ASPeCT data most closely (Figure 5A); however, all of the model runs simulate the observed snow thickness distribution quite well. Although the right-hand tail of the ASPeCT distribution is longer than any model run, Worby et al. [2008] note that the ASPeCT snow depths are biased toward thick snow due to observations by a single cruise to the Amundsen Sea where extreme snow cover was encountered. Examination of monthly means shows that model runs using five ice categories (STND, 5N, NCEP) produce 0.03-0.08 m higher monthly snow

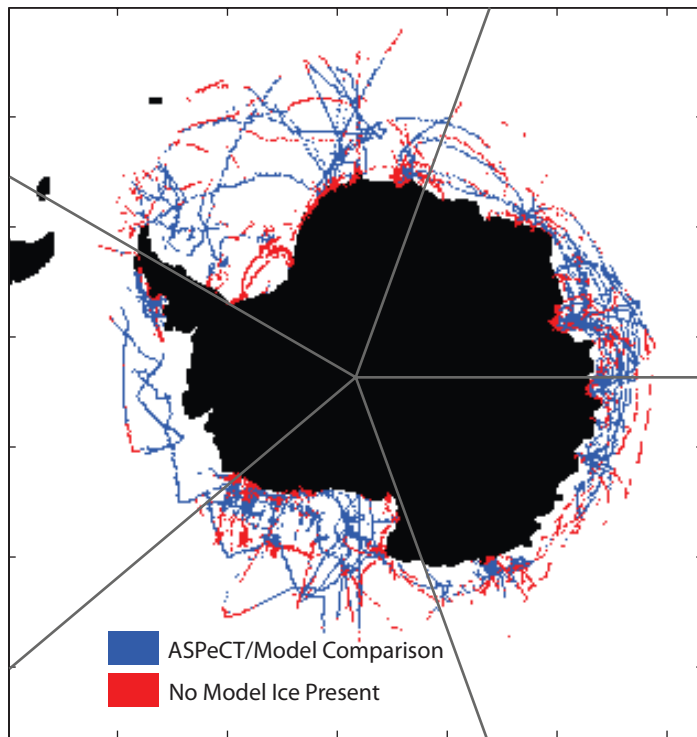


Figure 4. ASPeCT sea ice and snow cover observations, plotted according to location [Worby et al. 2008].

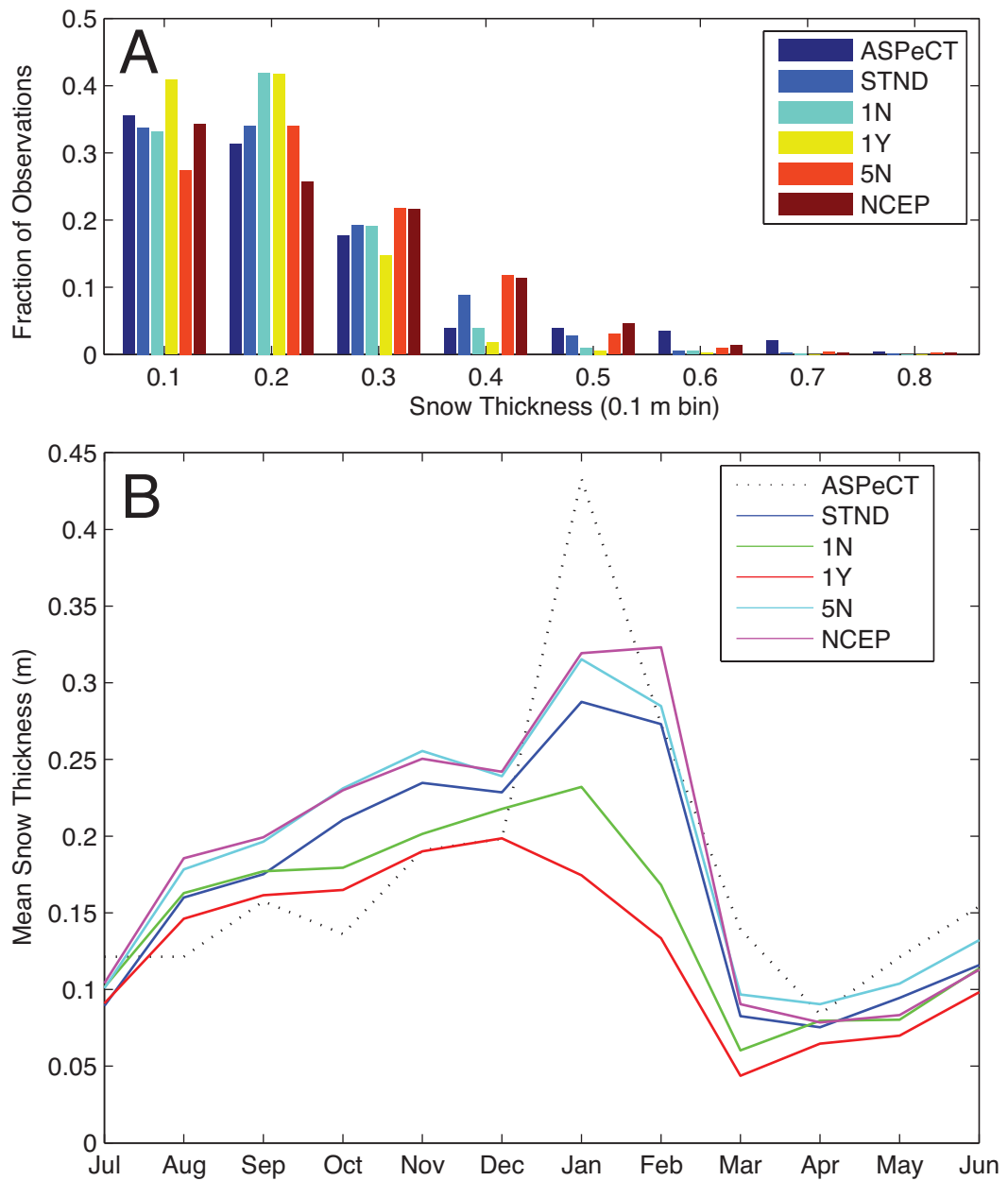


Figure 5. Comparison of the (A) frequency distribution and (B) monthly mean of snow thicknesses from ASPeCT observations and matching model output.

depths during Aug-Dec than in the ASPeCT dataset, while the single ice category model runs (1N, 1Y) match more closely (Figure 5B). The January ASPeCT data are biased by the aforementioned Amundsen Sea cruise data, but it is interesting to note that model runs also show the greatest variation in mean thickness during this month. Modeled autumn mean snow thicknesses are slightly smaller than ASPeCT observations, but overall, the model runs follow the ASPeCT monthly trend. Annual mean values of snow thickness from model runs using five ice categories (runs 5N and STND) are within 13% of the ASPeCT mean snow thickness of 0.174 m (Table 7).

In general, we expect the modeled ice thicknesses to be biased high because of the minimum ice thickness of 0.2 m used in the model. This is apparent in a histogram showing the ASPeCT-model paired ice thickness distributions, where no modeled ice is present in the smallest thickness bin (Figure 6A). However, the mean ASPeCT ice thickness is actually higher than all model runs except for the NCEP run (Table 7). This is in part due to the extreme ice thickness bias in the ASPeCT January data, but also reflects the fact that all model runs have lower a mean ice thickness than ASPeCT during spring (Figure 6B). The peak ASPeCT ice thickness distribution is in the 0.5 m ice thickness bin, while the model runs peak in the 0.3 m bin. After the peak, the ASPeCT distribution falls off steadily with increasing ice thickness, except for a small bump at 2.3 m. The model runs show higher proportions of 0.7 and 0.9 m ice relative to ASPeCT, falling away to similar distribution tail for thick ice. Overall, the STND run ice thickness distribution most closely matches the ASPeCT run.

Despite large monthly variability, model runs using five ice categories (STND, 5N, NCEP) capture the magnitude and trends of the ASPeCT ice thickness data fairly well, including the maintenance of the ice thickness during summer, the sharp drop in mean ice thickness as new ice begins to form in March and April, and an increase again in May. The single ice category runs (1N, 1Y) are similar but with smaller mean

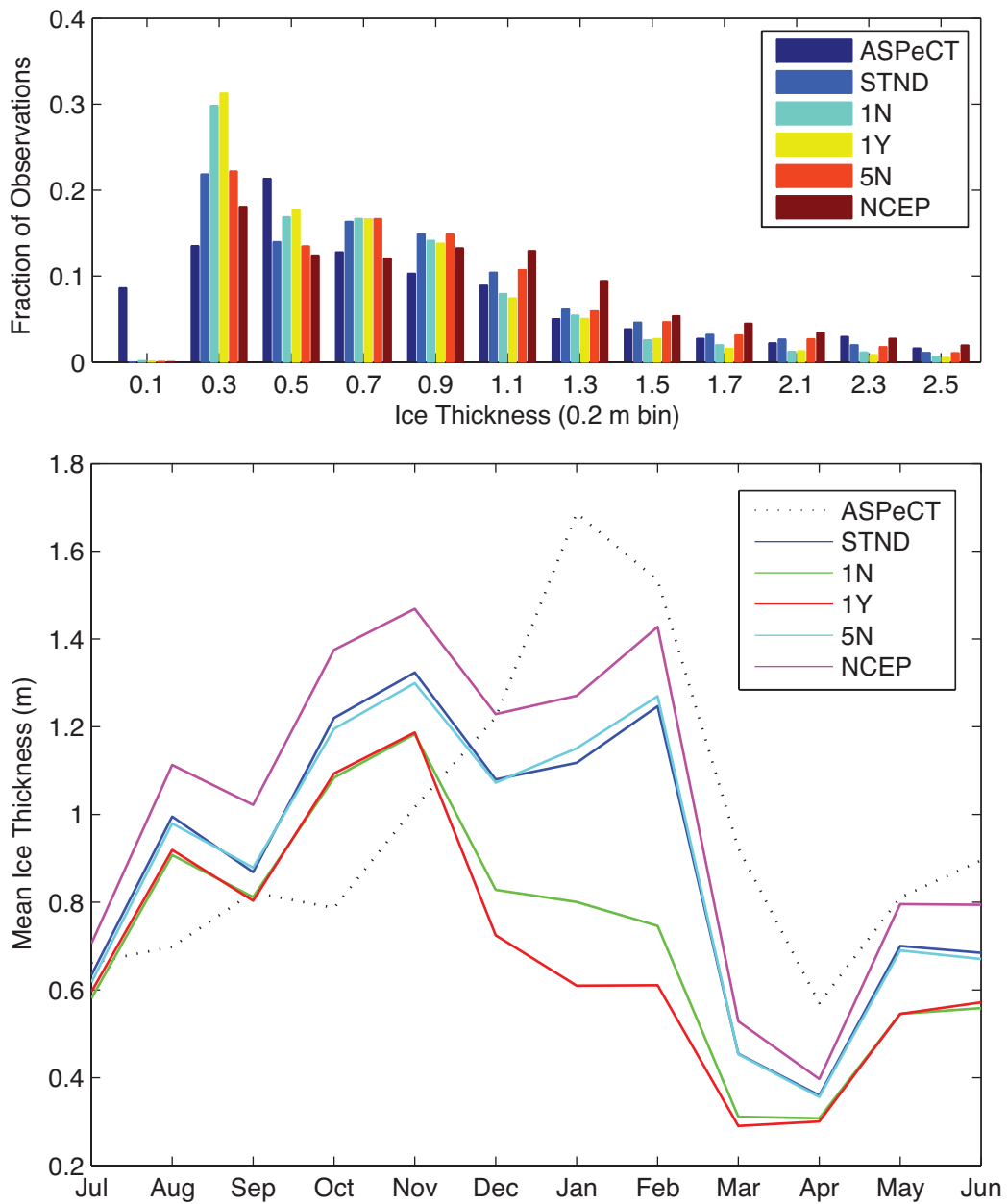


Figure 6. Comparison of the (A) frequency distribution and (B) monthly mean of sea ice thicknesses from ASPeCT observations and matching model output.

Table 7. Summary of matching ASPeCT observations and modeled snow and ice thicknesses (m)

<i>Dataset/Model Run</i>	<i>Mean Ice Depth (s.d.)</i>	<i>Mean Snow Depth (s.d.)</i>
ASPeCT	0.938 (0.825)	0.174 (0.174)
STND	0.887 (0.578)	0.166 (0.118)
1N	0.737 (0.493)	0.148 (0.096)
1Y	0.710 (0.468)	0.129 (0.081)
5N	0.882 (0.573)	0.183 (0.127)
NCEP	1.006 (0.627)	0.180 (0.136)
NSC	0.888 (0.579)	0.166 (0.118)
SS	0.899 (0.591)	0.151 (0.106)

thicknesses, and, in contrast, show a decreasing thickness during summer (December–March, Figure 6B).

4.2. Sea Ice Biology

The performance of the vertical sea ice model employed in each grid cell and/or ice category to simulate changes in sea ice evolution and ice algal growth was validated using time series measurements physical and biological sea ice parameters during the Ice Station Weddell experiment [Fristen et al. 1994; Ackely et al. 1996; Lytle and Ackley et al. 1996]. The model is able to reproduce specific patterns of ice temperature, salinity and ice algal growth with good vertical resolution, and is unique in its ability to simulate the evolution of high-brine fraction sea ice [Chapter 1].

Validation of sea ice algal production in the model is difficult due to paucity of observational data. In fact, the purpose of the model is to explore the bounds of primary production in the Antarctic sea ice ecosystem system since so little is known concerning its magnitude, location, and timing. The data that are available for validation are in the form of a moderate number of algal biomass measurements from studies in Arctic and Antarctic sea ice. The algal biomass measured in ice cores is

highly variable, even within a single ice floe at the meter scale or smaller [Garrison and Buck 1991; Eicken et al. 1994]. This observed variability is the reason for inclusion of ice and snow thickness distribution methods in the model. With ice categories able to simulate different representative ice thicknesses, as well as separate calculation of flooded and non-flooded ice, we will capture some of the heterogeneity of the ice pack in each 625 km² grid cell.

The variability of ice core biomass observations also makes comparison to model output difficult. The spatial and temporal bias of the ice core observations requires consideration as well. Therefore, we compiled mean areal biomass measurements across 17 different Antarctic cruises or field campaigns. Mean monthly algal biomass from the STND model run averaged across the entire model domain is plotted alongside observed biomass means (Figure 7). The biomass observations are plotted according to the approximate date that sampling took place.

Overall, the biomass measurements lend confidence that the model is conservatively estimating sea ice algal production in the Antarctic. With the exception of two summer cruises, the range of the modeled biomass approximately spans the range of mean observations. The two exceptions are the ANT IX/3 and ANT XI/3 cruises, which reported mean algal standing crops of 24.6 and 34.1 mg Chl a m⁻² respectively, values much higher than the model monthly means. Fortunately, examination of monthly histograms of algal biomass show that thousands of grids cells exceed 20 mg Chl a m⁻² (equivalent to 0.7 g C m⁻²) during summer (Figure 8). The model therefore encompasses the range of biomass of the ANT IX/3 cruise, although grid cell biomass very rarely reaches >34 mg Chl a m⁻² in the model, as was observed on ANT XI/3. This high mean biomass is from 29 ice cores taken from the Bellingshausen Sea (Amundsen sector) during summer in 1994, where extremely high algal biomass was observed at a majority of stations within gap layers in the ice pack.

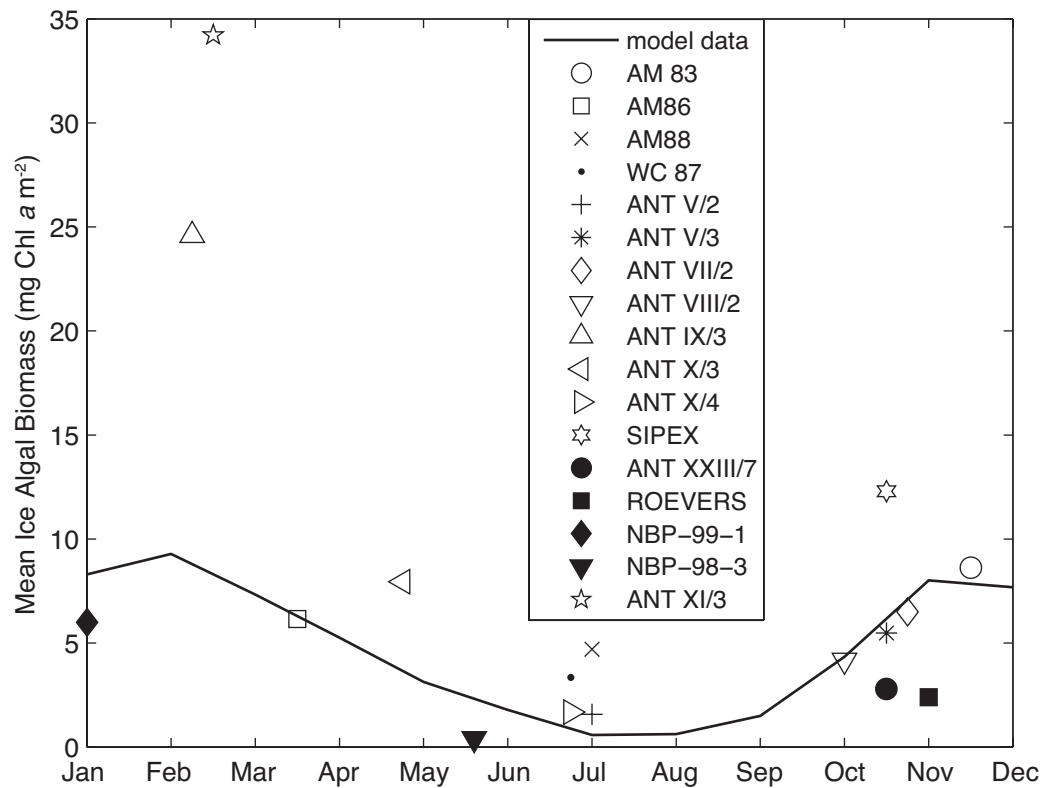


Figure 7. Plots of mean ice core algal biomass from 17 Antarctic field expeditions, overlaid with a line showing mean monthly sea ice biomass in the STND run. Field expedition dates are approximate, representing the middle of campaigns that were sometime several months in length.

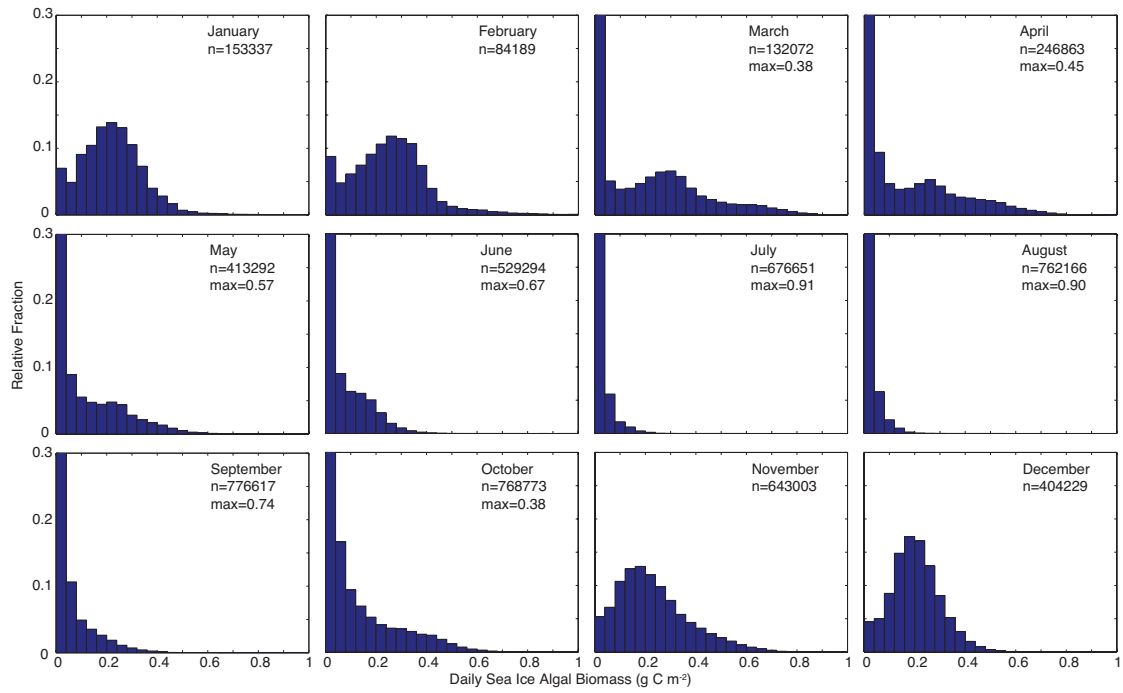


Figure 8. Monthly histograms of sea ice algal biomass from the STND run, where n is the number of daily grid cell observations. The relative fraction of the first biomass bin is listed as ‘max’ where it extends beyond the axis range. For reference, $1.0 \text{ g C m}^{-2} = 28.6 \text{ mg Chl } a \text{ m}^{-2}$ in the model.

The pack was apparently at a late stage of decay, with ~50% ice coverage. It is possible that the model underestimates sea ice algal production under these circumstances, but it is also possible that our chosen model year (1997-98) did not contain the climactic conditions necessary to produce such an intense bloom.

5. Results

5.1. Precipitation

Precipitation patterns over Antarctic sea ice during the model analysis period (1 July 1997 to 30 Jun 1998) show the expected trend of higher snowfall rates at more northerly latitudes, where warmer air holds more precipitable moisture (Figure 9A). The Amundsen, Ross and Pacific sectors experience higher snowfall rates overall than the Weddell and Indian sectors. The variability in precipitation rate at the outer edges of the ice pack is due to the short duration of ice there; sea ice that forms and disappears without encountering a snowstorm will exhibit a low precipitation rate, while short-lived sea ice that endures a snowstorm will have a high precipitation rate.

In contrast, total snowfall over more persistent sea ice (Figure 9B) exhibits a different pattern that is a function of both ice persistence (Figure 9D) and precipitation rate (Figure 9A). (We calculate total ice presence as a measure of the total ice area over time. Ice presence is integration of daily ice extent (km^2 per unit time), and as such represents both the area and duration of sea ice in a particular summary sector.) Annual snowfall over sea ice is especially high in the Western Amundsen and Eastern Ross sectors, as well as along the coast in the Pacific sector where the climatology shows that over 1.5 m of snow fell over a significant fraction of the annual ice extent. In contrast, snowfall over perennial ice in the Western Weddell sector averages only 0.6-0.8 m, a difference resulting from lower precipitation rates in this area. The mean annual snowfall over the model domain is 0.63 m, independent of ice concentration.

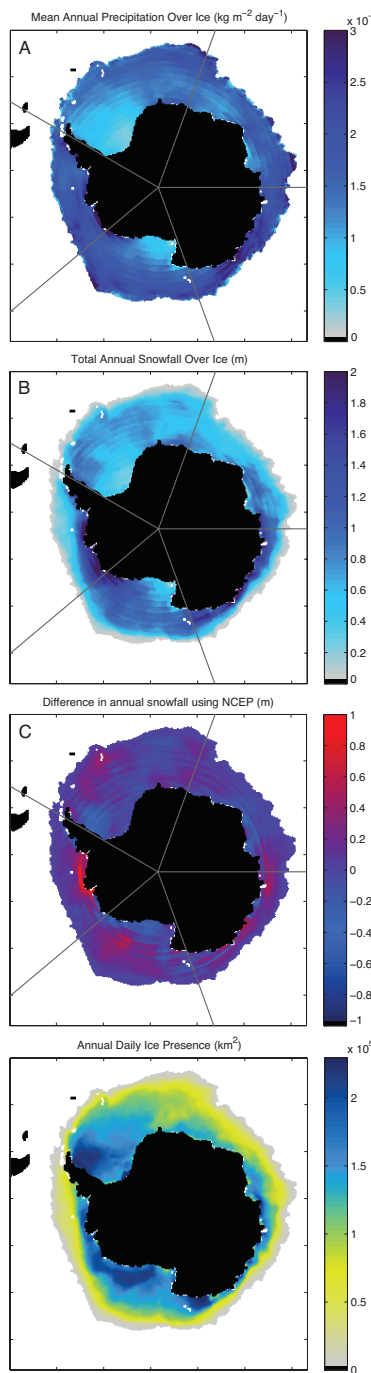


Figure 9. Spatial distribution of (A) mean model precipitation rate (ECMWF), (B) Total annual snowfall (ECMWF), (C) the difference in total annual snowfall over sea ice between the NCEP/DOE II reanalysis climatology, and the ECMWF Interim climatology, and (D) annual ice presence. Ice presence is calculated in order to measure of the total ice area over time. Ice presence is integration of daily ice extent (km^2 per unit time), and as such represents both the area and duration of sea ice in a particular summary area.

5.2. Snow Thickness

Snowfall patterns combine with the model sea ice dynamics to produce an annual mean snow thickness over sea ice of 0.17 m. The spatial variability of mean snow thickness is very high, as evidenced by the distribution of mean snow thicknesses from the STND run (Figure 10A) and by the sectional mean snow depths for specific geographic regions (Table 8). The Amundsen and Pacific sectors have greater mean snow depths than the Antarctic mean, a difference that is driven by a few small areas with extremely deep snow.

Comparing model runs, mean snow thicknesses in the 1N and 1Y model runs are lower than that of the STND run in all sectors (Table 8). Much of this difference is due to the use of a single ice category in the 1N and 1Y runs in conjunction with sea ice motion. With multiple ice categories, older, thicker ice survives longer and accumulates more snowfall, and is less likely to undergo ridging that can cause snow mass loss. This process is illustrated in the maps of snow thickness differences between the STND run and the 1N and 1Y runs (Figure 10A), where large negative differences can be seen over areas of persistent, thick ice along the coastlines in the Western Weddell, Amundsen, and Eastern Pacific sectors. The 1N and 1Y runs also have slightly greater mean snow thicknesses compared to the STND run over broad, offshore areas of the ice pack. These positive differences are due to a lack of snow loss from reduced snow ice formation in the 1N and 1Y runs. In the 1Y run, the use of only a single ice category means that more easily flooded thin ice is not well represented. In the 1N run, this issue is compounded by a lack of a STD routine that would have allowed partial flooding of a grid cell, resulting in greater snow thicknesses in these northerly regions compared to 1Y.

Snow thickness in the 5N run is higher than in the STND run in 97% of grid cells due to the omission of the STD and the reduced rate of conversion of snow into snow

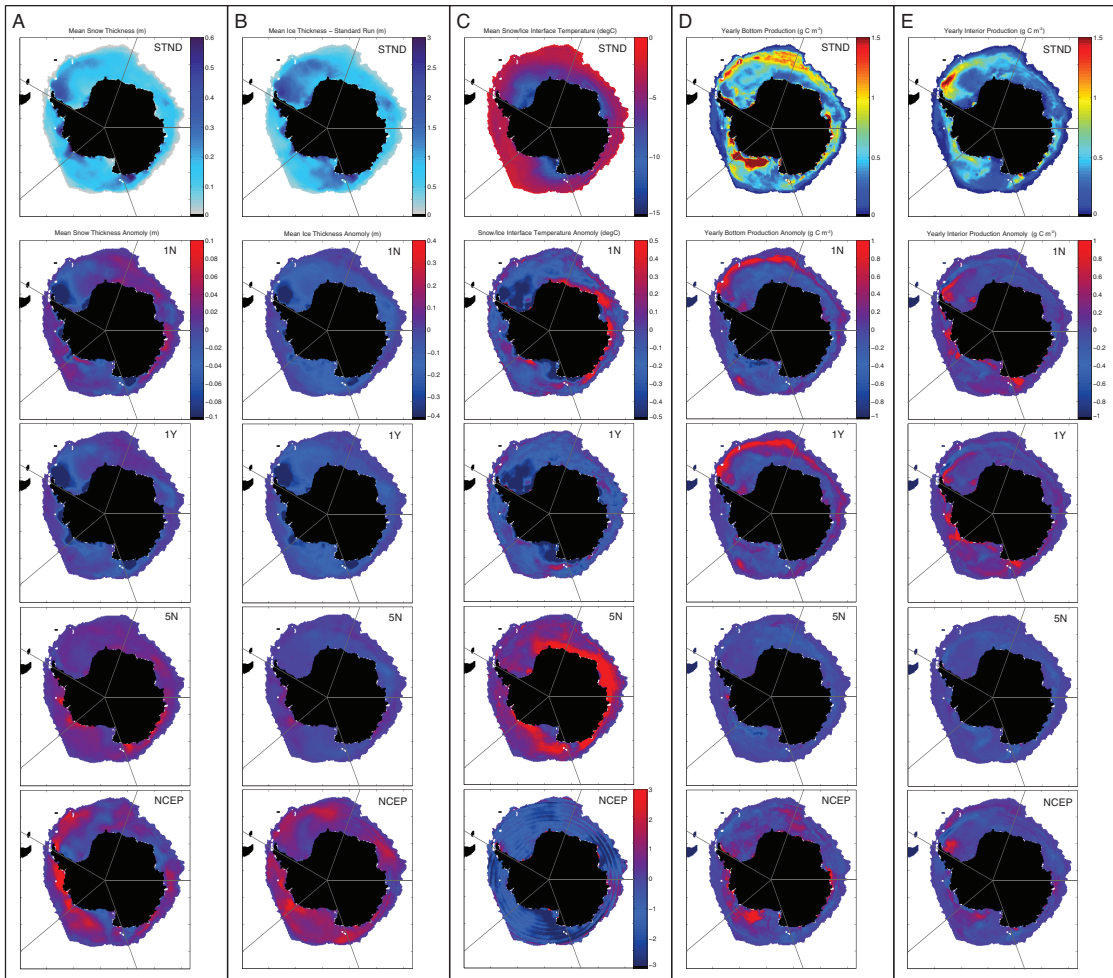


Figure 10. Spatial distribution of simulated (A) mean annual snow thickness, (B) mean annual sea ice thickness, (C) Mean annual snow/ice interface temperature, (D) total annual bottom sea ice algal production, and (E) total annual interior ice algal production. The bottom four rows of maps show the difference between the indicated model run (1N, 1Y, 5N, or NCEP) and the top row of STND run maps. Note the NCEP snow/ice interface temperature difference map has a different scale from the other model run maps.

Table 8. Annual Mean Snow and Ice Thickness (m)

<i>Dataset / Model Run</i>		<i>All</i>	<i>Weddell</i>	<i>Amundsen</i>	<i>Ross</i>	<i>Pacific</i>	<i>Indian</i>
STND	(snow)	0.18	0.18	0.23	0.18	0.22	0.12
	(ice)	1.04	1.19	0.91	1.03	0.98	0.79
1N	(snow)	0.16	0.15	0.20	0.17	0.19	0.13
	(ice)	0.90	1.02	0.83	0.89	0.85	0.69
1Y	(snow)	0.15	0.14	0.17	0.15	0.16	0.12
	(ice)	0.88	0.99	0.74	0.88	0.80	0.72
5N	(snow)	0.20	0.19	0.25	0.19	0.26	0.14
	(ice)	1.03	1.17	0.96	1.02	0.98	0.75
NCEP	(snow)	0.19	0.19	0.29	0.19	0.24	0.12
	(ice)	1.15	1.27	1.09	1.07	1.07	0.87
NSC	(snow)	0.18	0.18	0.23	0.18	0.22	0.12
	(ice)	1.04	1.19	0.91	1.03	0.98	0.79
SS	(snow)	0.17	0.16	0.22	0.17	0.21	0.12
	(ice)	1.05	1.21	0.91	1.04	0.99	0.79

ice (Figure 10A; Table 8). The areas with the deepest snow show the largest positive differences from the STND run since these areas produce a disproportionately large amount of snow ice in the STND run.

In the NCEP run, sea ice is subject to a different precipitation pattern (and melt-freeze cycling – see section 5.5), which produces patchy, moderate differences in mean snow depth across the ice pack (Figure 10A). Especially high NCEP snowfall in the Bellinghausen Sea (southeastern Amundsen sector) resulted in higher mean snow thickness there (Figures 9C, 10A). Differences in the sector mean snow thickness between NCEP and STND runs are largest in the Weddell and Pacific sectors, which show increased values in the NCEP run. Mean snow thickness in the Ross, Indian, and Weddell sectors are similar between the NCEP and STND runs, as are mean snow thickness over the entire model domain, illustrating how reducing data to means over large areas can mask important variability of small scale, patchy processes such as precipitation (Table 8; Figure 10A).

The SS run contains slightly reduced snow thicknesses in all sectors compared to the STND run. The lack of superimposed ice formation in the SS run causes faster ice melt as melt water is returned to the ocean immediately upon surface snow melt. The net effect of this process is the shift of heat from the snow surface to the interior of the snow and ice pack, effectively buffering the system against mass loss during rapid melt cycles. The NSC run is identical to the STND run except for reduced convective exchange under certain circumstances, and the two simulations exhibited identical mean snow thicknesses (Table 8).

Daily mean snow thickness is lowest in mid-autumn when sea ice extent is increasing rapidly and large expanses of new sea ice have not had time to accumulate snow. Modeled total mean daily snow thickness increases from a spring minimum of between 0.07-0.10 m to a summer maximum that differs markedly between model runs (Figure 11). In summer, model runs with five ice categories (STND, 5N, NCEP) maintain a relatively thick snow cover, while the single ice category runs (1N, 1Y) continually lose snow mass during summer. These summertime differences between model runs are carried through and affect the mean snow thickness during freeze-up in autumn, especially in the Amundsen and Pacific sectors. Thick snow in the Amundsen sector is maintained during the spring and summer by a balance between snow accumulation and the loss of snow as it is transformed into snow-ice. In the Pacific sector, the snow thickens until the onset of freezing. This increase is a result of accumulation as well as a reduction in sea ice area with lower snow cover, leaving only grid cells with thick snow.

Of the non-NCEP runs, the 5N run always shows the highest mean snow thickness, followed by the STND, 1N and 1Y runs in decreasing order (Figure 11). The NCEP run exhibits similar mean snow depths as runs that use five ice categories. During the melt season, NCEP mean snow thickness in the Weddell, Amundsen, and

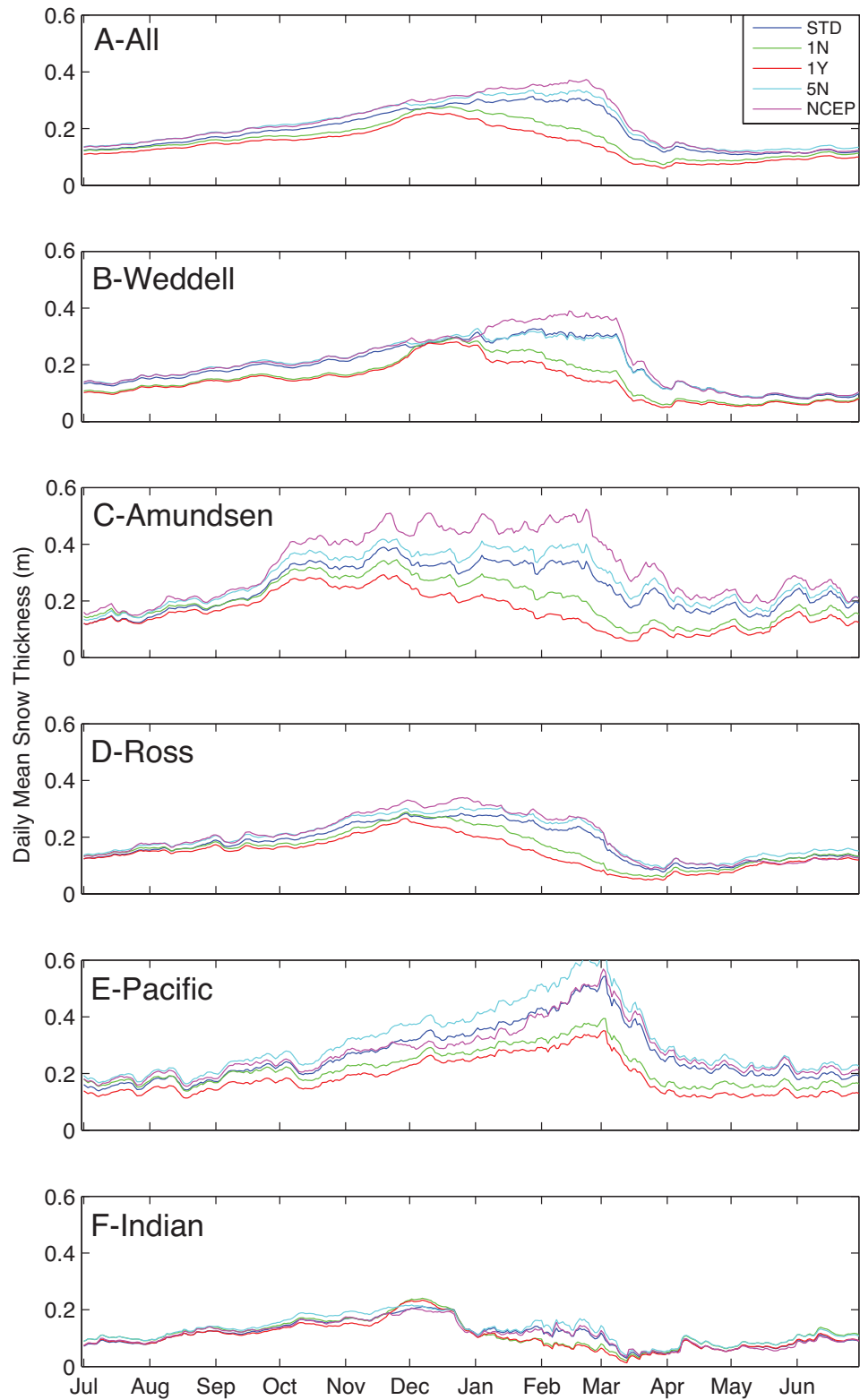


Figure 11. Time series plots of mean daily snow thickness from the entire model domain (A) and from different analysis sectors (B-F).

Ross sectors becomes larger than in other model runs, while in the Pacific and Indian sectors, snow depth in the NCEP run closely tracks the STND run.

5.3. Ice Thickness

The annual mean ice thickness in the STND run is 1.04 m (Table 8). One general pattern in ice thickness is that thinner ice dominates the northern boundary of the ice pack. Thick ice does exist toward the northern boundary of the ice pack in several places, including the Weddell and Ross sectors where significant northward advection of ice results in a thicker ice pack. Areas of deep snow correspond to regions of thick ice, since a thick ice pack is necessary to support a thick snowpack above freeboard. Thick ice does not always correspond to thick snow, however, as in large portions of the Weddell and Ross sectors where low atmospheric temperatures result in large amounts of congelation ice growth but snow is relatively thin (see section 5.5).

Mean annual ice thickness in the single ice category runs 1N and 1Y is 25% and 23% lower, respectively, than in the STND run across all sectors (Table 8). The largest ice thickness differences between these two runs and the STND run are in areas of thickest ice (Figure 10B). These differences are related to the use of the ITD, which provides for greater stability of thick ice categories and preserves ice thickness during advection. Differences in sector mean ice thickness between the 1N and 1Y runs are largest in Amundsen and Pacific sectors where snow is thickest, with lower values in the 1Y run. Lower mean sector ice thickness in the 1Y run is surprising given that there was 50% more ice production in the Amundsen sector and 56% more ice production in the Pacific sector (Table 9). This is due to the effects of modeling flooded and non-flooded ice columns without using the STD routine. When the snow floods and the flooded ice area is moved to the flooded ice category, the remaining ice is left with a thinner, and less insulating, mean snow cover, and is able to grow more

Table 9. Annual Ice Production¹ (10^{11} m^3)

<i>Model Run</i>	<i>Ice Type</i>	<i>All</i>	<i>Weddell</i>	<i>Amundsen</i>	<i>Ross</i>	<i>Pacific</i>	<i>Indian</i>
All	Frazil ²	10.78	2.97	1.49	2.43	1.79	2.08
STND	Snow Ice	22.78	5.96	3.63	5.82	3.73	3.64
	Congelation	89.77	40.41	3.87	22.9	6.08	16.52
1N	Snow Ice	5.40	0.81	1.44	1.66	1.13	0.36
	Congelation	70.20	33.68	2.32	17.2	3.85	13.14
1Y	Snow Ice	21.36	6.01	2.92	5.77	3.31	3.34
	Congelation	72.57	34.16	2.73	17.7	4.48	13.52
5N	Snow Ice	10.80	2.19	2.88	2.65	2.12	0.95
	Congelation	86.31	39.85	3.46	21.8	5.51	15.65
NCEP	Snow Ice	21.45	4.89	4.40	4.64	4.58	2.94
	Congelation	118.32	48.70	6.60	33.7	8.28	21.07
NSC	Snow Ice	22.78	5.97	3.63	5.81	3.72	3.65
	Congelation	89.88	40.46	3.87	22.9	6.085	16.54
SS	Snow Ice	19.86	4.15	3.27	5.39	3.59	3.45
	Congelation	89.89	40.45	3.84	22.9	6.099	16.59

¹ Volumes reported are total sea ice volumes that contain variable amounts of ice and brine, therefore results should not be used to directly estimate latent heat removal or brine salt rejection to the water column.

² Frazil ice represents new areal ice growth based upon changes in the SSM/I sea ice concentration. Our model assumes this new ice growth is in the form of 0.2 m of consolidated frazil ice, however the satellites do not distinguish ice type. Because new ice may contain snow or congelation growth before satellite detection, frazil ice production as listed here is likely an overestimate of that ice type.

coldwater ice. The flooded ice is apparently subject to significant bottom melt that is larger in magnitude than the combined growth of congelation ice and snow ice, thereby reducing mean ice depths in these sectors. The opposite result occurred in the Indian sector, where there was 25% more total ice production in the 1Y run than in the 1N run. However, the mean ice depth increased, indicating that additional bottom melt allowed by the STD did not fully compensate for the increased ice production.

In the 5N run, mean ice thickness is within 2% of that in the STND run, and sector means are also similar, although slightly thinner (Table 8). This thinning is spread evenly across the ice pack, as the 5N ice thickness difference map shows, with areas of thick ice in the STND run being even thicker in the 5N run (Figure 10B). The SS run

shows the opposite trend, with very slightly thicker mean sea ice than the STND run.

Using the NCEP climatology produced sea ice that was 11% thicker than in the STND run, with sector mean ice thicknesses being elevated by 1-20% (Table 8). A map of the spatial difference in mean ice thickness between NCEP and STND shows large, variable patches. The largest increases in ice thickness appear to co-occur with positive increases in snow thickness, negative snow/ice interface temperature differences, or both (Figure 10A-C).

The differences in mean ice thickness between model runs are established early in the simulations and generally continue throughout the simulations until melt begins in late spring. The main most consistent trend between the different runs was reduced summer ice thickness in the 1N and 1Y runs, especially during the ice retreat. In model run that used the ITD, thinner ice melts away first, causing the mean ice thickness to remain steady or even increase. The 1N and 1Y runs, with only a single ice thickness in each grid cell, respond directly to melting by decreasing mean ice thickness (Figure 12).

5.4. Ice Production

Snow ice. The Amundsen and Pacific sectors each produced 16% of the total snow ice volume in the STND run, which was disproportionately large compared to their relative ice total ice presence (10% and 9% respectively; Tables 9,10). The Weddell sector accounted for 40% of total ice presence in the Antarctic, yet produced only 26% of the snow ice volume in the STND run. The fractional snow ice production in the Ross and Indian sectors (26% and 16%, respectively) was more in accordance with their ice presence (26% and 15%, respectively; Tables 9 and 10). Mapped snow ice production shows concentrated nearshore production in the West Amundsen, Eastern Ross, and Pacific sectors. This distribution is primarily controlled by total snow

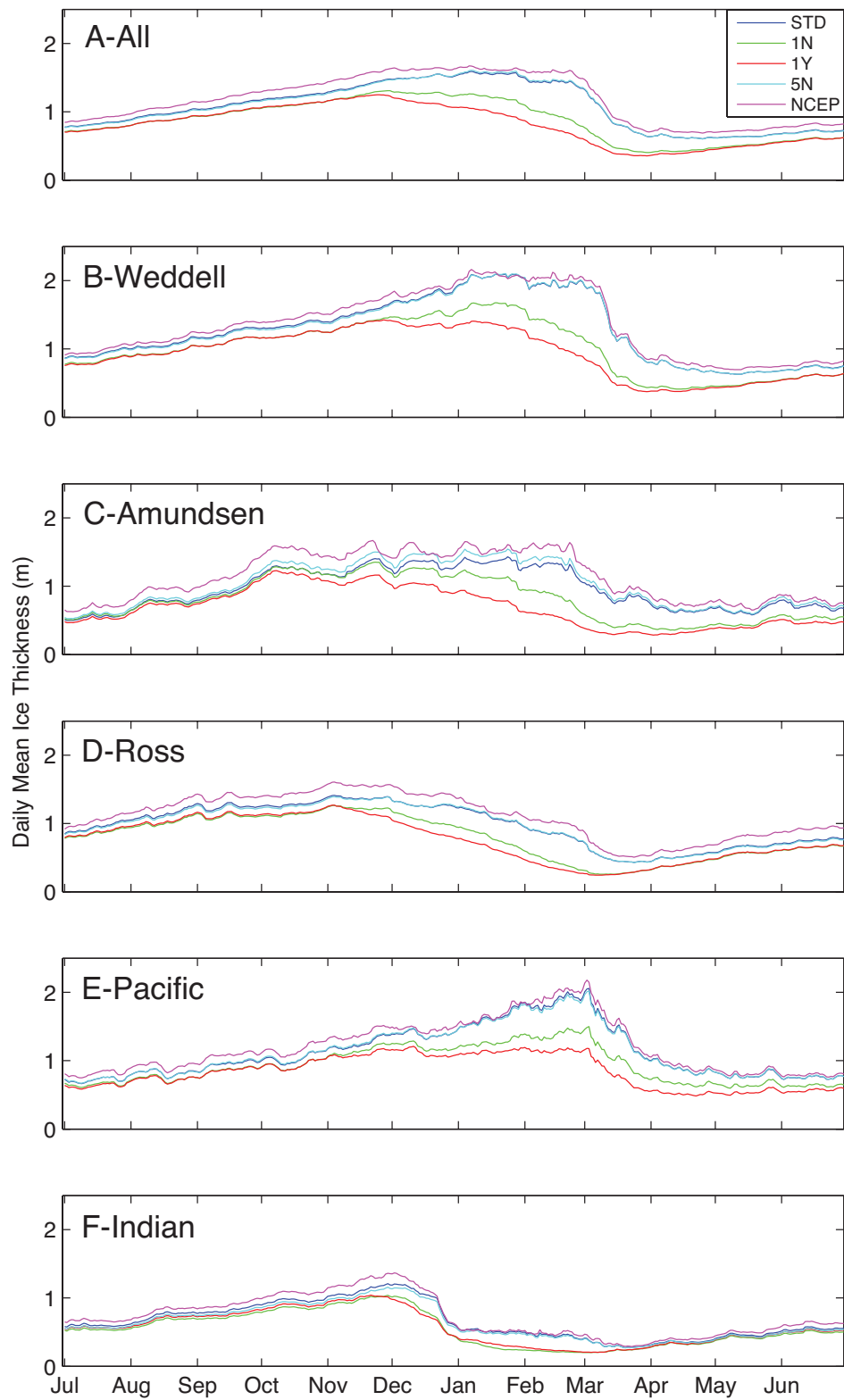


Figure 12. Time series plots of mean daily sea ice thickness from the entire model domain (A) and from different analysis sectors (B-F).

Table 10. SSM/I sea ice area and total ice presence (20% or greater SSM/I ice concentration)

<i>Units</i>	<i>All</i>	<i>Weddell</i>	<i>Amund -sen</i>	<i>Ross</i>	<i>Pacific</i>	<i>Indian</i>
Max. Area	10^6 km^2	14.02	5.52	1.87	3.43	1.53
Presence ¹ <i>fraction</i>	$10^8 \text{ km}^2 \text{ yr}^{-1}$	29.36	11.80	2.87	7.68	2.63
		1.00	0.40	0.10	0.26	0.09
						0.15

¹ Ice presence the integration of daily sea ice extent, and as a measurement captured both the ice extent, and how long it persisted.

accumulation; however, when areas moderate snow accumulation overlaps with very cold ice, such as in the eastern Ross and western Weddell sectors, snow ice production is curtailed (Figures 9, 10C, 13).

Snow ice production was extremely variable between model runs (Table 9), being lowest in the 1N run, which was only 25% of that in the STND run. Because the STD is included in the 1Y model run, the magnitude of total snow ice growth is very close to the STND model, although the timing is very different (Figure 14). The IY run produces less snow ice overall than the STND run throughout the winter, but a large pulse of snow ice is generated in November-December. In all model runs, snow ice production peaks during September-December. These peaks are tied in part to the maximal sea ice extent in September-October, although the area-normalized snow ice production rate (not shown) peaks during summer and shifts the period of maximal snow ice production toward summer.

The SS run produces slightly less snow ice in every sector than the STND run due to its slightly lower mean snow thickness. Snow ice production in the NCEP run is slightly lower than in the STND run as well, but in the NCEP run, snow is thicker on average. Thicker snow in the NCEP run is offset by thicker and colder congelation ice that is more difficult to flood (Table 9; Figure 10B,C).

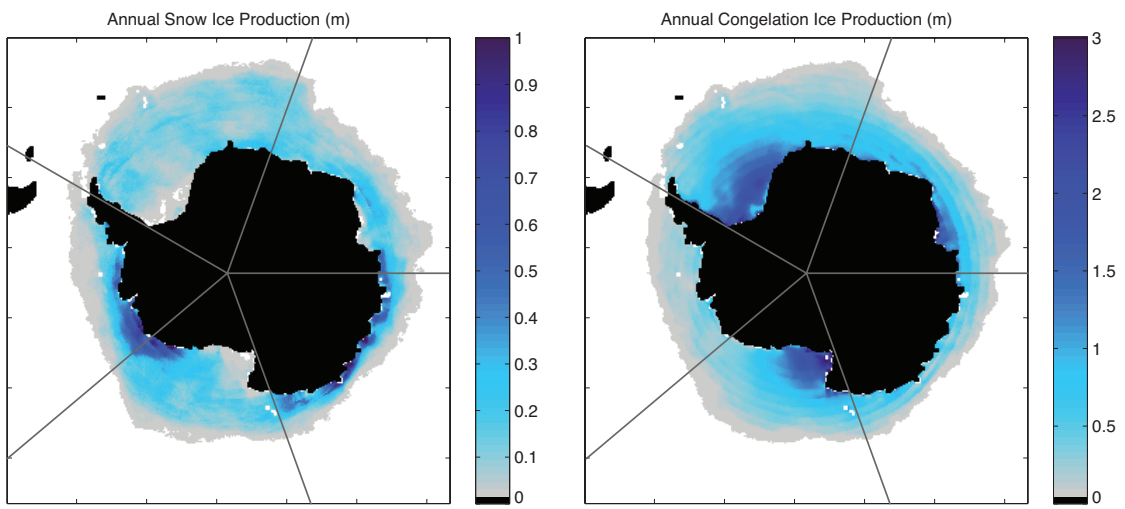


Figure 13. Spatial distribution of annual snow ice and congelation ice production the STND run. Note the scale of the congelation ice map is 3X that of the snow ice map.

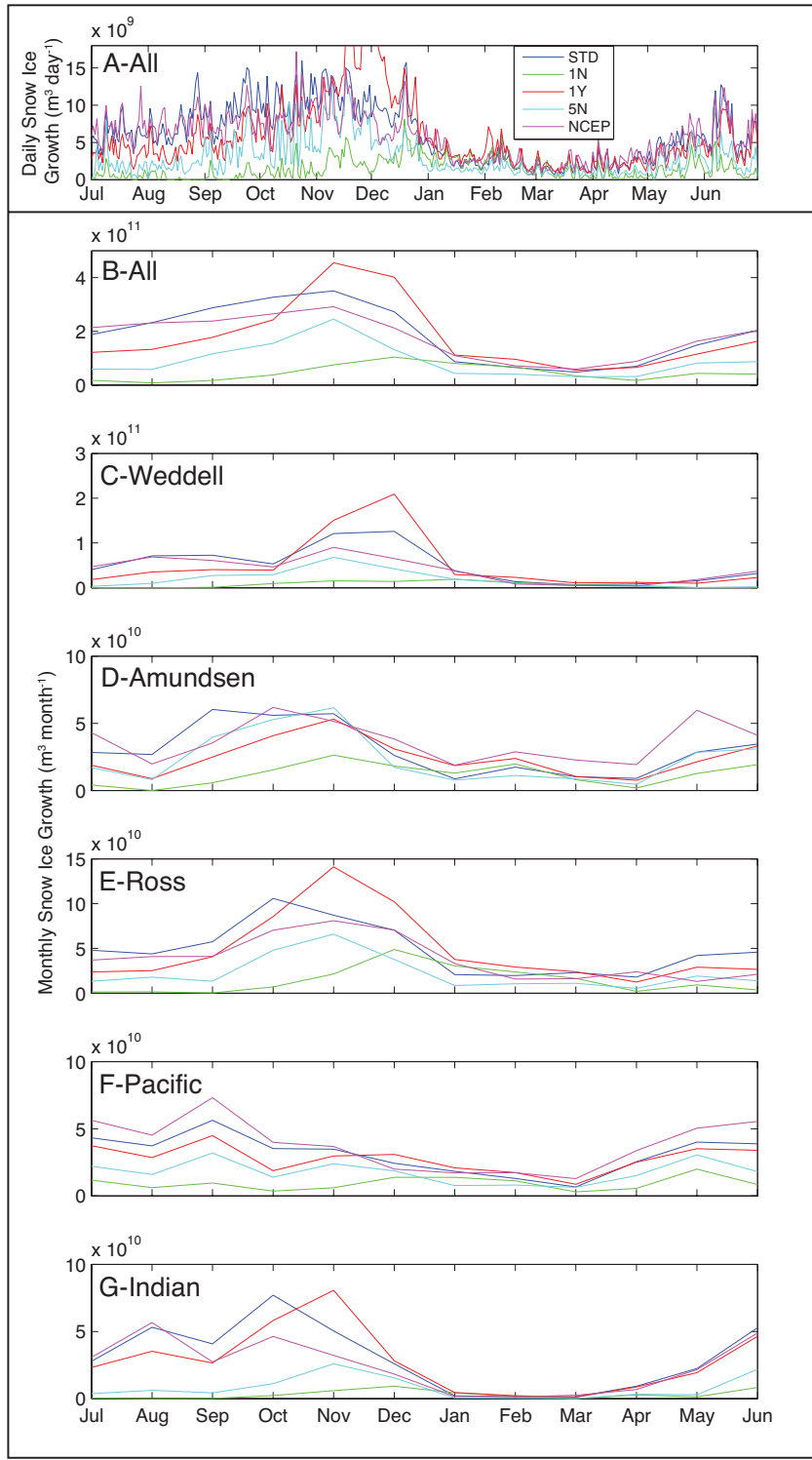


Figure 14. Time series plots of total daily (A) and monthly (B-G) snow ice production for select model runs. Daily snow ice growth is plotted to illustrate the extreme temporal variability of this process. Monthly sums are used in plots B-G to facilitate comparison between model runs. Total sector sums are presented in plots C-G, which have different scales.

Congelation ice. Congelation ice production varied between runs by approximately the same magnitude as snow ice production ($\sim 18 \times 10^{11} \text{ m}^3$). However, total snow ice production is overall much smaller, equivalent to only 8-25% of total congelation ice production (Table 9). Furthermore, variation in congelation ice production is very high between sectors. In the STND run, the Weddell Sector accounts for 45% of congelation ice production while the Amundsen sector accounts for just 4%. Congelation ice production is related to the mean snow/ice interface temperature, with colder regions, as indicated by mean snow/ice interface temperature, being responsible for the vast majority of congelation ice production (Figures 10C and 13).

Model runs 1N and 1Y that use a single ice category produced 22% and 20% less total congelation ice volume, respectively, than the STND run. Thin ice, which is underrepresented when using a single ice category but is well resolved in the STND run and other runs, is able to grow more quickly under cold conditions. Higher freezing rates in the runs using the ITD routine leads to higher congelation ice volumes. The 5N run exhibited somewhat reduced congelation ice growth in all sectors compared to the STND run, which is a consequence of not using the STD in the 5N run. The NCEP run grew 32% more congelation ice than the STND run, due to its lower temperatures, with substantial increases in all sectors. Congelation ice growth in the SS run was virtually indistinguishable from the STND run (Table 9).

Total daily congelation ice production showed markedly less variability than total daily snow ice production (Figures 14, 15). Variability in congelation ice production is related to the passing of cold fronts and weather systems that persist longer, and typically affect a larger area than surface flooding events. Total congelation ice production peaks in July or August in all sectors except the Weddell, where peak production is in June. In contrast to snow ice production, the rate of congelation ice

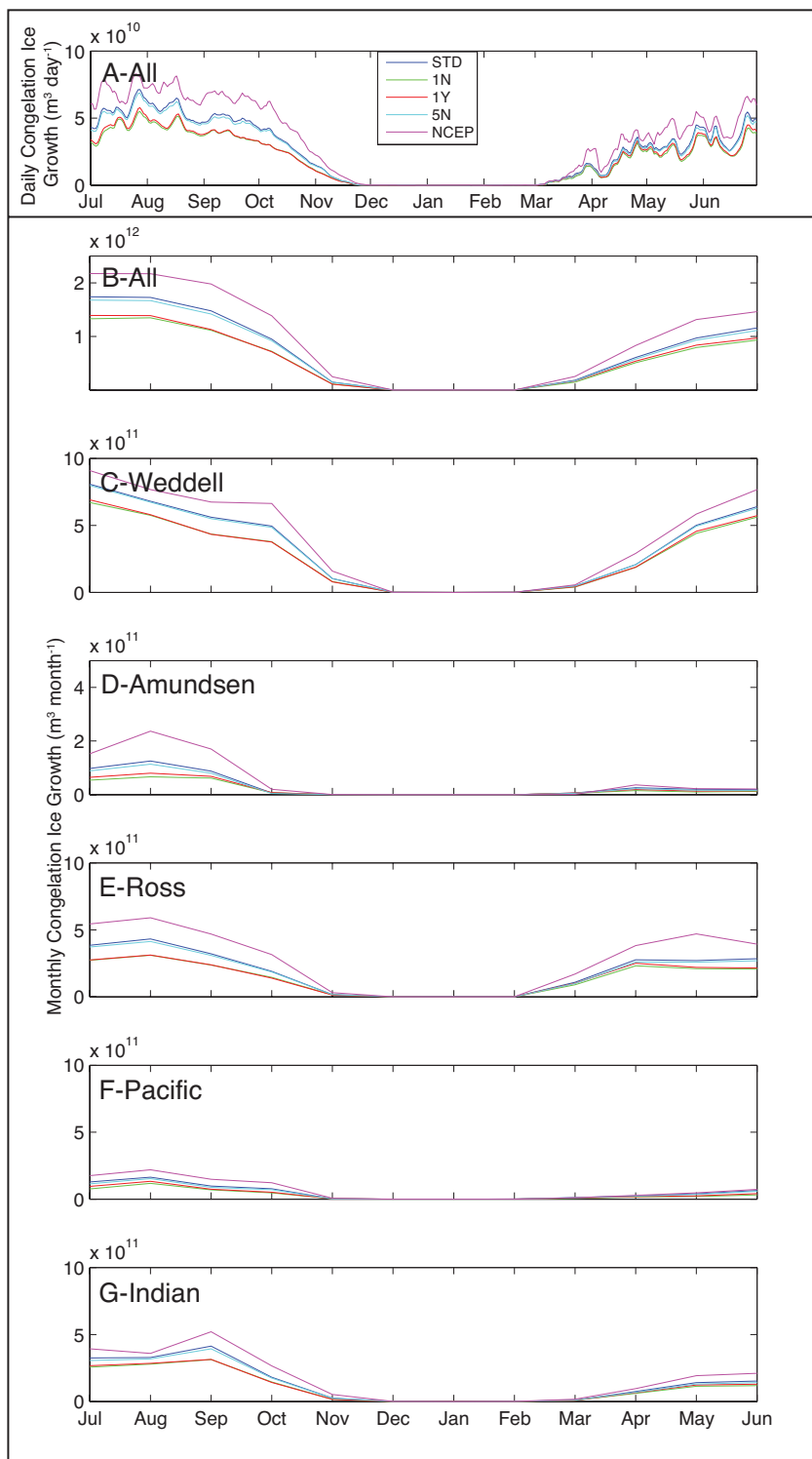


Figure 15. Time series plots of total daily (A) and monthly (B-G) congelation ice production for select model runs. Daily congelation ice growth is plotted to illustrate the extreme temporal variability of this process. Monthly sums are used in plots B-G to facilitate comparison between model runs. Total sector sums are presented in plots C-G, which have different scales.

production peaks before or during the peak in ice extent, in response to the coldest periods of the winter (not shown). There is very little variation in the timing of congelation ice production between model runs.

Growth of new ice over previously open water, which we assume is frazil ice in the model, constitutes 8.7% of ice production in the STND run. This is the result of initializing new areal ice extent (as indicated via SSM/I ice concentration) with 0.2 m of ice with a porosity fraction of 0.5. Because the amount of new ice is specified by the forcing data (with exceptions – see section 2.8), the volume of frazil ice production does not change significantly between model runs and is reported only once (Table 9).

5.5. Snow/Ice Temperature

The snow/ice interface temperature depends on the heat flux from the ice and through any overlying snow to the atmosphere. As such, it captures the insulating effects of the snow cover as well as the atmospheric forcing to provide an integrated estimate of the thermal forcing on the sea ice ecosystem below. Mean daily grid cell snow/ice interface temperature from the STND run shows consistent patterns of temperature forcing across the ice pack, with extremely cold areas close to the Antarctic coast in the Weddell, Ross and parts of the Indian sectors, and relatively warm temperatures ($> -5^{\circ}\text{C}$) everywhere else (Figure 10C).

Snow/ice interface temperatures are lower in the 1N and 1Y runs than in the STND run due to the effects of using a single ice category to represent the mean ice thickness. Both young, thin ice (due to the proximity of the ice/snow interface to the warm seawater) and thick, old ice (due to associated thick, insulating snow cover) can have higher mean interface temperatures than if they were combined and modeled as a single ice type. Therefore, the inclusion of the ITD has the potential for higher

snow/ice interface temperatures under a regime of snow accumulation and new ice growth.

Both the 1N and 5N runs have elevated mean snow/ice interface temperatures along Antarctic coastlines compared to the STND run, excluding the southern Ross and Weddell sectors. These areas roughly correspond to areas of thick snow cover and high rates of snow ice growth (Figures 10A,C and 14). The cause of the relatively cooler temperatures in runs that include a STD is their greater amount of snow ice generation and consequent reduction in insulating snow cover.

The NCEP climatology caused a much higher heat flux from the ice and water to the atmosphere, resulting much lower snow/ice interface temperatures (Figure 10C, note different figure scale). These low temperatures are further illustrated in time series plots of the mean snow/ice surface and interface temperatures for the STND and NCEP runs (Figure 16). NCEP run temperatures are below the STND run temperatures almost all the time in all sectors, by as much as 9°C. The annual mean snow/ice interface temperature for the NCEP run (-7.53°C) is 1.44°C colder than that of the STND run (-6.09°C; Figure 16).

5.6. Ice Algal Dynamics

Annual primary production by ice algae in the seven different model runs integrated over the entire model domain ranged from 13.0 to 18.3 Tg C yr⁻¹. Interestingly, the STND run also produced the median total production value for the seven model runs at 15.9 Tg C yr⁻¹ (Table 11). Most of sea ice algal production occurs either in porous interior and surface layers or near the bottom at the ice/water interface. These vertically distinct habitats are often inhabited by different types of algae [Garrison 1991; Garrison et al. 2005], and are subject to radically different environmental conditions, even within in the same ice floe. Therefore, we have

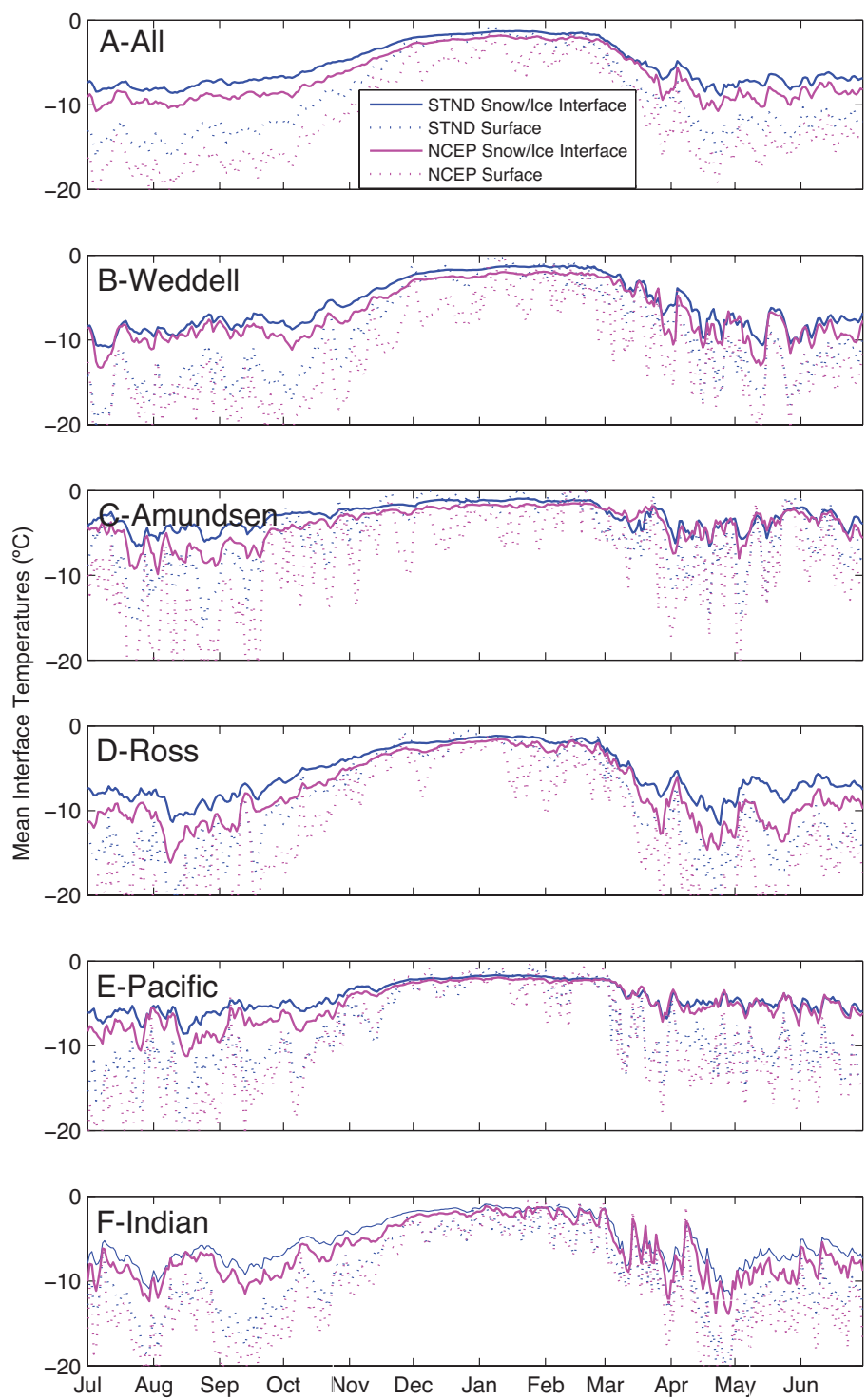


Figure 16. Comparison of mean surface and snow/ice interface temperatures over (A) the model domain and (B-F) analysis sectors for the STND and NCEP model runs. The model runs were identical except that the STND model run used the ECWMF Interim reanalysis, and the NCEP model used the NCEP/DOE II reanalysis, for purposes of atmospheric forcing.

Table 11. Annual Algal Productivity (Tg C)

<i>Model</i> <i>Run</i>	<i>location</i>	<i>All</i>	<i>Weddell</i>	<i>Amund-</i> <i>sen</i>	<i>Ross</i>	<i>Pacific</i>	<i>Indian</i>
STND	bottom	10.04	3.97	0.89	2.54	0.86	1.77
	interior	5.90	2.75	0.59	1.20	0.52	0.84
1N	bottom	9.39	4.45	0.70	1.90	0.70	1.64
	interior	6.42	2.73	0.88	1.36	0.74	0.71
1Y	bottom	11.16	5.03	0.84	2.38	0.93	1.98
	interior	7.16	2.76	1.01	1.71	0.78	0.91
5N	bottom	8.59	3.49	0.84	2.08	0.75	1.42
	interior	4.66	2.30	0.54	0.86	0.37	0.58
NCEP	bottom	10.63	3.97	1.06	2.88	0.80	1.91
	interior	5.60	2.68	0.50	1.22	0.50	0.70
NSC	bottom	7.76	3.50	0.55	1.64	0.66	1.42
	interior	5.34	2.33	0.52	1.19	0.49	0.82
SS	bottom	10.14	4.07	0.92	2.53	0.86	1.75
	interior	5.90	2.87	0.59	1.13	0.52	0.79

divided our analysis of production into two different vertical zones including bottom ice, which consists of the bottom 0.2 m of the ice pack, and interior ice, which is located >0.2 m above the ice/water interface.

Bottom ice algal production exceeded interior ice algal production in all model runs except the NSC run where nutrients were prevented from exchanging with underlying seawater in interior high-brine fraction sea ice layers. From a total ice volume perspective, the dominance of bottom ice algal production remarkable since the volume of interior ice is much greater on average than that of bottom ice, as we have defined them here. Interior ice algal production averaged 37% of total depth-integrated production over all model runs (excluding NSC) yet accounted for 82% of total ice volume, indicating that, on average, the bottom 0.2 m of ice is much more productive per unit volume than the remainder of the ice column. In the STND run, 37% of ice algal production occurred within the bottom 5 cm of ice, indicating that

even within the bottom ice (as we have defined it), habitats closer to the ice water interface were the most productive on average.

Interior Ice Production. In the STND run, interior ice accounted for 27% of total depth-integrated algal production over the model domain. Interior ice production was most important in the Weddell sector, which accounted for 47% of the interior ice algal production for the entire Antarctic ice pack, although all sectors contained significant amounts (Table 11). Total interior ice algal production was generally more evenly distributed across the ice pack compared to bottom production. Interior production ranged from 0.2-0.5 g C m⁻² yr⁻¹, with notably higher production in the northern Weddell and western Amundsen/eastern Ross sectors, as well as in pockets along the coastline in the Pacific sector (Figure 10E). Interior algal production peaked in November in the Ross, Indian, and Pacific sectors (Figure 17). In the Weddell sector, interior ice algal production peaked a month later, while in the Amundsen, it peaked a month earlier.

The 1N and 1Y runs show higher interior algae production than the STND run, particularly in areas of thicker ice (Figure 10B,E). Snow ice production was more highly concentrated during the spring and summer algal growth season in the 1N and 1Y runs, creating more habitat for interior algal growth during late springtime when light was available (Figures 14 and 18). The distribution of interior ice algal production in the 1Y run is similar to the 1N run, except for additional interior production in areas of very thick snow and ice (Figure 9D). Furthermore, in areas subject to flooding, the 1N and 1Y runs have relatively thinner snow than the STND run, allowing light to reach the interior ice algal community earlier in the springtime, facilitating higher algal growth rates and a longer growing season than in the STND model.

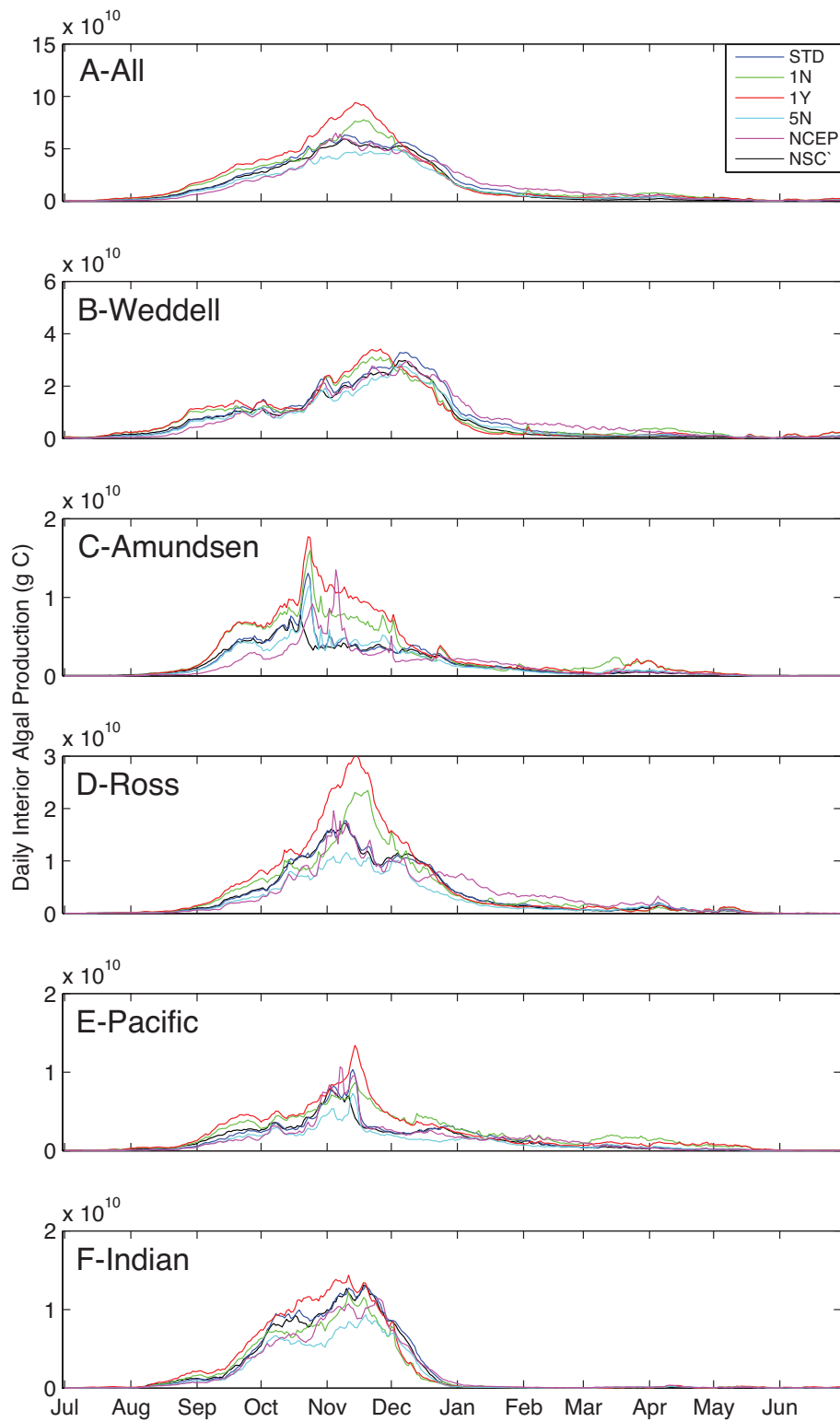


Figure 17. Daily interior (>0.2 m above ice bottom) ice algae production over (A) the entire model domain and (B-F) different analysis sectors for select model runs. Note difference scales between sector plots.

In the NCEP run, shifts in precipitation patterns and ice thickness (compared to the STND run) cause flooding to be focused in areas different from the STND run, leading to a modified interior ice algal production distribution. Gains in production over the STND run are apparent in areas of higher mean snow thickness, although this effect is mitigated where colder NCEP temperatures produce thicker ice that is more difficult to flood. The combination of thick ice and cold temperatures in the NCEP run means that there is not much gain overall in the magnitude of snow ice creation or interior ice algal production over the STND run, even in regions of the NCEP run with higher precipitation (Figures 10C-D and 13).

Algal interior production in the 5N run was similar to that in the STND run, except for some distinct patches under thick snow. These patches coincide with moderate snow ice production in the STND model (Figures 10E, 13). Surface flooding is greatly reduced in these areas in the 5N run, leading to a reduced amount of quality interior algal habitat compared to the STND run. However, areas with very thick snow and high snow ice production were common to both model runs, resulting in similarly levels of snow ice production and interior ice algal production (not shown).

The NSC run shows a 10% reduction of interior algal production compared to the STND run (Table 11). By preventing the exchange of nutrients with the water column during vigorous convective desalination of high-brine fraction sea ice in the NSC run [Chapter 1], growth of interior algal communities was truncated through earlier onset of nutrient limitation. Reduction of interior algal production compared to the STND was evident across all sectors (Table 11), and at most times during the algal growth season (Figure 17).

Bottom Ice Production. Algal production in bottom ice integrated spatially over the entire model domain ranged from 8.48 to 11.2 Tg C yr⁻¹ for all seven model runs and accounted for 59-65% of total depth-integrated ice algal production (Table 11).

Compared to the distribution of interior ice algal production, the distribution of bottom ice algal production was much more patchy (Figure 10D). In general, the spatial distribution of bottom algal production does not correspond to any particular class of ice; rather a specific set of environmental conditions is required to generate a bottom algal bloom. Because the bottom of the ice pack can respond quickly to changes in atmospheric forcing, bottom ice melt or accretion that may restrict or promote algae growth may arise ephemerally, and with less spatial predictability, than conditions optimal for interior ice algal production.

Daily bottom ice algal production reaches its annual peak in November in all sectors in all model runs. In the Ross, Amundsen, and Pacific sectors, bottom ice algal production is punctuated by positive spikes that correspond to cold fronts that bring lowered atmospheric temperatures, new ice accretion, and convective nutrient delivery. In the STND run, the Amundsen and Ross sectors contain sizeable autumn (March-July) blooms of bottom sea ice algae that constitute 28% and 23%, respectively, of the total annual bottom ice production in those sectors. The most productive sea ice type per unit area was autumn pack ice located in the Amundsen, Ross, and Indian sectors. However, the limited extent of autumn ice reduced its contribution to 13% of total bottom algal production in the STND run (Figure 18).

Model run 1N, despite having lower mean snow thickness than the STND run, had only 6% less bottom ice algal production. However, the spatial distribution of bottom algal production was very different between the two runs, with both higher production in the northern reaches of the ice pack and lower production toward the Antarctic continent in the 1N run (Figure 10D). Examination of the 1N run snow thickness anomaly map (Figure 10A) shows that snow was actually thicker than in the STND run over a majority of the ice pack, leading to higher light limitation and reduced production compared to the STND run. The 1Y run has a similar spatial pattern of

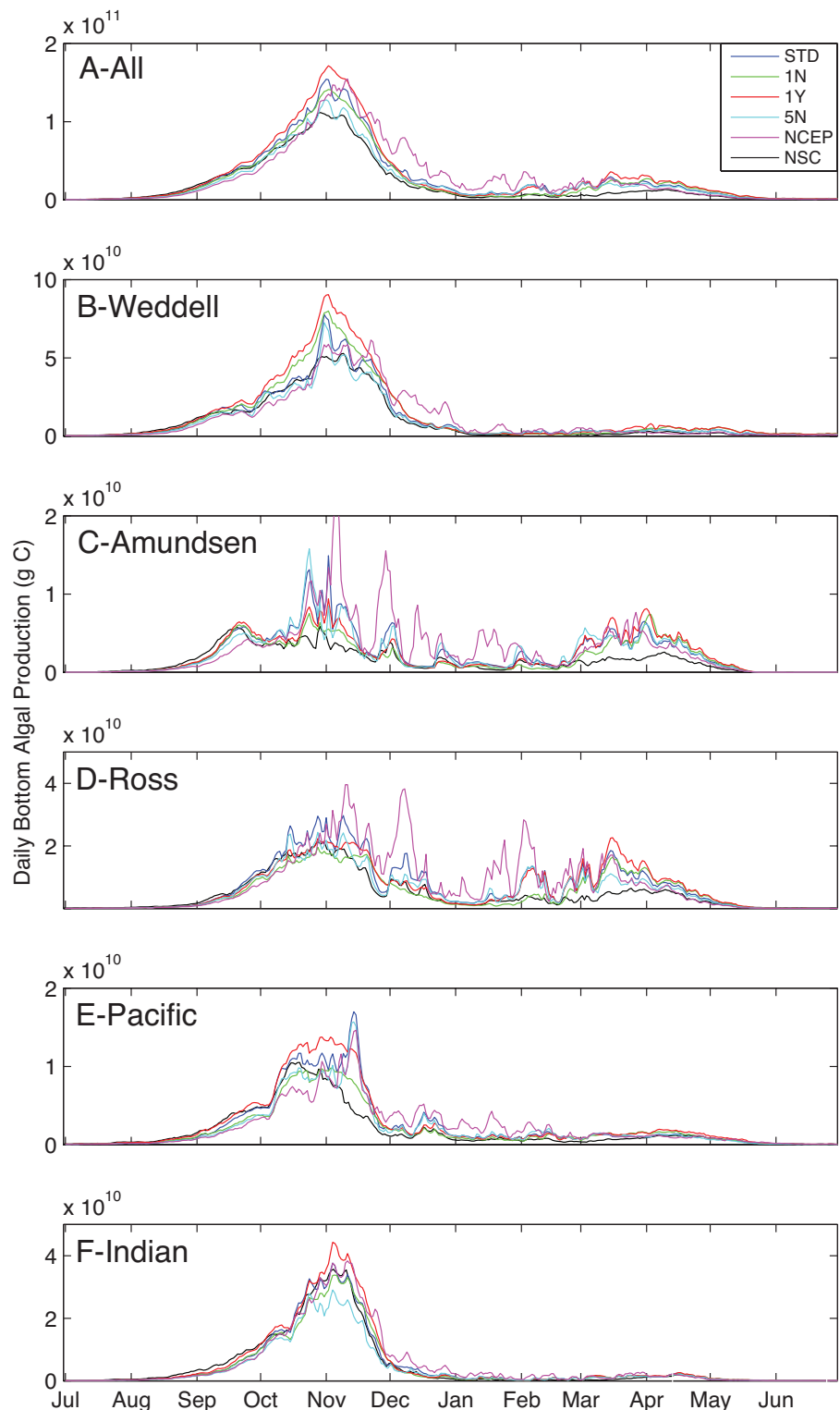


Figure 18. Daily bottom (up to 0.2 m from ice bottom) ice algae production over (A) the entire model domain and (B-F) different analysis sectors for select model runs. Note difference scales between sector plots.

bottom algal production to the 1N run (Figure 10D), but was 11% more productive than the STND run (Table 8). The inclusion of the STD in the 1Y run reduced mean snow depths compared to the 1N run (and STND run, regionally), allowing enhanced production through earlier and increased light transmission to bottom ice algae.

Bottom ice algal production in the 5N run is 15% less than in the STND run. This difference between runs is largely confined to areas of moderate snow and ice thickness, where the use of the STD in the STND run allows a percentage of the grid cell (after a surface flooding event) to have a reduced snow thickness relative to the mean. With better access to light caused by reduced snow thickness, areas of moderate snow thickness are able to support higher bottom algal production in the STND run compared to the 5N run (Tables 9 and 11).

The NCEP model run exhibited large shifts in the optimum locations for bottom algal production compared to the STND run, yet maintained a similar annual magnitude. Shifts in the distribution of bottom algal production in the NCEP run appear to reflect shifts in the snow thickness distribution (Figure 10A,E).

Bottom algal production in the NSC run was 33% lower than in the STND run, which was a larger relative percentage decrease than exhibited by interior communities. Examination of total daily bottom algal production time series shows that summer and autumn peaks of STND run production are cut short in the NSC run (Figure 18). High-salinity ice in the bottom 20 cm of the ice pack undergoes considerable convective nutrient replenishment during punctuated freezing events during the warmer portions of the year, and the absence of this process curtails summer and autumn bottom production in NSC run. Bottom algal production in the SS run differed by less than 1% from the STND run (Table 11).

6. Discussion

6.1. Ice Thickness Distribution

Here we show that consideration of different ice thickness classes has the benefit of improved simulation of ice thickness distribution, resulting in the thicker ice and higher total heat flux from the ocean to the atmosphere [Bitz et al. 2001; Holland et al. 2006]. Our simulations are consistent with other studies in that our single ice category runs 1N and 1Y grow less congelation ice and have thinner mean ice thicknesses than runs utilizing the ITD. By using the ITD, proper high summertime ice thicknesses are maintained, which are more in line with ASPeCT observations.

Furthermore, the use of a sub-grid scale ITD has large consequences for the magnitude and distribution of sea ice production. Irrespective of snow thicknesses distribution, the annual volume of snow ice approximately doubled and the total ice volume production increased by 30% between the 1N and 5N runs, indicating that single-ice category sea ice models have the potential to severely underestimate the volume of ice frozen seasonally in the Antarctic sea ice pack. Where and when ice freezes impacts oceanic circulation via density-driven water column convection and bottom water formation, processes that have important implications for climate warming and the global carbon cycle [Orsi et al. 1997].

The spatial distribution of peak sea ice algal production changed markedly as a result of the use of an ITD in the sea ice model. Changes to the distribution of interior ice algal production were linked primarily to shifts in the distribution of snow ice formation, which is in turn sensitive to ice thickness. In the model runs using the ITD, interior ice algal production was patchier in distribution and was distributed across a larger area of the ice pack. Such patterns of algal growth and snow ice formation fit with observations, where locally patchy areas of the sea ice with either surface flooding or a slush layer are associated with increased rates of algal growth [Fritsen

2001, Garrison et al. 2003]. The distribution of bottom ice algal production is also affected by the availability of light, which is in turn modified when using the ITD through changes in the distribution of snow and ice and, in particular, to an increase in the mean snow depth.

Use of the ITD also caused a shift in the vertical distribution of ice algal production, specifically from bottom towards more interior ice algal production. Since interior algal production is less accessible to larger organisms relative to bottom ice algae, the use of different ice parameterization can affect estimates of trophic transfer and food web dynamics in ecosystem models. Although our results show that different combinations of model parameterizations yield a similar amount of sea ice algal production when integrated over both space and time, it must be remembered that shifts in the temporal, vertical (bottom versus interior), and areal distribution of ice algal production is just as important as total integrated production, and can markedly impact sea ice ecology on regional and local scales. The timing of production in particular is very important in polar ecosystems, where the short growing season means organisms are highly sensitive to shifts in the availability of resources [Ainley et al. 2003]. The interior-most portions of pack ice are also unavailable to particular classes of organisms including marine mammals and birds that must surface to breathe [Ribic et al. 1991]. Small shifts in the regional timing of sea ice algal production between model runs may therefore lead to errors in estimations of habitat availability and quality for ice-obligate upper trophic level organisms.

6.2. Snow Thickness Distribution

The addition of a simple STD, that was used to calculate fractional grid cell flooding, followed by independent modeling the flooded and non-flooded ice fraction,

resulted in further positive changes to the modeled annual volume of sea ice. Snow production was effectively doubled when the SDT was used in conjunction with the ITD, and quadrupled when using a single ice category. Interestingly, the volume of congelation ice also increased as a result of adding the SDT, despite large amounts of latent heat added to the snow and ice by infiltrating seawater during snow ice production. The effect of lowering the mean thickness of insulating snow, as well as independent modeling of the non-flooded fraction of the snow distribution, causes a greater net heat flux from the ice to the atmosphere than in runs without the SDT. This enhanced heat flux negates more than compensates for the warming and extra latent heat associated with snow ice creation.

Snow ice accounted for 25% of annual Antarctic sea ice production in the STND run. This number falls within the 4-38% range of estimates of the contribution of snow ice to the total ice pack from isotopic analysis of ice cores [Eicken et al. 1994; Jeffries et al. 2001]. Snow ice was the dominant form of sea ice production in the southwest Amundsen sector, southeastern Ross sector, and in isolated coastal locations in the Pacific sectors. The importance of snow ice growth was demonstrated by Adolphs [1998] using repeated within-season visits to Ross sea pack ice. Despite its thick snow and perennial ice, snow ice contributed less to total ice production in the Weddell sector (15%) compared to the mean over the model domain. This result is consistent with observations of relatively low snow ice fractions in Weddell Sea compared to other regions, although it is several times larger than the actual estimate of 4% [Eicken et al. 1994]. Methods for determination of snow ice are not precise, however, and are subject to the same spatial and temporal biases of ice core sampling mentioned previously. Furthermore, brine convection may significantly reduce meteoric $\delta^{18}\text{O}$ signatures used to classify snow ice [Jeffries 2001], leading to an underestimation of snow ice production.

Use of the STD changed mean ice thicknesses very little when compared to the impact of adding an ITD or using the NCEP DOE climatology. Despite a 20% increase in total ice production, the mean ice thickness increased by less than 1% between the 5N and STND runs. The net balance in ice thickness requires that the extra ice production be offset by ice melt in the model. The spatial distributions between the 5N and STND run are also very similar, indicating that where extra snow ice was produced in the STND run compared to the 5N run, it was offset locally by additional ice melt. Apparently, the magnitude and timing of snow ice production in the STND run allows restoration to an equilibrium ice thickness.

Although snow ice production is offset by bottom melt, the freezing process creates dense brine that, upon leaving the sea ice, may enhance salt export to depth and influence the formation of Antarctic bottom water [Midttun 1985, Fritsen et al. 1994]. The use of an STD within coupled climate models has the potential to improve estimates of Southern Ocean circulation by providing more realistic estimates of snow ice growth and associated vertical salt fluxes.

6.3. Atmospheric Forcing

The noted differences in snow and ice thickness and the magnitude and distribution of algal production between the NCEP and STND runs illustrate the importance of surface forcing in simulations of sea ice physics and associated biology. The 6.7% higher total snowfall over ice in the NCEP reanalysis data, while significant, is less important than the large shift in the spatial distribution of precipitation (Figure 12), which leads to large differences in the patterns of snow distribution across the Antarctic ice pack. In terms of ice thickness, changes resulting from differences in snowfall between the two datasets were largely overshadowed by changes in the surface heat forcing in the NCEP run compared to the STND run. Thicker snow

should reduce congelation ice growth through greater insulation from the atmosphere, but production of congelation ice increased by 32% as result of cold ice temperatures, increasing the ice thickness in the coldest areas (Figure 10B,C). Shifts in the snow and ice distribution resulting from the use of different atmospheric forcing lead to very large changes in the temporal and spatial distribution of algal production, which has implications for analysis of ecosystem dynamics. For example, there is a significant shift toward greater bottom ice algal production coincident with a decrease in interior ice algal production in the sea ice pack west of the Antarctic Peninsula (extreme east of Amundsen sector) in the NCEP run versus the STND run (Figure 10D-E). This area is known as spawning habitat for what is considered the largest Antarctic krill population [Quetin and Ross 2003; Hoffman et al. 2004], and ice algae are considered an important food resource for larval krill [Daly et al. 1990]. Because of a shift toward accessible bottom ice algae growth and away from less accessible interior algal growth occurs, different conclusions about the quality of krill habitat could be drawn based on the use of different atmospheric forcing data.

6.4. Snow Physics

Exclusion of processes of snow melt-related physics, including superimposed ice, melt water percolation, and surface ice drainage, had a limited effect on annual mean ice and snow thickness. Superimposed ice formation (considered as snow layers in the model) should make it harder to melt snow completely, and there is a corresponding slight decrease in snow thickness, as well as snow ice production, between the STND and SS runs (Table 8,9). Differences in snow thickness and snow ice production are largest in the Weddell sea, which is not surprising since this sector contains the highest amount of summer sea ice where melt processes are likely to be important.

Overall, snow melt is rather limited across the Antarctic snow pack, which avoids

complete melt on multi-year ice floes [Andreas and Ackley 1982; Massom et al. 2001]. Consequently, we might expect the changes in SS run to have little effect on model results. However, these processes dominate summertime ice physics in the Arctic where snow over sea ice often completely melts [Andreas and Ackley 1982]. Therefore, small effects in the Antarctic should not be used to justify the exclusion of snow melt processes in simulation of Arctic sea ice.

6.5. Convective Nutrient Replenishment

The NSC run tested the effect of convective desalination and brine exchange in porous ice types on the growth of algal communities. If convection in porous sea ice is small in magnitude or a rare event, then ice algal production should be mainly fueled by nutrients present in infiltrating brine or seawater during the initial creation of the ice algal habitat. In contrast, if massive convection and nutrient replenishment is required to support ice algal production, then removing this nutrient source should decrease modeled algal production significantly. Based on the overall 18% reduction in total production in the NSC run, nutrients that had been entrained initially, either via bottom ice accretion or snow ice creation, supplied the majority (82%) of nutrients for annual sea ice algal growth. Convective nutrient exchange as tested here depends on the intersection of available slush layers and freezing events. Therefore, under different atmospheric forcing or during different years, the relative importance of slush ice desalination and nutrient convection may vary. Reductions in algal production in the NSC run were largest in bottom algal communities during summer and autumn, suggesting that algae in these habitats experience significant nutrient limitation. Models that ignore seawater mixing and brine convection during freezing of porous ice layers have the potential to underestimate sea ice algal production.

6.5 Sea Ice Ecology

Comparison to previous results. Total annual sea ice algal production in the STND run ($15.94 \text{ Tg C yr}^{-1}$) is substantially lower than previous estimates of production for the Antarctic ice pack ($35\text{--}70 \text{ Tg C yr}^{-1}$ [Legendre et al. 1992; Arrigo et al. 1997, 1998, Lizotte 2001]). In contrast to previous estimates, our model accounts for both large and small-scale physical and chemical processes known to affect sea ice algal growth and performs dynamic estimation of algal production. Therefore, our model results are likely to be a more accurate estimate of Antarctic sea ice production. Furthermore, our model results have been corroborated using biomass observations of Antarctic sea ice algae, whose mean values generally fall within the range of seasonal mean algal biomass produced in the STND model run (Chapter 1).

Previous estimates of total sea ice algal production based in extrapolations made from in situ data may be too high, in part due to their reliance on early biomass measurements [e.g. Burkholder and Mandelli 1965] that were based on what we now know were extremely large algal blooms, as compared to more recent and more widespread estimates of mean sea ice algal biomass [Dieckmann et al. 1998; McMinn et al. 2007]. Therefore, it is likely that actual production is likely lower than these early predictions, and more in line with our modeled production estimates. In addition, earlier modeling studies by Arrigo et al. [1997, 1998] included sea ice flooding without dynamic ice growth to re-freeze resulting slush, and assumed that nutrients were replete in porous ice, assumptions that lead to longer and more productive algal blooms in interior ice.

Simplifying model assumptions. Even though our model includes relatively complex parameterizations of sea ice and snow structure and physics, some types of sea ice (e.g. land-fast and platelet) and some physical process had to be ignored, likely resulting in slight underestimation of total annual production in the Antarctic ice pack.

For example, sea ice algal biomass at the edges of ice floes can be enhanced compared to the ice floe interior, presumably due to increased access to light and nutrients [McMinn and Hegseth 2003]. The ratio of the floe edge size to total interior floe area varies widely based on the size of the floe, complicating estimation of the relative abundance of this ice type. Steer et al [2008] estimated ice edge habitat to constituted 7-13% of total summertime ice floe area from two aerial surveys. Given this edge area, and assuming that ice algal production at the floe edge is triple that of the interior, excluding ice floe edge habitat in our model could underestimate total sea ice algal production by 14-26%. On the other hand, Ambrose et al. [2005] detected lower bottom ice algae pigments toward the edges of ice floes, indicating complex ice-edge process may enhance or degrade ice algal habitat.

In addition, land-fast ice, which represents 1-2% of total Antarctic ice pack, can contain ice algal concentrations an order magnitude higher than pack ice with correspondingly higher rates of production [Legendre et la. 1992, Lizotte et al. 2001; Arrigo 2003]. Due to masking of coastal grid cells, our model likely excludes a large fraction of land fast ice. If the model neglects 50% of a total fast ice area that is 2% of the total ice pack, and assuming that production is 10 times greater than the mean for the rest of the pack, there is potential for a 10% underestimation of total algal production in the Antarctic ice pack by the model. Often associated with land-fast ice is platelet ice, which harbors the highest concentrations of sea ice algae yet observed [Arrigo 2003]. Platelet ice consists of a layer of loosely consolidated ice crystals containing ~80% brine by volume that accumulate on the underside of congelation ice [Grossi et al. 1987; Arrigo et al. 1993]. Although this ice type is neglected in the model, the total amount of platelet production is likely to be small since this ice type is restricted to areas adjacent to floating ice shelves [Bindschadler 1990; Kipfstuhl 1991; Arrigo 2003].

Spatial variability. Variability in total annual sea ice algal production in each sector depends to the first order on both the sea ice extent and duration in that sector. However, the actual distribution of algal production varies at much smaller spatial scales, reflective of the control of ice algal growth by small-scale variability in local sea ice characteristics. Surprisingly, despite the similarity between model runs in total annual algal production over the model domain, small-scale patterns of sea ice algal production were highly variable between model runs. This variability is due to the complex interactions between atmospheric forcing, different combinations of ice and snow, and sea ice radiative transfer and thermodynamics and how these combine to define the habitat available for sea ice algal growth. As distributions of ice and snow thicknesses change between different model runs, so do the locations optimal for algal growth. This phenomena is most easily observed in the northwest Weddell sector, where conditions are optimal for interior algal growth, leading to a band of high annual production (Figure 10E). This band shifts intact north or south in different model runs, following similar band-like changes in the snow and ice thickness distributions (Figure 10A-B,E).

It is interesting to note that despite the variability in ice physics between different model runs, and the spatial distribution of sea ice algal production, total annual algal production varied by no more than 17% among model runs (excluding NSC and SS runs). Based on these results, physical changes to sea ice algal habitat caused by inclusion of the ITD and STD do not appear to be primary factors controlling total sea ice algal production when examined at the hemispheric or annual scale. However, sea ice algal production shows dramatic regional variability as a result of these more sophisticated representations of ice and snow. Control of sea ice algal production is driven locally by changes in ice characteristic predicted by the individual vertical ice models in each grid cell, as evidenced by the NSC run where modified nutrient

dynamics caused the difference in total algal production from the STND run. As such, improving the vertical representation of sea ice algal habitat in three-dimensional models would likely benefit study of sea ice algal dynamics to a greater extent than attempting to reproduce ice pack heterogeneity through the use of ITD or SDT methods.

6.6. Conclusions

Use of different snow and ice modeling parameterization has a large effect on ice pack physics, which in turns drives large differences in simulated sea ice ecosystem dynamics. Without an ITD, mean ice and snow thickness is lower and bottom sea ice algal production is increased relative to model runs with an ITD. Use of the SDT can greatly enhance sea ice formation, especially in the form of snow ice growth, and permits greater sea ice algal production within interior communities. The use of an SDT has a relatively minor effect on mean ice thickness since snow ice growth is largely offset by bottom ice melt. Atmospheric forcing from different reanalysis data sets cause mean and regional shifts in sea ice production and associated ecology, even when sea extent and motion is controlled. Snow cover represents a first-order control on ice algal production by limiting the light available to bottom ice algal communities, and changes to the regional, rather than mean, snow thickness due to the use of different ice and snow representation are responsible for large differences in the magnitude and distribution of sea ice algal production. Improved convective nutrient exchange in high-brine fraction (slush) sea ice [Chapter 1] is responsible for up to 18% of total sea ice algal production. Despite large differences in the vertical and horizontal distributions of ice algal production within the Antarctic ice pack for the seven model runs examined here, total annual sea ice algal production was predicted by ice presence, and was surprisingly constant between years. Future studies of sea ice

algae should consider using ITD and SDT methods when examining the spatial distribution of sea ice algae.

CHAPTER 3

Spatial and temporal Antarctic sea ice algal dynamics

1. Introduction

Sea ice seasonally covers over 7% of the Earth's surface and constitutes a marine biome roughly equivalent in area to the world's continental shelves. Primary production in the sea ice ecosystem is accomplished by sea ice algae, which grow attached to ice crystals and in liquid brine inclusions within the sea ice matrix that forms as a consequence of the sea ice freezing process [Horner et al. 1992; Krembs et al. 2001; Janech et al. 2006]. Sea ice algae are capable of attaining volumetric biomass concentrations over an order of magnitude higher than is observed for water column algal blooms and frequently visibly color ice floes [Fristen et al. 1994].

Due primarily to the timing and location of their blooms, sea ice algae may considerably influence biotic and abiotic processes in polar marine ecosystems. Sea ice algae are able to grow under seasonal conditions that concurrently severely limit photosynthesis in the water column below and, as such, may represent an important resource for higher trophic level marine organisms during the long polar winter [Siegel and Loeb 1995; Quetin et al. 1996]. Survival of the early life stages of Antarctic krill, a keystone species in the Antarctic food web, is correlated with sea ice cover [Guzman 1983, Daly and Macaulay 1988, Marschall 1988, Smetacek et al. 1990, Loeb et al. 1997], and larval krill have been shown to require a winter food source to prevent starvation [Daly 1990]. Ice algae are often the same species that form water column blooms after the retreat of sea ice cover; therefore, algae released from melting ice may 'seed' phytoplankton blooms [Smith and Nelson 1985; Garrison et al. 1987; Arrigo 2003]. Finally, as net consumers of inorganic carbon, sea ice algae

may affect the cycling of carbon in polar oceans. Under the rectification hypothesis, spring ice algal blooms, in conjunction with ice-edge water column blooms, may lower the CO₂ concentration of waters underlying the ice to below saturation before significant exchange with the atmosphere is possible after ice retreat. In this way, sea ice algae have been proposed to prevent outgassing from high CO₂ water generated during winter [Yager et al. 1995].

Despite these hints of their importance, little is known about the total magnitude or spatial and temporal variability of sea ice algal production. The difficulty of obtaining biological measurements in sea ice has necessitated a theoretical approach to study this ecosystem on a large scale, guided by regional observations, when available. Most previous estimates of Antarctic sea ice algal production were made by extrapolating a limited number of sea ice algal biomass measurements to the entire ice pack, using mean ice conditions to characterize the sea ice. Over the years, estimates of annual ice algal productivity in the Antarctic that have been made using this approach have risen, from 0.03 Tg C yr⁻¹ [Bunt 1968] to 50-70 Tg C yr⁻¹ [Heywood and Whitaker 1984; Legendre et al. 1992; Lizotte 2001] as a greater number of sea ice samples became available showing a high algal biomass. Productivity estimates like these depend on both the types of ice included in the calculation and the productivity of each ice type. However, observed sea ice algal biomass and physical sea ice conditions are extremely heterogeneous over scales ranging from tens of km to less than a cm in the vertical dimension [Wadhams et al. 1987; Eicken et al. 1991; Massom et al. 2001; Garrison et al. 2005]. This variability, combined with constant evolution of the ice pack, severely reduces the possibility that a description of the mean sea ice state, and its habitability to algae, is widely representative of actual sea ice conditions.

Ice algal growth is controlled by temperature, salinity, light, and nutrient availability of the local sea ice habitat [Arrigo and Sullivan 1994]. Therefore,

estimates of the spatial and temporal distributions of sea ice algal production require consideration of the distribution and temporal variability in the physicochemical characteristics of sea ice. Arrigo et al. [1997, 1998] recognized that snow drives much of the horizontal variability in the Antarctic ice pack and developed a coupled biological/physical sea ice model that incorporated estimates of snow depth over sea ice generated from satellite passive microwave measurements [Arrigo et al 1996]. This model generated temporal and spatial estimates of seawater surface flooding, a process that can generate large blooms of sea ice algae when nutrient-rich seawater is introduced to the relatively well-lit sea ice surface [Ackley et al. 1979; Garrison and Buck 1991; Ackley and Sullivan 1994; Fritsen et al. 1994]. Neglecting algal growth in the ice below these surface layers, Arrigo et al. [1997; 1998] estimated that a total of 35.7 Tg C yr⁻¹ was fixed by ice algae during a typical growth season. Flooding was calculated using a static model of ice, however, which neglected ice growth and other important processes related to brine physics and ice thermodynamics that can either curtail or enhance ice algal blooms, depending upon the atmospheric and oceanic forcing upon the sea ice [Fritsen et al. 1994; Ackley et al. 1996; Chapter 1]. Furthermore, enhanced algal production at the bottom of the ice pack, near the ice-seawater interface, has since been determined to be a significant feature across Antarctic pack ice [McMinn and Hegseth 2003].

Here, we present new hemispheric estimates of Antarctic sea ice algal dynamics and production for the years 1996-2006 using a coupled biological/physical model of sea ice that assimilates relevant sea ice satellite observations. For the first time, we have included dynamic, thermodynamic, and hydrodynamic processes necessary to simulate the vertical distribution and evolution of sea ice characteristics that include salinity, porosity, nutrient flux, and spectral light availability into a global-scale model. Real-time estimates of the sea ice state and sub-grid scale snow and ice

thickness distributions permit the development of a heterogeneous pattern of simulated sea ice algal growth in our model [Chapter 2]. We describe the results across ten modeled years in an effort to capture interannual variability, using forcing data from 1996-2006.

2. Methods

2.1. Model description

The model employed in this study is described in detail in Chapters 1 and 2. Here we briefly present model features most salient to estimation of large-scale sea ice algal production. The ice temperature dictates the maximum algal growth rate [Epply 1972; Bissinger et al. 2008] and determines brine salinity (assuming the ice and brine are in thermal equilibrium), an important factor controlling algal growth within the ice interior [Arrigo and Sullivan 1992; Arrigo et al. 1994]. We take care to accurately simulate changes in ice temperature via the inclusion of temperature-, salinity-, and porosity-dependent parameterizations of thermal conductivity and heat capacity of ice [Bitz et al. 1999; Pringle et al. 2007; Chapter 1]. Enhanced vertical resolution and adaptive model time stepping at the boundaries between the atmosphere, snow, ice, and ocean ensure that physicochemical characteristics change at the appropriate temporal and spatial scale [Pogson et al. 2011; Chapter 2]. Because nutrient limitation of algae is observed within sea ice [Maestrini et al. 1986; Gosselin et al. 1990; McMinn et al. 1999], the model calculates desalination-related convective brine and seawater fluxes to transport nutrients and other tracers [Fritsen et al. 1994; Ackley et al. 1996; Chapter 1]. Snow cover modulates the light available to algae in the sea ice below and provides thermal insulation that affects freezing and melting rates of the ice. Snow can also transform the sea ice directly, either through creation of snow ice following flooding of the snow cover or during snow melt when runoff can either form

superimposed fresh ice layers or percolate through the sea ice and replace saltier brine [Massom et al. 2001; Arrigo 2003]. The model considers these transformative snow processes and utilizes a two-stream model of light transmission using 32 wavelength bins to estimate both the magnitude and spectral quality of solar radiation within the snow and sea ice [Briglieb and Light 2007; Chapter 1].

The mobile ice pack exposes ice algae to varying conditions that depend on the specific path taken by sea ice as it is advected by the wind and prevailing currents. Dynamic ice movement is assimilated into the model using Special Sensor Microwave Imager (SSM/I) satellite-based estimates of ice motion and ice concentration available from the National Snow/Ice Data Center (NSIDC) [Nolin et al. 1998; Heil et al. 2006]. Changes in ice thickness due to ice convergence are accounted for using a sea ice ridging participation and redistribution scheme [Bitz et al. 2001; Lipscomb et al. 2007; Chapter 2]. Incorporation of sub-grid scale snow and ice thickness distributions allow tracking and more accurate evolution of sea ice habitats [Bitz et al. 2001; Holland et al. 2006; Chapter 2]. Models without these features average out differences between adjacent grid cells during advection, producing areal mean of sea ice properties that differ profoundly from the ice from which it was originally composed. Ice algal physiology, including C:Chl *a* ratios, photoacclimation capacity, nutrient uptake kinetics, and vertical migration are used to calculate sea ice algal production in the model [Arrigo et al. 1994; Chapter 1].

2.2. Model initialization and run parameters

The model run was initiated on 1 March 1996, the approximate date of minimum seasonal sea ice extent. Areal sea ice cover was initialized using the SSM/I sea ice concentration on this date, and was assumed to have a multi-year ice salinity profile [Chapter 2]. The initial sea ice thickness was assigned as a function of fractional ice

coverage, ranging from 0.56-1.28 m [Chapter 2]. Initial snow thickness on 1 March 1996 was derived from EASE gridded SSM/I brightness temperatures [Armstrong et al. 1994] using the algorithm and methods of Markus and Cavalieri [1998]. Sub-grid scale snow and ice thickness distributions are assumed to be flat at the model start.

The model was run continuously until model day July 1 2006.

2.3. Analysis and Statistical methods

We analyzed model output between the dates of 1 July 1996 and 30 June 2006 and consider an analysis year to begin on 1 July. For ease of interpretation, we classify sea ice algal production according to their vertical location in the ice pack. Locally high levels of biomass can be found at any level depth within sea ice. However, the sea ice characteristics that promote algal growth are vertically distinct, especially between the ice bottom and interior [Ackley and Sullivan 1994; Lizzote et al. 2001; Arrigo 2003]. Therefore, we define bottom sea ice algal production as that which occurs in the bottom 0.2 m of the ice pack. Interior sea ice algal production refers to all production >0.2 m from the sea ice/ocean interface.

For purposes of comparison, we divide the Antarctic sea ice zone into five geographic sectors that have been used in previous studies of Antarctic sea ice [Arrigo et al. 1997, 1998; Worby et al. 2008] (Figure 1). We provide summary statistics for these sectors and investigate the correlations between sector sea ice characteristics, mean climate indices, and sea ice algal production. We used mean monthly values of for the Southern Annual Mode (SAM, [Gong and Wang 1999; Nan and Li 2002]) and the Multivariate ENSO index (MEI [Wolter and Timlin 1993, 1998]) for comparison with modeled algal production to investigate linkages between the climate state and sea ice algal ecology. Spatial and temporal auto-correlation was found to be insignificant within sector statistics, likely due to the yearly loss and regrowth of the

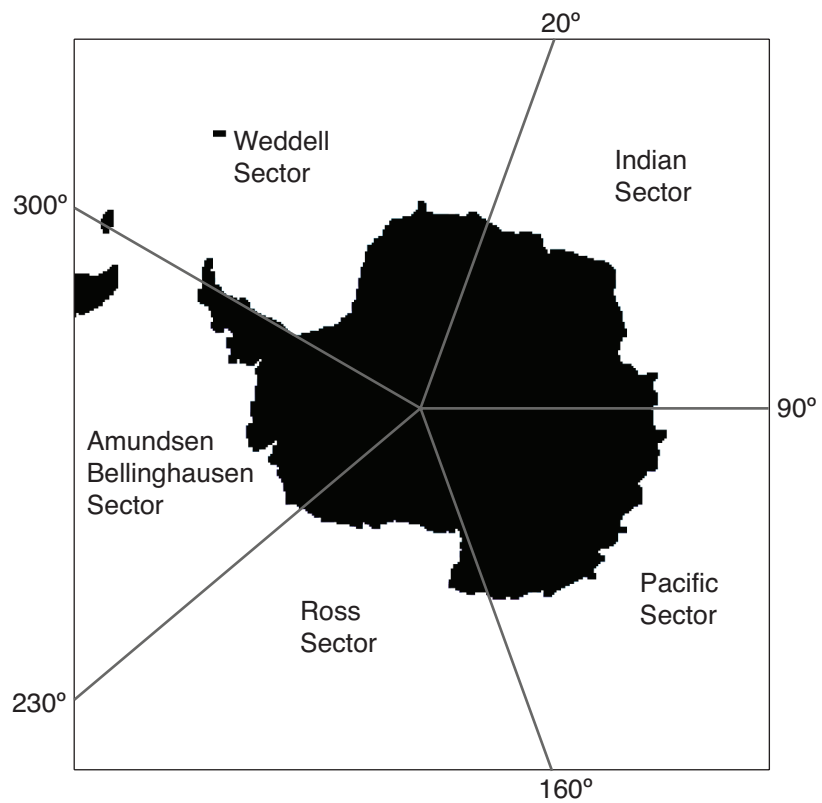


Figure 1. The sea ice model domain with black representing the land mask, divided into 5 sectors used to perform regional spatial analysis of model results.

vast majority of the Antarctic ice pack that creates novel ice qualities. The lack of autocorrelation allowed pooling of yearly sector observations, on which we performed exploratory piecewise correlation analysis using the Stata statistical software package (Version 7).

We calculated total ice presence as a way to quantify the total amount of ice algal habitat. Ice presence is the temporal integral of daily ice concentration (km^2 per unit time), and as such, includes both the concentration and persistence of sea ice in each geographic sector. A similar term from the literature is ‘ice days,’ which is the total number of days that ice (usually defined by a threshold of some sort) was present in a given area [Stammerjohn et al. 2008]. Ice presence is more precise however, because it considers the exact area of ice over a designed period.

To investigate the possibility of preferential growth of sea ice algae in different types of sea ice, we generated weighted means of the ice thickness, snow thickness, and surface temperature in each grid cell within a geographic sector, where the weighting factor was the mean rate of algal primary productivity. Thus approach allowed us to compare ice thickness, snow thickness, and surface temperature in areas with and without ice algal blooms to better understand factors controlling ice algal distributions.

We used similar methods to investigate the controls of algal production. Algal biomass was used to weight daily means of limitation terms, to compensate for the fact that communities of sea ice algae may experience different limitations on growth according to their vertical location within the ice. Limitation terms are calculated for light, nutrients, and salinity and are used to reduce the maximum non-limited algal growth rate to a rate that is more representative of local conditions [Arrigo and Sullivan 1994]. If the limitation term for a given factor is calculated to be unity, as in the case of supersaturating light, that factor would not be limiting algal growth. If a

limitation term drops to zero, as in the case where nutrients are fully depleted from the sea ice interior, that factor would be expected to reduce algal growth rate to zero. The factor having the lowest limitation term at any point in time is the factor most responsible for controlling algal growth rate at that time. We present the daily hemispheric mean of each limitation term.

3. Model Validation

Model performance with respect to mean snow and ice thickness distributions was analyzed for a 1-year standard model run using parameters described in Chapter 2. Mean model ice and snow thickness distributions were in good agreement with the 8227 observations from the ASPeCT database [Worby et al. 2008] and matched monthly trends of in situ observations to within 4.5% and 5.4%, respectively.

We performed a similar analysis using data from the 10-year model run presented here. Instead of comparing a monthly climatology of ASPeCT sea ice and snow thickness observations to modeled sea ice and snow thickness for 1996 [Chapter 2], the ten year length of this model run allowed us to pair specific ASPeCT observations of snow and ice thickness with modeled sea ice and snow thickness at the same place and time. The model does not simulate ice thinner than 0.2 m or consider ice concentrations <20%, therefore, a percentage of ASPeCT observations had no corresponding model value and were not included in the comparison. A total of 5779 paired ASPeCT and model observations were used.

Mean ASPeCT and model paired ice thicknesses were 0.96 m and 1.03 m, respectively, a difference of only 7%. Mean snow thickness in the model was 11% greater (0.21 m) than ASPeCT observations (0.19 m). Model deviations from the ASPeCT data are in the expected directions; since the minimum ice thickness in the model is 0.2 m, we expect the model mean thickness to be somewhat high (Figure

2A). The ASPeCT snow thickness observations are considered to be biased low [Worby et al. 2008a, 2008b], since observations were restricted to flat ice and neglect ridges and other features around which deep snow is likely to accumulate. Histograms comparing the thickness distribution of paired model and ASPeCT observations show that the snow thickness distribution matches quite well, except for a slight shift toward thicker snow in the model (Figure 3A). The model peak in sea ice thickness was slightly less than the peak of 0.6 m in the ASPeCT data, although the overall shape of the ice thickness distributions is very similar (Figure 2A). Monthly trends in model snow and ice thickness continue to mirror the trends in ASPeCT observations (Figures 2B, 3B).

The biological component of the model was validated using time series observations of sea ice algal production and associated physical measurements from Ice Station Weddell [Chapter 1]. Mean daily ice algal biomass from a 1-year run of the model was consistent with the range in sea ice algal biomass from 15 Antarctic field expeditions [Chapter 2]. We perform the same analysis here, and find that modeled algal biomass spans a similar range as the 1-year model run, where model mean summertime algal biomass was significantly lower than the mean biomass from two expeditions (24.6 and 34.2 mg Chl *a* m⁻²; Figure 4). However, locally summertime model biomass achieved > 20 mg Chl *a* m⁻². During the main sea ice algal growth season (October-March), model daily sea ice algal biomass exceeded 20 mg Chl *a* m⁻² in 0.86% of grid cells on average, ranging from 0.3-1.5% annually. Modeled algal biomass rarely reached the mean value of 34.2 mg Chl *a* m⁻² observed on the ANT XI/3 research cruise [Dieckmann et al. 1998]. This high mean biomass is from 29 ice cores from the Bellingshausen Sea (Amundsen sector) during summer in 1994, where extremely high algal biomass was observed at a majority of stations within gap layers in the ice pack. The pack was apparently at a late stage of decay, with ~50% ice

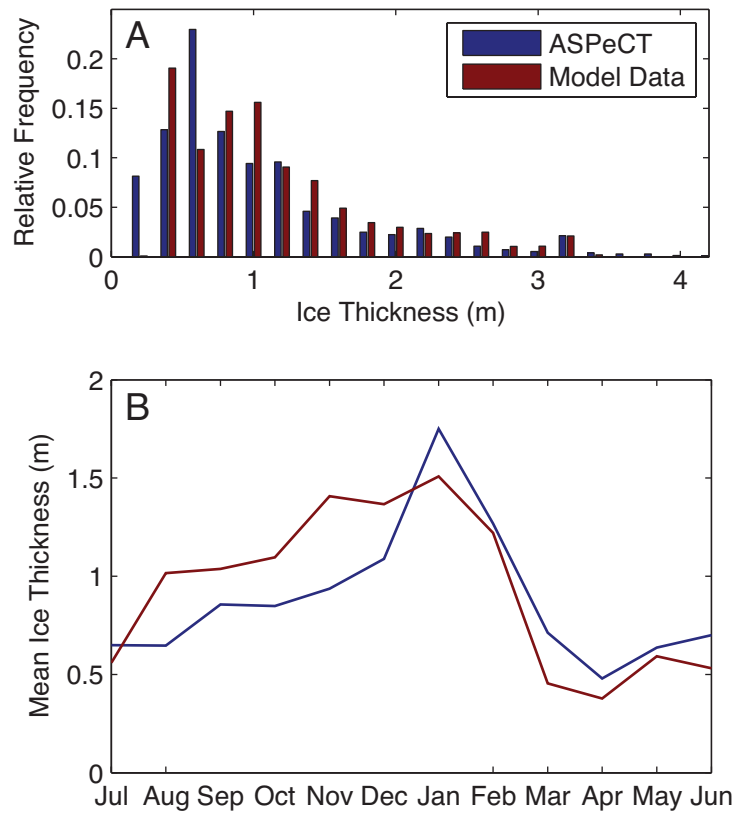


Figure 2. Comparison of the (A) frequency distribution and (B) monthly mean ice thicknesses from ASPeCT sea ice observations and matching model output.

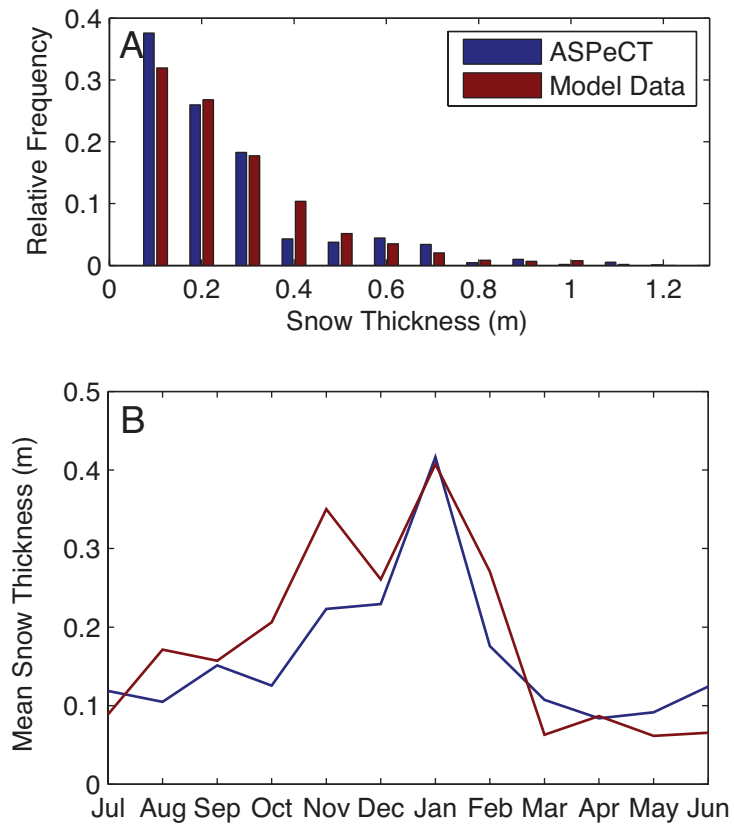


Figure 3. Comparison of the (A) frequency distribution and (B) monthly mean snow thicknesses from ASPeCT sea ice observations and matching model output.

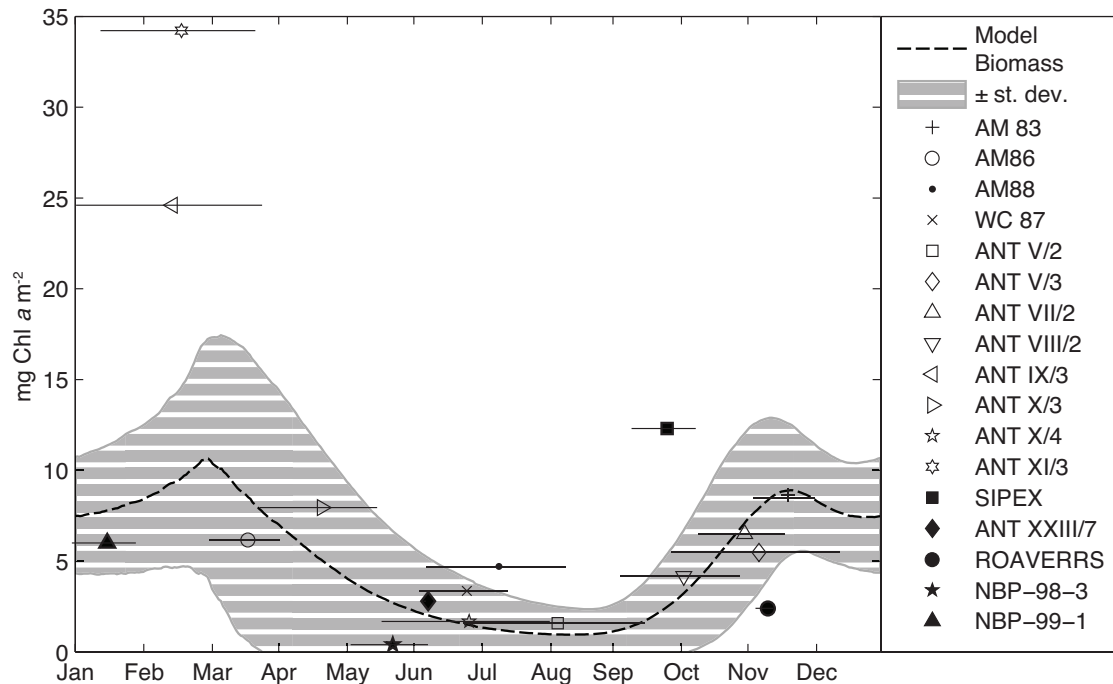


Figure 4. Plots of mean ice core algal biomass from 17 Antarctic field expeditions, overlaid with modeled mean daily sea ice biomass, average over the 10-year model run. Field expedition durations are shown as horizontal lines crossing the identifying marker. Observations excepting high biomass the ANT X1/3 and ANT IX/3 were represented in the standard variability of model biomass. Model biomass does reach over 25 mg Chl a m^{-2} frequently in individual areas, but the mean biomass is everywhere much lower. Mean grid cell biomasses of over 30 mg Chl a m^{-2} were rare.

coverage. It is possible that the model underestimates sea ice algal production under these circumstances, but it is also possible, given the small number of measurements and high standard deviation of measured biomass ($26.28 \text{ mg Chl } a \text{ m}^{-2}$), that the reported mean was not representative of the ice [Dieckmann et al. 1998].

4. Results

4.1. Sea ice algal production

Annual production by sea ice algae ranged interannually from 15.5 to 18.1 Tg C yr⁻¹, with a mean of 16.8 Tg C yr⁻¹. Interior algal production comprised 64% of mean annual production, with bottom production accounting for the remaining 36%. Interannual variability (standard deviation) of total interior algal production (7%) was higher than that of total bottom ice production (4%) when examined over the entire model domain (Tables 1-3).

Spatial distribution of production – The Weddell Sector, with a mean annual production rate of 6.58 Tg C yr⁻¹, was responsible for 39% of total annual sea ice algal production (Table 1). The Ross sector was the second most productive, at 4.05 Tg C yr⁻¹, followed by the Indian (2.91 Tg C yr⁻¹), Amundsen (1.82 Tg C yr⁻¹) and Pacific (1.41 Tg C yr⁻¹) sectors (Table 1). On average, this geographic pattern applied to both interior and bottom ice communities, except in 2005-06 when interior ice algal production in the Pacific sector was greater than in the Amundsen sector (Tables 1 and 2). We also note that interior algal production was similar in the Pacific and Amundsen sectors in 1998-99 (0.52 and 0.53 Tg C yr⁻¹, respectively, Table 3). In addition, bottom algal production was remarkably close in the Weddell and Ross sectors in 1998-99 (3.99 and 3.50 Tg C yr⁻¹, respectively) despite the Ross Sea having 35% less ice over the year, indicating that bottom sea ice in the Ross sector was 35% more productive than in the Weddell sector (Tables 2,4). Despite large interannual

Table 1. Total Annual (July – June) Sea Ice Algal Production (Tg C yr⁻¹)

<i>Analysis Year</i>	<i>All</i>	<i>Weddell</i>	<i>Amund -sen</i>	<i>Ross</i>	<i>Pacific</i>	<i>Indian</i>
<i>1996-97</i>	16.27	6.66	1.79	3.45	1.51	2.85
<i>1997-98</i>	15.53	6.49	1.42	3.70	1.35	2.57
<i>1998-99</i>	18.08	6.15	1.96	5.04	1.67	3.26
<i>1999-00</i>	17.56	6.29	1.77	4.68	1.30	3.51
<i>2000-01</i>	17.61	6.29	2.22	4.95	1.54	2.60
<i>2001-02</i>	15.90	6.12	1.99	3.99	1.14	2.67
<i>2002-03</i>	16.67	7.06	1.56	4.16	1.36	2.54
<i>2003-04</i>	16.74	6.85	2.12	3.56	1.41	2.80
<i>2004-05</i>	17.07	6.95	2.11	3.38	1.28	3.34
<i>2005-06</i>	16.45	6.98	1.28	3.61	1.60	2.98
<i>Mean (s.d.)</i>	16.79 (0.80)	6.58 (0.36)	1.82 (0.32)	4.05 (0.63)	1.42 (0.16)	2.91 (0.35)

Table 2. Annual (July – June) Bottom Ice Algal Production (Tg C yr⁻¹)

<i>Analysis Year</i>	<i>All</i>	<i>Weddell</i>	<i>Amund -sen</i>	<i>Ross</i>	<i>Pacific</i>	<i>Indian</i>
<i>1996-97</i>	9.87	3.58	1.20	2.18	1.06	1.86
<i>1997-98</i>	9.94	3.96	0.87	2.52	0.85	1.74
<i>1998-99</i>	12.20	3.99	1.42	3.50	1.16	2.13
<i>1999-00</i>	11.23	3.66	1.25	3.23	0.84	2.25
<i>2000-01</i>	11.42	3.86	1.48	3.36	1.10	1.62
<i>2001-02</i>	9.89	3.44	1.32	2.70	0.76	1.66
<i>2002-03</i>	10.52	4.07	1.08	2.87	0.92	1.58
<i>2003-04</i>	10.65	4.05	1.47	2.40	0.92	1.82
<i>2004-05</i>	10.50	4.06	1.32	2.33	0.88	1.91
<i>2005-06</i>	10.49	4.29	0.86	2.35	1.01	1.98
<i>Mean (s.d.)</i>	10.67 (0.75)	3.90 (0.26)	1.23 (0.23)	2.74 (0.47)	0.95 (0.13)	1.86 (0.22)

Table 3. Annual (July – June) Interior Ice Algal Production (Tg C yr⁻¹)

<i>Analysis Year</i>	<i>All</i>	<i>Weddell</i>	<i>Amund -sen</i>	<i>Ross</i>	<i>Pacific</i>	<i>Indian</i>
<i>1996-97</i>	6.40	3.09	0.60	1.27	0.46	0.99
<i>1997-98</i>	5.59	2.53	0.56	1.18	0.50	0.82
<i>1998-99</i>	5.88	2.16	0.53	1.54	0.52	1.13
<i>1999-00</i>	6.33	2.63	0.53	1.45	0.46	1.26
<i>2000-01</i>	6.19	2.43	0.74	1.59	0.44	0.98
<i>2001-02</i>	6.01	2.68	0.66	1.28	0.38	1.00
<i>2002-03</i>	6.15	2.99	0.48	1.29	0.44	0.96
<i>2003-04</i>	6.09	2.80	0.65	1.16	0.49	0.98
<i>2004-05</i>	6.58	2.89	0.79	1.06	0.40	1.44
<i>2005-06</i>	5.95	2.68	0.42	1.26	0.59	0.99
<i>Mean (s.d.)</i>	6.12 (0.28)	2.69 (0.27)	0.60 (0.12)	1.31 (0.17)	0.47 (0.06)	1.06 (0.18)

Table 4. Annual mean daily (July – June) ice extent (10⁶ km²)

<i>Analysis Year</i>	<i>All</i>	<i>Weddell</i>	<i>Amund -sen</i>	<i>Ross</i>	<i>Pacific</i>	<i>Indian</i>
<i>1996-97</i>	7.82	3.08	0.85	2.12	0.71	1.05
<i>1997-98</i>	8.05	3.24	0.78	2.10	0.72	1.20
<i>1998-99</i>	8.16	2.88	0.78	2.44	0.79	1.27
<i>1999-00</i>	8.16	2.99	0.85	2.23	0.75	1.34
<i>2000-01</i>	8.37	3.38	0.84	2.25	0.68	1.22
<i>2001-02</i>	7.61	2.94	0.84	2.02	0.59	1.23
<i>2002-03</i>	8.30	3.63	0.73	2.17	0.67	1.11
<i>2003-04</i>	8.21	3.41	0.87	2.00	0.71	1.23
<i>2004-05</i>	8.15	3.17	1.00	1.95	0.65	1.38
<i>2005-06</i>	7.83	3.18	0.72	1.94	0.73	1.26
<i>Mean (s.d.)</i>	8.07 (0.24)	3.19 (0.23)	0.83 (0.08)	2.12 (0.16)	0.70 (0.06)	1.23 (0.10)

differences in the horizontal distributions of sea ice algal blooms within a given geographic sector, the annual magnitude of bottom and interior sea ice algal production is remarkably consistent within sectors, as evidenced by low standard deviations of yearly means. Surprisingly, interior and bottom ice algal production exhibit the same degree of interannual variability across geographic sectors (14%, calculated from Tables 2-3).

Although interannual variability in mean annual algal production within a given geographic sector is small, variability at the grid-cell scale is high, although with significant clustering of algal production in different areas during each year (Figure 5). Much of the change in the distribution of the most productive regions is due to differences in the distribution of summer sea ice, which, by virtue of its longevity, allows high total algal biomass accumulation and production.

The maximum annual mean sea ice algal production ranged from 4.8 to 7.8 g C m⁻² yr⁻¹ over the 10 modeled years, with bottom and interior sea ice algal production reaching maxima of 7.1 and 1.9 g C m⁻² yr⁻¹, respectively. Values this high were relatively rare, as the areal distribution of production is lognormal in both interior and bottom algal communities (Figure 6). A histogram of total production (interior plus bottom) exhibits a peak distribution significantly higher than that of either the interior or the bottom community, indicating that interior and bottom production were often elevated in the same location.

Mean sea ice algal production per unit area across all years and over the entire model domain was 0.89 g C m⁻² yr⁻¹ (Table 5). The annual production within geographic sectors varied by up to a factor of two, ranging from a low of 0.6 g C m⁻² yr⁻¹ in the Ross sector (1987-88) to a high of 1.22 g C m⁻² yr⁻¹ in the Weddell sector (1999-00). Annual differences in mean sector algal productivity ranged from 11-17%, with the highest variability in the Ross sector. Across all modeled years, the Weddell

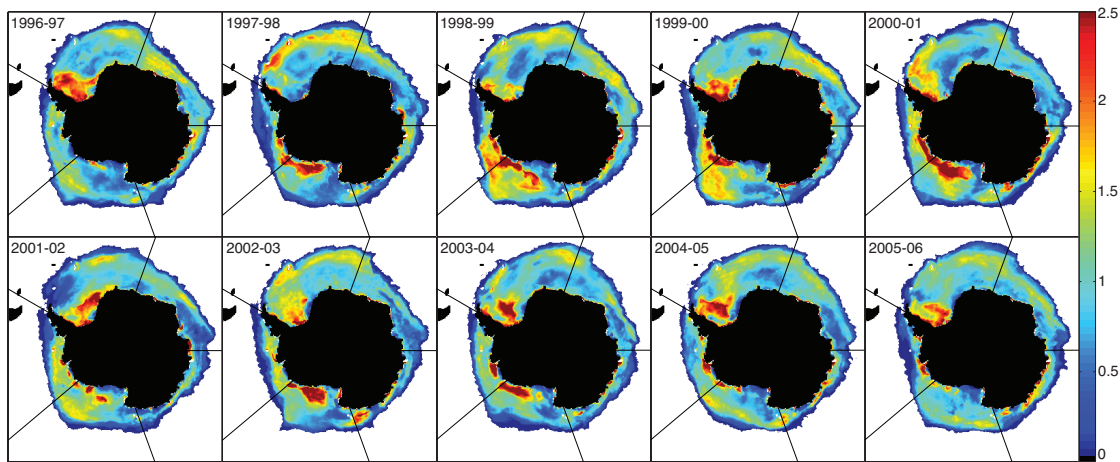


Figure 5. Maps of the spatial distribution of total annual sea ice algal production over 10 model years (g C yr^{-1}), showing patchy productivity within each sector and high spatial variability of production between different years.

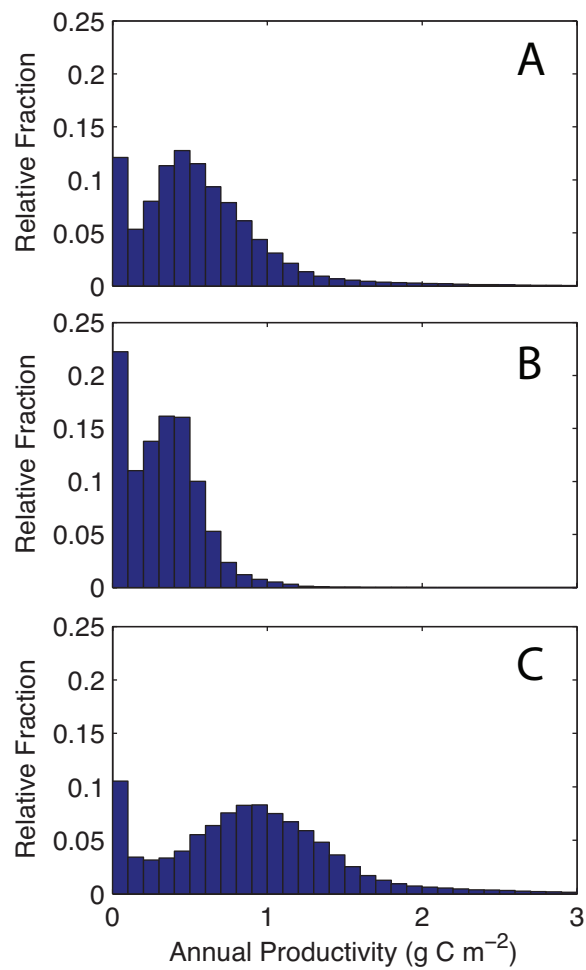


Figure 6. Histograms of grid cell (A) bottom, (B) interior, and (C) total ice column annual productivity. Histograms reflect pooled annual grid cells over 10 modeled years.

Table 5. Annual (July – June) Mean Areal Algal Productivity ($\text{g C m}^{-2} \text{ yr}^{-1}$)

<i>Analysis Year</i>	<i>All</i>	<i>Weddell</i>	<i>Amundsen</i>	<i>Ross</i>	<i>Pacific</i>	<i>Indian</i>
<i>1996-97</i>	0.87	1.19	0.78	0.75	0.75	0.89
<i>1997-98</i>	0.83	0.86	0.60	0.90	0.67	0.73
<i>1998-99</i>	0.96	0.88	0.95	1.10	0.78	0.93
<i>1999-00</i>	0.94	1.22	0.79	1.04	0.62	0.93
<i>2000-01</i>	0.92	0.94	0.98	1.10	0.77	0.71
<i>2001-02</i>	0.84	0.86	0.85	0.93	0.57	0.75
<i>2002-03</i>	0.91	1.05	0.69	0.99	0.75	0.70
<i>2003-04</i>	0.87	0.92	0.94	0.84	0.66	0.74
<i>2004-05</i>	0.90	0.95	0.89	0.87	0.68	0.81
<i>2005-06</i>	0.85	0.93	0.60	0.85	0.73	0.78
<i>Mean (s.d.)</i>	0.89 (0.04)	0.98 (0.13)	0.81 (0.14)	0.94 (0.12)	0.70 (0.07)	0.80 (0.09)

sector was the most productive ($0.98 \text{ g C m}^{-2} \text{ yr}^{-1}$) and the Pacific sector the least ($0.70 \text{ g C m}^{-2} \text{ yr}^{-1}$)

Examination of the 10-year mean spatial distribution of algal production indicates that the highest bottom algal production is located adjacent to the coastline in all sectors, as well as in large patches in the southern Weddell, southwestern Amundsen, and southeastern Ross sectors (Figure 7A), with production typically exceeding $1.2 \text{ g C m}^{-2} \cdot \text{yr}^{-1}$. These areas are characterized by their high mean annual ice presence, as well as relatively thick snow (Figure 8A). Bottom sea ice algal production was also elevated in a band encircling the Antarctic continent, with lower production toward the shore. In general, this band of elevated productivity lies closer to the coastline in the Amundsen and Pacific sectors. Composed of annual ice that melts seasonally, areas of this band in the Weddell, Indian, and Ross sectors stand out as consistently producing $>1 \text{ g C m}^{-2} \text{ yr}^{-1}$.

Interior algal production averaged over the 10-year model run was highest offshore in the southern Weddell sector (Figure 7B). This area of the pack is unique in being

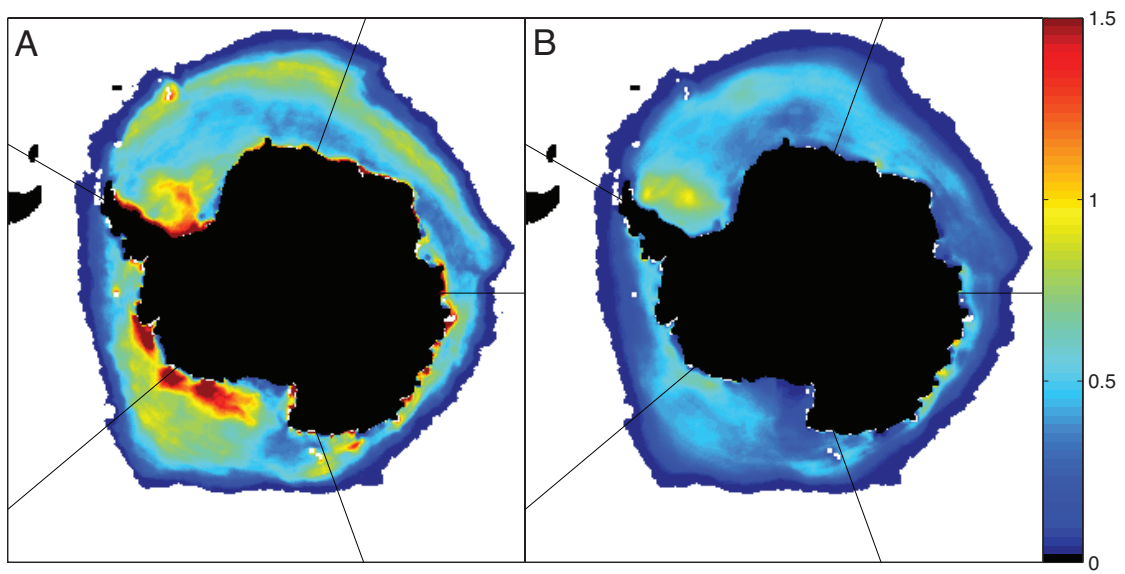


Figure 7. Spatial distribution of mean annual bottom (A) and interior (B) sea ice algal production ($\text{g C m}^{-2} \text{ yr}^{-1}$) over the 10 years of the model run.

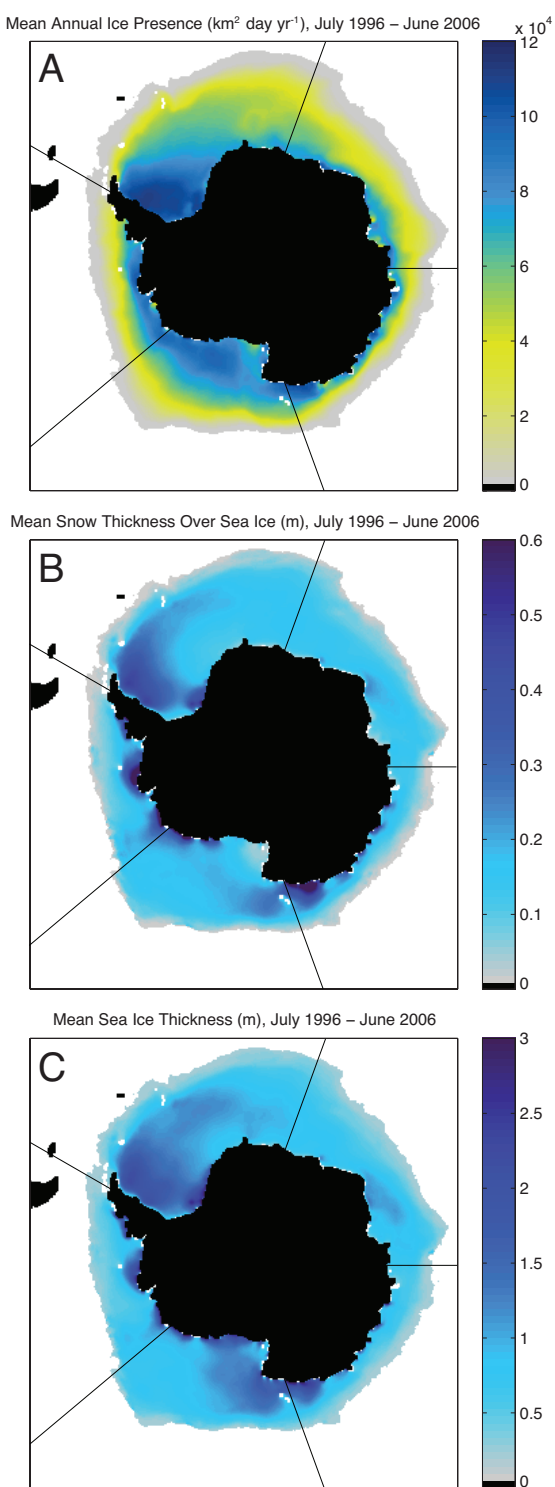


Figure 8. Maps of mean annual modeled ice presence (A) snow thickness (B), and ice thickness (C) over the 10 modeled years.

very cold, and for frequently containing thick sea ice year-round (Figure 8A). Mean interior algal productivity is lower than bottom algal productivity virtually everywhere in the ice pack and is also less spatially variable. An offshore band of elevated interior algal production approximately mirrors the pattern of offshore interior algal production.

Both bottom and interior sea ice productivity are relatively low near major polynyas where reduced and intermittent sea ice cover and low temperatures prevent significant biomass accumulations. The most northerly pack ice displays low productivity due to short total ice duration in these regions (Figure 7B, 8A).

Timing of production - Seasonal mean ice algal biomass is lowest in winter (July-September), averaging 48 mg C m^{-2} ($1.4 \text{ mg Chl } a \text{ m}^{-2}$) across the model domain (Figures 4 and 9A). Production begins in the outer Weddell sector during this period, visible as a band of elevated biomass east of the Antarctic Peninsula (Figure 9A). Biomass is also elevated relative to the mean along the Antarctic coastline, which represents remnant sea ice algal blooms from the preceding growth season. Spring (October-December) mean algal biomass is characterized by higher values in the northern reaches of the ice pack, reflective of increasing day length and alleviation of light limitation of algal production in these regions (Figure 9B). Mean springtime algal biomass over the model domain was 237 mg C m^{-2} ($6.8 \text{ mg Chl } a \text{ m}^{-2}$), exhibiting moderate interannual variability (Figure 9B, inset). Summer (January-March) biomass was consistently high in the western Weddell sector (Figure 9C), above 450 mg C m^{-2} ($12.9 \text{ mg Chl } a \text{ m}^{-2}$) and was also elevated close to the coast in the southeastern Ross sector, reflective of the large amount of internal production in this region. Mean algal biomass during the summer was somewhat higher than in spring, averaging 298 mg C m^{-2} ($8.5 \text{ mg Chl } a \text{ m}^{-2}$) across the Antarctic ice pack. During autumn, mean algal biomass is elevated in areas where sea ice survived the summer without melting and

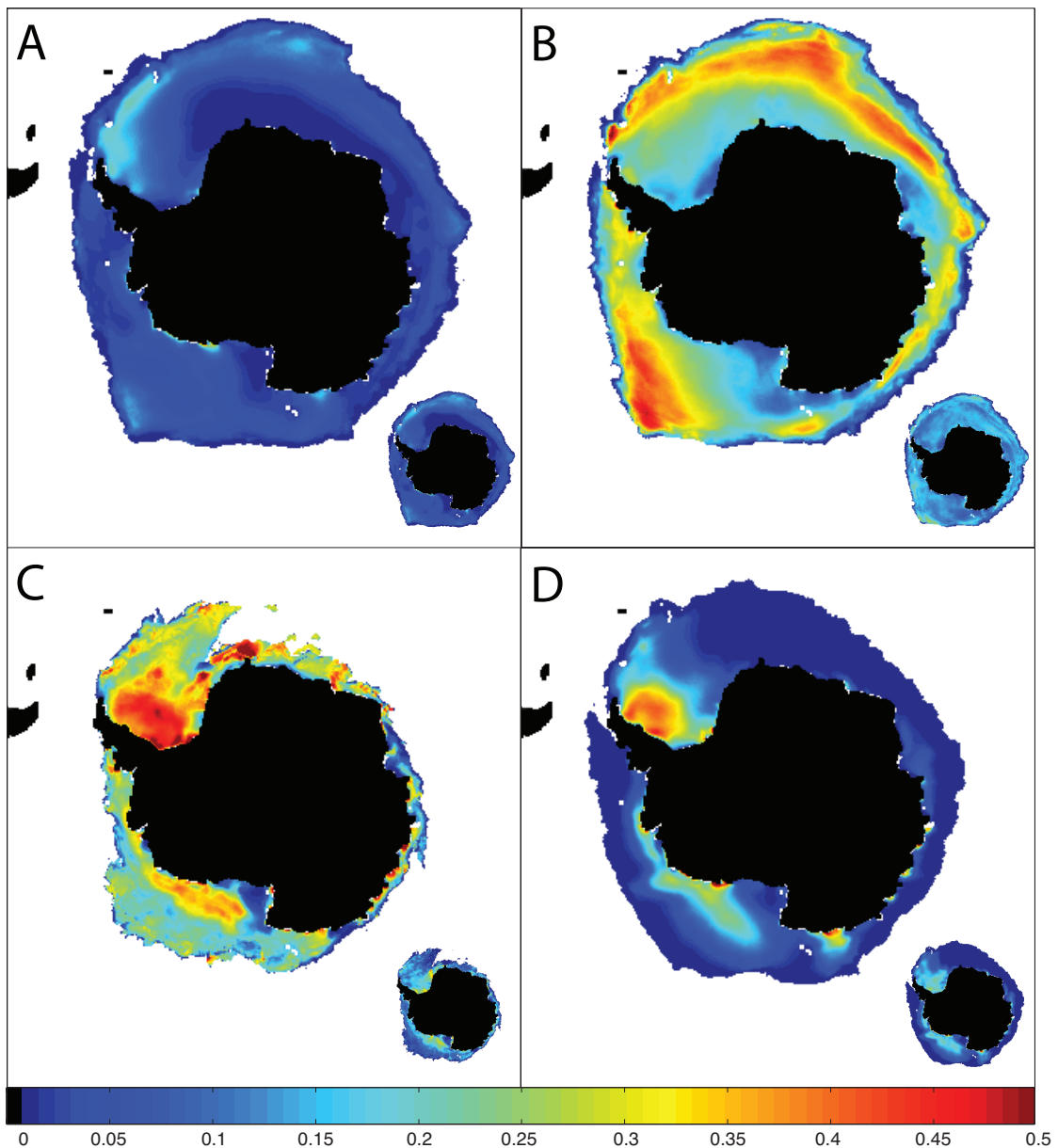


Figure 9. Mean seasonal sea ice algal biomass (g C m^{-2}) over 10 years of model output. Winter (A) is defined as July – September, Spring (B) as October – November, Summer (C) as January – March, and Autumn (D) as April – June. Standard deviations of individual grid cells are show in smaller inset maps.

was suitable for the development of an autumn sea ice algal bloom. These autumn blooms are highly variable in magnitude and location in the Amundsen and Ross sectors compared to the Weddell sector, which is reflected in the higher mean and lower standard derivations for algal biomass in the Weddell sector (Figure 9D). Mean algal biomass during autumn fell to only 108 mg C m^{-2} ($3.1 \text{ mg Chl } a \text{ m}^{-2}$) across the model domain, reflecting the increased area of new ice with a correspondingly low algal biomass.

In general, the annual cycle of production per unit area averaged over the model domain in the bottom community differed markedly from that in the interior community, with the former exhibiting both a marked spring and autumn bloom and the latter exhibiting a single long-lived summer bloom (Figure 10A). Peak rates of production in the bottom community averaged 10 and $14 \text{ mg C m}^{-2} \text{ d}^{-1}$ during the spring and autumn blooms, respectively, with summer rates of only $2\text{-}3 \text{ mg C m}^{-2} \text{ d}^{-1}$. In contrast, the peak rate of production in the interior community was only about $5 \text{ mg C m}^{-2} \text{ d}^{-1}$.

The annual cycle of algal total algal production in both bottom and interior communities averaged over the 10-year model run and integrated across the model domain exhibited extremely low values in July ($<0.003 \text{ Tg C day}^{-1}$) that rose exponentially until mid-October (Figure 10B). Annual production in the bottom community peaked on 1 November at $0.14 \text{ Tg C day}^{-1}$; interior algal production peaked 6 days later at $0.06 \text{ Tg C day}^{-1}$. Between early December and late January, interior ice algal production exceeded that by the bottom algal community by a modest amount. In austral autumn, productivity of the bottom algal community increased again, but to a value only about one third as high as during the spring bloom. This relatively small autumn peak, as compared to the much higher peak in autumn production per unit area (Figure 10B), is due to the relatively small amount of sea ice

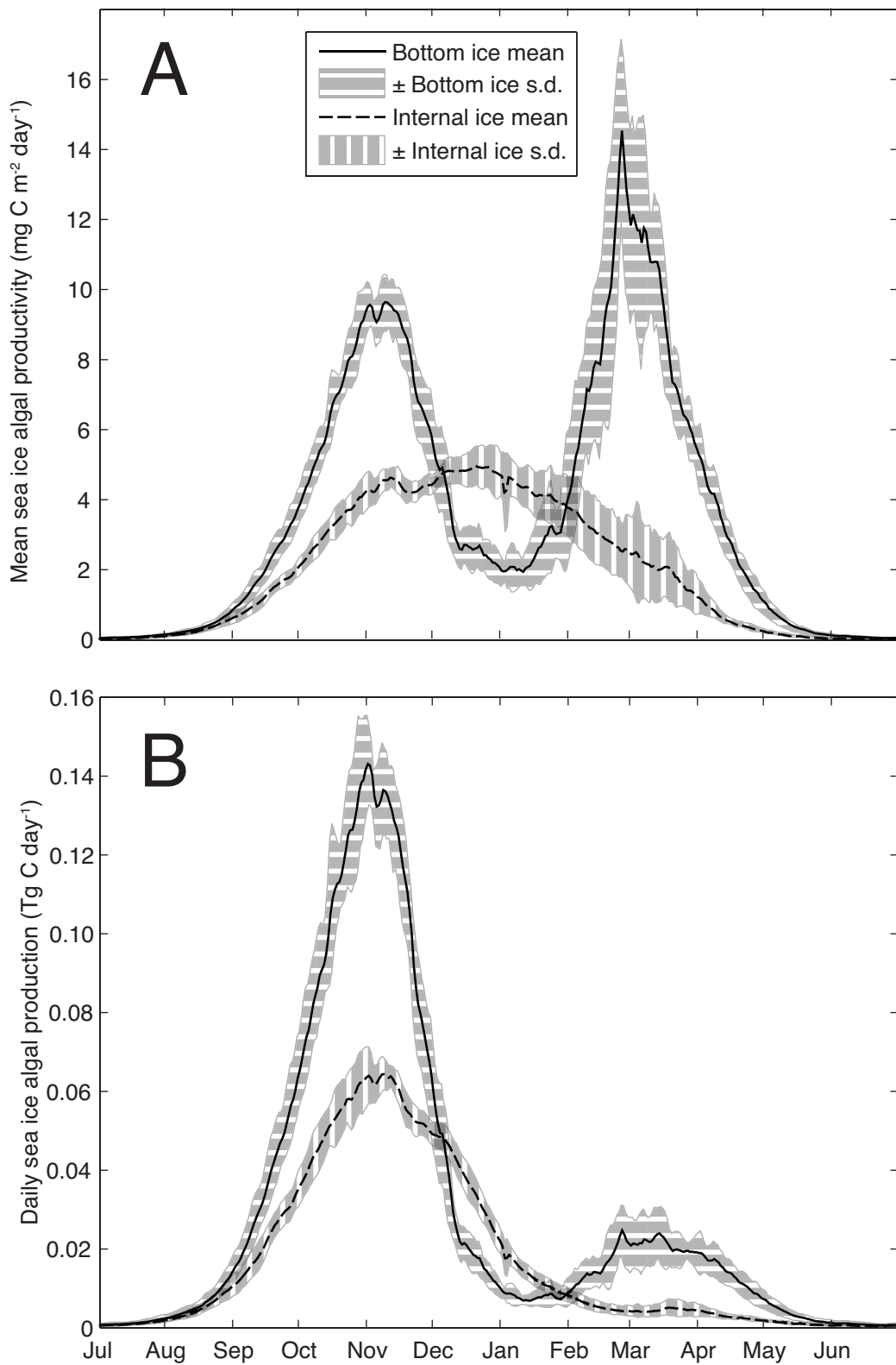


Figure 10. Mean total daily sea ice algal areal productivity (A) and mean total daily productivity (B), over 10 modeled years.

cover in autumn. Because of low rates of production per unit area and reduced sea ice cover, production in the interior community remained low throughout the austral autumn. When integrated over February to April, the autumn bloom constituted 11.2% of total production.

Controls of primary production –Throughout much of the year, light was the factor most limiting to algal growth (Figure 11). Although the light limitation term increased from 0.06 in June to 0.6 in October, reflecting the seasonal increase in solar radiation, it continued to be the dominant limiting factor of algal growth during this time period. By late October, continued increases in light and substantial rates of nutrient drawdown by the developing algal bloom caused nutrients to become more limiting than light, resulting in a drop in the minimum growth limitation term from 0.55 to 0.35 by late December. Nutrient limitation decreases slightly after December, but remains the factor most limiting to algal growth until light once again becomes the dominant limiting factor in late January. This slow decrease in mean nutrient limitation occurs as the ice pack retreat accelerates (Figure 11). The most nutrient-limited algae are found northward in the ice pack, due to earlier seasonal alleviation of light limitation. As ice retreat accelerates southward, the most nutrient limited algae are lost to the water column faster than the remaining algae are exhausting nutrients, resulting in a slight alleviation of mean levels of nutrient limitation over the model domain.

Typical sea ice algae do not grow well at salinities that are either too high (>60 psu) or too low (<15 psu) [Arrigo and Sullivan 1992]. Furthermore, brine salinity is determined by brine temperature (assuming thermodynamic equilibrium). Therefore, the salinity limitation term is generally high (permissive of growth) in the summer when the ice is relatively warm and moderately low in the winter when brine salinities are high. Although salinity limitation is regionally important as a control on algal

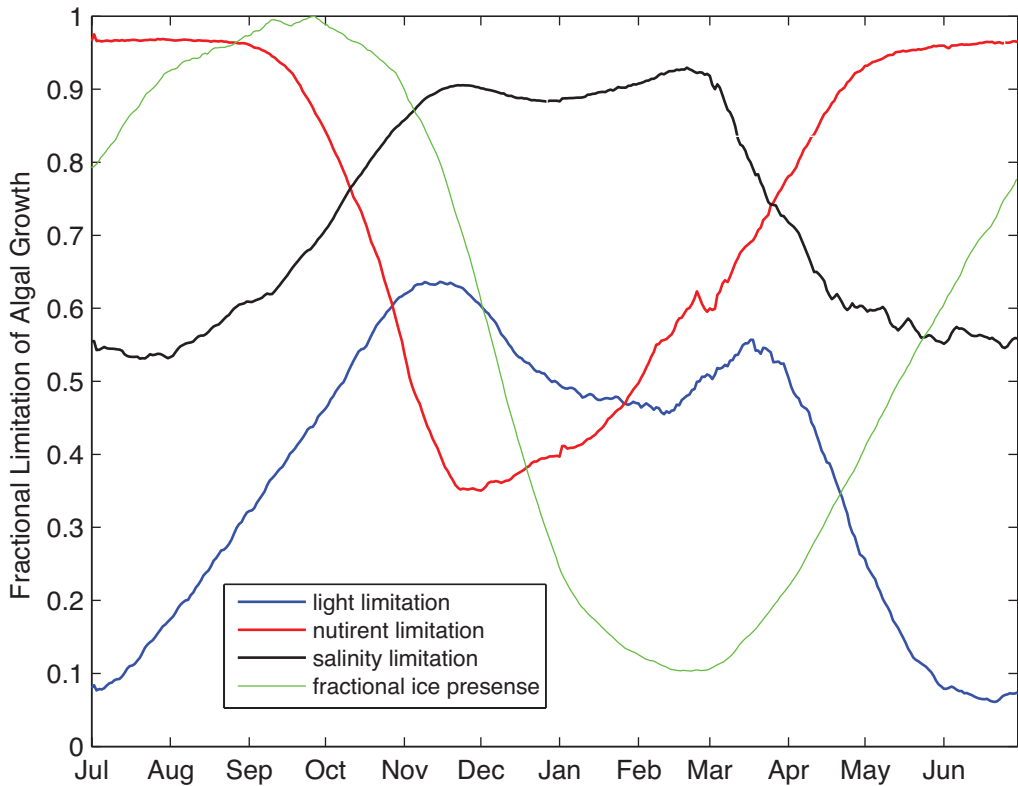


Figure 11. Mean daily biomass-weighted algal growth limitation terms. Higher values permit higher growth. Mean daily fractional ice presence is plotted for comparison.

growth in cold areas such as the Weddell and Ross Seas, model results indicate that net Antarctic sea ice algal growth is always more limited by light.

The switch from light to nutrient limitation in late austral spring and summer effectively caps peak sea ice algal production. Coincident with the onset of nutrient limitation in late October, the productivity of bottom ice algae peaks and then decreases rapidly as nutrient limitation intensifies. Increases in the rate of interior algal productivity largely peak at this time as well (Figure 10B).

To illustrate the effect of springtime nutrient limitation on total sea ice algal production, we calculated total sea ice algal production with nutrient limitation removed. From modeled algal biomass and production, we derived biomass-weighted measures of daily algal productivity. These productivity values were scrubbed of the effect of nutrient limitation by multiplying by the ratio of light limitation to nutrient limitation, where nutrient limitation was observed to be the primary limiting factor. By assuming a completely homogenous ice pack, and that there are no feedbacks associated with modified algal production, we use the adjusted daily productivities to grow an alternative algal biomass, accounting for changes in ice extent. The fixed algal loss rate from the model was applied to this biomass estimation [Chapter 1].

Bottom and interior production peaked approximately two weeks later when relieved of nutrient stress, and resulted in 46% and 53% higher peak daily interior and bottom algal production, respectively (Figure 12). When integrated over the model domain, bottom algal production increased by $2.72 \text{ Tg C yr}^{-1}$, and interior algal production increased by $1.81 \text{ Tg C yr}^{-1}$, resulting in a 27% increase in annual algal production.

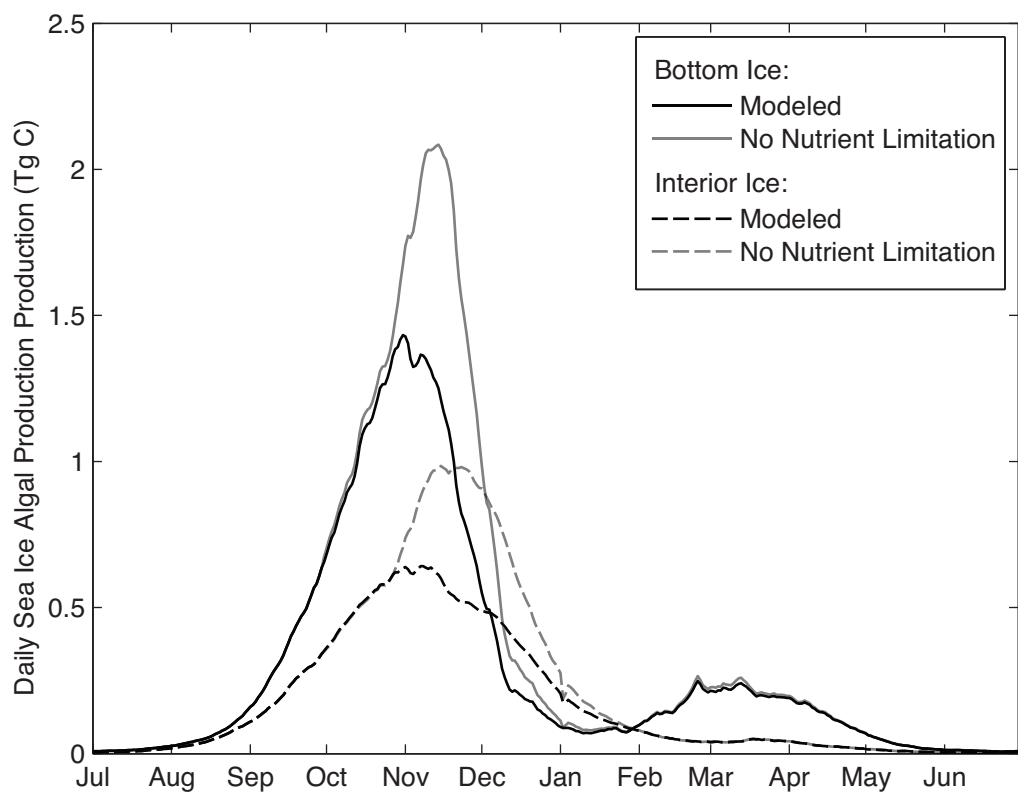


Figure 12. Modeled mean daily interior and bottom sea ice algal production, compared to potential daily production with nutrient limitation removed.

4.2. Biotic/abiotic relationships

Sector scale relationships - Total annual sea ice algal production is linearly correlated to the total presence of sea ice, both by sector and over the entire model domain (Figure 13). This relationship is not unexpected; a greater amount of ice provides more habitat for algae to grow. However, ice presence is not a good predictor of inter-annual variability in total or sector-specific productivity, indicating that across a given area, factors other than the amount of ice determine annual ice algal production.

To examine the possibility of linear relationships between algal productivity and variability in the physical characteristics of sea ice and environmental forcing, we detrended summary variables of ice presence where appropriate and performed exploratory correlation analysis using annual, springtime, and summer/autumn sum and mean sector algal productivities for each model year, with interior and bottom ice algal productivity considered separately.

This exercise produced no significant correlations at the sector level between annual sea ice algal production and any combination of annual mean ice thickness, snow thickness, snow/ice temperature, snow ice growth, or congelation ice growth. There was also no linear relationship between annual algal productivity and concurrent annual mean values for the SAM or the MEI, although time lag correlations were not investigated. Furthermore, there was no linear relationship between bottom and interior algal production within sectors.

However, a small number of significant relationships emerged when analysis was restricted to the spring and autumn growth seasons (Table 6). Over the September to December time period, mean normalized interior and bottom algal productivity anomalies were negatively correlated with the snow ice production rate as well as with mean snow thickness. Congelation ice production was positively associated with algal

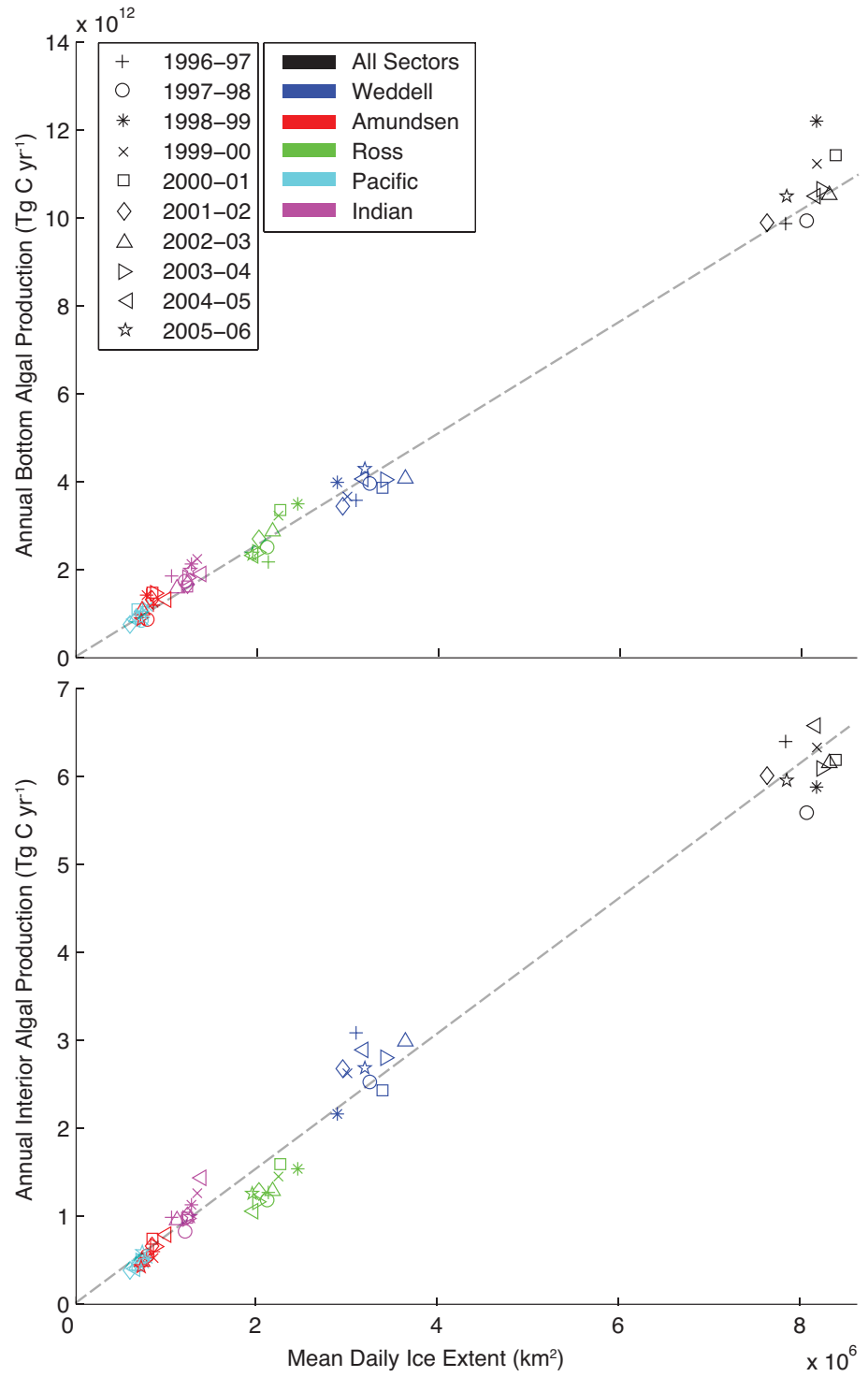


Figure 13. Annual total and sector sea ice algal production plotted against ice presence. The dashed lines represent regressions of pooled sector productions (total production values [black symbols] were excluded).

Table 6. Significant pairwise correlations between measures of algal production and sea ice characteristics in pooled analysis sectors

<i>Productivity Type</i>	<i>Predictive Variable</i>	<i>Summary Period</i>	<i>R</i>	<i>p > t </i>
Bottom ¹	Snow thickness (m)	Sep-Dec	-0.428	0.002
Bottom ¹	Snow Ice Production (m)	Sep-Dec	-0.594	<0.001
Bottom ¹	Cong Ice Production (m)	Sep-Dec	0.322	0.023
Bottom	MEI	Sep-Dec	-0.369	0.008
Interior ¹	Snow thickness	Sep-Dec	-0.306	0.031
Interior ¹	Snow Ice Production (m)	Sep-Dec	-0.431	0.002
Interior ¹	Cong Ice Production (m)	Sep-Dec	0.292	0.040
Bottom	Minimum Ice Extent (km ²)	Feb-Apr	0.346	0.014

¹Predictive variables from these relationships were also correlated, indicating a single mode of co-variation

production in both bottom and interior sea ice communities. Bottom and interior production anomalies are also correlated to each other, as are snow thickness, snow ice production, and congelation ice production. Therefore, these correlations represent just a single mode of co-variation. The negative association with snow depth indicates that this relationship is a manifestation of springtime light limitation of algal production. The bottom algal productivity anomaly was also negatively associated with the MEI during the spring. Bottom algal productivity during the autumn (February through April) was positively correlated with both snow depth and minimum ice extent.

Mean sea ice algal habitat - To examine the characteristics of sea ice that promote algal growth, we calculated production-weighted means of sea ice thickness, snow thickness, and snow/ice interface temperatures. We note that interior production used for weighted averaging of ice thicknesses, snow thicknesses, and interface temperatures occurs over a variable vertical depth, meaning that thicker ice has greater potential for production given the larger volume of sea ice habitat composed of interior ice. If production is equal in all interior sea ice, we would still expect to see an elevated interior production-weighted mean ice thickness, compared to the standard mean ice thickness, since thicker ice would be weighted more heavily by a larger areal

production. Despite this caveat, interior productivity-weighted means provide a guide to the mean interior sea ice habitat as we have defined it. Bottom ice production is always integrated over 0.2 m depth; therefore, weighed means using bottom algal production are independent of ice depth.

The mean bottom algal production-weighted ice thickness (1.01 m; Table 7) was similar to the overall mean ice thickness (1.05 m). A time series plot shows that, on average, bottom algae grew in ice that was thinner than the mean available ice (Figures 10, 14A). In contrast, the mean interior algal production-weighted ice thickness (1.27 m) was much larger than the mean ice thickness. In the winter and early spring, both bottom and interior algae grew preferentially in thinner ice, reflecting the dominance of light limitation at this time of year.

Mean production-weighted snow thicknesses followed the same patterns as ice thickness, where the bottom-weighted mean (0.21 m) was similar to the standard mean (0.20 m), and the interior-weighted mean was higher (0.27 m; Table 7, Figure 14B)). Bottom algae grow more often in ice with below-mean snow thickness for most of the year, except in the fall when ice algal blooms are concentrated in older ice with thicker snow. Interior algal growth is more cosmopolitan during the winter and spring and grows under the mean snow depth. During late spring and summer, interior algal growth shifts to ice with thicker snow cover on average.

Mean bottom and interior production-weighted snow/ice interface temperatures (-3.5, -2.9 °C) were much higher than the standard mean of (-5.8 °C), reflecting the lowered algal growth rates and salinity limitation present at cold temperatures (Table 7, Figure 14C). Interior algae are expected to experience colder temperatures on average than bottom ice algae due to their position further from the relative warmth of the underlying ocean, and the higher mean growth temperature of interior algal communities is reflective of this. At colder temperatures, interior communities

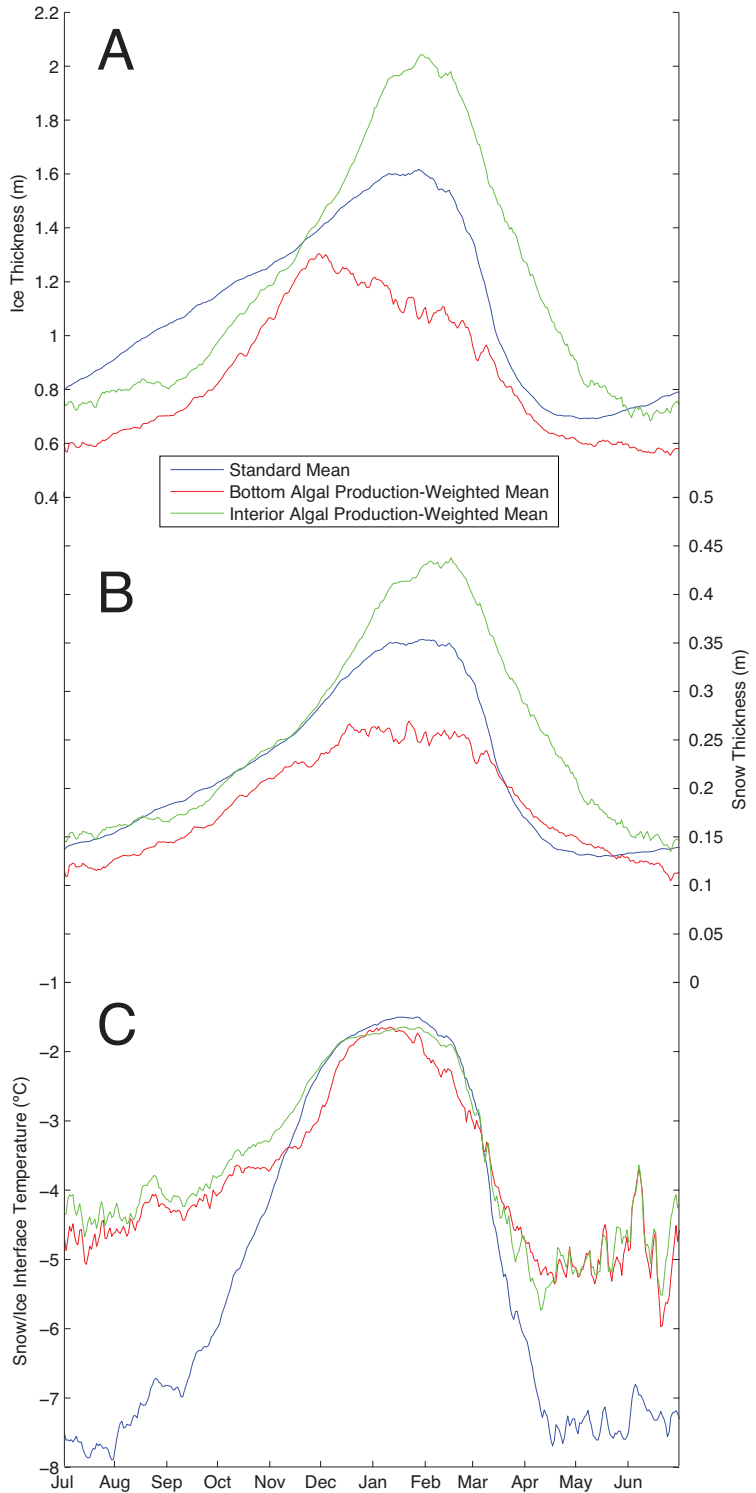


Figure 14. Daily means of model ice thickness, snow thickness, and snow/ice interface temperature, compared to bottom and interior productivity weighted means of the same measures. Daily means span the entire model domain and across 10 modeled years.

Table 7. Algal production-weighted mean snow and ice characteristics

Analysis Year	Total Ice Algal Production Weighting			Bottom Ice Algal Production Weighting			Interior Ice Algal Production Weighting		
	Ice (m)	Snow (m)	°C ¹	Ice (m)	Snow (m)	°C ¹	Ice (m)	Snow (m)	°C ¹
1996-97	1.13 (0.56)	0.231 (0.115)	-3.2 (1.74)	1.00 (0.49)	0.205 (0.103)	-3.4 (1.89)	1.32 (0.60)	0.271 (0.121)	-2.8 (1.41)
1997-98	1.12 (0.62)	0.218 (0.119)	-3.4 (1.95)	0.98 (0.53)	0.193 (0.102)	-3.6 (2.08)	1.36 (0.70)	0.263 (0.133)	-2.9 (1.57)
1998-99	1.02 (0.52)	0.217 (0.106)	-3.3 (1.70)	0.94 (0.46)	0.203 (0.102)	-3.5 (1.78)	1.20 (0.57)	0.246 (0.108)	-3.0 (1.48)
1999-00	1.10 (0.55)	0.227 (0.119)	-3.4 (1.75)	1.00 (0.50)	0.203 (0.106)	-3.6 (1.85)	1.29 (0.59)	0.270 (0.129)	-3.0 (1.48)
2000-01	1.12 (0.53)	0.225 (0.125)	-3.4 (1.99)	1.03 (0.50)	0.206 (0.115)	-3.7 (2.13)	1.29 (0.56)	0.262 (0.135)	-3.0 (1.62)
2001-02	1.10 (0.55)	0.229 (0.124)	-3.3 (1.77)	1.00 (0.51)	0.203 (0.111)	-3.5 (1.87)	1.27 (0.58)	0.272 (0.133)	-2.9 (1.49)
2002-03	1.15 (0.58)	0.212 (0.114)	-3.4 (1.89)	1.04 (0.52)	0.191 (0.105)	-3.7 (1.96)	1.35 (0.61)	0.249 (0.121)	-3.0 (1.68)
2003-04	1.13 (0.58)	0.244 (0.136)	-3.2 (1.64)	1.02 (0.52)	0.219 (0.124)	-3.5 (1.72)	1.34 (0.63)	0.288 (0.147)	-2.9 (1.39)
2004-05	1.18 (0.58)	0.251 (0.143)	-3.0 (1.53)	1.08 (0.54)	0.225 (0.130)	-3.2 (1.66)	1.35 (0.60)	0.292 (0.154)	-2.7 (1.22)
2005-06	1.08 (0.52)	0.226 (0.141)	-3.1 (1.60)	1.01 (0.47)	0.205 (0.125)	-3.3 (1.70)	1.21 (0.57)	0.263 (0.159)	-2.8 (1.32)
Mean	1.11 (0.56)	0.228 (0.125)	-3.3 (1.76)	1.01 (0.50)	0.205 (0.113)	-3.5 (1.87)	1.30 (0.60)	0.268 (0.135)	-2.9 (1.47)

¹ Snow/Ice interface temperature, or ice surface temperature if snow was present

Standard deviations of means are found in parentheses.

would be subject to faster freezing, as well as associated lower growth rates and reduced access to convective nutrient replenishment. Bottom algae benefit from slightly colder mean interface temperatures that encourage new bottom ice growth, convection, and the prevention of bottom ablation. Time series plots of temperature show that mean algal production is restricted to areas where the ice temperature is generally > -5.5 °C. Bottom algae are notable for growing preferentially in ice that is colder than the standard mean during late spring and summer, where otherwise bottom ice melt causes loss of these algae to water column.

Algal habitat classification - To investigate the relationship between sea ice

physical characteristics and ice algal production, we pooled daily grid-cell measurements of sea ice algal production from all analysis years, and categorized them by ice thickness, snow thickness, and snow/ice interface temperature. To emphasize the interaction between these sea ice properties, we use surface plots of mean volumetric productivity and total algal primary production, plotted against both sea ice and snow thickness. We note that each grid cell contains a distribution of snow and ice, and the grid cell measurements of production presented are cumulative over multiple ice types present in a grid cell. The snow and ice physical parameters shown are means across the grid cell sea ice distribution.

Bottom productivity was highest in the thinnest ice, and for the most part decreases linearly with increasing ice thickness (Figure 15A). Bottom productivity remains high along an axis defined by the 1:2.5 ratio of snow to ice thickness, which is the approximate maximum snow depth possible for a given ice depth before the surface floods and snow is transformed into snow ice. Along this axis, mean bottom productivity is relatively high under very heavy snow, a result that is an artifact of sub-grid cell averaging (i.e., a grid cell with a mean snow depth of 0.8 m may contain ice with much less snow). There is a remarkable trough of low bottom algal productivity that is apparent under low snow thicknesses of 0.0 - 0.15 m and corresponding to ice depths between 0.2 m and 1.5 m. This combination of ice and snow is reflective of fast-growing wintertime ice that has not had time to accumulate snow, where low light levels and fast bottom ice accretion severely restrict bottom ice algal growth. Productivity is elevated, however, under similarly low snow depths but with higher ice thicknesses (1.0-2.5 m). Thick ice with little snow at all is typical of summertime pack ice that has lost snow due to melting or sublimation. These environments allow bottom ice algal communities greater access to light.

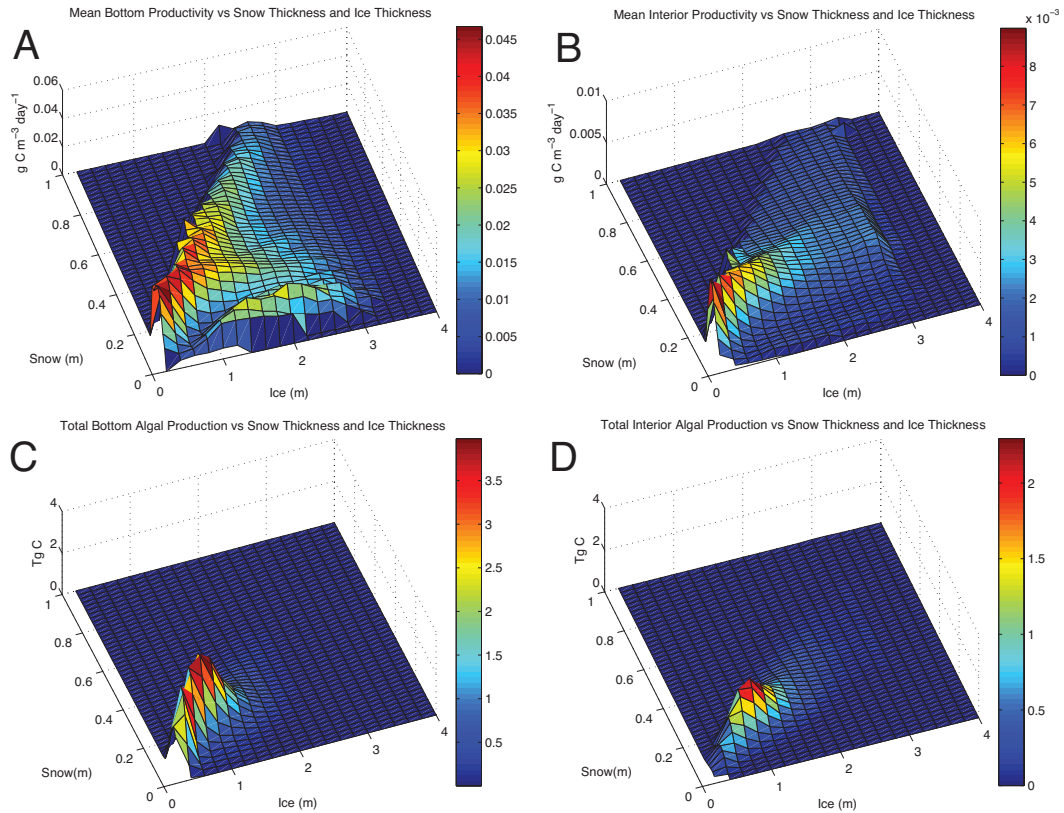


Figure 15. Algal grid cell productivities (A-bottom community, B-interior community) and total algal production (C-bottom community, D-interior community) classified by the ice snow thicknesses in which they occurred.

Similar to bottom ice algae, the volumetric productivity of interior sea ice algae generally decreases in response to increasing ice thickness (Figure 15B). However, there is a plateau of moderately elevated interior ice algal productivity that occurs where 1-3 m ice is associated with 0.2-0.4 m of snow. Lower interior productivities are found under >0.4 m of snow due to severe light limitation. Mean interior algal productivity is extremely low at snow thicknesses < 0.2 m, since substantial snow thickness is usually required to generate the flooded, porous habitats that are optimal for interior ice algal blooms.

The distribution of total algal production in bottom and interior ice was similar with respect to snow and ice thickness, with most production occurring along an axis with a 1:5 ratio of snow to ice thickness (Figure 15C-D). Algal production was generally restricted to ice <1.5 m thick and snow <0.3 m thick. This distribution matches closely that total distribution of ice and snow thickness (not shown). Bottom production was greatest in 0.9 m thick ice and 0.2 m thick snow, which is in approximate agreement with the bottom-production weighted mean ice depth of 1.01 m (Table 7). Peak bottom production (Figure 15C) also coincided with the snow and ice thickness of peak modeled bottom productivity (Figure 15A). Interior ice algae show a peak in production at 1.0 m and 0.2 m snow depth, while mean interior production-weighted mean ice and snow thicknesses are higher, at 1.27 m and 0.268 m, respectively. The snow and ice thicknesses of the peak in total interior ice algal production (Figure 15D) was dissociated from peak productivity (Figure 15B), the later of which took place at much thicker snow and ice depths.

5. Discussion

Here we have provided the first interannual estimates of Antarctic sea ice algal production that dynamically consider the light, temperature, salinity, and nutrient

conditions that control algal growth, with special care taken to simulate the warm porous ice types where algae are most commonly observed. The model results are characterized by high spatial and temporal variability over the range of algal productivity, reflecting the wide variety of ice conditions the model was able to simulate. The large interannual differences in both the location and intensity of ice algal blooms produced by the model illustrate clearly the difficulty of extrapolating sparse point measurements of sea ice algal biomass to estimate total production of the Antarctic ice pack.

In the few cases where regional patterns of sea ice algal variability have been characterized, the model results are consistent with observations. For example, the model produces a distinct offshore band of elevated ice algal production, with significantly lower values to the north and south (Figure 7). Similarly, Arrigo et al. [2003] measured a peak in ice algal biomass along a north-south transect through the interior of the Ross Sea ice pack at approximately 72°S, which decreased markedly toward the Antarctic continent. This same longitudinal pattern in ice algal biomass was found by McMinn and Hegseth [2003] along a north-south transect through sea ice in East Antarctica. In addition, the model produced large blooms of interior sea ice algae in the southern Amundsen, southeastern Ross, and western Weddell sectors, consistent with multiple observations of elevated sea ice algal biomass in these areas during the algal growth season [Ackley et al. 1979; Garrison et al. 1991; Fristen et al. 1994; Fristen et al. 2001; Kattner et al. 2004; Garrison et al. 2005].

Our simulation constitutes a substantial downward revision of total primary production in Antarctic sea ice. At 16.8 Tg C yr⁻¹, our mean annual production for 1996-2006 is only 24-34% of estimates of total annual sea ice algal production based on direct observations of algal biomass [Heywood and Whittaker 1984; Legendre et al. 1992] and 47% of the estimate for interior sea ice algae made by Arrigo et al. [1997,

1998] using a simpler model than was employed here. Interestingly, both Heywood and Whittaker [1984] and Legendre et al. [1992] based their estimate of Antarctic ice algal production on measurements of algal standing stock collected from two ice floes using a bucket in the summer of 1965 [Burkholder and Mandelli 1965]. These floes contained massive blooms in surface layers with Chl *a* concentrations of 305 and 407 mg m⁻³ (10,675-14,245 mg C m⁻³ assuming a C:Chl *a* ratio of 35 as used in the model). Studies considering a spectrum of sea ice algal biomass measurements have since shown that mean sea ice algal biomass is typically much lower than this [Dieckmann et al. 1998; McMinn et al. 2007], and generally agree with the range of mean biomass estimated by our model (Figure 4). Although the model of Arrigo et al. [1997, 1998] focused on interior sea ice algal communities, sea ice in the model was allowed to remain at negative freeboard with nutrients fixed at deep-water values, providing for relatively high rates of algal production. By not accounting for freezing of the slush layer or stagnation of convection under isothermal conditions, both of which can quickly restrict high-biomass interior algal communities via nutrient limitation, nutrient fluxes and rates of algal growth in the model of Arrigo et al. [1997, 1998] are probably too high. Furthermore, their algal growth model was tuned using biomass measurements from the Weddell Sea, which contains the highest rates of Antarctic sea ice algal production in our model.

Overall, the magnitude of sea ice algal production by the model is likely to be conservative, although there is some potential over overestimation as well. Ridging during ice convergence creates ice rubble that is comprised of ~30% void space [Leppäranta and Hakala 1992; Ackley and Sullivan 1994]. While this void space has the potential to support interior ice algal growth, it is neglected in the model. Given that sea ice during the algal growth season is mostly melting and breaking up, rather than converging, we do not expect these void spaces to contribute significantly to total

ice algal production. In addition, McMinn and Hegseth [2003] observed increased biomass of interior sea ice algal communities during summer at the periphery of ice floes. Our model does not account for enhanced light transmission and nutrient transport at ice flow edges and likely underestimates production in these areas. Brash ice, or areas of sea ice composed of ice chunks <2 m in size, can contain algal biomass sufficiently high to be visible to the naked eye [Steer et al. 2008]. Although this type of ice is not considered in the model, no biological measurements are available for this ice type and it is unclear whether these algae should be classified as ice algae or phytoplankton. Finally, the highest measured sea ice algae biomass comes from land fast sea ice, where massive bottom communities can form [Arrigo et al. 1993, 1995]. Coastal areas, where most land fast ice is found, are not included in the model due to the contamination of satellite pixels by land in these areas. Fortunately, fast ice constitutes a small portion (~1-2% [Legendre et al. 2002]) of the total ice area, so despite its high productivity, this ice type likely contributes only a small fraction of total sea ice algal production. The model may overestimate Antarctic ice algal production due to the assumption that nutrients are replete in surface waters under sea ice. Nutrient transfer from the water column to the sea ice may be overestimated since fixed deep-water nutrient values were used (although the rate of delivery was controlled by eddy diffusion). Fortunately, there is very little evidence of reduced surface water nutrient concentrations under sea ice in the Antarctic [Barry 1988; Melnikov 1998], indicating our use of deep-water values is valid.

One striking characteristic of sea ice algal production was the development of severe nutrient limitation early in the spring growth season that curtailed peak production in all years of our simulation. A comparison of the rates of primary production and nutrient limitation terms for bottom and interior ice algae communities indicates that bottom algae were on average more severely nutrient limited. Nutrient

limitation of bottom ice algal communities has been observed in the Arctic and Antarctic [Maestrini et al. 1986; Cota et al. 1987; Gosselin et al. 1990; Robinson et al. 1998], with the degree of nutrient limitation increasing upward from the ice-water interface [McMinn et al. 1999]. Nutrient limitation of interior algal communities has not been directly measured but can be inferred from depleted nutrient concentrations that are observed in ice core measurements [Garrison et al. 1991; Dieckmann et al. 1991; Fritsen et al. 2001, Arrigo et al. 2003]. Consequently, estimates of sea ice algal production based solely upon the availability of light, without consideration of nutrient dynamics, are likely to overestimate production and biomass accumulation [Raymond et al. 2009, Fritsen et al. 2010].

Antarctic sea ice extent has been studied extensively and has been found to co-vary with indices of the ENSO phenomenon and the Antarctic dipole (or Southern Annular Mode, SAM). The directions and modes of variability are regionally distinct and are typically explained by the prevailing wind direction and associated changes in atmospheric properties that these winds bring [Yuan and Maritinson 2000, 2001; Yuan 2004; Stammerjohn et al. 2008]. Inter-sector comparisons of sea ice algal production indicate that at the gross scale, total sea ice algal production is linearly related to sea ice extent and is therefore likely to co-vary with the same climate indices.

Interannual differences in sea ice presence were not correlated with total ice algal production, however, indicating that other sea ice characteristics are more important drivers of variability in sea ice algal production over the modeled time period. Characterizing the relationship between sea ice algal production and physicochemical characteristics of the sea ice habitat is difficult, however, as evidenced the few significant linear relationships produced by our correlation analysis at the scale of our analysis sectors. This is not surprising when one considers the complexity of sea ice physics, and the resulting observed (and modeled) level of heterogeneity in present in

the Antarctic sea ice pack. Future efforts wishing to establish relationships of sea ice algal ecology to environmental variability should conduct examinations at smaller spatial scales than attempted in this study.

The relationship of the MEI to mean bottom algal productivity (mg C m^{-2} sector, as opposed to total internal production Tg C sector^{-1}) is intriguing, despite our short 10-year model run. We note that annual algal production was lowest (15.5 Tg C) during the massive El Niño event of 1997-98, while annual production was highest (18.1 Tg C) the following season during a strong La Niña event. The dependence of sea ice algal production on specific sea ice characteristics indicates that small- and/or vertical-scale sea ice characteristics, or some combination of those sea ice characteristics that reduce algal productivity, may be predictable by climate indices.

Based on the productivity-weighted mean ice and snow depths, as well as surface plots of production, sea ice algae generally grew non-preferentially in the ice that was available. Since sea ice algae in the model are very sensitive to the ice environment, these results indicate that physical forcing may create sea ice microhabitats conducive to algal growth in commonly-available ice of a variety of different thickness and snow covers. The notable exception was thin ice (0.2-0.4 m), which exhibited the highest volumetric productivities (Figure 15A), but failed to exhibit correspondingly high levels of production (Figure 15C). Thin ice, while extremely common, is ephemeral, thereby limiting its contribution to total production at it either melts or grows thicker.

Overall, temperature and precipitation in the Antarctic are forecast to increase by 1-3°C and 20%, respectively, during the next century [IPCC report]. Changes to the sea ice system will vary regionally, however, making it difficult to predict the overall response of sea ice algae to climate change. Where significant regional warming has already been observed in the Antarctic, the sea ice responds by forming later and retreating earlier [Stammerjohn et al. 2008]. Based on our model results, an earlier ice

retreat alone might not impact sea ice algal production, since sea ice algae are already nutrient limited by the time of ice retreat. However, early ice retreat is likely to be associated with earlier melting conditions, which can induce stratification within the ice pack and prevent the convection-driven brine exchange that can resupply nutrients to ice-bound algae. Earlier warming could potentially offset decreased production by alleviating salinity limitation and increasing algal growth rates, although the positive impact of early warming on total algal production is likely to be small since algae are net limited by light during springtime. Therefore, early sea ice warming, even if it is not accompanied by ice retreat, is likely to shorten the ice algal growing season. We plan to use the model to address possible climate change scenarios in future studies.

The most recent estimate of pelagic primary productivity in the Southern Ocean is 1949 Tg C yr⁻¹, of which ~180.1 Tg C yr⁻¹ was associated with the sea ice zone [Arrigo et al. 2008b]. Primary production in Antarctic pack ice therefore contributes less than 1% of total primary production in the Southern Ocean, and constitutes ~8.5% of total primary production in the seasonal sea ice zone. A simple calculation demonstrates that annual sea ice production is likely to have little impact on dissolved inorganic carbon (DIC) concentrations in ice-covered waters. Assuming a surface mixed layer of 70 m [Yager et al. 1995] and a DIC concentration of 2200 µM [Arrigo et al. 2008b], there would be 1863 g DIC m⁻² within the surface mixed layer.

Assuming a mean annual production rate of 0.89 g C m⁻² yr⁻¹, sea ice algae have little potential to influence DIC content in the surface ocean of the sea ice zone. Even if DIC removal by sea ice algae is restricted to the top 2 m of the water column, DIC would only drop by 1.7% and, using standard under-ice water properties, lower pCO₂ by about 10 µatm. Typical mixed layers in the sea ice zone of the Southern Ocean are much deeper than 2 m [Ikeda 1986; Sirevaag et al. 2010], therefore model results indicate that early-season drawdown of DIC by sea ice algae is not of sufficient

magnitude to affect CO₂ flux or the carbon cycle [Yager et al. 1995].

Widespread ice algal growth within the sea ice zone occurs relatively early in the springtime and extends locally well into the autumn (Figures 8,9) when accessible algal biomass could serve as food to consumers in ice-covered areas. The large spatial variability in annual production means that even if sea ice is consistently present, it provides an unpredictable food source for pelagic grazers. Spatial and temporal variability in sea ice algal production might consequently play a role in the ecology and life histories of marine organisms such as Antarctic krill, which likely benefit from ice algae as a winter food source [Daly 1990], yet are characterized by highly episodic population recruitment [Quetin and Ross 2003].

LIST OF REFERENCES

- Ackley, S., K. Buck, and S. Taguchi (1979), Standing crop of algae in the sea ice of the Weddell Sea region, *Deep-Sea Research*, 26A, 269-281.
- Ackley, S., C. Fritsen, V. I. Lytle, and C. W. Sullivan (1996), Freezing driven upwelling in antarctic sea ice biological systems, *Proceedings of the 17th NIPR Symposium on Polar Biology*, 9, 45-59.
- Ackley, S. F., M. J. Lewis, C. H. Fritsen, and H. Xie (2008), Internal melting in Antarctic sea ice: Development of “gap layers”, *Geophys. Res. Lett.*, 35(L11503), 1-5, doi:10.1029/2008GL033644.
- Ackley, S., and C. Sullivan (1994a), Physical controls on the development and characteristics of Antarctic sea ice biological communities: a review and synthesis, *Deep-sea research. Part 1. Oceanographic research papers*, 41(10), 1583-1604.
- Ackley, S., and C. Sullivan (1994b), Physical controls on the development and characteristics of Antarctic sea ice biological communities - a review and synthesis, *Deep Sea Research Part I: Oceanographic Research Papers*, 41, 1583, doi:10.1016/0967-0637(94)90062-0.
- Adolphs, U. (1998), Ice thickness variability, isostatic balance and potential for snow ice formation on ice floes in the south polar Pacific Ocean, *J. Geophys. Res.*, 103(C11), 24675-24692, doi:10.1029/98JC02414.
- Ainley, D. G., C. Tynan, and I. Stirling (2003), Sea Ice: A Critical Habitat for Polar Marine Mammals and Birds, *Sea Ice: An Introduction to its Physics, Chemistry, Biology and Geology*, edited by D. N. Thomas, and G. S. Dieckmann, pp. 240-266, Wiley-Blackwell, Hoboken, N. J.
- Andreas, E. L., R. E. Jordan, and A. P. Makshtas (2005), Parameterizing turbulent exchange over sea ice: the ice station weddell results, *Boundary-Layer Meteorology*, 114, 439-460, doi:10.1007/s10546-004-1414-7.
- Andreas, E. L., and S. F. Ackley (1982), On the Differences in Ablation Seasons of Arctic and Antarctic Sea Ice, *Journal of the Atmospheric Sciences*, 39, 440-447.
- Armstrong, R. L., K. W. Knowles, M. J. Brodzik and M. A. Hardman (1994), DMSP SSM/I Pathfinder daily EASE-Grid brightness temperatures. <http://nsidc.org/data/nsidc-0032.html>, Natl. Snow and Ice Data Cent., Boulder, C. O. (Updated 2008.)
- Arrigo, K. (2003), Primary production in sea ice, in *Sea Ice: An Introduction to its Physics, Chemistry, Biology and Geology*, edited by D. N. Thomas, and G. S. Dieckmann, pp. 143-183, Wiley-Blackwell, Hoboken, N. J.
- Arrigo, K., C. Sullivan, and J. Kremer (1991), A bio-optical model of Antarctic sea ice, *J. Geophys. Res.*, 96(C6), 10581-10592.
- Arrigo, K., and C. Sullivan (1992), The influence of salinity and temperature covariation on the photophysiological characteristics of antarctic sea ice microalgae, *J. Phycol.*, 28, 746-756.
- Arrigo, K., G. Dieckmann, M. Gosselin, D. Robinson, C. Fritsen, and C. Sullivan (1995), High resolution study of the platelet ice ecosystem in McMurdo Sound, Antarctica: biomass, nutrient, and production profiles within a dense microalgal bloom, *Mar. Ecol. Prog. Ser.*, 127, 255-268.

- Arrigo, K., D. Worthen, M. Lizotte, and P. Dixon (1997), Primary production in Antarctic sea ice, *Science* 276, 394-397.
- Arrigo, K. R. (2003), Physical control of chlorophyll a, POC, and TPN distributions in the pack ice of the Ross Sea, Antarctica, *J. Geophys. Res.*, 108(C10), 23, doi:10.1029/2001JC001138.
- Arrigo, K. R., D. H. Robinson, and C. W. Sullivan (1993a), A high resolution study of the platelet ice ecosystem in McMurdo Sound, Antarctica: photosynthetic and bio-optical characteristics of a dense microalgal bloom, *Mar. Ecol. Prog. Ser.*, 98, 173-185.
- Arrigo, K. R., J. N. Kremer, and C. W. Sullivan (1993b), A simulated Antarctic fast ice ecosystem, *J. Geophys. Res.*, 98(C4), 6929-6946.
- Arrigo, K. R., and C. W. Sullivan (1994), A high-resolution bio-optical model of microalgal growth: testing using sea-ice algal community time-series data, *Limnology and Oceanography*, 39(3), 609-631.
- Arrigo, K. R., G. L. van Dijken, and J. C. Comiso (1996), Estimating the Thickness of Sea Ice Snow Cover in the Weddell Sea from Passive Microwave Brightness Temperatures, *NASA Technical Memorandum*, 104640.
- Arrigo, K. R., D. L. Worthen, P. Dixon, and M. P. Lizotte (1998), Primary productivity of near surface communities within Antarctic pack ice, *Antarctic Research Series*, 73, 23-43.
- Arrigo, K. R., and D. N. Thomas (2004), Large scale importance of sea ice biology in the Southern Ocean, *Antarctic Science*, 16(4), 471-486, doi:10.1017/S0954102004002263.
- Arrigo, K. R., and G. L. van Dijken (2007), Interannual variation in air-sea CO₂ flux in the Ross Sea, Antarctica: A model analysis, *J. Geophys. Res.*, 112, C03020, doi:10.1029/2006JC003492.
- Arrigo, K. R., M. C. Long, and G. van Dijken (2008a), Coastal Southern Ocean: A strong anthropogenic CO₂ sink, *Geophys. Res. Lett.*, 35(L21602), doi:10.1029/2008GL035624.
- Arrigo, K. R., G. L. van Dijken, and S. Bushinsky (2008b), Primary production in the Southern Ocean, 1997–2006, *J. Geophys. Res.*, 113(C8), C08004, doi:10.1029/2007JC004551.
- Assur, A. Composition of sea ice and its tensile strength, in *Arctic Sea Ice, N. A. S. N. R. C. Publ.*, 598, 106-138, 1958.
- Barber, D., R. De Abreu, and E. LeDrew (1991), Optical Extinction And Microwave Scattering Within A Seasonally Varying Snow Covered Sea Ice Surface, *Geoscience and Remote Sensing Symposium*, 799-802.
- Barry, J. (1988), Hydrographic patterns in McMurdo Sound, Antarctica and their relationship to local benthic communities, *Polar Biology*, 8(5), 377-391.
- Battle, M., M. L. Bender, P. P. Tans, J. W. C. White, J. T. Ellis, T. Conway, and R. J. Francey (2000), Global Carbon Sinks and Their Variability Inferred from Atmospheric O₂ and δ¹³C, *Science*, 287, 2467-2470.
- Bindschadler, R. (1990), SeaRISE: a multidisciplinary research initiative to predict rapid changes in global sea level caused by collapse of marine ice sheets, NASA Conference Publication 3075, NASA Office of Management, Scientific and Technical Division, Washington, D. C.

- Bissinger, J., D. Montagnes, J. Sharples, and D. Atkinson (2008), Predicting marine phytoplankton maximum growth rates from temperature: Improving on the Eppley curve using quantile regression, *Limnology and Oceanography*, 53(2), 487-493.
- Bitz, C., M. Holland, and M. Eby (2001), Simulating the ice-thickness distribution in a coupled climate model, *J. Geophys. Res.*, 106(C2), 2441-2464.
- Bitz, C., and W. Lipscomb (1999), An energy-conserving thermodynamic model of sea ice, *J. Geophys. Res.*, 104(C7), 15669-15677.
- Briegleb, B. P., and B. Light (2007), A Delta-Eddington Multiple Scattering Parameterization for Solar Radiation in the Sea Ice Component of the Community Climate System Model, *NCAR Technical Note*, 1-108.
- Brodzik, M. J. and K. W. Knowles (2002), EASE-Grid: A Versatile Set of Equal-area Projections and Grids, in *Discrete Global Grids*, edited by M. Goodchild, National Center for Geographic Information & Analysis, Santa Barbara, C.A.
- Bunt, J. S. (1968), Microalgae of the Antarctic pack ice zone, in *Symposium on Antarctic Oceanography*, edited by R Currie, pp. 198-218, W. Heffner & Sons Ltd., Cambridge, U.K.
- Burkholder, P., and E. Mandelli (1965), Productivity of microalgae in Antarctic sea ice, *Science*, 149, 872-874.
- Comiso, J. C. (1986), SSM/I Sea Ice Concentrations Using the Bootstrap Algorithm, NASA Reference Publication 1380, 40 pp., Goddard Space Flight Center, M. L.
- Comiso, J. C., and C. W. Sullivan (1986), Satellite Microwave and In-Situ Observations of the Weddell Sea Ice Cover and its Marginal Ice Zone, *J. Geophys. Res.*, 91(C8), 9663-9681.
- Comiso, J. C., C .L. Parkinson, R. Gersten, and L. Stock (2008), Accelerated decline in the Arctic sea ice cover, *Geophys. Res. Lett.*, 35, 1-6, doi:10.1029/2007GL031972.
- Cota, G. F., J. L. Anning, N. H. F. Watson, S. J. Prinsenberg, E. B. Bennett, and M. R. Lewis (1987), Nutrient fluxes during extended blooms of Arctic ice algae, *J. Geophys. Res.*, 92, 1951, doi:10.1029/JC092iC02p01951.
- Cox, G. F. N., and W. F. Weeks (1983), Equations for determining the gas and brine volumes in sea-ice samples, *CRREL Res. Rep.* 354, U.S. Army Cold Reg. Res. and Eng. Lab., Hanover, N. H.
- Cox, G., and W. Weeks (1975), Brine drainage and initial salt entrapment in sodium chloride ice, *J. Geophys. Res.*, 93(C10), 12449-12460.
- Cox, G., and W. Weeks (1988), Numerical simulations of the profile properties of undeformed first-year sea ice during the growth season, *J. Geophys. Res.*, 93(C10), 12449-12460.
- Curry, J. A., J. L Schramm, and E. E. Ebert (1995), Sea ice-albedo climate feedback mechanism, *J. Climate*, 8, 240-247.
- Daly, K. (1990), Overwintering development, growth, and feeding of larval Euphausia superba in the Antarctic marginal ice zone, *Limnology and Oceanography*, 35(7), 1564-1576.

Daly, K., and M. Macaulay (1988), Abundance and distribution of krill in the ice edge zone of the Weddell Sea, austral spring 1983, *Deep Sea Research Part A. Oceanographic Research Papers*, 35, pp. 21-41, doi:10.1016/0198-0149(88)90055-6.

Dieckmann, G., M. Lange, S. Ackley, and J. Jennings (1991), The nutrient status in sea ice of the Weddell Sea during winter: effects of sea ice texture and algae, *Polar Biology*, 11(7), 449-456.

Dieckmann, G. S., H. Eicken, C. Haas, D. L. Garrison, M. Gleitz, M. Lange, E.-M. Nothig, M. Spindler, C. W. Sullivan, D. N. Thomas, and J. Weissenberger (1998), A compilation of data on sea ice algal standing crop from the Bellingshausen, Amundsen, and Weddell Seas from 1983 to 1994, in *Antarctic Sea Ice: Biological Processes, Interactions and Variability, Antarct. Res. Ser.*, vol. 73, edited by M. P. Lizotte and K. R. Arrigo, pp. 85-92, AGU, Washington, D. C.

Dieckmann, G. S., and H. H. Hellmer (2003), The importance of sea ice: an overview, in *Sea Ice: An Introduction to its Physics, Chemistry, Biology and Geology*, edited by D. N. Thomas, and G. S. Dieckmann, pp. 1-21, Wiley-Blackwell, Hoboken, N. J.

Ebert, E., and J. Curry (1993), An intermediate one-dimensional thermodynamic sea ice model for investigating ice-atmosphere interactions, *J. Geophys. Res.*, 98(C6), 10085-10109.

Ehn, J. K., T. N. Papakyriakou, and D. G. Barber (2008), Inference of optical properties from radiation profiles within melting landfast sea ice, *J. Geophys. Res.*, 113(C9), 15, doi:10.1029/2007JC004656.

Eicken, H. (1992), Salinity profiles of Antarctic sea ice: field data and model results, *J. Geophys. Res.*, 97(C10), 15545-15557.

Eicken, H. (2003), From the microscopic, to the macroscopic, to the regional scale: growth, microstructure and properties of sea ice, *Sea Ice: An Introduction to its Physics, Chemistry, Biology and Geology*, edited by D. N. Thomas, and G. S. Dieckmann, pp. 22-81, Wiley-Blackwell, Hoboken, N. J.

Eicken, H., M. Lange, and G. Dieckmann (1991), Spatial variability of sea-ice properties in the northwestern Weddell Sea, *J. Geophys. Res.*, 96(C6), 10603-10615.

Eicken, H., M. A. Lange, and P. Wadhams (1994), Characteristics and distribution patterns of snow and meteoric ice in the Weddell Sea and their contribution to the mass balance of sea ice, *Annales Geophysicae*, 12, 80-93.

Eicken, H., H. R. Krouse, D. Kadko, and D. K. Perovich (2002), Tracer studies of pathways and rates of meltwater transport through Arctic summer sea ice, *J. Geophys. Res.*, 107(C10), 20, doi:10.1029/2000JC000583.

Eppley, R. W. (1972), Temperature and phytoplankton growth in the sea, *Fish. Bull.*, 70, 1063-1085.

Feltham, D. L., N. Untersteiner, J. S. Wetlaufer, and M. G. Worster (2006), Sea ice is a mushy layer, *Geophys. Res. Lett.*, 33, L14501, doi:10.1029/2006GL026290.

Flato, G., and W. Hibler III (1995), Ridging and strength in modeling the thickness distribution of Arctic sea ice, *J. Geophys. Res.*, 100(C9), 18611.

Freitag, J. (1999), Untersuchungen zur Hydrologie des arktischen Meereises - Konsequenzen für den kleinskaligen Stofftransport (in German), *Berichte zur Polarforschung* 325, Alfred-Wegener Institut für Polar- und Meeresforschung, Bremerhaven, Germany.

- Freitag, J., and H. Eicken (2003), Meltwater circulation and permeability of Arctic summer sea ice derived from hydrological field experiments, *Journal of Glaciology*, 49, 349.
- Fritsen, C. H., V. Lytle, S. F. Ackley, and C. Sullivan (1994), Autumn Bloom of Antarctic Pack-Ice Algae, *Science*, 266, 264-266.
- Fritsen, C. H., S. L. Coale, D. R. Neenan, A. H. Gibson, and D. L. Garrison (2001a), Biomass, production and microhabitat characteristics near the freeboard of ice floes in the Ross Sea, Antarctica, during the austral summer, *Annals of Glaciology*, 33, 280-286.
- Fritsen, C. H., S. F. Ackley, J. N. Kremer, and C. W. Sullivan (1998), Flood-freeze cycles and microalgal dynamics in Antarctic pack ice, in *Antarctic Sea Ice: Biological Processes, Interactions and Variability, Antarct. Res. Ser.*, vol. 73, edited by M. P. Lizotte and K. R. Arrigo, pp. 1-22, AGU, Washington, D. C.
- Fritsen, C. H., J. Memmott, and F. Stewart (2008), Inter-annual sea-ice dynamics and micro-algal biomass in winter pack ice of Marguerite Bay, Antarctica, *Deep Sea Research Part II: Topical Studies in Oceanography*, 55(18-19), 2059-2067, doi:10.1016/j.dsr2.2008.04.034.
- Fritsen, C. H., J. C. Memmott, R. M. Ross, L. B. Quetin, M. Vernet, and E. D. Wirthlin (2010), The timing of sea ice formation and exposure to photosynthetically active radiation along the Western Antarctic Peninsula, *Polar Biology*, 34(5), 683-692, doi:10.1007/s00300-010-0924-7.
- Fukusako, S. (1990), Thermophysical properties of ice, snow, and sea ice, *International Journal of Thermophysics*, 11(2), 353-372.
- Garrison, D. L., S. F. Ackley, and K. R. Buck (1983), A physical mechanism for establishing algal populations in frazil ice, *Nature*, 306, 363-365.
- Garrison D. L., C. W. Sullivan, and S. F. Ackley (1986), Sea ice microbial communities in Antarctica. *BioScience*, 36, 243-250.
- Garrison, D., K. Buck, and G. Fryxell (1987), algal assemblages in antarctic pack ice and in ice-edge plankton, *J Phycol*, 23, 564-572.
- Garrison D.L., and S. Mathot (1996), Pelagic and sea ice microbial communities, in *Foundations for ecological research west of the Antarctic Peninsula, Antarctic Research Series*, 70, edited by R. M. Ross, E. E. Hofmann, and L. B. Quetin, pp. 155-172, AGU, Washington, D. C.
- Garrison, D., A. Gibson, S. Coale, M. Gowing, Y. B. Okolodkov, C. H. Fritsen, and M. O. Jeffries (2005), Sea-ice microbial communities in the Ross Sea: autumn and summer biota, *Mar. Ecol. Prog. Ser.*, 300, 39-52.
- Garrison, D. L., M. O. Jeffries, A. Gibson, S. L. Coale, D. Neenan, C. Fritsen, Y. B. Okolodkov, and M. M. Gowing (2003), Development of sea ice microbial communities during autumn ice formation in the Ross Sea, *Mar. Ecol. Prog. Ser.*, 259, 1-15.
- Garrison, D., and K. Buck (1989), The biota of Antarctic pack ice in the Weddell Sea and Antarctic Peninsula regions, *Polar Biology*, 10(3), 211-219.
- Garrison, D., and K. Buck (1991), Surface-layer sea ice assemblages in Antarctic pack ice during the austral spring: Environmental conditions, primary production and community structure., *Marine ecology progress series. Oldendorf*, 75(2), 161-172.

- Gille, S. T. (2008), Decadal-scale temperature trends in the Southern Hemisphere ocean, *J. Clim.*, 21, 4749-4765.
- Golden, K. M., S. F. Ackley, and V. I. Lytle (1998), The percolation phase transition in sea ice, *Science*, 282, 2238-2241.
- Golden, K. M., H. Eicken, A. L. Heaton, J. Miner, D. J. Pringle, and J. Zhu (2007), Thermal evolution of permeability and microstructure in sea ice, *Geophys. Res. Lett.*, 34(16), 6, doi:10.1029/2007GL030447.
- Gong, D., and S. Wang (1999), Definition of Antarctic oscillation index, *Geophys. Res. Lett.*, 26(4), 459-462, doi:10.1029/1999GL900003.
- Gosselin, M., L. Legendre, C. Therriault, and S. Demers (1990), Light and nutrient limitation of sea-ice microalgae (Hudson Bay, Canadian Arctic), *J Phycol.*, 26(2), 220-232.
- Gregg, W., and K. Carder (1990), A simple spectral solar irradiance model for cloudless maritime atmospheres, *Limnology and Oceanography*, 35(8), 1657-1675.
- Grenfell, T. C., and G. A. Maykut (1977), The optical properties of ice and snow in the Arctic Basin, *Journal of Glaciology*, 18, 445-463.
- Grossi, S. M., S. T. Kottmeier, R. L. Moe, G. T. Taylor, and C. W. Sullivan (1987), Sea ice microbial communities. VI. Growth and primary production in bottom ice under graded snow cover, *Mar. Ecol. Prog. Ser.*, 35, 153-164.
- Guzman, O. (1983), Distribution and abundance of Antarctic krill (*Euphausia superba*) in the Bransfield Strait, in *On the Biology of Krill Euphausia superba*, edited by S. B. Schnack, pp. 169-190, Alfred-Wegener-Institute, Bremerhaven, F. R. G.
- Haas, C. (2003), Dynamics versus Thermodynamics: The Sea Ice Thickness Distribution, *Sea Ice: An Introduction to its Physics, Chemistry, Biology and Geology*, edited by D. N. Thomas, and G. S. Dieckmann, pp. 1-30, Wiley-Blackwell, Hoboken, N. J.
- Heil, P., C. Fowler, and S. Lake (2006), Antarctic sea-ice velocity as derived from SSM/I imagery, *Annals of Glaciology*, 44, 361-366.
- Heywood, R. B., and T. M. Whitaker (1984), The marine flora, in *Antarctic Ecology*, vol. 2, edited by R. M. Laws, pp. 373-419, Academic Press, London, U.K.
- Hibler, W. (1980), Modeling a variable thickness sea ice cover, *Monthly Weather Review*, 108, 1943-1973.
- Hibler, W. D., III (1979), A Dynamic Thermodynamic Sea Ice Model, *Journal of Physical Oceanography*, 9, 815-846, doi:10.1175/1520-0485(1979)009<0815:ADTSIM>2.0.CO;2.
- Hofmann, E., and E. Murphy (2004), Advection, krill, and Antarctic marine ecosystems, *Antarctic Science*, 14(4), 487-499, doi: 10.1017/S0954102004002275.
- Holland, M., C. Bitz, E. Hunke, W. Lipscomb, and J. Schramm (2006), Influence of the sea ice thickness distribution on polar climate in CCSM3, *J Climate*, 19(11), 2398-2414.

- Holland, M. M., M. C. Serreze, and J. Stroeve (2008), The sea ice mass budget of the Arctic and its future change as simulated by coupled climate models, *Climate Dynamics*, 34(2-3), 185-200, doi:10.1007/s00382-008-0493-4.
- Horner, R., S. Ackley, G. Dieckmann, B. Gulliksen, T. Hoshiai, L. Legendre, I. Melnikov, W. Reeburg, M. Spindler, and C. Sullivan (1992), Ecology of sea ice biota, *Polar Biology*, 12, 417-427.
- Houghton, R. A. Balancing the global carbon budget. *Annu. Rev. Earth Planet. Sci.*, 35, 313–347.
- Hudier, E., R. Ingram, and K. Shirasawa (1995), Upward flushing of sea water through first year ice, *Atmosphere-Ocean*, 33(3), 569-580.
- Hunke, E. C., and W. H. Lipscomb (2001), CICE: *The Los Alamos Sea Ice Model documentation and software, version 3*, Los Alamos National Laboratory Tech. Rep. LA-CC-98-16 v. 3, 52 pp, Los Alamos, N. M.
- Hunke, E., and J. Dukowicz (1997), An elastic-viscous-plastic model for sea ice dynamics, *Journal of Physical Oceanography*, 1849-1867.
- Hunt, G. L., P. J. Stabeno, G. Walters, E. Sinclair, R. D. Brodeur, J. M. Napp, and N. A. Bond (2002), Climate change and control of the southeastern Bering Sea pelagic ecosystem, *Deep Sea Research, Part II*, 49, 5821-5853.
- Ikeda, M. (1986), A mixed layer beneath melting sea ice in the marginal ice zone using a one-dimensional turbulent closure model, *J. Geophys. Res.*, 91(C), 5054-5060, doi:10.1029/JC091iC04p05054.
- IPCC (2007), *Climate Change 2007: Impacts, Adaptation and Vulnerability—Contribution of Working Group II to the Third Assessment Report of the Intergovernmental Panel on Climate Change*, edited by M. L. Parry, O. F. Canziani, J. P. Palutikof, P. J. van der Linden and C. E. Hanson, pp. 683-686, Cambridge Univ. Press, New York.
- Jackson, M., and M. Cheadle (1998), A continuum model for the transport of heat, mass and momentum in a deformable, multicomponent mush, undergoing solid-liquid phase change, *International Journal of Heat and Mass Transfer*, 41(8-9), 1035-1048.
- Janech, M. G., A. Krell, T. Mock, J. Kang, and J. A. Raymond (2006), ICE-BINDING PROTEINS FROM SEA ICE DIATOMS (BACILLARIOPHYCEAE)1, *J Phycol.*, 42(2), 410-416, doi:10.1111/jpy.2006.42.issue-2.
- Jeffries, M. O., H. Roy Krouse, and B. Hurst-Cushing (2001), Snow-ice accretion and snow-cover depletion on Antarctic first-year sea-ice floes, *Annals of Glaciology*, 32, 51-60.
- Jin, Z., K. Stamnes, W. F. Weeks, and S. Tsay (1994), The effect of sea ice on the solar energy budget in the atmosphere-sea ice-ocean system: A model study, *J. Geophys. Res.*, 99(C12), 25281-25294, doi:10.1029/94JC02426.
- Jin, M., C. Deal, J. Wang, V. Alexander, R. Gradinger, S. Saitoh, T. Iida, Z. Wan, and P. Stabeno (2007), Ice-associated phytoplankton blooms in the southeastern Bering Sea, *Geophys. Res. Lett.*, 35, L06612, doi:10.1029/2006GL028849.
- Kanamitsu, M., W. Ebisuzaki, J. Woolen, S. K. Yang, J. J. Hnilo, M. Fiorino, and G. L. Potter (2002). NCEP-DOE AMIP-II Reanalysis (R-2), *Bulletin Amer. Metero. Soc.*, 83, 1631-1643.

- Kattner, G., D. Thomas, C. Haas, H. Kennedy, and G. Dieckmann (2004), Surface ice and gap layers in Antarctic sea ice: highly productive habitats, *Mar. Ecol. Prog. Ser.*, 277, 1-12.
- Keeling, R. F., S. C. Piper, and M. Heimann (1996), Global and hemispheric CO₂ sinks deduced from changes in atmospheric O₂ concentration, *Nature*, 381, 218-221.
- Kipfstuhl, J. (1991), On the formation of underwater ice and the growth and energy budget of the sea ice in Atka Bay, Antarctica, *Ber. Polarforsch.*, 85, pp. 1-88.
- Kottmeier, C., K. Frey, M. Hasel, and O. Eisen (2003), Sea ice growth in the eastern Weddell Sea in winter, *J. Geophys. Res.*, 108(C4), 1-13, doi:10.1029/2001JC001087.
- Krembs, C., T. Mock, and R. Gradinger (2001), A mesocosm study of physical-biological interactions in artificial sea ice: effects of brine channel surface evolution and brine movement on algal biomass, *Polar Biology*, 24(5), 356-364, doi:10.1007/s003000000219.
- Lavoie, D., K. Denman, and C. Michel (2005), Modeling ice algal growth and decline in a seasonally ice-covered region of the Arctic (Resolute Passage, Canadian Archipelago), *J. Geophys. Res.*, 110, C11009, doi:10.1029/2005JC002922.
- Legendre, L., S. Ackley, G. Dieckmann, B. Gulliksen, R. Horner, T. Hoshiai, I. Melnikov, W. Reeburgh, M. Spindler, and C. Sullivan (1992), Ecology of sea ice biota, *Polar Biology*, 12, 429-444.
- Lei, R., Z. Li, B. Cheng, Z. Zhang, and P. Heil (2010), Annual cycle of landfast sea ice in Prydz Bay, east Antarctica, *J. Geophys. Res.*, 115(C2), C02006, doi:10.1029/2008JC005223.
- Leppäranta, M., M. Lensu, P. Kosloff, and B. Veitch (1995), The life story of a first-year sea ice ridge, *Cold Regions Science and Technology*, 23(3), 279-290.
- Li, L., and J. Pomeroy (1997), Probability of occurrence of blowing snow, *J. Geophys. Res.*, 102(D18), 21955.
- Light, B., G. Maykut, and T. C. Grenfell (2003), A two-dimensional Monte Carlo model of radiative transfer in sea ice, *J. Geophys. Res.*, 108(3219), 10.1029.
- Light, B., G. A. Maykut, and T. C. Grenfell (2004), A temperature-dependent, structural-optical model of first-year sea ice, *J. Geophys. Res.*, 109, 06013, doi:10.1029/2003JC002164.
- Light, B., T. C. Grenfell, and D. K. Perovich (2008), Transmission and absorption of solar radiation by Arctic sea ice during the melt season, *J. Geophys. Res.*, 113(C3), 19, doi:10.1029/2006JC003977.
- Lipscomb, W. H., E. C. Hunke, W. Maslowski, and J. Jakacki (2007), Ridging, strength, and stability in high-resolution sea ice models, *J. Geophys. Res.*, 112(C3), doi:10.1029/2005JC003355.
- Lipscomb, W., and E. Hunke (2004), Modeling Sea Ice Transport Using Incremental Remapping, *Monthly Weather Review*, 132(6), 1341-1354.
- Lizotte, M. (2001), The Contributions of Sea Ice Algae to Antarctic Marine Primary Production, *American Zoology*, 41, 57-73.
- Lizotte, M., and C. Sullivan (1992), Biochemical composition and photosynthate distribution in sea ice microalgae of McMurdo Sound, Antarctica: evidence for nutrient stress during the spring bloom, *Antarctic Science*, 4(01), 23-30.

- Loeb, V., V. Siegel, O. Holm-Hansen, R. Hewitt, W. Fraser, W. Trivelpiece, and S. Trivelpiece (1997), Effects of sea-ice extent and krill or salp dominance on the Antarctic food web, *Nature*, 387(6636), 897-900.
- Lytle, V., and S. F. Ackley (1996), Heat flux through sea ice in the western Weddell Sea: Convective and conductive transfer processes, *J. Geophys. Res.*, 101(C4), 8853-8868.
- Maestrini, S., M. Rochet, L. Legendre, and S. Demers (1986), Nutrient limitation of the bottom-ice microalgal biomass (southeastern Hudson Bay, Canadian Arctic), *Limnology and Oceanography*, 969-982.
- Maksym, T., and M. O. Jeffries (2001), Phase and compositional evolution of the flooded layer during snow-ice formation on Antarctic sea ice, *Annals of Glaciology*, 33, 37.
- Manes, S. S., and R. Gradinger (2009), Small scale vertical gradients of Arctic ice algal photophysiological properties, *Photosynth Res.*, 102(1), 53-66, doi:10.1007/s11120-009-9489-0.
- Markus, T., and D. J. Cavalieri (1998), Snow depth distribution over sea ice in the Southern Ocean from passive microwave data, in *Antarctic Sea Ice: Physical Processes, Interactions and Variability*, *Antarct. Res. Ser.*, vol. 74, edited by M. O. Jefferies, pp. 19-39, AGU, Washington, D. C.
- Marschall, H. (1988), The overwintering strategy of Antarctic krill under the pack-ice of the Weddell Sea, *Polar Biology*, 9, 129-135.
- Massom, R. A. et al. (2001a), Snow on Antarctic sea ice, *Rev. Geophys.*, 39(3), 413-445.
- Massom, R., H. Eicken, C. Haas, M. Jeffries, M. Drinkwater, M. Sturm, A. Worby, X. Wu, V. Lytle, and S. Ushio (2001b), Snow on Antarctic sea ice, *Rev. Geophys.*, 39(3), 413-445.
- Mayewski, P. A., M. P. Meredith, C. P. Summerhayes, J. Turner, A. Worby, P. J. Barrett, G. Casassa, N. A. N. Bertler, T. Bracegirdle, A. C. Naveira Garabato, D. Bromwich, H. Campbell, G. S. Hamilton, W. B. Lyons, K. A. Maasch, S. Aoki, C. Xiao, and T. van Ommen (2009), State of the Antarctic and Southern Ocean climate system, *Reviews of Geophysics*, 47, RG1003, doi:10.1029/2007RG000231.
- Maykut, G. A., and N. Untersteiner (1971), Some results from a time-dependent thermodynamic model of sea ice, *J. Geophys. Res.*, 76(4), 1550-1576.
- McClain, C. R., K. Arrigo, K. Tai, and D. Turk (1996), Observations and simulations of physical and biological processes at ocean weather station P, 1951-1980, *J. Geophys. Res.*, 101, 3697-3713, doi:10.1029/95JC03052.
- McMinn, A., J. Skerratt, T. Trull, C. Ashworth, and M. Lizotte (1999), Nutrient stress gradient in the bottom 5 cm of fast ice, McMurdo Sound, Antarctica, *Polar Biology*, 21, 220-227.
- McMinn A., and E. N. Hegseth (2003), Early spring pack ice algae in the Arctic and Antarctic, in *Antarctic biology in a global context, proceedings of the VIIIth international biology symposium 27 August–1 September 2001*, edited by A. H. L. Huiskes, W. W. C. Gieskes, J. Rozema, R. M. L. Schorno, S. M. van der Vies, and W. J. Wolff, pp. 182-186, Vrije Universiteit, Amsterdam, The Netherlands.
- McMinn, A., K. G. Ryan, P. J. Ralph, and A. Pankowski (2007), Spring sea ice photosynthesis, primary productivity and biomass distribution in eastern Antarctica, 2002–2004, *Mar Biol.*, 151(3), 985-995, doi:10.1007/s00227-006-0533-8.

- McPhee, M., C. Kottmeier, and J. Morison (1999), Ocean Heat Flux in the Central Weddell Sea during Winter, *Journal of Physical Oceanography*, 29, 1166-1178.
- Melnikov, I. (1998), Winter production of sea ice algae in the western Weddell Sea, *Journal of Marine Systems*, 17(1-4), 195-205.
- Morel, A. (1978). Available, usable, and stored radiant energy in relation to marine photosynthesis. *Deep Sea Research*, 25, 673-688.
- Mundy, C., D. Barber, and C. Michel (2005), Variability of snow and ice thermal, physical and optical properties pertinent to sea ice algae biomass during spring, *Journal of Marine Systems*, 58(3-4), 107-120.
- Nakawo, M., and N. Sinha (1981), Growth rate and salinity profile of first-year sea ice in the high Arctic, *Journal of Glaciology*, 27(96), 315-330.
- Nan, S., and J. Li (2003), The relationship between summer precipitation in the Yangtze River valley and the previous Southern Hemisphere Annular Mode. *Geophys. Res. Lett.*, 30(24), 2266, doi: 10.1029/2003GL018381.
- Nicolaus, M., C. Haas, and J. Bareiss (2003), Observations of superimposed ice formation at melt-onset on fast ice on Kongsfjorden, Svalbard, *Physics and Chemistry of the Earth*, 28, 1241-1248, doi:10.1016/j.pce.2003.08.048.
- Nicolaus, M., C. Haas, J. Bareiss, and S. Willmes (2006), A model study of differences of snow thinning on Arctic and Antarctic first-year sea ice during spring and summer, *Annals of Glaciology*, 44(1), 147-153.
- Nolin, A., R.L. Armstrong, and J. Maslanik (1998), Near-Real-Time SSM/I EASE-Grid Daily Global Ice Concentration and Snow Extent, http://nsidc.org/data/docs/daac/nise1_nise.gd.html, Natl. Snow and Ice Data Cent., Boulder, C. O. (Updated daily.)
- Notz, D., and M. G. Worster (2009), Desalination processes of sea ice revisited, *J. Geophys. Res.*, 114, 05006, doi:10.1029/2008JC004885.
- Orsi, A. H., G. C. Johnson and J. L. Bullister (1999), Circulation, mixing, and production of Antarctic Bottom Water, *Prog. Oceanogr.*, 43, 55-109.
- Oshima, K. I., and S. Nihashi (2005), A simplified ice-ocean coupled model for the Antarctic ice melt season, *J. Physical Oceanography*, 35, 188-201.
- Palmisano, A. C., J. B. SooHoo, R. L. Moe, and C. W. Sullivan (1987), Sea ice microbial communities. VII. Changes in under-ice spectral irradiance during the development of Antarctic sea ice microalgal communities, *Mar. Ecol. Prog. Ser.*, 35, 165-173.
- Petrich, C., P. J. Langhorne, and H. Eicken (2006a), Fluid Dynamics Simulations of Sea Ice Structure in the Context of Biological Activity and Meltwater Percolation, *Eos Transactions AGU*, 87(52), C41D-0364.
- Petrich, C., P. J. Langhorne, and Z. F. Sun (2006b), Modelling the interrelationships between permeability, effective porosity and total porosity in sea ice, *Cold Regions Science and Technology*, 44(2), 131-144, doi:10.1016/j.coldregions.2005.10.001.

- Petrich, C., P. Langhorne, and Z. Sun (2006c), Modelling the interrelationships between permeability, effective porosity and total porosity in sea ice, *Cold Regions Science and Technology*, 44(2), 131-144.
- Pogson, L., B. Tremblay, D. Lavoie, C. Michel, and M. Vancoppenolle (2011), Development and validation of a one-dimensional snow-ice algae model against observations in Resolute Passage, Canadian Arctic Archipelago, *J. Geophys. Res.*, 116(C04010), 1-16.
- Pringle, D., H. Eicken, H. Trodahl, and L. Backstrom (2007), Thermal conductivity of landfast Antarctic and Arctic sea ice, *J. Geophys. Res.*, 112(C4).
- Quetin, L. B., R. M. Ross, T. K. Frazer, and K. L. Haberman (1996), Factors affecting distribution and abundance of zooplankton, with an emphasis on Antarctic krill, *Euphausia superba*, in *Foundations for ecological research West of the Antarctic Peninsula*, edited by R. M. Ross, E. E. Hofmann, and L. B. Quetin, *Antarctic Res. Ser.*, 70, pp. 357-371.
- Quetin, L., and R. Ross (2003), Episodic recruitment in Antarctic krill *Euphausia superba* in the Palmer LTER study region, *Mar. Ecol. Prog. Ser.*, 259, 185-200.
- Raymond, B., K. Meiners, C. W. Fowler, B. Pasquer, G. D. Williams, and S. Nicol (2009), Cumulative solar irradiance and potential large-scale sea ice algae distribution off East Antarctica (30°E–150°E), *Polar Biology*, 32(3), 443-452, doi:10.1007/s00300-008-0538-5.
- Reeburgh, W. (1984), Fluxes associated with brine motion in growing sea ice, *Polar Biology*, 3(1), 29-33.
- Ribic, C., D. Ainley, and W. Fraser (1991), Habitat selection by marine mammals in the marginal ice zone, *Antarctic Science*, 3(2), 181-186.
- Robinson, D., K. Arrigo, Z. Kolber, M. Gosselin, and C. Sullivan (1998), Photophysiological evidence of nutrient limitation of platelet ice algae in McMurdo Sound, Antarctica, *J Phycol.*, 34(5), 788-797.
- Rothrock, D. A., Y. Yu, and G. A. Maykut (1999), Thinning of Arctic Sea-Ice Cover, *Geophys. Res. Lett.*, 26, 3469-3472.
- Sabine, C. L. et al. (2004), The ocean sink for anthropogenic CO₂. *Science*, 305, 367-371.
- Schulze, T. P., and M. G. Worster (1999), Weak convection, liquid inclusions and the formation of chimneys in mushy layers, *Journal of Fluid Mechanics*, 388, 197.
- Siegel, V., and V. Loeb (1995), Recruitment of Antarctic krill *Euphausia superba* and possible causes for its variability, *MEPS*, 123, 45-56.
- Sirevaag, A., M. G. McPhee, J. H. Morison, W. J. Shaw, and T. P. Stanton (2010), Wintertime mixed layer measurements at Maud Rise, Weddell Sea, *J. Geophys. Res.*, 115(C2), doi:10.1029/2008JC005141.
- Smetacek, V., R. Scharek, and E.-M. Nöthig (1990), Seasonal and regional variation in the pelagic and its relationship to the life cycle of krill, in *Antarctic Ecosystems, Ecological Change and Conservation*, edited by K. R. Kerry and G. Hempel, pp. 103-114, Springer-Verlag, Berlin, Germany.

- Smith, W., and D. Nelson (1985), Phytoplankton bloom produced by a receding ice edge in the Ross Sea: spatial coherence with the density field, *Science*, 227, 163-166.
- Smith, R. E. H., J. Anning, P. Clement, and G. Cota (1988), Abundance and production of ice algae in Resolute Passage, Canadian Arctic, *MEPS*, 48, 251-263.
- Stammerjohn, S., D. Martinson, R. Smith, X. Yuan, and D. Rind (2008), Trends in Antarctic annual sea ice retreat and advance and their relation to El Niño–Southern Oscillation and Southern Annular Mode variability, *J. Geophys. Res.*, 113, C03S90.
- Steer, A., A. Worby, and P. Heil (2008), Observed changes in sea-ice floe size distribution during early summer in the western Weddell Sea, *Deep Sea Research Part II: Topical Studies in Oceanography*, 55(8-9), 933-942, doi:10.1016/j.dsr2.2007.12.016.
- Sturm, M., and C. Benson (1997), Vapor transport, grain growth and depth-hoar development in the subarctic snow, *Journal of Glaciology*, 43(143), 42-59.
- Sturm, M., K. Morris, and R. Massom (1998), The winter snow cover of the West Antarctic pack ice: its spatial and temporal variability, in *Antarctic Sea Ice: Physical Processes, Interactions and Variability*, *Antarct. Res. Ser.*, vol. 74, edited by M. O. Jeffries, pp. 1–18, AGU, Washington, D. C.
- Sturm, M., D. Perovich, and J. Holmgren (2002), Thermal conductivity and heat transfer through the snow on the ice of the Beaufort Sea, *Journal of Geophysical Research Oceans*, 107(C10), 8043.
- Sturm, M., and R. A. Massom (2009), Snow and sea ice, in *Sea Ice*, 2nd ed., edited by D. N. Thomas and G. S. Dieckmann, Wiley-Blackwell, Hoboken, N. J.
- Sweeney, C. (2003), The annual cycle of surface water CO₂ and O₂ in the Ross Sea: A model for gas exchange on the continental shelves of Antarctica, in *Biogeochemistry of the Ross Sea, Antarct. Res. Ser.*, vol. 78, edited by R. B. Dunbar and G. R. DiTullio, pp. 295-312, AGU, Washington, D. C.
- Takahashi, T., J. Olafsson, J. Goddard, D. W. Chipman, and S. C. Sutherland (1993), Seasonal variation of CO₂ and nutrients in the high-latitude surface oceans: a comparative study, *Global Biogeochemical Cycles*, 7, 843–878.
- Takahashi, T., S. C. Sutherland, C. Sweeney, A. Poisson, N. Metzl, B. Tilbrook, N. Bates, R. Wanninkhof, R. A. Feely, C. Sabine, J. Olafsson, and Y. Nojiri (2002), Global sea-air CO₂ flux based on climatological surface ocean pCO₂, and seasonal biological and temperature effects, *Deep Sea Res., Part II*, 49, 1601-1622.
- Tannehill, J. C., D. A. Anderson, and R. H. Pletcher (1997), *Computational fluid mechanics and heat transfer*, 2nd ed., 792 pp., Taylor & Francis, Philadelphia.
- Toyota, T., S. Takatsuji, K. Tateyama, and K. Naoki (2007), Properties of sea ice and overlying snow in the Southern Sea of Okhotsk, *Journal of Oceanography*, 63, 393-411.
- Tucker, W., III, D. Perovich, A. Gow, W. Weeks, and M. Drinkwater (1992), Physical properties of sea ice relevant to remote sensing, *Microwave Remote Sensing of Sea Ice. Geophysical Monograph* 68, 9-28.
- Turner, J., W. M. Connolley, S. Leonard, G. J. Marshall, and D. G. Vaughan (1999), Spatial and temporal variability of net snow accumulation over the Antarctic from ECMWF re-analysis project

- data, *International Journal of Climatology*, 19(7), 697-724, doi:10.1002/(SICI)1097-0088(19990615)19:7<697::AID-JOC392>3.3.CO;2-V.
- Turner, J., S. R. Colwell, G. J. Marshall, T. A. Lachlan-Cope, A. M. Carleton, P. D. Jones, V. Lagun, P. A. Reid, and S. Iagovkina (2005), Antarctic climate change during the last 50 years, *Int. J. Climatol.*, 25, 279–294, doi:10.1002/joc.1130.
- Vancoppenolle, M., T. Fichefet, H. Goosse, S. Bouillon, G. Madec, and M. A. M. Maqueda (2009), Simulating the mass balance and salinity of Arctic and Antarctic sea ice. 1. Model description and validation, *Ocean Modelling*, 27(1-2), 33-53, doi:10.1016/j.ocemod.2008.10.005.
- Vancoppenolle, M., H. Goosse, A. de Montety, T. Fichefet, B. Tremblay and J.-L. Tison (2010), Modelling brine and nutrient dynamics in Antarctic sea ice : the case of dissolved silica, *J. Geophys. Res.*, 115, C02005, doi:/10.1029.2009JC005369.
- Wadhams, P., M. A. Lange, and S. F. Ackley (1987), The ice thickness distribution across the Atlantic sector of the Antarctic Ocean in midwinter, *J. Geophys. Res.*, 92(C13), 14535-14552, doi:10.1029/JC092iC13p14535.
- Wakatsuchi, M. and N. Ono (1983), Measurements of salinity and volume of brine excluded from sea ice, *J. Geophys. Res.*, 88(C5), 2943-2951.
- Warren, S. (1982), Optical properties of snow, *Reviews of geophysics and space physics*, 20(1), 67–89.
- Warren, S., and W. Wiscombe (1980), A model for the spectral albedo of snow. II: Snow containing atmospheric aerosols, *Journal of the Atmospheric Sciences*, 37(12), 2734-2745.
- Weeks, W. F. (1962), Tensile strength of NaCl ice, *J. Glaciol.*, 4, 25-52.
- Weeks, W. F. (1998), On the history of research on sea ice, in *Physics of ice-covered seas*, edited by M. Leppäranta, vol. 1, pp. 1-24, University of Helsinki, Helsinki, Finland.
- Weeks, W. F. and S. F. Ackley (1986), The growth structure and properties of sea ice, in *Geophysics of sea ice*, edited by N. Untersteiner, NATO ASI Series 3, volume 146, pp. 9-164, Plenum Press, New York.
- Welch, H., and M. Bergmann (1989), Seasonal development of ice algae and its prediction from environmental factors near Resolute, NWT, Canada, *Canadian Journal of Fisheries and Aquatic Sciences*, 46(10), 1793-1804.
- Wettlaufer, J., M. G. Worster, and H. Huppert (1997), Natural convection during solidification of an alloy from above with application to the evolution of sea ice, *Journal of Fluid Mechanics*, 344, 291-316.
- Wettlaufer, J. S., M. G. Worster, and H. E. Huppert (1997), The phase evolution of young sea ice, *Geophys. Res. Lett.*, 24, 1251-1254, doi:10.1029/97GL00877.
- Winton, M. (2000), A Reformulated Three-Layer Sea Ice Model, *Journal of Atmospheric and Oceanic Technology*, 17, 525-531, doi:10.1175/1520-0426(2000)017<0525:ARTLSI>2.0.CO;2.
- Wiscombe, W., and S. Warren (1980), A model for the spectral albedo of snow. I: Pure snow, *Journal of the Atmospheric Sciences*, 37(12), 2712-2733.

- Wolter, K., and M. S. Timlin (1993), Monitoring ENSO in COADS with a seasonally adjusted principal component index, *Proc. of the 17th Climate Diagnostics Workshop*, Norman, OK, NOAA/NMC/CAC, NSSL, Oklahoma Clim. Survey, CIMMS and the School of Meteor., Univ. of Oklahoma, 52-57.
- Wolter, K., and M. S. Timlin (1998), Measuring the strength of ENSO events - how does 1997/98 rank?, *Weather*, 53, 315-324.
- Worby, A., C. Geiger, M. Paget, and M. Van Woert (2008a), Thickness distribution of Antarctic sea ice, *J. Geophys. Res.*, 113, C05S92, doi:10.1029/2007JC004254
- Worby, A. P., T. Markus, A. D. Steer, V. I. Lytle, and R. A. Massom (2008b), Evaluation of AMSR-E snow depth product over East Antarctic sea ice using in situ measurements and aerial photography, *J. Geophys. Res.*, 113(C05S94), 1-13, doi:10.1029/2007JC004181.
- Worster, M. G. (1997), Natural convection in a mushy layer, *Journal of Fluid Mechanics*, 224, 335-359.
- Worthen, D. L., and K. R. Arrigo (2003), A coupled ocean-ecosystem model of the Ross Sea: 1. Interannual variability of primary production and phyto- plankton community structure, in *Biogeochemistry of the Ross Sea, Antarct. Res. Ser.*, vol. 78, edited by R. B. Dunbar and G. R. DiTullio, AGU, Washington, D. C..
- Wu, X., W. F. Budd, V. I. Lytle, and R. A. Massom (1999), The effect of snow on Antarctic sea ice simulations in a coupled atmosphere-sea ice model, *Climate Dynamics*, 15, 127, doi:10.1007/s003820050272.
- Yager, P. L., D. W. R. Wallace, K. M. Johnson, W. O. Smith, P. J. Minnett, and J. W. Deming (1995), The Northeast Water Polynya as an atmospheric CO₂ sink: A seasonal rectification hypothesis, *J. Geophys. Res.*, 100(C3), 4389-4398, doi:10.1029/94JC01962.
- Yuan, X. (2004), ENSO-related impacts on Antarctic sea ice: a synthesis of phenomenon and mechanisms, *Antarctic Science*, 16(4), 415-425, doi:10.1017/S0954102004002238.
- Yuan, X., and D. Martinson (2000), Antarctic sea ice extent variability and its global connectivity, *J. Climate*, 13(10), 1697-1717.
- Zeebe, R., H. Eicken, D. Robinson, D. Wolf-Gladrow, and G. Dieckmann (1996), Modeling the heating and melting of sea ice through light absorption by microalgae, *J. Geophys. Res.*, 101(C1), 1163-1182.
- Zhang, J., and D. Rothrock (2003), Modeling global sea ice with a thickness and enthalpy distribution model in generalized curvilinear coordinates, *Monthly Weather Review*, 131(5), 845-861.